

About the Flameless Combustion of Pulverized Coal at the Pilot Scale: Experiment and Simulation

Von der Fakultät für Energie-, Verfahrens- und Biotechnik
der Universität Stuttgart
zur Erlangung der Würde eines
Doktors der Ingenieurwissenschaften (Dr.-Ing.)
genehmigte Abhandlung

vorgelegt von
Max Christoph Weidmann
aus Prien am Chiemsee

Hauptberichter: Prof. Dr. techn. Günter Scheffknecht
Mitberichter: Prof. Dr.-Ing. Reinhold Kneer

Tag der mündlichen Prüfung: 17.07.2018

Institut für Feuerungs- und Kraftwerkstechnik
der Universität Stuttgart
2018

Preface

This work came into being during my time at the Institute of Combustion and Power Plant Technology (IFK) at Stuttgart University. Experiments and simulations were conducted in the course of the FLOX-COAL-II project, by the European Research Fund for Coal and Steel.

I would like to extend special thanks to Professor Scheffknecht, head of IFK, for overtaking the head of reporting. Secondly, I would like to thank Professor Kneer for being responsible for the vice-head of reporting.

My thorough thanks go to the departments DEU, FDS and KWF for the active support and the fruitful discussions. Here, I would like to single out Professor Schnell, who often discussed parts of my work with me. In addition, I want to thank all of my co-workers at IFK for the great atmosphere and the great time at the institute, with many colleagues becoming friends. Finally, I would like to express my deep gratefulness to all the co-workers of the FLOX-COAL-II research project for the great cooperation.

Lastly, my beloved wife Regina, my family and friends continuously motivated me during the process of writing and finalizing this work, which was a great support and for which I am very thankful.

Chieming, June 2017

Max Weidmann

Abstract

Flameless combustion has shown a great potential for nitric oxides (NO_x) abatement, reaction zone and temperature field homogenization. NO_x is one of the main pollutants emitted from power plants. As NO_x is minimized during combustion, the required effort in the downstream flue gas cleaning can be reduced. This is especially relevant if stronger regulations are expected in the future. Different identification methods of flameless combustion are summarized in this work. Flameless combustion is characterized by a strong internal recirculation of hot flue gases and a strong dilution of the fresh reactants combustion air and pulverized coal, amongst others. On the one hand, the homogenized reaction zone and temperature field are the guarantors for the NO_x abatement, jointly with the O_2 -deficient atmosphere. On the other hand, the homogenized temperature field allows for an increased flue gas temperature level, since lower safety factors against temperature peaks can be applied during furnace design, as this is currently possible because of the higher temperature fluctuations of conventional flame burners. Thus, an increased burnout due to better fuel conversion at higher temperatures can be expected.

This work investigates the flameless combustion of a pulverized high-volatile bituminous coal in both experiment and simulation at the pilot scale. It aims to show how different burner designs and different coal-carrier-gases influence the flameless combustion of pulverized coal. Therefore, two different burner prototypes are investigated: the first one has a central coal-carrier-gas annulus and two eccentrically located combustion air nozzles; the second one features two coal-carrier-gas annuli located on the same pitch-circle diameter as the two combustion air nozzles. Both prototype burners ensure sufficiently high internal flue-gas recirculation necessary for establishing flameless combustion. Detailed experimental data are available for the flow field by laser Doppler velocimetry (LDV), for the reaction zone, its topology and its reaction intensity, by OH^* chemiluminescence imaging, and for the main reactive species and the prevailing temperatures by suction-probe sampling. In addition, the total and the radiative heat fluxes are analyzed. Two different flameless operating conditions have been tested for each prototype burner. It is shown that the choice of the coal-carrier-gas, CO_2 or air, can strongly influence the burnout and NO_x formation for the central coal-carrier-gas annulus. As the pulverized coal directly emerges into the hot and oxygen-deficient flue-gas recirculation zone, similar results are achieved, regardless of the applied coal-carrier-gas type.

A state-of-the-art low- NO_x flame burner has been investigated in air-staged and unstaged

operation modes for reference. It performs well regarding the low NO_x concentration which is similar or lower to that of the flameless burners, if it is operated in an air-staged mode. This leads to the conclusion that a lower O_2 concentration in the reaction zone of the flameless burner prototypes needs to be striven for to achieve lower NO_x concentrations, either by air-staging or by emphasizing the internal flue gas recirculation. It is recommended that the threshold of the internal recirculation is surpassed for solid fuels, as the limit for gaseous fuels of approximately 350 % seems too low.

Flameless combustion is secondly investigated by means of computational fluid dynamics (CFD). Therefore, IFK's in-house program code AIOLOS is deployed which describes the reactive fluid flow based on the Reynolds-averaged Navier-Stokes equations. The CFD program code is validated for flameless pulverized coal combustion using the experimental data. The main focus is drawn on the mixing of the entering reactants and the recirculated flue gas, and on the chemical reactions taking place in this highly diluted atmosphere. Thus, the turbulence model, the turbulence-chemistry interaction model and the chemical reaction model including pollutants, such as NO_x , are investigated. Three $k-\varepsilon$ turbulence models are compared against the velocity data obtained by LDV, and the RNG $k-\varepsilon$ model gives the best agreement. Different model constants of the eddy-dissipation concept (EDC) model are tested to reproduce the turbulence-chemistry interaction, and one best-fitting set of constants is identified. The global combustion reaction model is assessed with regards to the application of a detailed pyrolysis pre-processing. The modeling of the NO_x formation and reduction is realized in a post-processing step, based on the converged combustion simulation. A global reaction model respecting the fuel-NO and thermal NO paths is applied. As for the combustion reaction model, the influence of detailed pyrolysis pre-processing is researched. The initial nitrogen split into char-N, tar-N and light-gas-N can strongly alter the result of the NO_x post-processing. The char-N release path is found to be of key interest.

The experimental results highlight the requirement for establishing a highly diluted atmosphere at a temperature level well above the auto-ignition temperature of the fuel, in order to ensure good NO_x reduction and fuel conversion. The computational results emphasize the importance of a detailed analysis of the pyrolysis products. This holds for both the combustion and the NO_x reaction models.

Kurzfassung

Die flammlose Verbrennung hat in der Vergangenheit ihr großes Potential zur Vermeidung von Stickoxiden (NO_x) und zur Homogenisierung der Reaktionszone und des Temperaturfeldes bewiesen. NO_x ist einer der Hauptschadstoffe, der von Feuerungsanlagen ausgestoßen wird. Eine Senkung der NO_x -Konzentrationen am Feuerraumende reduziert den Aufwand bei der anschließenden Rauchgasreinigung, der sonst durch die in Zukunft zu erwartenden strengeren Grenzwerte stiege. Verschiedene bekannte Methoden zur Charakterisierung der flammlosen Verbrennung sind in dieser Arbeit zusammengefasst. Die flammlose Verbrennung ist durch eine hohe interne Rezirkulation heißer Rauchgase und einer dadurch hervorgerufenen starken Verdünnung der neu eintretenden Reaktanden Verbrennungsluft und Kohlenstaub charakterisiert. Eine homogene Reaktionszone und ein entsprechend vergleichmäßigt Temperaturfeld sind neben der Senkung des lokalen Sauerstoffgehalts die Garantien für die Senkung der NO_x -Konzentration. Des Weiteren erlaubt ein homogenes Temperaturfeld ein höheres Rauchgastemperaturniveau, da bei der Brennkammerauslegung geringere Sicherheiten gegen Temperaturspitzen berücksichtigt werden können, als dies aufgrund der größeren Temperaturschwankungen bei konventionellen Brennern notwendig ist. Somit kann ein besserer Ausbrand aufgrund besserer Brennstoffkonversion durch ein erhöhtes Temperaturniveau erwartet werden.

Diese Arbeit untersucht experimentell und simulativ die flammlose Verbrennung einer hochflüchtigen Steinkohle im Pilotmaßstab. Es wird aufgezeigt, wie unterschiedliche Brennerdesigns und verschiedene Kohle-Traggastypen die flammlose Verbrennung von Kohlenstaub beeinflussen. Dafür werden zwei verschiedene Brennerprototypen untersucht: der erste Brenner hat einen zentralen Ringspalt für das Kohle-Traggasgemisch sowie zwei exzentrische, einander gegenüberliegende Verbrennungsluftdüsen, beim zweiten Brenner sind auch die Ringspaltdüsen für das Kohle-Traggasgemisch exzentrisch angeordnet. Beide Brennerprototypen sind darauf ausgelegt, eine ausreichend hohe interne Rauchgasrezirkulation zu gewährleisten.

Detaillierte experimentelle Daten stehen zum Strömungsfeld durch Laser-Doppler-Anemometrie (LDV), zur Reaktionszone mit ihrer Topologie und der vorherrschenden Reaktionsintensität durch die Abbildung der OH^* -Chemilumineszenz und zu den Hauptreaktanden und den vorherrschenden Temperaturen durch Absaugsonden zur Verfügung und werden analysiert. Des Weiteren werden auch die Gesamt- und Strahlungswärmestromdichten analysiert. Zwei unterschiedliche flammlose Versuchsbedingungen werden für jeden Brennerprototypen evaluiert. Die Wahl des Kohle-Traggases, CO_2 oder Luft, beeinflusst den Ausbrand und die NO_x -

Entstehung stark, wenn die Ringspaltdüse für das Kohle-Traggasgemisch zentral im Brenner angeordnet ist. Sobald der Kohlenstaub direkt in die heiße und sauerstoffarme Rauchgasrezirkulationszone eingeblasen wird, werden ähnliche Ergebnisse, unabhängig vom Kohle-Traggastyp, erreicht. Ein moderner Low-NO_x-Flammenbrenner mit und ohne Luftstufung dient als Referenz. Dieser zeigt gute Ergebnisse hinsichtlich der gemessenen NO_x-Konzentrationen, die ähnlich gut oder sogar niedriger sind als die der flammlosen Brennerprototypen, wenn Luftstufung genutzt wird. Daraus wird geschlossen, dass für geringere NO_x-Konzentrationen eine weitere Absenkung der O₂-Konzentration in der Reaktionszone der flammlosen Brennerprototypen erreicht werden muss, entweder durch Luftstufung oder durch Verstärkung der internen Rauchgasrezirkulation. Um eine stabile flammlose Verbrennung zu erreichen, wird für feste Brennstoffe ein Grenzwert der internen Rauchgasrezirkulation empfohlen, der über dem Grenzwert von 350 % für gasförmige Brennstoffe liegt.

Die flammlose Verbrennung wird zweitens mit Hilfe der numerischen Strömungssimulation (CFD) untersucht. Hierfür wird das IFK-eigene Programm AIOLOS eingesetzt, das die reaktive Strömung auf Basis der Reynolds-gemittelten Navier-Stokes-Gleichungen beschreibt. Das CFD-Programm wird anhand der experimentellen Daten für die flammlose Verbrennung von Kohlenstaub validiert. Das Hauptaugenmerk liegt auf der Vermischung von eintretenden Reaktanden und rezirkuliertem Rauchgas, sowie den in einer verdünnten Atmosphäre stattfindenden chemischen Reaktionen. Somit wird die Modellierung der Turbulenz, der Turbulenz-Chemie-Interaktion und der chemischen Reaktionen, einschließlich der NO_x-Schadstoffreaktionen, untersucht. Drei $k-\varepsilon$ Turbulenzmodelle werden mit den experimentellen Geschwindigkeitsdaten verglichen, wobei das RNG $k-\varepsilon$ Modell die besten Übereinstimmungen liefert. Verschiedene Modellkonstanten des Eddy-Dissipation-Concept (EDC) Modells werden zur Beschreibung der Turbulenz-Chemie-Interaktion getestet, und ein Bestsatz identifiziert. Das globale Verbrennungsreaktionsmodell wird hinsichtlich der Anwendung eines detaillierten Pyrolysemodells evaluiert. Die Modellierung der NO_x-Entstehung und -Reduktion erfolgt im sogenannten Post-Processing, auf Basis der konvergierten Verbrennungssimulation. Dafür wird ein globales Reaktionsmodell eingesetzt, das die Bildungspfade Brennstoff-NO und thermisches NO berücksichtigt. Wie bereits für das Verbrennungsreaktionsmodell wird der Einfluss eines detaillierten Pyrolyse-Pre-Processing untersucht, da die Aufteilung des Brennstoff-N in Koks-N, Teer-N und Flüchtigen-N zu Beginn des NO_x-Post-Processings dessen Ergebnis signifikant beeinflussen kann. Dabei spielt die Freisetzung von Koks-N eine wichtige Rolle für die berechnete NO_x-Konzentration am Brennkammerende.

Die experimentellen Ergebnisse stellen die Notwendigkeit einer hoch verdünnten Atmosphäre bei gleichzeitig hohem Temperaturniveau oberhalb der Selbstentzündungstemperatur des Brennstoffs heraus, um eine gute NO_x-Reduktion und Brennstoffkonversion zu erreichen. Die numerischen Ergebnisse heben die Wichtigkeit einer detaillierten Analyse der Pyrolyseprodukte hervor. Dies gilt sowohl für das Verbrennungs- als auch das NO_x-Reaktionsmodell.

Contents

Abstract	v
Kurzfassung	vii
Nomenclature	xi
1 Introduction	1
1.1 History of flameless combustion	1
1.2 Characteristics and characterization of flameless combustion	4
1.3 NO _x conversion and abatement	9
1.4 Previously published parts of the work at hand	13
1.5 The FLOX-COAL-II project	13
2 Methodology of This Work	14
3 Experimental Investigation of Flameless Combustion at 250 kW_{th}	17
3.1 KSVA test facility and applied flameless burners	17
3.2 Measurement techniques and uncertainties	20
3.3 Operating conditions	26
3.4 Fuel	28
3.5 Reference flame burner tests	30
3.6 Influence of CCG dilution and coal dispersion – PT1 tests	31
3.7 Influence of CCG nozzle positioning - PT2 tests	44
4 Mathematical Modeling	54
4.1 Basic equations in computational fluid dynamics	55
4.2 Boundary conditions	66
4.3 Heat transfer	69
4.4 Fluid flow	72
4.5 Chemical reactions	80
4.6 Grid evaluation for high velocity problems	96
4.7 Simulation results of flameless pulverized coal combustion	98
5 Conclusion and Outlook	118
Bibliography	122
Appendices	137
A An Alternative Approach to Derive the Recirculation Rate K_v	139
A.1 Definition of prior-to-mixing length L_v	139

A.2	Definition of recirculation rate K_v	140
B	The Influence of Nozzle Positioning on the Recirculation Rate and the De- volatilization	144
B.1	Investigated burner geometries	144
B.2	Applied grids and numerical setup	145
B.3	Results	147
C	Modeling Know-How	149
C.1	Clues and knowledge in numerics	149
C.2	The simple Cartesian test case	154
C.3	Furnace wall temperatures measured in experiments and simulations	161
C.4	Nitrogen balance in AIOLOS	163

Nomenclature

Latin symbols

Symbol	Unit	Quantity
a_{ext}	$m^2 kg^{-1}$	specific external surface area
A	—	coefficient matrix
A_ϕ	—	matrix coefficient
b	—	temperature exponent
c_k	$mg m^{-3}$	mass concentration of species k
c_p	$J (kg K)^{-1}$	specific heat capacity
C	—	constant
D	m	diameter
\tilde{D}_k	$m^2 s^{-1}$	diffusivity of species k
Da	—	Damköhler number
E_i	$J kmol^{-1}$	activation energy of reaction i
g	$m s^{-2}$	gravity constant
G_k	<i>var.</i>	production term of kinetic energy
I_{rad}	$W m^{-2} sr^{-1}$	radiative intensity
I_{turb}	—	turbulence intensity
H	m	height
h	$kJ kg^{-1}$	specific enthalpy
H_o	$kJ kg^{-1}$	gross calorific value
H_u	$kJ kg^{-1}$	net calorific value
k	$m^2 s^{-2}$	turbulent kinetic energy
k_{RR}	—	Rosin-Rammler parameter
K	<i>var.</i>	reaction speed constant
K_v	—	recirculation rate

Symbol	Unit	Quantity
K_0	<i>var.</i>	frequency factor
L	m	length, distance
L_v	m	prior-to-mixing length
M	kg	mass
\tilde{M}	kg kmol ⁻¹	molar mass
\dot{M}	kg s ⁻¹	mass flow
Ma	—	Mach number
n	—	air ratio, reaction order
N	—	load, number
p	Pa	pressure
Pr	—	Prandtl number
\dot{Q}''	W m ⁻²	heat flux
R	m	radius
\tilde{R}	J (mol K) ⁻¹	universal gas constant (8.134)
\dot{R}_i	<i>var.</i>	reaction rate of reaction i
Re	—	Reynolds number
\vec{s}	—	direction of propagation of radiation
S	<i>var.</i>	general sink / source term
Sc	—	Schmidt number
St	—	Stokes number
t	s	time
T	K	absolute temperature
V	m ³	volume
\dot{V}	m ³ s ⁻¹	volumetric flow
w	m s ⁻¹	velocity
W	m	width
x	m	coordinate
x_k	%	mass fraction of species k
y	m	coordinate
y_k	% or ppm	volumetric fraction of species k

Symbol	Unit	Quantity
z	m	coordinate

Greek symbols

Symbol	Unit	Quantity
α	—	coefficient, angle
α_W	$W (m^2 K)^{-1}$	heat transfer coefficient
β	—	coefficient
β_ν	—	spectral extinction coefficient
γ_i	$kg kg^{-1}$	mass fraction of fuel component i
γ^*	$kg kg_{tot}^{-1}$	fine structure mass fraction
Γ_ϕ	$kg (m s)^{-1}$	general diffusion coefficient
Γ_{turb}	$kg (m s)^{-1}$	turbulent diffusion coefficient
δ	—	iteration update
δ_{ij}	—	Kronecker delta
ϵ	—	iteration error vector
ε	$m^2 s^{-3}$	turbulent dissipation rate
η	—	expansion parameter of k - ε turbulence model
η_{abs}	—	absorption efficiency factor
η_{scat}	—	scattering efficiency factor
ϑ	$^\circ C$	temperature
κ	—	EDC exponent
κ_{abs}	—	absorption coefficient
λ_{RR}	—	Rosin-Rammler parameter
μ	$kg(m s)^{-1}$	dynamic viscosity
μ	$kg_{oxi} kg_f^{-1}$	fuel-specific oxidant demand
ν	$m^2 s^{-1}$	kinematic viscosity
ν	m^{-1}	wave number
$\nu_{i,j}$	$mol_j (mol)^{-1}$	stoichiometric coefficient of species j in reaction i
ξ	—	relative nitrogen split
Ξ	—	flameless characterization ratio

Symbol	Unit	Quantity
π	—	circle constant
ρ	kg m^{-3}	density
ϱ	—	residual vector of iteration process
σ	N m^{-2}	normal stress
σ_{ij}	N m^{-2}	strain rate tensor
σ_k	—	constant of k - ε turbulence model
σ_ε	—	constant of k - ε turbulence model
σ_{scat}	—	scattering coefficient
τ_{ij}	N m^{-2}	shear stress
ϕ	<i>var.</i>	general variable
φ	—	solution vector in equation system
Φ_ν	—	spectral scattering coefficient
χ	mol mol^{-1}	mole fraction
ψ	<i>var.</i>	boundary condition vector
ω	—	relaxation factor
$\dot{\omega}_k$	$\text{kg}(\text{m}^3 \text{s})^{-1}$	net production rate of species k
Ω	sr	spatial angle of radiation

Subscripts

Symbol	Quantity
A	ash
aAv	area-averaged
abs	absorption
air	air
as	air-staged
auto	auto
b	black
BL	boundary layer
coal	coal
C	carbon, char

Symbol	Quantity
CA	combustion air
CCG	coal-carrier-gas
CC	combustion chamber, furnace
chem	chemical
cum	cumulative
daf	dry and ash free
diff	diffusion
dyn	dynamic
EDC	eddy dissipation concept
eff	effective
eq	equilibrium
ext	external, outer
f	fuel
Fla	flame
FO	flame occupation
FS	flame supervision
G	gas
heat	heat
hyd	hydraulic
i	index number
in	in
j	index number
jet	jet
k	index number
kin	kinetic
min	minimum
med	medium
max	maximum
mix	mixture
nb	neighbor

Symbol	Quantity
noz	nozzle
OM	oxidation mixture
out	out
oxi	oxidant
p	pressure
P	particle
rad	radiative
rea	reaction, reactive
reatt	reattachment
rec	recirculation
rel	relative
res	residence
rot	rotated
RC	raw coal
RJ	reactive jet
RMS	root-mean-square
RTE	radiative transfer equation
s	solid
samp	sample
scat	scattering
soot	soot
st	stoichiometric
start	start
sub-st	sub-stoichiometric
STP	standard temperature and pressure
t	time
th	thermal
tot	total
turb	turbulent
TU	temperature uniformity

Symbol Quantity

TV	total volatile
UC	unburned carbon
vAv	volume-averaged
Wa	wall
WGS	water-gas-shift
Y	cell number

Superscripts**Symbol Quantity**

*	assigned to fine structures
^	unrelaxed variable of n+1-th iteration
-	Reynolds-averaged
~	Favre-averaged
'	Reynolds-fluctuation
"	Favre-fluctuation
cbo	char burnout
n	iteration counter
pyr	pyrolysis
SF	surrounding fluid

Abbreviations**Symbol Quantity**

APH	air preheater
CA	combustion air
C-in-ash	carbon in ash
CCD	charge-coupled device
CCG	coal-carrier-gas
CFD	computational fluid dynamics
CPD	chemical percolation devolatilization
CL	chemiluminescence

Symbol	Quantity
CORIA	Inter-professional Research Complex of Aerothermochemistry (Complexe de Recherche Interprofessionnel en Aerothermochimie)
daf	dry-ash-free
DIN	German Institute of Standardization (Deutsches Institut für Normung)
DNS	direct numerical simulation
EDC	eddy dissipation concept
EN	European standard (Europäische Norm)
ESP	electro-static precipitator
FD	forced draught
FG-DVC	functional group - depolymerization, vaporization cross-linking
FTIR	Fourier transform infrared spectroscopy
FLOX	flameless oxidation
FS	flame supervision
HiTAC	high temperature air combustion
HPAC	highly preheated air combustion
ID	induced draught
IEA	International Energy Agency
IFK	Institute of Combustion and Power Plant Technology (Institut für Feuerungs- und Kraftwerkstechnik)
IFRF	International Flame Research Foundation
INSA	National Institute of Applied Sciences (Institute Nationale de Sciences Appliquees)
KSVA	pulverized coal combustion rig (Kohlenstaubverbrennungsanlage)
LDV	laser Doppler velocimetry
LES	large eddy simulation
MILD	moderate and intense low oxygen dilution
NDIR	non-dispersive infrared spectroscopy
PISO	pressure implicit with the splitting of operator
PSR	perfectly stirred reactor
PT	prototype

Symbol	Quantity
RANS	Reynolds-averaged Navier-Stokes
RNG	re-normalization group
RMS	root-mean-square
RR	Rosin-Rammler
RSM	Reynolds stress model
RTE	radiative transfer equation
RWTH	Rhenish-Westphalian technical university (Rheinisch-Westfälische Technische Hochschule)
SCR	selective catalytic reduction
SIMPLE	semi-implicit method for pressure-linked equations
SIMPLEC	semi-implicit method for pressure-linked equations consistent
STP	standard temperature pressure
TOC	total organic carbon
UC	unburned carbon
UV	ultraviolet
WSA	Institute of Heat and Mass Transfer (Institut für Wärme- und Stoffübertragung)
WSGGM	weighted sum of gray gases model

1 Introduction

Electricity demand is rising worldwide, with coal-fired power generation remaining the backbone of a reliable power supply. Despite the massive expansion of renewable sources in the past years, the share of coal is still approximately 40 % [1]. Air pollution from stationary sources such as power plants or industrial furnaces is one of the major reasons for environmental damage and health issues. The International Energy Agency IEA mentions sulfur oxides (SO_x) and nitric oxides (NO_x) as two of the main pollutants besides particulate matter, emitted from power plants, with a share of 33 % and 14 % of global SO_x and NO_x emissions, respectively [1]. Additionally, the Paris Agreement has set a goal for an increase of the average global temperature well below 2 °C, and a global peaking of greenhouse gas emissions [152]. Increased efficiency and decarbonization of the power-generating sector can contribute to these goals and reduce the global SO_x and NO_x emissions.

Advanced post-combustion measures can be applied, as well as highly developed combustion concepts, mitigating pollutant formation during the combustion process. This is where flameless combustion of coal can greatly contribute, if the development of this combustion technology is successful as has been done for gaseous fuels. Besides the pollutant abatement, flameless combustion is thought to allow for a higher overall combustion temperature level because of its homogeneity in temperature fields and heat release, promoting lower stresses of components exposed to a high temperature region by temperature peaks.

1.1 History of flameless combustion

In the early 1990s, flameless combustion was discovered in the course of improving industrial heating processes fueled with natural gas. Substantial fuel savings up to 15 %, compared to a recuperative furnace, were reported with the so-called excess enthalpy combustion by recovering waste heat to preheat the combustion air close to the furnace temperature levels [144, 168]. However, this method suffered from drastically increased NO_x emissions caused by the increase of furnace temperatures boosting thermal NO_x formation. To overcome this penalty, researchers proposed sufficient separation of fuel and oxidant inlets, achieving low NO_x emissions while maintaining the desired fuel savings [72]. They stated that the key is intensive dilution of highly preheated combustion air with combustion products, prior to mixing with the

fuel and the consecutive reaction. Moreover, they defined the auto-ignition temperature of the fuel-air-mixture as the lower limit for the combustion air preheating, see equation (1.1). The auto-ignition temperature ϑ_{auto} therefore can be understood as specific to each mixture of fuel, oxidizer and diluent. The inlet temperature ϑ_{in} is the mean temperature of this mixture, when it enters the furnace. Processes obeying this condition are named highly preheated air combustion (HPAC) which was later replaced by the term high temperature air combustion (HiTAC).

$$\vartheta_{auto} < \vartheta_{in} \quad (1.1)$$

Wünning and Wünning [174] extended the combustion regime to moderate air preheating temperatures, as known from conventional flame combustors. They explain that a high recirculation rate of hot combustion products can ensure a temperature increase of reactants above the auto-ignition temperature. Consequently, the internal recirculation rate K_v is postulated as the key operating parameter, see equation (1.2).

$$K_v = \frac{\dot{M}_{rec}}{\dot{M}_{in}} \quad (1.2)$$

Therein, \dot{M}_{in} incorporates the incoming mass flow rates and \dot{M}_{rec} represents the mass flow rate of hot, inert combustion products recirculating internally in the zone prior to combustion. Flameless combustion without any air preheating can be established, achieving very low NO_x emissions and very good burnout [9, 75, 92, 120, 146].

In the late 1990s, additional fuels besides gaseous ones attracted attention and the International Flame Research Foundation IFRF started investigations at the 580 kW_{th} scale. Experiments were first conducted with natural gas [156], then with light and heavy fuel oil [157] and finally with high-volatile bituminous pulverized coal [100]. The burner in use featured a central vitiated air jet (O_2 content: 21%), preheated to 1300 °C in a pre-combustor and two fuel nozzles located aside of the central combustor nozzle injecting the fuel directly in the recycled hot combustion products. Weber et al. [161] presented an overview and analysis of the four experiments. They confirmed a drastically reduced pollutant formation, especially of NO_x , and good burnout indicated by CO below the detection limit at the furnace exit during the combustion of all different fuels. The observed uniformity of temperature field and heat flux is considered outstanding in pulverized coal combustion. Weber et al. [161] concluded that the great homogeneity of the reaction zone and the fuel oxidation in a sub-stoichiometric reaction zone contribute essentially to the very good performance regarding pollutant abatement and fuel conversion. Contrary to the luminous appearance of natural gas and light fuel oil combustion with no evidenced flame, the same combustion regime produced constantly visible flamelets and sparks in the cases of heavy fuel oil and pulverized coal combustion. These observations

are reported by various researchers [72, 82, 130, 167].

Cavaliere and de Joannon [17] introduced the term “moderate or intense low-oxygen dilution” (MILD) combustion for a combustion regime occurring in a diluted low oxygen atmosphere and at gentle reaction intensities. The authors correlate the gentle reaction intensities with the temperature increase between educts and products of the combustion process. They state that the maximum achieved temperature can be decreased by a great dilution of reaction educts. Due to this dilution, the mass of educts, except of fuel, and products, i.e. flue gas, becomes much greater than that of fuel and thus, the impact of heat release of the combusting fuel on the maximum temperature becomes smaller, see equation (1.3).

$$\vartheta_{CC,max} = \vartheta_{ref} + \frac{\bar{c}_{p,oxi}|_{\vartheta_{ref}}^{\vartheta_{oxi}} \cdot \vartheta_{oxi} \cdot \dot{M}_{oxi} + \bar{c}_{p,dil}|_{\vartheta_{ref}}^{\vartheta_{dil}} \cdot \vartheta_{dil} \cdot \dot{M}_{dil} + \left(\bar{c}_{p,f}|_{\vartheta_{ref}}^{\vartheta_f} \cdot \vartheta_f + H_{u,f} \right) \cdot \dot{M}_f}{\bar{c}_{p,G}|_{\vartheta_{ref}}^{\vartheta_{CC,max}} \cdot \left(\dot{M}_{oxi} + \dot{M}_{dil} + \dot{M}_f \right)} \quad (1.3)$$

The temperature increase can be thus described by equation (1.4) as the difference between the mean inlet temperature of reactants ϑ_{in} and the maximum temperature $\vartheta_{CC,max}$ established in the furnace. Equation (1.5) constrains the MILD combustion regime accordingly.

$$\Delta\vartheta = \vartheta_{CC,max} - \vartheta_{in} \quad (1.4)$$

$$\Delta\vartheta < \vartheta_{auto} < \vartheta_{in} \quad (1.5)$$

Besides laboratory scale and pilot scale flameless burners, scaled-up flameless pulverized coal burners have been successfully investigated in test rigs at 12 MW_{th} [184] and at 30 MW_{th} [93] thermal input.

Flameless pulverized coal oxy-fuel combustion with different diluents (CO₂, Ar) has been investigated in a laboratory scale furnace [61, 137]. Pilot scale studies on oxy-fuel flameless pulverized coal combustion are reported with burners providing a large separation between coal and the oxidants by [82, 130]. Improvements were recommended on their burner and operating conditions, to ensure a stable and safe combustion [130]. It can be summarized that flameless oxy-fuel combustion of pulverized coal has, to-date, only insufficiently been experimentally investigated.

Numerical studies of flameless combustion have been focused either on the assessment of distinct parameters or on the improvement of accuracy of the computational models. Influence of different combustion air diluents (N₂, CO₂, He, Ar) has been shown by Yuan and Naruse [182] for a gaseous flameless combustion system. They found that the flame temperature is highest for noble gas diluents and lowest for CO₂ diluent, whereas N₂ is in between. This is explained by the increasing specific heat capacity and molecular weight. As a side effect,

reduced O_2 concentration in the combustion air jet promotes temperature homogeneity. Other numerical studies point out enhanced homogeneity for increased jet momentum [90].

The flow field prediction attracted attention early in flameless combustion modeling. Therein, turbulence modeling has been identified as a key issue and will be discussed in Chapter 4. Simulations revealed too little entrainment into the weak jet, whereas strong jets are correctly predicted [87]. The authors developed a system of perfectly stirred reactor models with entrainment ratios calculated from LDV measurement results to verify their findings. With this approach, they obtained very good agreement between temperature, O_2 and NO_x predictions and measured values.

The trustworthiness of the underlying turbulence-chemistry interaction model has also been subjected to detailed investigations. Whilst the eddy dissipation model (EDM) has been successfully applied [47, 90, 123, 124], the more sophisticated eddy dissipation concept (EDC) proved its applicability [3, 32, 61, 74, 86, 91] and is considered superior by several authors [14, 26, 93, 154].

Kim [74] applied a detailed reaction mechanism to natural gas flameless combustion. Based on the results, he numerically investigated the pulverized coal flameless combustion in the 580 kW_{th} IFRF furnace.

Schaffel et al. [123] set up a model of the 580 kW_{th} IFRF furnace with a high-volatile bituminous coal. The model utilizes the sophisticated chemical percolation devolatilization (CPD) model as a pyrolysis preprocessor. The prediction of O_2 , CO and NO_x concentrations, and temperature show very good agreement with the measurement results. However, the authors state that the good agreement of predicted and measured CO concentrations is likely coincidental and that the application of more detailed CO formation and oxidation schemes e.g. of Kim [74] is preferable. The design of a down-fired pulverized coal flameless combustion boiler has been presented and analyzed in [124].

Stadler [136] numerically and experimentally researched flameless combustion of pulverized coal. He investigated the application of flameless combustion to a tangentially fired utility boiler. He concluded that the best performance is achieved as coal and combustion air nozzles are well separated, and as the primary, i.e. reducing, reaction zone is extended.

1.2 Characteristics and characterization of flameless combustion

Flameless combustion shall be described in the following, together with the most common characterization approaches. It can be characterized by its visual and audible experience, the temperature increase within the furnace, the volumetric, thus homogeneous reaction zone and the intense dilution, often accompanied by a high internal recirculation.

The visibility condition When gaseous fuels or light fuel oil are oxidized in a highly diluted atmosphere, no radiation in the visible range is emitted, yielding the denomination “flameless” or “colorless” combustion. This is reported for a variety of test rigs [56, 72, 157, 174]. However, this can be misleading in terms of heavy fuel oil or pulverized solid fuel combustion, as sparks and flamelets may occur [72, 82, 130, 161, 167]. Nevertheless, the term “flameless combustion” is used in this work, relating to its origin and possibly to its ideal appearance. No criterion is known by the author which quantifies the intensity of radiation in the visible range and defines an allowable maximum threshold. The analysis of a flame supervision signal is regarded as an approach for quantification of visibility. It has been observed during experiments presented in Chapter 3 that the intensity of a flame supervision signal is low when a flameless combustion regime is approached or achieved.

The audibility condition The audible phenomenon of a conventional turbulent flame is often experienced as a roar caused by the highly turbulent flame front. In flameless conditions, this roar is reported to disappear due to the lack of a concentrated flame front [93, 130]. As for the visibility criterion, there are no quantitative limits known potentially serving as a criterion.

The temperature condition As previously described, early definitions of flameless combustion - here HPAC, HiTAC or MILD combustion - require the preheating of reactants above the auto-ignition temperature, see equation (1.1). Stable conditions are reported in HiTAC conditions for high, medium and low volatile coals at combustion air temperatures of $\vartheta_{CA} = 800\text{ }^{\circ}\text{C}$ [142]. In contrast to the precondition that reactants must be preheated above the auto-ignition temperature at the inlet, cf. equation (1.5), an adapted MILD combustion definition is proposed including non-premixed, moderately preheated conditions. The temperature at the beginning of the reaction zone ϑ_{start} instead of the inlet temperature ϑ_{in} must be higher than the auto-ignition temperature of the mixture. This accommodates for the fact that the reaction zone can be lifted from the burner exit. The beginning of the reaction zone is defined to be where fuel and oxidant jets start mixing. $\Delta\vartheta$ is same as defined in equation (1.4).

$$\Delta\vartheta < \vartheta_{auto} < \vartheta_{start} \quad (1.6)$$

The volumetric condition Flameless combustion is distinguished as a volumetric combustion regime, with a reaction zone spreading over a wide furnace volume. In contrast, conventional turbulent flame combustion exhibits a concentrated reaction zone along the flame front which can be visually characterized by the flame length [180]. The wide-spread reaction zone leads to homogenized species, heat flux and temperature fields. In order to define the barely visible or invisible reaction zone under flameless conditions, the authors suggest to determine its border by means of the local O_2 demand. Therefore, they define the oxidation mixture ratio Ξ_{OM} by

the available O_2 related to the sum of available O_2 , x_{O_2} , and the stoichiometric O_2 demand, $\mu_{O_2,st}$, of the combusted fuel x_f , see equation (1.7).

$$\begin{aligned}\Xi_{OM} &= \frac{x_{O_2}}{x_{O_2} + \mu_{O_2,st} \cdot x_f} \\ &= \frac{1}{1 + \mu_{O_2,st} \cdot \frac{x_f}{x_{O_2}}}\end{aligned}\quad (1.7)$$

It can be seen that Ξ_{OM} becomes 1 if no fuel is present; it can approach 0 at the fuel inlet, if a fuel without O_2 or with an O_2 -free carrier-gas is used. The latter limit can be regarded as the fuel-rich reaction limit. The fuel-lean limit, i.e. when Ξ_{OM} approaches 1, can be derived by means of the fuel flammability limit according to Yang and Blasiak [180]. The flame can now be assumed to exist anywhere in which Ξ_{OM} is between 0 and 0.99. The flame volume V_{Fla} is the volume within these limits. The extended reaction zone and its impact can be captured by the flame occupation ratio Ξ_{FO} proposed by Yang and Blasiak [180]. It is obtained from equation (1.8), where V_{CC} is the furnace volume.

$$\Xi_{FO} = \frac{V_{Fla}}{V_{CC}} \quad (1.8)$$

The homogeneity condition Homogeneity is a key characteristic and major advantage of a flameless combustion regime. It results from the strong dilution of the reactants before they mix. As dilution is enhanced, gradients of heat release, reaction intensity and temperature become smoother as has numerically and experimentally been shown [18, 47, 68, 115, 137, 182]. Yang and Blasiak [180] introduced the gas temperature uniformity ratio Ξ_{TU} as a characteristic parameter for the homogeneity condition. It can be more easily derived from simulation than from experimental results, as it relates the temperature deviations from the furnace mean temperature $\bar{\vartheta}$ to the latter, see equation (1.9). It can be seen from equation (1.9) that Ξ_{TU} becomes 0 if no gradients occur in the furnace, and that it grows as gradients increase in the furnace.

$$\Xi_{TU} = \sqrt{\frac{(\vartheta_i - \bar{\vartheta})^2}{\bar{\vartheta}^2}} \quad (1.9)$$

In a different publication, Yang and Blasiak [181] presented additional characteristic parameters such as the flame entrainment ratio, the flame heat release and the flame heat occupation coefficient. Especially the parameter of flame entrainment ratio seems not to offer new insights in the process, in contrast to the recirculation rate K_v to be described below.

The dilution condition Wüning [173] introduced the recirculation rate K_v in 1991 as given in equation (1.2) and utilized it as a characteristic number to define the flameless combustion regime with the fulfilled precondition of furnace temperature above auto-ignition temperature. It characterizes two of the most relevant prerequisites to establish flameless combustion which is, on the one hand, the degree of dilution, and, on the other hand, the heat provided to preheat fuel and combustion air before combustion takes place [174].

$$K_v = \frac{\dot{M}_{rec}}{\dot{M}_{in}} = \frac{\dot{M}_{rec}}{\dot{M}_f + \dot{M}_{CA} + \dot{M}_{CCG}} \quad (1.10)$$

In this extended equation (1.10), the incoming mass flows are specified as fuel (\dot{M}_f), combustion air (\dot{M}_{CA}) and fuel-carrier-gas (\dot{M}_{CCG}), if required. An increase in the recirculation mass flow \dot{M}_{rec} results in the heating and the dilution of reactants before they mix and burn. The relationship between emerging combustion air and fuel jets with the recirculating hot flue gases and thus the control of the aerodynamics in the burner vicinity by the emerging jets has been confirmed at the laboratory [119] and pilot [90, 115] scales.

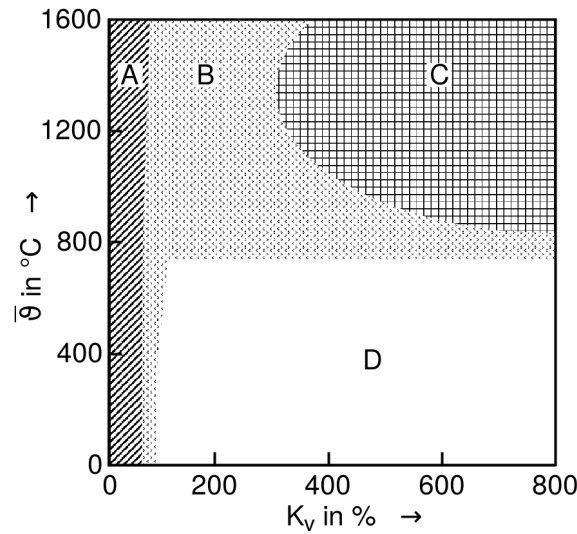


Figure 1.1: Combustion regimes defined by recirculation rate K_v and mean furnace temperature $\bar{\vartheta}$ (adapted from [176])

Wüning [176] drew a commonly accepted diagram, see Figure 1.1, classifying four regimes defined by the recirculation rate K_v and the mean furnace temperature $\bar{\vartheta}$. The diagram was derived for natural gas combustion from experimental observations without any additional calculations [175]. The lines differentiating the regimes are consequently to be judged rather as approximations than as exact delineations. The regime of stable flame combustion A is limited by recirculation rates of approx. 30 %, if furnace temperatures are below the auto-ignition temperature ϑ_{auto} of the mixture [18, 150, 174]. The recirculation rate can be increased up to 100 % for very high furnace temperatures which would result in high NO_x emissions. Increasing

the recirculation rate K_v , the stable and attached flame starts to lift, and the regime switches to unstable lifted flame combustion B. At temperatures above the auto-ignition temperature of the mixture, the combustion regime changes to the flameless combustion regime C, if recirculation rates above 300 % are realized. A flameless combustion regime can be extended to very high recirculation rates (up to 800 %) and high temperatures. Cavigiolo et al. [18] derived similar graphs from experimental investigations of methane and ethane flameless combustion, with a reduced extent of the transition regime B. Temperatures confining the regimes A, C and D are reported in a similar range. In a nutshell, the internal recirculation rate K_v defines the combustion regime as the furnace temperature remains above the auto-ignition temperature. Otherwise, the furnace temperature and recirculation rate determine the realizable operational window.

For pulverized coal combustion, the definition of a flameless combustion regime on the basis of Figure 1.1 is difficult at a first glance, since it is derived for flameless natural gas combustion and it has not yet been validated for other fuels. It can be argued that volatile combustion taking place after coal devolatilization is similar to natural gas combustion. Whilst this might be an interesting approach for light volatiles, reactions and time scales are different for heavy volatiles and even more for char particles. It is thought that the establishment of flameless combustion with pulverized coal would require higher recirculation rates due to higher heat demand in the devolatilization zone for heating and pyrolysis of coal particles and cracking devolatilization products. The definition of the recirculation rate in equation (1.10) requires knowledge of the recirculating mass flow \dot{M}_{rec} which usually can not be obtained from experimental data. To overcome this drawback, Cavigiolo et al. [18] related K_v to the O_2 concentration in the jets and thus to the reaction zone. With the mean O_2 concentration $\bar{x}_{O_2,in}$ of all incoming jets at the burner exit and the mean O_2 concentration $\bar{x}_{O_2,mix}$ of the reactive jet, in which mixing between combustion air and fuel jet occurs, the recirculation rate can then be written as follows in equation (1.11). The air ratio is denoted by n and μ_{O_2} is the specific stoichiometric O_2 demand. Its derivation is given in Appendix A.

$$K_v = \frac{\left(\frac{\bar{x}_{O_2,in}}{\bar{x}_{O_2,mix}} - 1 \right) \cdot n \cdot \mu_{O_2} - 1}{n \cdot \mu_{O_2} + 1} \quad (1.11)$$

Applying the B to C regime limit of $K_v = 300\%$ to equation (1.11), a maximum allowable O_2 concentration in the reactive jet of 6.19 % is determined. If this concentration $\bar{x}_{O_2,mix}$ is higher when fuel and oxidizer jets merge to form the reactive jet, an unstable combustion regime B will occur. Thus, the key parameter K_v needs to be derived at the beginning of the reaction zone, i.e. where mixing of the reactant jets starts, to ensure the required dilution. Therefore, a prior-to-mixing length L_v can be derived from the free jet theory [176], see equation (1.12).

$$L_v \approx 2.99 L_{noz} \quad (1.12)$$

Any recirculating mass flow beyond the beginning of the reaction zone additionally dilutes the reaction zone, but the dilution at the reaction zone start point is mainly responsible for the development of the reaction zone. The derivation of equation (1.12) is detailed in Appendix A.

1.3 NO_x conversion and abatement

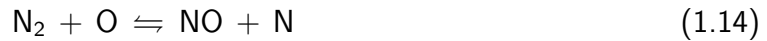
The strong impact of flameless combustion on NO_x formation and the great potential for NO_x abatement was discovered early. Amongst others, the potential of NO_x emission reduction with pulverized coal combustion was investigated during a European research project in a 20 kW_{th} and a 100 kW_{th} furnace [114, 116]. The conversion paths have been experimentally and numerically researched for disclosing the main reaction mechanisms responsible for the outstanding NO_x mitigation. The most relevant nitrogen conversion paths and combustion parameters are summarized below.

Prompt NO Prompt NO is formed in fuel-rich conditions by the attack of hydrocarbon radicals CH_i on molecular nitrogen N₂. Therein, *i* equals 1 or 2. The mechanism, as shown in equation (1.13), was first presented by Fenimore [36].



It plays an important role in natural gas or methane combustion having locally high CH_i concentrations. As hydrocarbon concentration is much lower in coal combustion than in natural gas combustion, a relevant contribution of this mechanism can be neglected [41].

Thermal NO Thermal NO is formed by the oxidation of molecular nitrogen mainly originating from combustion air. This mechanism is highly temperature sensitive, as indicated by its naming, and it significantly contributes to NO_x formation at temperatures above 1300 °C. In conventional pulverized coal combustion systems, thermal NO typically accounts for around 15 % of the total NO_x emission. Thermal NO contributions of 65 % and 40 % to the total NO_x emissions have respectively been reported for a conventional flame burner and a flameless burner in pulverized coal laboratory scale experiments by Ristic [115]. A formal reaction mechanism has been postulated by Zeldovich [183], as is shown in the following.



NO formation from nitrogen radicals, equation (1.15), is very fast in comparison with the attack of O₂ radicals on the intact nitrogen molecule, equation (1.14), due to its stable bonds. Thermal NO formation in sub-stoichiometric conditions is represented by the OH oxidation mechanism in equation (1.16).

The formation of thermal NO can be effectively suppressed by avoiding the presence of molecular nitrogen, as in oxy-fuel furnaces, or by controlling the temperature in the reaction zone. Therefore, an attenuation of the reaction intensity with consequently lowered temperature peaks can be achieved by the external or internal recirculation of flue gases. The recirculation additionally moderates the local O₂ concentration, providing less O₂ to the Zeldovich mechanism. Moderation of temperature and O₂ by the recirculation leads to the successful NO_x abatement in flameless combustion, as fuels without fuel-bound nitrogen, i.e. mainly gaseous fuels are used. Of the same importance is the homogeneous reaction zone and thus the homogeneous temperature profile, triggered by the flameless combustion regime. This allows for a high overall temperature level without temperature peaks. NO_x emissions below 50 ppm at reference O₂ concentration of 11 % are obtained by Suzukawa et al. [144] in a gas-fired flameless combustor with air preheat temperatures up to 1327 °C. For flameless combustion of pulverized coals, a strong cut in thermal NO has been found by Ristic [114] at the laboratory scale, when they compared the combustion of coal with conventional air and with an Ar/O₂ mixture.

Fuel NO NO generated from fuel inherent nitrogen (fuel-N) is the major contributor to NO_x emissions from pulverized coal combustion. It is generally assumed that up to 30 % of the nitrogen contained in the fuel is converted to NO. Fuel-N concentration by weight ranges from 0.5 % to 2.5 % for coals. It is mostly bound in five-membered (pyrrolic) and six-membered (pyridinic) functional groups, with a larger portion, up to 80 % being in the pyrrolic group [50]. Fuel-N is partially released during pyrolysis as tar-N and light gas N (HCN and NH₃), whilst some nitrogen retained in the char is released during char burnout. This split depends mainly on coal rank and pyrolysis temperature, but prevailing conditions and residence time are also of importance [13, 50, 109, 169].

Char-N increases with the coal rank, as less volatile matter in the parent coal allows for less volatile release [50]. Augmented pyrolysis temperatures, on the other hand, strongly enhance the amount of nitrogen being released from the coal, thus lowering the retained char-N [109, 132]. Similarly, residence time in the pyrolysis zone has a promoting effect on nitrogen release; thus, char-N decreases with increasing pyrolysis residence time. During the subsequent char burnout,

HCN does not seem to evolve from the char [64].

Light gas nitrogenous components HCN and NH_3 are released during primary pyrolysis on the one hand, and they are products of the tar-N release during secondary pyrolysis (HCN) and soot-N release during soot oxidation (NH_3) on the other hand [20]. It is still not fully determined whether the split between primary pyrolysis light gases HCN and NH_3 is more temperature [50] or coal rank [21, 22, 71] dependent. In fact, the NH_3 portion increases with lower coal rank: bituminous coals tend to have more HCN, but NH_3 portion increases for lignites [21]. However, if temperatures reach values higher than 1400 K, HCN becomes the more abundant light gas component [50]. Reducing conditions additionally favor the HCN release [21].

Tar as one of the main carriers of fuel-N is released during primary pyrolysis from coal, often exhibiting a similar nitrogen percentage as the parent coal [132]. Tar is subsequently decomposed during secondary pyrolysis, releasing its nitrogen load mainly as HCN, and to a lower extent as soot-N. Soot-N is known to be converted to NH_3 . It is known from experiments [114] and simulations [90] of flameless pulverized coal combustion that the fuel-NO path prevails over both thermal NO and prompt NO. Its importance increases, as the nitrogen content of the fuel increases and the temperature level remains low, thus the thermal NO path contribution becomes negligible. Fuel-NO formation is promoted by combustion air temperature, O_2 and residence time. Investigations of fuel-N conversion are often subjected to modeling, since single reaction mechanisms can hardly be quantified by experiments. It is noted that this quantification can only be of a relative manner, and that the numerical investigations presented in the following strongly depend upon the underlying models.

Fuel-NO formation can be minimized with strong dilution and a homogenized temperature field. Pershing and Wendt [106] found that the conversion of the volatile-N portion of the coal can be strongly reduced in such conditions. According to Chen and Niksa [19], this can be explained by the shift of the devolatilization in regions heavily diluted by flue gas. This delays the mixing between coal and oxidizer.

A strong reduction of oxidizer availability has been identified by several studies as a key strategy of fuel-NO control in gas-fired and NO doped, and coal-fired flameless combustion tests. Strong dilution ensured by a sufficiently high jet momentum has been found essential by Mi et al. [91] in experimental and numerical investigations of gas-fired flameless combustion. This conclusion can be drawn as well for pulverized coal flameless combustion, as Ristic [115] reported stagnation in NO_x reduction for jet velocities above a certain threshold, here $w_{CA} = 150 \text{ m s}^{-1}$. This was observed for lignite and bituminous coals at $300 \text{ kW}_{\text{th}}$. For NO doped methane flameless combustion, Galbiati et al. [46] found substantial fuel-NO reduction to be almost temperature independent if O_2 concentration remains low. Whilst temperature independence can not be confirmed by their experiments for ethane combustion, O_2 dependence is maintained. From gaseous fuel experiments [18], it is known that decreasing the O_2 concentration to 3% homogenizes the temperature field and reduces the NO_x emissions.

Orsino et al. [100] state that NO_x has been found to diminish for low and high inflow velocities as the nozzle spacing of the flameless burner increases. The latter delays the mixing of reactants, thus a stronger dilution and control of O_2 availability in the primary reaction zone due to intense entrainment of inert flue gas is established. This was confirmed by Li et al. [82] and Weber et al. [161]. They also found O_2 and thus NO_x concentration to be higher if the coal-carrier-gas, here air, mass flow was increased. Despite the faster jet velocity, the nozzle arrangement hindered a sufficient dilution of the coal-carrier-gas jet. Moreover, increasing coal-carrier-gas jet momentum at higher coal-carrier-gas mass flow rates might cause earlier mixing with the combustion air jets at a less diluted state. Both could be avoided by a larger nozzle spacing, increasing the mixing delay.

Air staging is another method of moderating the local oxidizer availability. Its influence in flameless combustion has been investigated for lignite and bituminous coals at different wall temperatures, combustion air velocities and combustion air compositions, such as air or Ar/O_2 mixtures [118, 137]. Accordingly, NO_x emissions are effectively reduced in sub-stoichiometric conditions, whereas strong NO_x formation was found in unstaged conditions. This behavior is emphasized in the positive and negative direction by the fraction of volatile matter content [117].

Raising combustion air preheating temperatures induce rising NO_x emissions in a pulverized coal HiTAC system, as numerically investigated for temperatures between 777°C and 1077°C [121]. This was also found in gas-fired flameless combustors for combustion air temperatures between 768°C and 1300°C [145, 180]. On the contrary, fuel preheat temperatures below 300°C barely affect the NO_x emissions. In contrast to the significant dependence of NO_x emissions on the combustion air temperature, the influence between 1000°C and 1300°C of the overall temperature level on NO_x emissions is found to be low for a coal-fired laboratory scale furnace [118].

NO_x modeling approaches Different modeling approaches can be found in flameless combustion NO_x modeling. The majority is a control volume based reaction model during post-processing of CFD calculations. It accounts for the local atmosphere, temperatures and the impact of turbulence on the chemical reactions. As flameless combustion features great homogeneity, some authors modeled the whole furnace as one perfectly stirred reactor (PSR) which usually fails [46, 145]. The procedure of a PSR network model described by Mancini et al. [87] can be seen as a hybrid approach exhibiting a lower complexity than the control volume based approach but higher spatial resolution than a single PSR approach. The prediction of NO_x emissions resulted in good agreement with natural gas flameless combustion experiments. Stadler [136] carried out an extensive comparison of different NO_x models, identifying one acceptable NO_x model. It reveals good agreement in the fuel-lean regions, whereas nitric species are over-predicted in fuel-rich conditions. Further improvements eventually led to improved

results of the NO_x model [57, 165]. This will be discussed in more detail in Chapter 4.

1.4 Previously published parts of the work at hand

The work at hand contains parts which have already been published under the leadership of the author of this work. These parts shall be compactly highlighted here, and are disclosed in the chapters afterwards as well.

The results obtained during the first experimental campaign were presented during the Clean Coal Technology Conference 2013 in Thessalonki, Greece, and published in the conference proceedings [162] and as journal article [166]. Additional analyses of these experiments were contributed at German flame day in Düsseldorf [163]. The burner development by means of computational simulations was discussed and presented at the Clean Coal conference in Clearwater, Florida, and subsequently published in the conference proceedings [164]. A comprehensive comparison between the investigated two burner prototypes was discussed in [167].

The author of the work at hand planned the experiments for the above cited publications, and conducted them in co-operation with the mentioned co-authors. The post-processing of experimental results was split in accordance to the work packages during experiments. The simulations cited above were planned and executed by the author of this work. He also took over the elaboration of the publications.

The author contributed to the publication of his co-researchers presented at German flame day [55].

1.5 The FLOX-COAL-II project

The work at hand is based on the experiments and simulations conducted in the course of the FLOX-COAL-II project. This project has been funded by the Research Fund of Coal and Steel controlled by the European Commission. Within the project, eight research partners, four from research and four from energy industry, worked together to develop a pilot scale flameless burner for pulverized coal combustion, to develop a burner scale-up methodology and to develop and to validate flameless combustion specific CFD models. Three CFD program codes were evaluated and their results cross-compared in the course of CFD model development, implementation and validation. The resulting scale-up methodology was applied to bring the evolved burner design from the pilot to the industrial and the full scale. Full scale burners were finally investigated by means of CFD in three different boiler types: wall-fired, tangentially fired and all-wall-fired.

Besides the above mentioned publications of the author of this work, parts of the results are published in the final report of the FLOX-COAL-II project [165].

2 Methodology of This Work

As described in the previous chapter, flameless combustion offers advantages regarding NO_x emissions, fuel conversion, flue gas heat recovery and homogeneity in the furnace. It was also described which combustion settings favor the achievement of flameless conditions. Experimental investigations of this combustion regime have been conducted at several scales (from $20 \text{ kW}_{\text{th}}$ to approx. $12 \text{ MW}_{\text{th}}$) for various fuels such as natural gas, light and heavy fuel oil, biomass and coals. Few experimental investigations of flameless pulverized coal combustion provide a complete data set required for detailed investigation and subsequent validation of CFD models for this combustion regime, and those which do, were obtained for conditions with highly preheated air. These conditions can be easily obtained in test rigs fired with gaseous fuels, but they are not suitable for application in coal-fired utility power plants. The assessment of flameless combustion is usually done by qualitative statements as “homogeneous profile” or “no visible flame”, but rarely are characteristic numbers used for assessment or even definition of operational windows. Few numbers, such as the internal recirculation rate or recycle rate K_v proposed by Wüning [176], the flame occupation ratio Ξ_{FO} and the furnace gas temperature uniformity Ξ_{TU} proposed by Yang and Blasiak [181], exist (see Section 1.2).

The major preceding works have been published by Orsino et al. [100], Kim [74], Schaffel-Mancini [124], Stadler [136] and Ristic [115], in chronological order.

At the experimental research stage, Orsino et al. [100] conducted the initial investigations of the HiTAC of pulverized coal in IFRF’s furnace No. 1. A combustion air preheat temperature of around $1350 \text{ }^\circ\text{C}$ was realized by a pre-combustor. The applied burner featured one central combustion air nozzle and two high-velocity coal guns, delocated from the furnace central axis. In-flame measurements of gas components and temperature were conducted, as well as total radiative heat flux measurements, ash sampling and velocity measurements by an intrusive water-cooled LDV probe. Orsino et al. [100] prove the feasibility of pulverized coal flameless combustion and provided a suitable set of experimental data.

Kim [74] investigated flameless combustion numerically based on the IFRF experiments [100] and demonstrated the applicability of the EDC turbulence-chemistry interaction model for flameless conditions. He developed a reduced natural gas reaction mechanism derived from the detailed GRI-Mech 3.0 mechanism and applied it to a 20 kW laboratory scale reactor. Moreover, Kim investigated three soot formation and destruction mechanisms which affected the computed results to a little extent. Based on the NO_x model of Förtsch [41], Kim developed

a global NO_x model for natural gas and coal combustion.

Schaffel-Mancini [124] numerically investigated the ecological impact of flameless combustion of coal. She emphasized the influence of pyrolysis on flameless combustion and applied a detailed pre-processor, similarly to Stadler [136]. Based on the CFD code validated with the measurements conducted by Orsino et al. [100], Schaffel-Mancini proposed several designs of a boiler equipped with flameless burners. These are quoted by Stadler when he analyzed his own full-scale simulations.

The outcome of the first FLOX-COAL project served as the basis of two PhD theses: Ristic [115] focuses more on the experimental investigation of pulverized coal flameless combustion, and Stadler [136] concentrates on the numerical modeling. Stadler [136] presented a comprehensive work including detailed experimental investigations in an electrically heated laboratory scale facility at 40 and 60 kW_{th} and numerical evaluation of models for turbulence, turbulence-chemistry interaction, radiation, pyrolysis and NO_x prediction. In contrast to the other experiments presented here, Stadler also used OH^* chemiluminescence imaging in order to identify the reaction zones and intensities. His elaborated comparison of four different NO_x prediction models carved out one good model with good agreement of computed and measured concentrations in fuel-rich, i.e. under-stoichiometric, conditions. Ristic [115] investigated the combustion of Lausatian lignite, Polish high-volatile and South-African medium-volatile bituminous coal in an electrically heated 20 kW_{th} reactor with regard to thermal and fuel NO formation under different flameless conditions, without extreme air preheating. He showed the strong influence of the burner aerodynamics on NO_x emissions, e.g. that a quarl, as it is known from flame burners, promotes the NO_x formation due to downgraded mixing in the burner vicinity. Ristic developed the basis of the flameless burner applied in the work at hand, and tested it with Lausatian lignite and high-volatile bituminous coal at a pilot scale in the 500 kW_{th} KSVA test rig. The tests were accompanied by in-furnace measurements of gas concentrations, temperature and ash sampling. Ristic presented numerical results of the laboratory scale facility with good agreement of computed and measured results, whereas simulations of the pilot scale furnace remained without comparison against measurement results.

None of the aforementioned authors provided a detailed and sound set of experimental data allowing for the experimental and numerical investigation of pulverized coal flameless combustion without extremely high combustion air preheating. With the aimed application of flameless combustion technology in coal-fired utility boilers, burner and combustion settings based on moderately preheated combustion air needs to be understood.

Consequently, experiments were conducted at the approximately 250 kW_{th} scale, combusting the high-volatile bituminous coal Calentur under air firing conditions in a water-cooled test rig. It is well-known to be close to industrial furnace conditions, as no electrical heating is applied, heat extraction through the walls occurs and air preheating up to 150 °C is realized. The burner of Ristic [115] was further developed, now featuring annulus-shaped coal guns. Two

burner prototypes were investigated and measured at a high level of detail in air firing conditions with in-furnace gas concentration and temperature measurements, heat flux measurements, ash sampling and flame photography / videography. The first burner prototype was the subject of OH* chemiluminescence imaging and laser Doppler velocimetry (LDV), revealing information on the local reaction density and the established flow field, respectively. An outstanding attribute is the measurement of the undisturbed flow field by a state-of-the-art LDV technique. These measurements were performed in co-operation with the research group of CORIA, INSA Rouen, France, and WSA, RWTH Aachen, Germany, and have been reported in Gövert et al. [51] and Weidmann et al. [163, 166, 167]. The complete experimental procedure, the boundary conditions and the results are described in Chapter 3.

Numerical assessment of pulverized coal flameless combustion allows for a detailed insight and understanding of the combustion regime. Moreover, numerical results are required for the application of the characteristic numbers presented in Chapter 1. In the work at hand, IFK's in-house CFD program AIOLOS is used, adapted and validated against the obtained measurement results. Despite the knowledge of not being the first one investigating the CFD sub-models of turbulence, turbulence-chemistry interaction and pyrolysis, this investigation and the resulting adaptations have been found to be necessary. The NO_x model of Förtsch [41] is adapted to allow for its application in flameless combustion simulations. A second NO_x model by Taniguchi et al. [148] and recommended for flameless combustion [136] was tested in the course of the FLOX-COAL-II project, and was rejected due to its poor performance. The numerical part of this work is presented in Chapter 4.

Finally, Chapter 5 gives a summary of the experimental and numerical findings. Conclusions are drawn based on the experiences made in both research fields and an outlook to future flameless combustion applications is given.

3 Experimental Investigation of Flameless Combustion at 250 kW_{th}

Flameless combustion of pulverized coal was experimentally investigated at a 250 kW_{th} scale to prove achievement of flameless combustion with the current burner design on the one hand and to generate detailed data for the validation of CFD program codes on the other hand. Different measurement techniques were applied in order to obtain results of in-furnace gas composition and temperature, heat flux to the walls, reaction zone intensities as well as flow field data. They are presented in the following in conjunction with the test facility and the basic burner setup.

3.1 KSVa test facility and applied flameless burners

IFK's 500 kW_{th} pilot-scale test facility KSVa is a down-fired combustion reactor. The furnace is cylindrical in shape and its vertical orientation minimizes asymmetry due to natural convection or biased ash particle deposition. It is made up of one uncooled and six water-cooled segments with a total length of 7000 mm and an inner diameter of 750 mm. Each of the three upper segments is equipped with five series of four measurement ports, distributed at 90° intervals in the segment periphery. Further downstream, measurement ports with a larger axial spacing are available. They allow for the in-furnace measurement of combustion quantities e.g. gas composition, gas temperature and ash sampling in vertical and horizontal direction by means of specially designed probes. Cooling water flowing in the upwind direction provides protection from heat in all segments, the upper segments of the furnace and the burner plate are additionally protected by a refractory lining. An overall sketch of the furnace is shown in Figure 3.1.

The forced draft (FD) fan supplies combustion air (CA) which is heated by flue gas up to 200 °C in the recuperative air preheater (APH). Coal is conveyed to the burner by the coal-carrier-gas (CCG) which can be air, N₂ or CO₂. The flue gas leaving the furnace exchanges heat in the air preheater and can be cleaned in a high-dust selective catalytic reduction (SCR) catalyst, an electro-static precipitator (ESP) and a bag filter further downstream. The bag filter, the ESP and the SCR catalyst can be by-passed individually. The SCR catalyst was by-passed in the presented experiments. Measurement ports allow for ash sampling in the filter

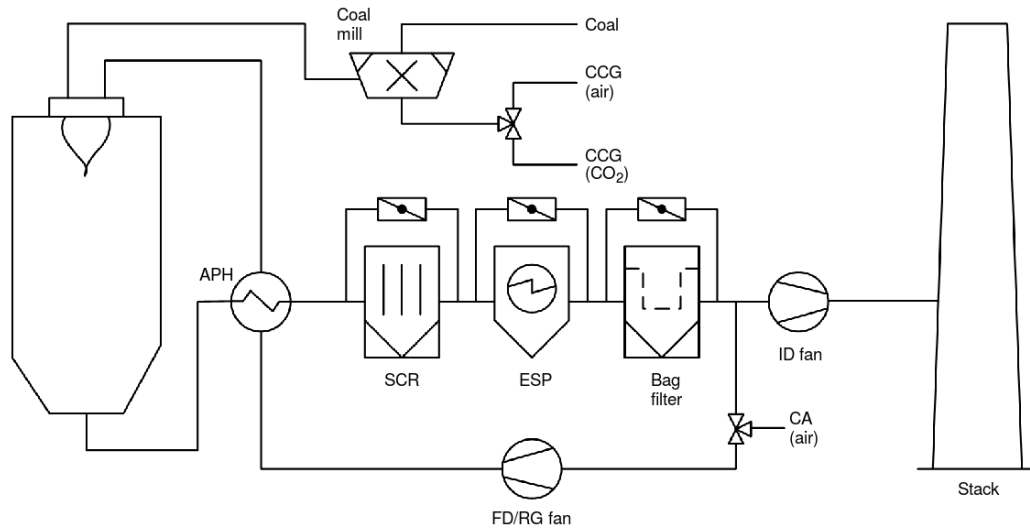


Figure 3.1: Schematic diagram of the 500 kW_{th} test facility KSVa with furnace and flue gas treatment facilities

facilities. An induced draft (ID) fan brings the cleaned exhaust gas to the stack, where it is released into the environment.

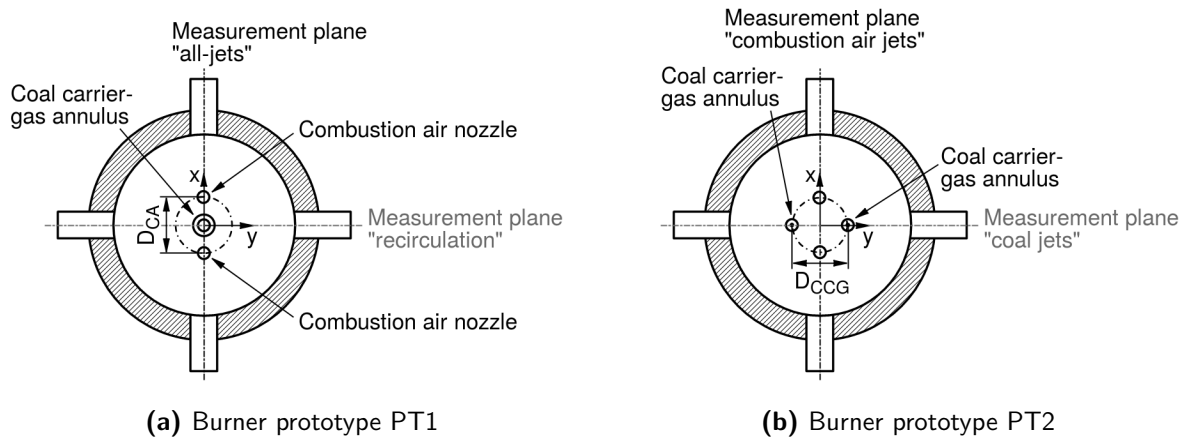


Figure 3.2: Sketch of the applied flameless burner prototypes PT1 and PT2

The design of the flameless burners used in the presented experiments derives from that of previous studies conducted by Ristic et al. at the laboratory [116, 118] and the pilot [115] scale. The first prototype burner PT1 is schematically illustrated in Figure 3.2, as is implemented in the furnace. It features a central annular nozzle with an inner diameter of 38 mm and an outer diameter of 46 mm, to supply the coal-carrier-gas mixture to the burner. In addition, two combustion-air nozzles with a diameter of 25 mm eccentrically placed on a pitch-circle with a

diameter of $D_{CA} = 270$ mm are used. A large pitch-circle diameter D_{CA} promotes the delayed mixing between fuel and combustion-air jets and thus their dilution with recirculating flue gas prior to mixing. This has been reported from experiments [82, 100, 130] and was confirmed by a numerical study detailed in Appendix B. This study can be summarized briefly by “fewer nozzles and larger spacing lead to a higher internal recirculation rate”.

The second burner PT2, shown in Figure 3.2b, is developed incorporating the experience obtained from the first prototype PT1 testing. The development is driven by the awareness of the options to influence the different NO types prompt NO, thermal NO and fuel-NO.

The evolution of the internal recirculation rate K_v , see equation (1.10), downstream of the burner and the development of the averaged temperature are presented in Figure 3.3 for the PT1 burner prototype. It is observable that the peak recirculation rate increases when the distance between the nozzle increases. The peak recirculation rate increases again when doubling the nozzle number from two to four and maintaining the mass flow. However, the recirculation rate is lower in the burner vicinity, i.e. for axial distances below 500 mm. It can be concluded that the mixing of hot inert combustion products in the entering cold combustion-air and coal-carrier-gas jets is less intense for the four-nozzle arrangement in this region. This is also expressed by the plotted area-averaged temperature ϑ_{aAv} which is higher and experiences a steeper increase for the two-nozzle option with the maximum nozzle distance.

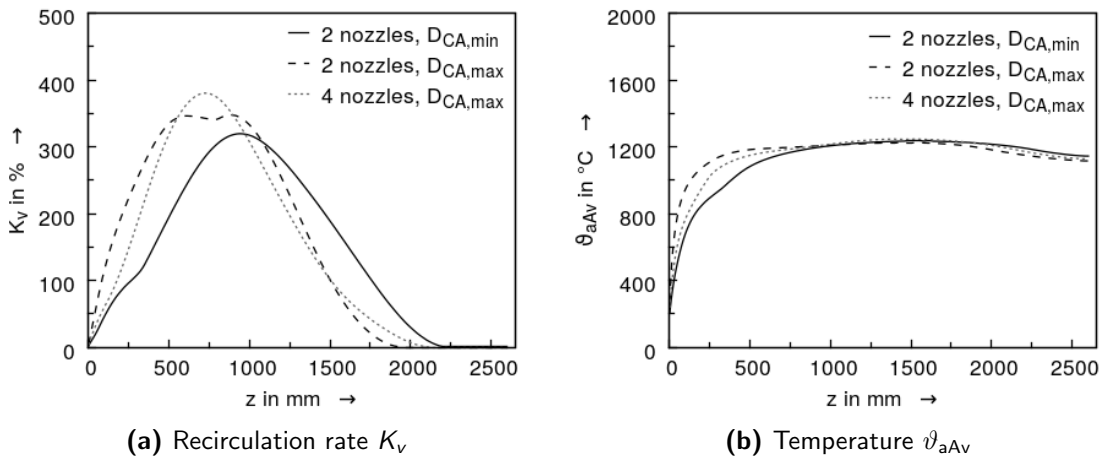


Figure 3.3: Effect of combustion-air nozzle position on the recirculation rate and area-averaged temperature, evaluated with the PT1 burner prototype

As explained in Chapter 1, NO_x emissions are mainly driven by the thermal NO and the fuel-NO path. Spinti and Pershing [135] state four possibilities for influencing the NO formation from fuel-N in their work:

1. Influencing the volatile-N / char-N split
2. Minimizing the char-N oxidation
3. Minimizing the volatile-N oxidation
4. Enhancing the reduction mechanisms of already formed volatile-NO / thermal NO during char oxidation

These findings are reflected in the criteria applied to the PT2 burner design. As the internal recirculation rate K_v is responsible for ensuring sufficient heat and inert flue gas supply for heating and diluting the incoming gas and coal streams, it is aimed to keep it at a high level. A high recirculation rate K_v accompanied by good mixing promotes a fast devolatilization of the coal in a diluted atmosphere. Fast devolatilization leads to an increased amount of volatile-N and thus less nitrogen is retained in the char which would be oxidized further downstream. This suits the requirement of influencing the volatile-N / char-N split and thus minimizing the char-N oxidation. Volatile-N evolving in a diluted or even fuel-rich atmosphere tends to reduce to N₂ rather than to oxidize to NO. Thus, the premise of minimizing the volatile-N oxidation is respected.

The idea behind the PT2 burner is to utilize the recirculated hot flue gases in the recirculation plane to realize the above discussed measures. The main modification is thus the split of the coal-carrier-gas nozzle in two annular nozzles, now located on the same pitch-circle as the combustion-air nozzles, i.e. $D_{CCG} = D_{CA}$. This design was numerically investigated prior to its realization and it was found advantageous in several aspects. The results of the analysis is discussed in Chapter 4, Section 4.7.2.

3.2 Measurement techniques and uncertainties

Measurement techniques are chosen to assess the driving forces and the main characteristics of flameless combustion, such as strong burner aerodynamics and internal recirculation, homogenized temperature and gas concentration fields, moderate heat release and reaction intensities, good fuel conversion and burnout. Some of the measurements were conducted and analyzed by the FLOX-COAL-II partner research institutions. Researchers of CORIA, INSA Rouen, were in charge of OH* chemiluminescence imaging and laser Doppler velocimetry, and researchers of WSA, RWTH Aachen, were in charge of FTIR spectroscopy based on suction-probe sampling.

Reaction zone topology by OH* chemiluminescence imaging

Chemiluminescence imaging of OH* radicals present in flames reveals information about the local heat release and thus the reaction intensity. Excited electrons of OH* radicals spontaneously

emit radiation when falling back to the unexcited state. This is called chemiluminescence. The intensity of the radiation depends on the density of excited electrons, and thus directly on the intensity of chemical reactions. To distinguish between hot wall and visible soot radiation and the radiation emitted by excited electrons, filters are applied allowing only the detection of radiation in a narrow UV-range centered on 308 nm [9, 65, 120]. The UV emissions of the OH^* radicals are detected by a highly sensitive charge-coupled device (CCD) camera which is located in front of a UV permissive window outside of the furnace. The window is purged by nitrogen in order to avoid deposition of ash or coal particles. A sketch of the setup is presented in Figure 3.4a. Figure 3.4b shows the view restrictions of the furnace and the resulting section

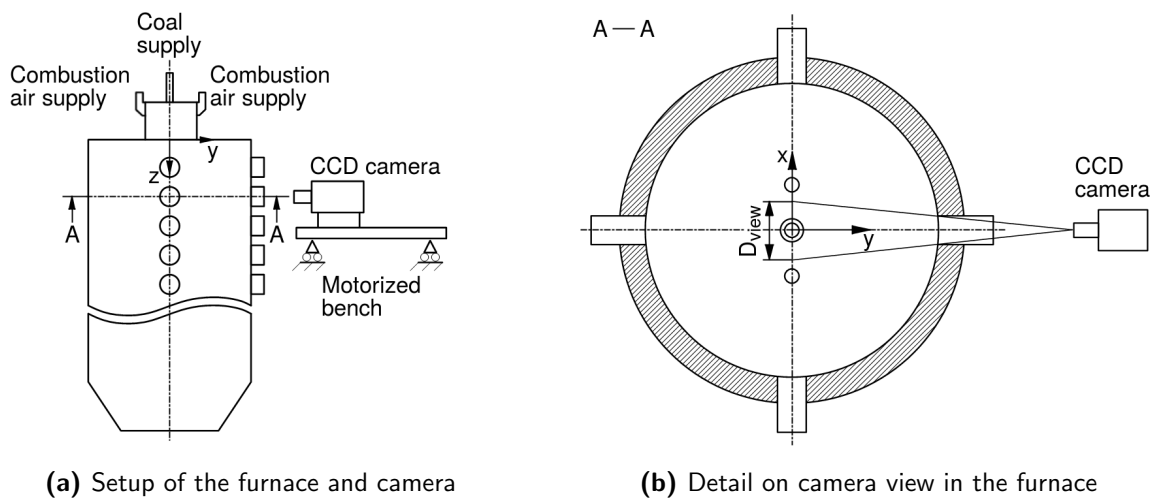


Figure 3.4: Sketch of OH^* chemiluminescence imaging setup

observable by the CCD camera. The port has a diameter of about 100 mm and the viewable section in the all-jets plane is of $D_{view} = 188 \text{ mm}$ in diameter. After the image collection, the results are corrected by the background radiation emitted from the hot walls. Therefore, images were taken from the walls in the hot state directly after shutting off the coal flame.

Local velocity measurements by laser Doppler velocimetry

Aerodynamics of the burner and the established flow field are of major interest in flameless combustion. Laser Doppler velocimetry (LDV) is an optical measurement technique based on the scattering of light by particles which provides highly accurate information on present velocities. An interference pattern is generated by a coupling of two coherent laser beams. The Mie scattering induced by the crossing particles in the flow is then collected and processed. By the application of highly sophisticated optics, the size of the interference fringe is kept very small and thus results can be regarded as point measurements without significant averaging. For each direction in space, a separate beam couple is required. The collecting device can be set up at any direction to the sampling flow direction. The first requirement for the application of this

technique is the presence of particles which is naturally given in the coal jet and the recirculation zone by coal and ash particles. In the combustion-air jet, particle seeding is required. This is realized by the application of ZrO₂ particles in a fluidized-bed dosing system developed by CORIA. The particles are characterized by a mean diameter of 5 μm with a distribution ranging between 3 and 30 μm. Given sufficient seeding, LDV gives a detailed and instantaneous view of the present flow field.

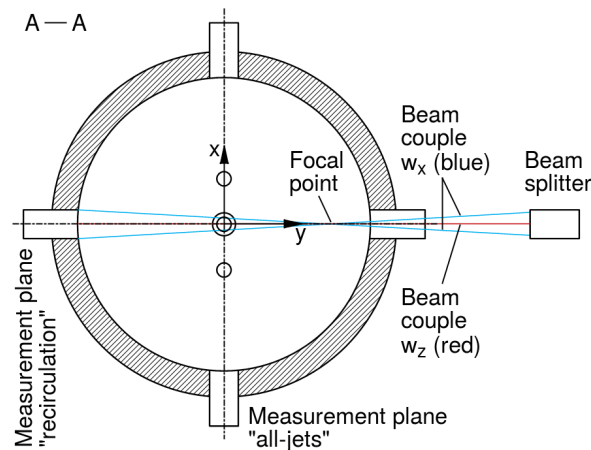


Figure 3.5: Sketch of the LDV setup

With the realized setup of laser beams and collector mounted in the same direction, the velocity components in the axial and tangential directions can be measured. The laser is moved on a motorized bench, allowing for a repeatable and accurate positioning. Therefore, the same setup is used as for the OH* chemiluminescence imaging, see Figure 3.4a. As displayed in Figure 3.5, two laser beams of the same color originating from the beam splitter intersect in the furnace at the desired measurement position. Since the furnace is top-viewed in Figure 3.5, the second laser beam pair is represented by one beam only with the other one lying directly beneath. As the setup of the furnace and the LDV is rotationally fixed, the burner is rotated clockwise by 90° in order to enable velocity field measurements in the recirculation plane and in the all-jets plane.

It is a great advantage of the chosen setup that LDV optics are not introduced into the furnace, thus preserving the flow field. In regions where high velocity gradients could be expected, the measurement grid is refined for a better resolution. A potential difficulty of this measurement technique shall not be concealed: particle velocity is measured by proxy of the gas velocity. In case of strong streamline curvatures, gas-particle-slip can occur due to the particle inertia, resulting in different gas and particle velocities. However, this effect is minimized by the application of very fine seeding particles and is regarded to be of minor importance for characterization of the predominant flow field.

Gas concentration and temperature measurements by suction-probe sampling

In-furnace measurements of gas species concentrations and gas temperature were conducted by the insertion of two different suction-probes into the furnace. Suction probe sampling is a widely applied measurement technique [62]. Both probes have a water-cooled jacket to avoid overheating and damage of the probe. In the case of gas concentration sampling, the sample gas has to be cooled down to stop the species reactions in the sample gas. However, since condensation in the probe would destroy hydrophilic species like NH₃ and would lead to formation of corrosive species such as H₂SO₄, the gas sampling probe features a heated core and sample line. Consequently, the sample gas is tempered to approximately 180 °C. Downstream of the probe, the sample gas stream is filtered from particles, divided and subsequently supplied to the FTIR spectroscope and the NDIR, UV, CL and paramagnetic measurement devices. In the suction pyrometer, the measurement thermocouple remains uncooled but protected by a ceramic shield to prevent influence of radiation for other parts of the furnace.

Table 3.1: List of measured species detailing measurement device and range

Species	Analyzer	Range	Adopted uncertainties
O ₂	paramagnetic	0-25 %	1 % of max. range
CO ₂	FTIR	0-70 %	2 % of reference spectrum
	NDIR	0-26 %	1 % of max. range
CO	FTIR	0-5 %	2 % of reference spectrum
	NDIR	0-5000 ppm	1 % of max. range
SO ₂	FTIR	0-2 %	2 % of reference spectrum
	UV	0-750 ppm	1 % of max. range
H ₂ O	FTIR	0-20 %	2 % of reference spectrum
NO	FTIR	0-1000 ppm	2 % of reference spectrum
	CL	0-1000 ppm	1 % of max. range
NO ₂	FTIR	0-1000 ppm	2 % of reference spectrum
	CL	0-1000 ppm	1 % of max. range
HCN	FTIR	0-3000 ppm	2 % of reference spectrum
NH ₃	FTIR	0-3000 ppm	2 % of reference spectrum
Volatile species i ‡	FTIR	0-50 mol _i m ⁻³	2 % of reference spectrum

‡light and heavy volatile species i: alkanes, alkenes, alkynes, aldehydes, carbocyclic acids, carbonyls, aromatic hydrocarbons

The measured species are listed in Table 3.1 per device with the applied measurement ranges. Seven volatile species are respected for the current measurement setup, see beneath Table 3.1. Each volatile species is measured in its molar quantity per flue gas volume, for the later comparison in diagrams all measured volatiles species are summarized by means of their molar carbon percentage per flue gas volume. Additionally, the device-inherent uncertainties

are displayed. They are derived from the manufacturer specifications and from the accuracy of the applied calibration gases. Moreover, gas concentration measurements are conducted over a period of one minute steady-state operation, storing and subsequently averaging a measured value every 10 s. The standard deviation calculated from the measured values gives a measure of the uncertainty inherent to each measurement method and due to unsteady nature of turbulent combustion. Both uncertainties are summed up and displayed as error bars in the diagrams showing measurement results.

Both sampling probes face similar challenges: Due to their intrusive nature, the flow field is locally perturbed which can be of importance if thin or weak flow structures are affected. This might apply to the burner vicinity. Due to their sucking nature, measurements in particle-dense regions are difficult, since particles can cause clogging in the probe. This appears especially in coal flames close to the burner, when coal particles devolatilize and can be in a semi-liquid and thus sticky state. Moreover, gas sampling suction techniques always inherit local volumetric averaging, due to the required amount of gas to be supplied to the measurement devices. These characteristics should be quantified and then applied to the measurement results in terms of uncertainties. In addition, they should be considered if measured and computed results are compared or if the measured values are interpreted as a standalone result. A quantification is not realizable using other measurement techniques and their impact is additionally strongly dependent on the measurement position: significant effect in the case of steep local gradients, no effect in the case of low local gradients. Thus, a practical way is the consideration of the characteristics when interpreting the measured values, and when comparing measured and computed results. From the author's experience, the volumetric averaging can be well captured in the computed results by applying a sphere of a radius of 25 mm as proposed by Parente et al. [102]. The sphere represents the sucked volume around the actual measurement point in the computed results. Analogously to the uncertainties of gas measurement devices given in Table 3.1, an uncertainty of 12 °C for temperatures of around 1200 °C can be estimated [102]. This leaves gas temperature fluctuations aside, leveled out by the slow response time of the suction pyrometer.

Total and radiative heat flux measurements

In addition to the local heat release detection by OH* chemiluminescence imaging, heat flux measurements are conducted using two special probes. These measurements are meant to be used for the comparison of heat to the walls and for the validation of the radiative heat flux with computed results. In contrast to gas sampling probes, the heat flux probes are not introduced into the furnace, but leveled evenly with the walls. Thus, the incident total heat and radiation at the walls is measured.

Measurement of total heat flux is based on the thermal voltage established between a cooled

and an uncooled metal part at the front end of the probe. Due to the different temperatures of the metal plates, there is a difference in electric resistance, and thus in the resulting current when applying a voltage. This difference is characteristic for a certain heat flux. The measurement of radiative heat flux is based on the voltage resulting from the measurement of the radiative intensity over all wave lengths. A detailed description of total and radiative heat flux measurement techniques can be found elsewhere [43, 44]. Total and radiative heat flux measurements exhibit uncertainties which are quantified by Coraggio and Laiola [28]. They are applied to the measured results in terms of error bars if displayed in diagrams.

Flue gas sampling, fly ash sampling and analysis

In addition to the in-furnace measurements described above, continuous flue gas analysis of the species O₂, CO₂, CO, SO₂, NO and NO₂ is performed at the furnace exit. As for the in-furnace measurements, the standard deviation and the accuracy of the device are summed up, resulting in an uncertainty displayed as error bars in the diagrams. However, the obtained standard deviation is very small, due to a very uniform flow-field and completed reactions.

Over a period of at least 15 minutes, fly ash samples are collected at an axial distance of 5900 mm from the burner just above the flue gas sampling allowing for a direct link of measured gas and present ash particle composition. Ash particles are analyzed regarding the total carbon content and other major elements such as Ca or S compounds according to DIN 51733. Comparison of TOC and total carbon content disclosed that barely no inorganic carbon is present in the ash. The combustion efficiency can be expressed by several numbers:

- Carbon content in ash (C-in-ash): This gives the percentage of all carbon left in the sample, i.e. $\text{kg}_C \text{kg}_{fly\ ash}^{-1}$. It is an important figure if further use of the ash in e.g. landfilling is envisaged.
- Unburned carbon (UC): This is related to the coal analysis. UC refers to the amount of carbon that remains unburned compared to the amount of carbon initially present in the coal, i.e. $\text{kg}_C \text{kg}_{coal}^{-1}$. UC is given in equation (3.1).
- Burnout: This is calculated from the ash content in the sample and the parent coal by means of the ash tracer method [141], assuming that the mineral matter is conserved during combustion. The burnout is defined by equation (3.2).

$$\text{Unburned carbon} = \frac{\gamma_{A,coal}}{\gamma_{A,samp}} \cdot \gamma_{C,samp} = \frac{\dot{M}_{UC}}{\dot{M}_{coal}} \quad (3.1)$$

$$\text{Burnout} = \frac{1 - \frac{\gamma_{A,coal}}{\gamma_{A,samp}}}{1 - \gamma_{A,coal}} \quad (3.2)$$

3.3 Operating conditions

During the experimental investigations in IFK's 500 kW_{th} facility, two different flameless conditions are investigated, plus a reference flame condition. The two flameless conditions differ by the applied primary gas, i.e. coal-carrier-gas which is CO₂ in the first case and air in the second case. The two cases are correspondingly referred to as FLOX_{CO₂} and FLOX_{air}.

The first case is researched for gaining knowledge on the effectiveness of coal-carrier-gas dilution and on the structure of the flow in the furnace. It is known from former investigations that combustion-air dilution by forced external flue gas recirculation is helpful in achieving flameless combustion. Coal-carrier-gas dilution can reduce the required effort and might be as effective as combustion-air dilution and flame propagation can be suppressed. This was demonstrated for natural gas combustion by Dally et al. [30] and Szegö et al. [145] in experiment, and by Oryani et al. [101] in simulation. For the velocity measurements conducted in the FLOX_{CO₂} case, the velocities are measured in the plane of all jets, and in the perpendicular recirculation plane. Therefore, the burner was rotated by 90°, as position of measurement equipment was fixed. This case features similar boundary conditions as the standard FLOX_{CO₂} case of the first prototype burner and consequently does not show up in Table 3.2.

The flameless air case is investigated regarding a more economic application without additional effort for flue gas recirculation to the coal conveying system. The FLOX_{air} condition contains a case with the burner rotated by 90°, FLOX_{air,rot} which was performed in order to measure the devolatilization behavior of the further developed second burner prototype.

The conventional flame case provides data of a state-of-the-art swirl burner giving a reference in terms of temperatures, heat fluxes, burnout and flue gas species. Specifications of the burner are well described by Grathwohl et al. [54].

The settings of operating conditions relevant to compare the flameless burner prototypes to each other and to the flame burner are described in Table 3.2. A combustion-air flow rate \dot{V}_{CA} is chosen to ensure a velocity of around 100 m s⁻¹ at the nozzle exit. Increasing the inlet velocity above this threshold does not affect the flameless conditions positively, as was found by Ristic [115]. In order to determine whether compressible or incompressible flow prevails, the Mach number Ma is calculated by equation (3.3) with $\kappa_{air} = 1.402$ and $R_{air} = 287.22 \text{ J (kg K)}^{-1}$.

$$Ma = \frac{w}{c} = \frac{w}{\sqrt{\kappa_{air} R_{air} T}} \quad (3.3)$$

Table 3.2: Settings of investigated operation conditions

Burner prototype	FLOX _{CO₂}		FLOX _{air}		FLOX _{CO₂}		FLOX _{air}		FLOX _{air,rot}		FLAME		FLAME _{as}	
	PT1		PT2		PT2		PT2		PT2		unstaged		air-staged	
\dot{M}_{coal} in kg h ⁻¹	33.7	32.4	33.0	32.0	33.0	32.0	33.0	32.0	33.0	33.0	32.4	33.1	32.4	33.1
\dot{V}_{CA} in m ³ h ⁻¹ (STP)	250	216	254	219	254	219	237	205	237	237	205	201	205	201
\dot{V}_{CCG} in m ³ h ⁻¹ (STP)	26.0	34.5	34.0	34.8	34.0	34.8	33.8	36.2	33.8	33.8	36.2	36.3	36.2	36.3
$y_{CO_2,CCG}$ in %	79.0	0.0	79.0	0.0	79.0	0.0	0.0	0.0	0.0	0.0	0.0	0.0	0.0	0.0
$y_{air,CCG}$ in %	21.0	100.0	21.0	100.0	21.0	100.0	100.0	100.0	100.0	100.0	100.0	100.0	100.0	100.0
Ma at CA-inlet	0.262	0.225	0.272	0.232	0.272	0.232	0.245	0.208	0.245	0.245	0.208	0.147	0.208	0.147
n	1.15	1.16	1.13	1.13	1.13	1.13	1.17	1.15	1.17	1.17	1.15	1.13	1.15	1.13
ϑ_{CA} in °C	144	149	172	162	172	162	183	148	183	183	148	131	148	131
ϑ_{CCG} in °C	45.0	45.0	65.0	65.0	65.0	65.0	65.0	40.0	65.0	65.0	40.0	40.0	40.0	40.0

The chosen coal-carrier-gas flow rate \dot{V}_{CCG} results in an inlet velocity of approximately 25 m s^{-1} which is state-of-the-art in current pulverized coal burners. All flow rates were recorded in a 10 s pattern over the whole measurement period. The average volumetric flow rates and their standard deviation are determined from these values. Standard deviations of $5.3 \text{ m}^3 \text{ h}^{-1}(\text{STP})$ and of $0.2 \text{ m}^3 \text{ h}^{-1}(\text{STP})$ are found for \dot{V}_{CA} and \dot{V}_{CCG} respectively.

While early flameless combustion researchers postulated that high air preheating is required to achieve that state [72], it has meanwhile been acknowledged that flameless combustion is feasible without air or fuel preheating [9, 120, 146, 177]. Nonetheless, air preheating prevents energy losses after the combustion process and a heat exchanger is installed in every boiler. Thus, moderate preheating of combustion air is realized in the pilot scale tests and temperatures ϑ_{CA} of around $150 \text{ }^\circ\text{C}$ are achieved. The detailed temperatures are given in Table 3.2.

It is stated that the PT1 flameless burner prototype and the flame burner are characterized by all of the above described measurement techniques with two exceptions: heat flux and velocity measurements are only applied to the FLOX_{CO₂} and the flame case. LDV and OH* chemiluminescence imaging techniques are not used during the PT2 flameless burner prototype investigation.

It is important to note that additional cooling gas is introduced into the furnace via the flame supervision (FS) ducts. The volumetric flow rate $\dot{V}_{FS} = 5 \text{ m}^3 \text{ h}^{-1}(\text{STP})$ of CO₂ in the flameless combustion cases and $\dot{V}_{FS} = 7 \text{ m}^3 \text{ h}^{-1}(\text{STP})$ of air in the flame case. It is respected in the calculation of the air ratio n . For this reason, \dot{V}_{CA} is lower in the flame case than in the FLOX_{air} case at almost similar air ratios. For the air-staged flame combustion, the air-staging volumetric flow rate \dot{V}_{as} is $56 \text{ m}^3 \text{ h}^{-1}(\text{STP})$, resulting in a volumetric flow rate of combustion air of $\dot{V}_{CA,as} = \dot{V}_{CA} - \dot{V}_{as} = 145 \text{ m}^3 \text{ h}^{-1}(\text{STP})$. The air ratio n_{sub-st} in the sub-stoichiometric reduction zone is about 0.86. This reduction zone expands until staging-air is fed at $z = 1890 \text{ mm}$.

3.4 Fuel

The coal used in the presented experiments is a Columbian sub-bituminous coal called “Calentur”. This coal exhibits characteristics similar to the Columbian coal “El Cerrejón” used in previous experiments [115]. It has a large volatile portion, facilitating the ignition of the coal. Moreover, the nitrogen and sulfur content are in a medium range, so that no excessive pollutant formation is expected.

The coal is pre-dried from approximately 11 % to a residual moisture of about 4 %. The coal is then ground online during the experiments in a hammer mill attached to the test rig and fed directly into the furnace. During grinding, the coal continues to dry due to mill temperatures of around $160 \text{ }^\circ\text{C}$. Samples are taken from the storage just before the pulverized coal is transported

Table 3.3: Ultimate and proximate analysis data of the Calentur coal burned in PT1 and PT2 experiments

γ_i, H_o, H_u			PT1	PT2
Ultimate analysis				
C	daf	in %	77.35	76.79
H	daf	in %	5.09	5.71
N	daf	in %	1.51	1.54
S	daf	in %	1.08	0.84
O (by difference)	daf	in %	14.97	15.12
Proximate analysis				
Moisture	as fired	in %	4.10	3.91
Ash	dry	in %	11.03	7.50
Volatiles	daf	in %	42.28	42.86
Fixed C	daf	in %	57.72	57.14
H_o	as fired	in kJ kg ⁻¹	27837	28781
H_u	as fired	in kJ kg ⁻¹	26804	27597

to the coal dosing system. Thus, the state of the coal which is analyzed, can be seen as “as fired”. Proximate and ultimate analyses were undertaken in the IFK laboratory, and their results are compiled in Table 3.3.

The particle size distribution of the coal is derived by laser diffraction on volume basis. The figures D_{10} , D_{50} and D_{90} reported in Table 3.4 are given in μm . This means that 10% of the sample particles are characterized by a diameter which is smaller or equal to D_{10} . D_{50} and D_{90} refer to 50% and 90%, respectively. The fineness shown in Table 3.4 is increased compared to the fineness usually achieved in utility boilers, where 70% to 80% of particles pass through a 75 μm sieve. In the test rig exhibiting a reduced residence time compared to a full-scale utility boiler, a finer grinding of the coal might be advantageous for a good combustion performance.

Table 3.4: Particle size distribution of the Calentur coal burned in PT1 and PT2 experiments

D_i		PT1	PT2
D_{10}	in μm	6.55	4.88
D_{50}	in μm	31.1	26.0
D_{90}	in μm	65.3	70.5

3.5 Reference flame burner tests

A reference conventional flame burner is tested and measured in the course of the first flameless prototype burner testing. The goal of this experiment is to obtain detailed data of a state-of-the-art flame burner that can subsequently be used to understand how the combustion regimes of flame-existent and flameless coal combustion differ. As stated in Table 3.2, two flame conditions are assessed: unstaged (FLAME) and air-staged (FLAME_{as}) combustion. The unstaged condition FLAME was run for a shorter time period in steady-state conditions, allowing wall temperatures to settle and flue gas and fly ash sampling to be conducted. The detailed and excessive measurements such as LDV, OH* chemiluminescence imaging and in-furnace gas concentration and temperature sampling have been conducted for the air-staged condition FLAME_{as}. The results of both flame conditions are presented here, but are discussed more extensively in the course of flameless combustion analysis in Section 3.6.

Table 3.5: Results of continuous flue gas measurements at the furnace exit for FLAME and FLAME_{as} conditions

Concentrations, dry basis		FLAME	FLAME _{as}
Air staging mode		unstaged	air-staged
y _{O₂}	in %	2.9	2.8
y _{CO₂}	in %	16.1	16.0
y _{CO}	in ppm	167	230
y _{NO_x}	in ppm	279	149
y _{SO₂}	in ppm	666	651
c _{CO}	in mg m ⁻³ (STP) ‡	172	238
c _{NO_x}	in mg m ⁻³ (STP) ‡ †	473	253
c _{SO₂}	in mg m ⁻³ (STP) ‡	1607	1572

‡ @ 6% O₂; † NO_x as NO₂

Table 3.6: Carbon in ash, unburned carbon and burnout of FLAME and FLAME_{as} experiments

Dry basis		FLAME	FLAME _{as}
C-in-ash	in %	10.7	21.1
Unburned carbon	in %	1.34	3.00
Burnout	in %	98.3	96.4

Table 3.5 exhibits similar O₂ and CO₂ concentrations at the furnace exit, but the CO concentration is increased for the air-staged case. The hindered burnout in the air-staged case

is also reflected by Table 3.6, where C-in-ash almost doubles in comparison to the unstaged FLAME case. The opposite trend is observed for the presented NO_x concentrations, reduced by almost one half from 473 mg m⁻³ (STP) to 253 mg m⁻³ (STP). Here, the positive influence of air-staging on NO_x reduction becomes obvious. In contrast to the varying pollutants CO and NO_x, the SO₂ concentration remains around 1600 mg m⁻³ (STP) in both cases.

It has been demonstrated that the performance of the flame burner is outstanding regarding the NO_x emission level. On the other hand, the combustion efficiency figures reveal a lack of fuel conversion in the applied setting, resulting in unusually high combustion losses and CO emissions. In subsequent tests (not shown here), the burner setup has been changed and the combustion losses decreased. However, the good NO_x emission performance of the burner suffered accordingly.

3.6 Influence of CCG dilution and coal dispersion – PT1 tests

The goal of this first test campaign has been to evaluate the development of the burner regarding the dispersion of the incoming coal and the influence of coal-carrier-gas dilution by CO₂, and finally to obtain insights in the governing flow pattern.

3.6.1 Flue gas analysis and combustion efficiency

In Table 3.7, the results of continuous flue gas measurements at the furnace exit are showcased for the PT1 flameless burner tests. Flue gas concentrations are given on a dry basis. Additionally, pollutant emissions (CO, NO_x and SO₂) in mg m⁻³ (STP) are reported for a O₂ reference level of 6 %.

Due to very similar air ratios, the resulting excess O₂ concentration is almost equal for both configurations. The CO₂ concentration is significantly changed by the use of CO₂ as the coal-carrier-gas. One can see the advantages of flameless combustion from the pollutant results. Compared to the FLAME condition (unstaged operation), a reduction in NO_x and SO₂ concentrations of 17 % and 25 %, respectively, is achieved with FLOX_{CO₂}. The CO concentration increases moderately by 8 %. In contrast, FLOX_{air} increases the NO_x concentration by 29 % compared to FLAME. On the other hand, CO and SO₂ concentrations decrease in FLOX_{air} by 71 % and 18 %, respectively, referring to the FLAME condition. Focusing on the two flameless conditions, reduction and increase are similar as between FLOX_{air} and flame conditions, except for the SO₂ result.

When the flame burner is run in air-staged mode, NO_x concentration falls below the flameless results. They are 58 % lower in the FLAME_{as} than in the FLOX_{air} condition. The drawback

Table 3.7: Results of continuous flue gas measurements at the furnace exit for flameless conditions FLOX_{CO₂} and FLOX_{air}

y_i and c_i , dry basis		FLOX _{CO₂}	FLOX _{air}
y_{O_2}	in %	2.8	2.9
y_{CO_2}	in %	22.3	17.6
y_{CO}	in ppm	181	48
y_{NO_x}	in ppm	231	359
y_{SO_2}	in ppm	501	545
c_{CO}	in mg m ⁻³ (STP) ‡	188	50
c_{NO_x}	in mg m ⁻³ (STP) ‡ †	391	611
c_{SO_2}	in mg m ⁻³ (STP) ‡	1206	1323

‡ @ 6 % O₂; † NO_x as NO₂

can be identified for the combustion efficiency, where the air-staged flame condition exhibits disadvantages for CO concentration, C-in-ash and burnout compared to flameless combustion. These results demonstrate the importance of establishing a highly diluted zone with a reducing atmosphere in order to control the NO_x concentration. But, high turbulence and mixing must be achieved to ensure excellent fuel conversion.

Table 3.8: Carbon in ash, unburned carbon and burnout of flameless conditions FLOX_{CO₂} and FLOX_{air}

Dry basis		FLOX _{CO₂}	FLOX _{air}
C-in-ash	in %	15.4	4.00
Unburned carbon	in %	2.07	0.46
Burnout	in %	97.3	99.4

Table 3.8 contains the results of the fly ash analysis relevant for the evaluation of the combustion efficiency. As one can see, FLOX_{air} exhibits the best combustion performance with regards to fuel conversion. Comparing it to the FLAME condition (unstaged operation), C-in-ash is 63 % lower. In contrast, FLOX_{CO₂} gives the lowest results regarding the combustion efficiency as it is easily observed from the burnout and the C-in-ash figures. The inhibition in carbon burnout might be caused by the slower kinetics at lower overall temperature level in FLOX_{CO₂}. Additionally, the increased CO₂ concentration in the surrounding atmosphere can reduce the oxygen diffusivity [15, 73, 80]. Since the air ratio n is about 1.15 for all three cases, it can be eliminated as a reason for hindered carbon conversion. The results are in good agreement with the CO and NO_x concentrations presented in Table 3.7, showing a well-known mechanism: NO_x concentration decreases as C-in-ash and CO concentration increase

[112]. Low char burnout is reported from other researchers using a separated-nozzle burner configuration [82]. By reference to a conventional unstaged swirl burner, all flameless burner configurations result in good temperature homogeneity and low NO_x concentration, but in low char burnout.

3.6.2 Flow field analysis

Investigation of flow fields was conducted for FLOX_{CO₂} and FLAME_{as}. The relevant characteristics of FLOX_{CO₂} are thought to be found in a similar manner in the FLOX_{air} case. The first paragraph of this analysis was mostly contributed by Honoré of CORIA, INSA Rouen [167].

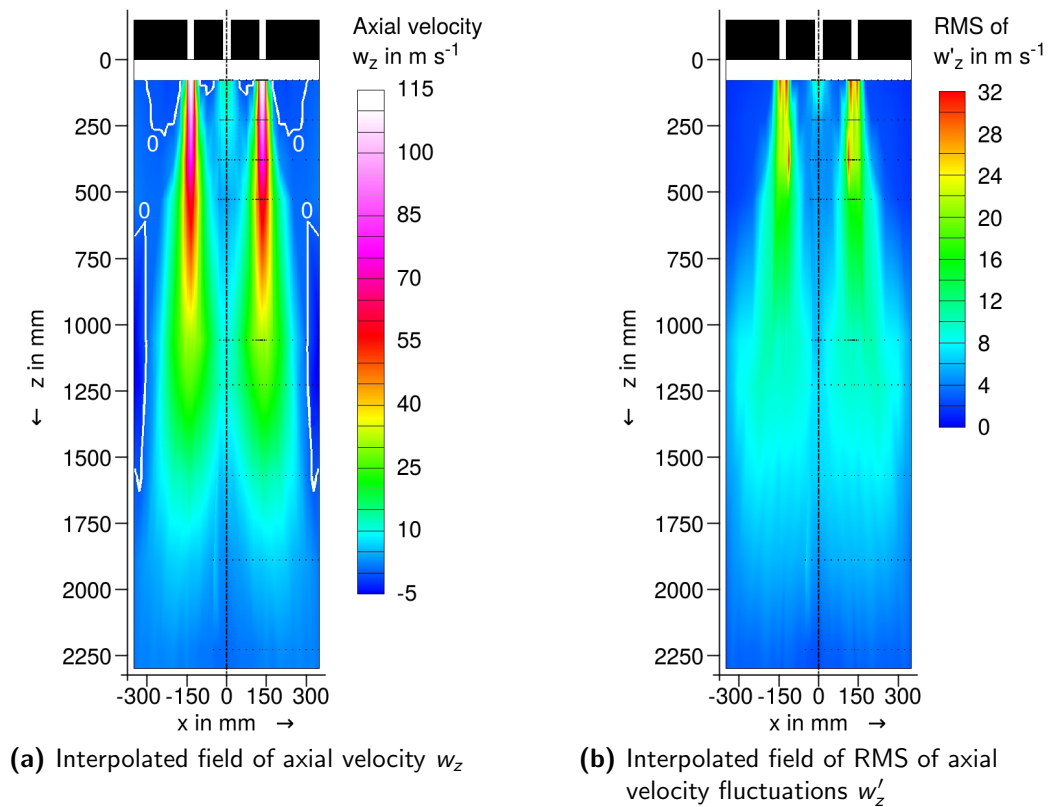


Figure 3.6: Flow field of FLOX_{CO₂} (adapted from [167])

Figure 3.6 presents the maps of the mean axial velocity w_z and of the root-mean-square (RMS) of the axial velocity fluctuations w'_z measured by LDV in the measurement plane “all-jets”. The actual measurement locations can be identified from the small black dots. Measurements were undertaken from the furnace wall to the furnace axis and 50 mm beyond. Consequently, their interpolation is done on the right side of the map, the left side is then reconstituted by symmetry for the ease of viewing. The zero axial velocity iso-line in white represents the boundary of the recirculation zones characterized by a negative axial component.

It is apparent that the velocity field is strongly marked by the high velocity air jets emerging from the combustion-air nozzles. They are characterized by a length of about 1.8 m, a maximal axial velocity of approximately 115 m s⁻¹ and turbulence intensity of 26 % at the upper port. As is typical for turbulent round jets, the fluctuations are large along their boundaries. The turbulence intensity can be derived by the ratio of the RMS of the velocity fluctuations w' to the total velocity magnitude $\|w\|$ and gives information on the relevance of the flow fluctuations, see equation (3.4). It can be computed from all velocity directions.

$$I_{turb} = \frac{w'_{RMS}}{\|w\|} \quad (3.4)$$

One can also notice a slight increase of turbulence intensity in the air jets at approximately $z = 380$ mm, as a result of the interaction between the coal and air jets. The central coal jet is then rapidly entrained by the air jets: its axial velocity decreases up to $z = 530$ mm, whereupon, it can not be distinguished from the air jets.

Figure 3.7a shows the axial velocity w_z just downstream the burner at $z = 80$ mm. The peak velocity below the combustion-air nozzle at $x = 135$ mm is well displayed for the FLOX_{CO₂} case. On account of the high momentum, small recirculation zones appear in the near field around the air jets with a peak negative axial velocity of -1.5 m s⁻¹. The annular coal jet, along the centerline, has a maximum axial velocity of 12.5 m s⁻¹ and a turbulence intensity of 84 %.

Along the second profile at $z = 230$ mm, cf. Figure 3.7b, the mean axial velocity between the air and coal jets remains positive. Local recirculation does not exist between the air and coal jets, indicating the onset of an interaction.

Downstream at $z = 1060$ mm, the air jets continue their expansion in the combustion chamber. The axial velocity in the centerline region increases, the coal jet cannot be distinguished from the expanding combustion-air jet. A thin recirculation zone along the wall can be observed, see Figures 3.6a and 3.7c. The latter turns out to be stronger in the plane perpendicular to the three jets, the so-called "recirculation" plane. Along this plane, the recirculation is only limited by the weaker coal jet expansion close to $y = 100$ mm, and negative axial velocities can be observed: down to -10 m s⁻¹, until the large recirculation zone ends before $z = 1890$ mm.

All these results show that the high momentum flux from the air jets totally controls aerodynamics within the furnace and therefore the achievement of a flameless combustion regime. As a matter of fact, the related entrainment process in a confined combustion chamber induces large recirculation zones besides the jets.

Additionally to the FLOX_{CO₂} axial velocity results, those of FLAME_{as} are presented in Figure 3.7. At $z = 80$ mm, the coal-carrier-gas and combustion-air streams are clearly identified whilst at $z = 230$ mm, the combustion air has already lost most of its axial velocity component. This can be attributed to the strong swirl of the flame burner.

The swirl can be seen from the tangential velocity component w_y in Figure 3.8a. It drives the

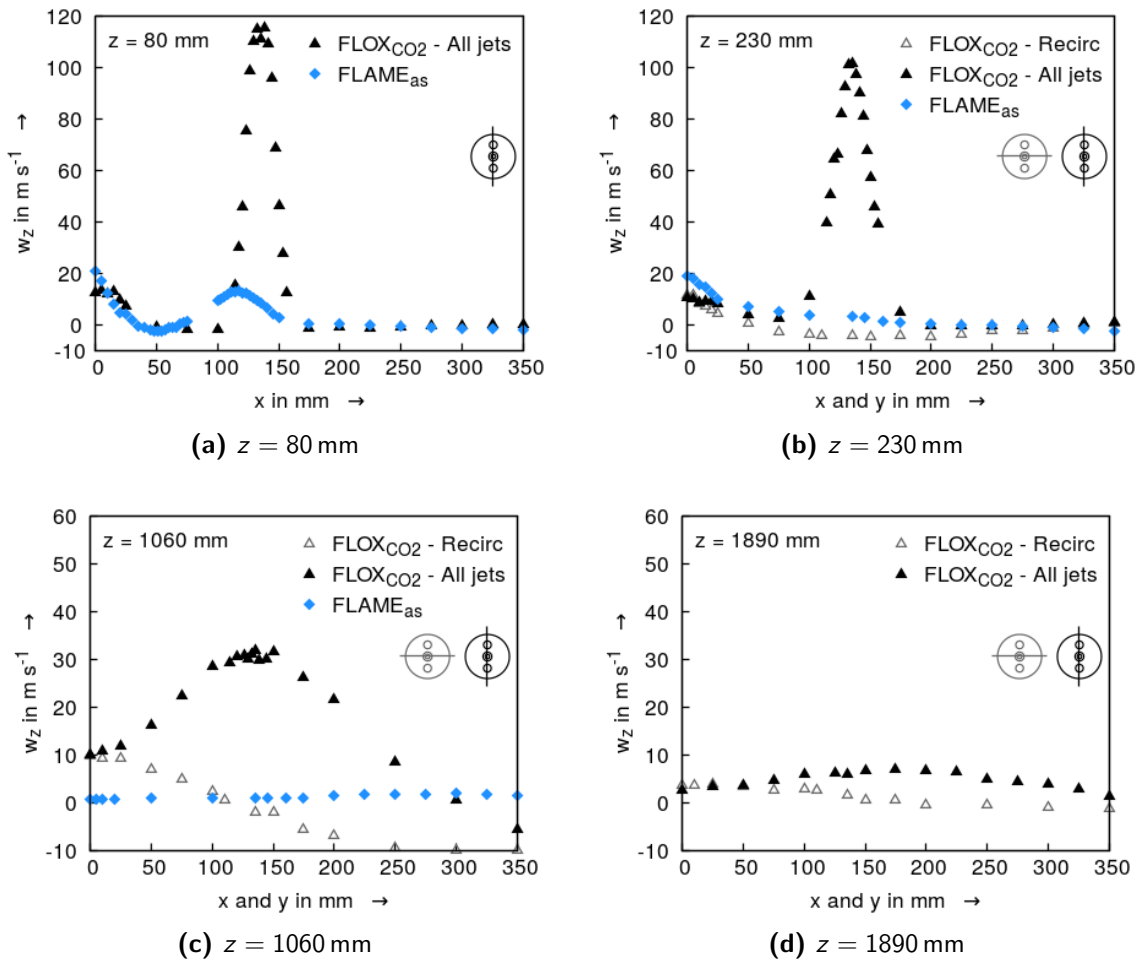


Figure 3.7: Comparison of axial velocity w_z in the “all-jets” and the “recirculation” (only in sub-figures (b), (c), (d)) plane for FLOX_{CO₂} and FLAME_{as} conditions

combustion air of the flame burner to transform its kinetic energy in strong turbulence. Looking at the measurements of w_y at $z = 230$ mm in Figure 3.8b and $z = 380$ mm in Figure 3.8c, one can see that the tangential velocity quickly reduces and finally disappears at $z = 530$ mm. Consequently, the flame burner achieves a homogeneous axial velocity profile more quickly than the flameless burner, as indicated by Figures 3.7c and 3.7d, respectively.

The tangential velocity results of flameless burner shown in Figure 3.8 indicate a slightly rotating flow in the furnace, interrupted by the impinging combustion air jet at $x = 135$ mm, where tangential velocity equals 0. However, it was expected that tangential velocity is about 0 along the complete radial profile, as at the combustion air jet position. The three-jets-plane was thought to be stabilized by the impinging jets. The reason for this observation remains undisclosed, supposedly to be found in the interaction of large vortex structures of the neighbored combustion air jets.

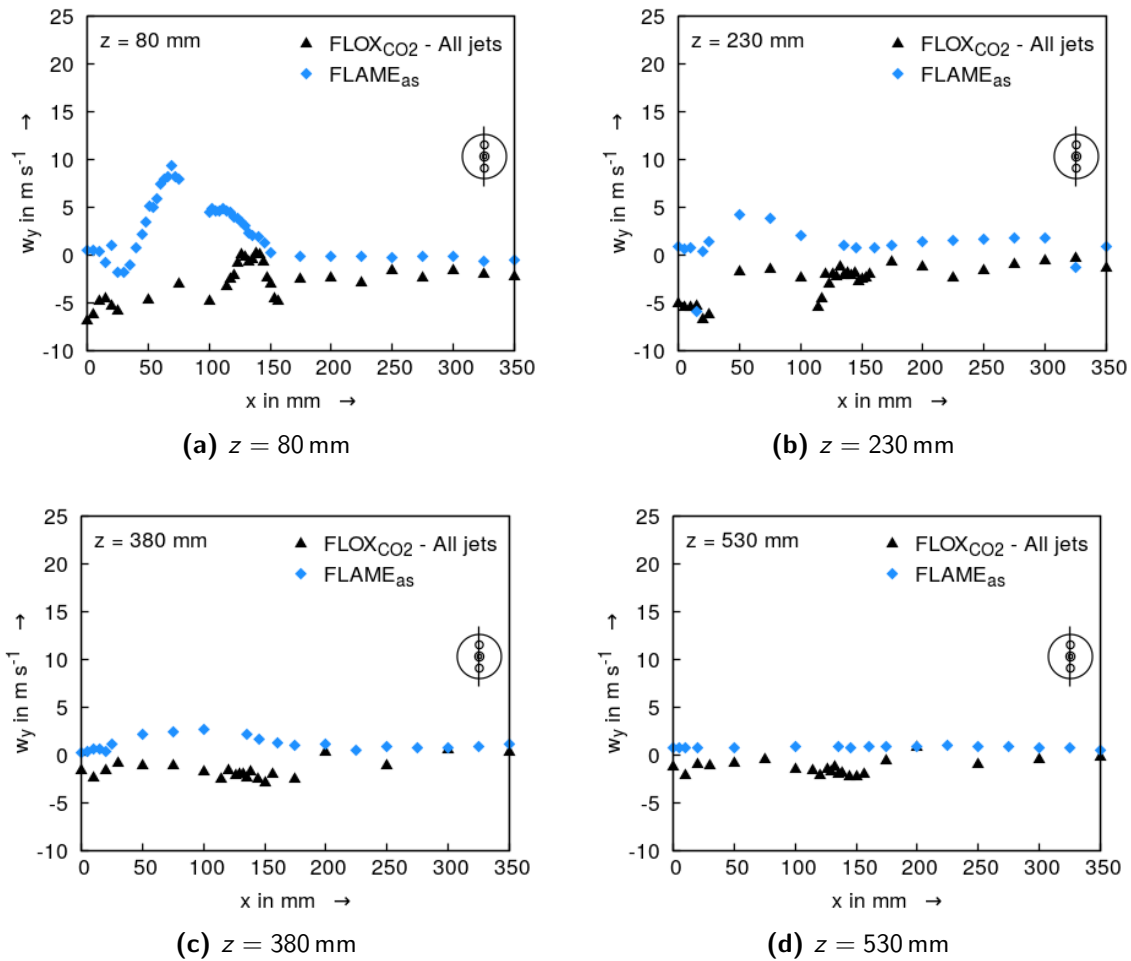


Figure 3.8: Comparison of tangential velocity w_y in the “all-jets” plane for FLOX_{CO₂} and FLAME_{as} conditions

3.6.3 Reaction zone visualization, temperature field and heat flux analysis

Reaction intensity and reaction zone topology are visualized by means of OH* chemiluminescence imaging. Results in Figure 3.9 are obtained from optical accesses normal to the jets plane (see Figure 3.4) and are normalized by the maximum measured intensity which is found in the FLAME_{as} case. The size of recorded images is limited by the viewport diameter, and results in an image diameter of 188 mm (see also Section 3.2).

The difference in location and intensity of the reaction zone can be clearly seen: the reaction zone is attached to the burner for the conventional flame, whereas it is shifted downstream for the flameless combustion regime. In the latter case, no OH* spontaneous emission, i.e. no reaction zone, can be observed at the exit of the burner. One can see that both flameless cases depict much lower reaction intensity than the FLAME_{as} case, i.e. 15 % (FLOX_{air}) and 7 % (FLOX_{CO₂}). The reaction intensity then increases between $z = 400$ mm and $z = 1200$ mm,

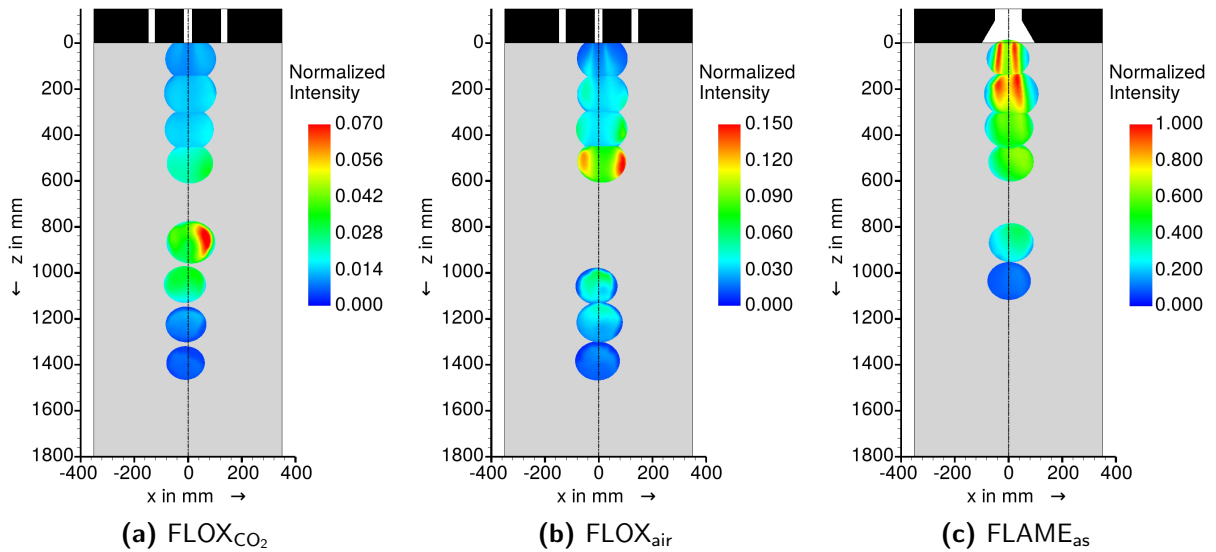


Figure 3.9: Reaction zone topology observed with flameless and low-NO_x flame burners (adapted from [167])

with a maximum at around $z = 900$ mm. The onset of the reaction zone corresponds to the region where combustion-air jets start interacting with the central coal jet. This can be verified from the LDV results presented above, see Figure 3.6a. Another striking difference is found by comparison of OH* and LDV results: when the flow field achieves the plug flow characteristics, reactions are mostly completed. In the FLAME_{as} condition, this can be seen at $z = 1060$ mm, whereas in flameless conditions, the reaction intensity turns down for $z > 1400$ mm. Plug flow is then almost achieved as indicated by Figure 3.7d. The much lower reaction intensity highlights the very small heat release in this reaction zone, owing to the dilution of the reactants. This exhibits the known characteristics of flameless combustion.

Temperature distribution and heat flux give interesting insights into the combustion process. While the temperature field is interpolated from a dense grid of in-furnace measurements, the heat flux trends are taken from a wall-even position. The heat flux is measured twice by different techniques to differentiate between the radiative and the convective portion. The radiative heat flux is measured directly by the ellipsoidal radiometer, whereas the convective heat flux can be obtained by subtraction of the radiative heat flux from the total heat flux measured by a heat flux meter, see also Section 3.2.

Figure 3.10 gives the temperature field in the furnace, interpolated from the in-furnace temperature measurements. Similar to the OH* intensities shown in Figure 3.9, the flameless conditions can easily be distinguished from flame conditions. Even if the two intruding combustion-air jets are well pronounced, the temperature fields in flameless conditions are relatively homogeneous. In the FLAME_{as} condition, the temperature increase occurs in a more concentrated manner upstream of $z = 1000$ mm, and drops more quickly further downstream.

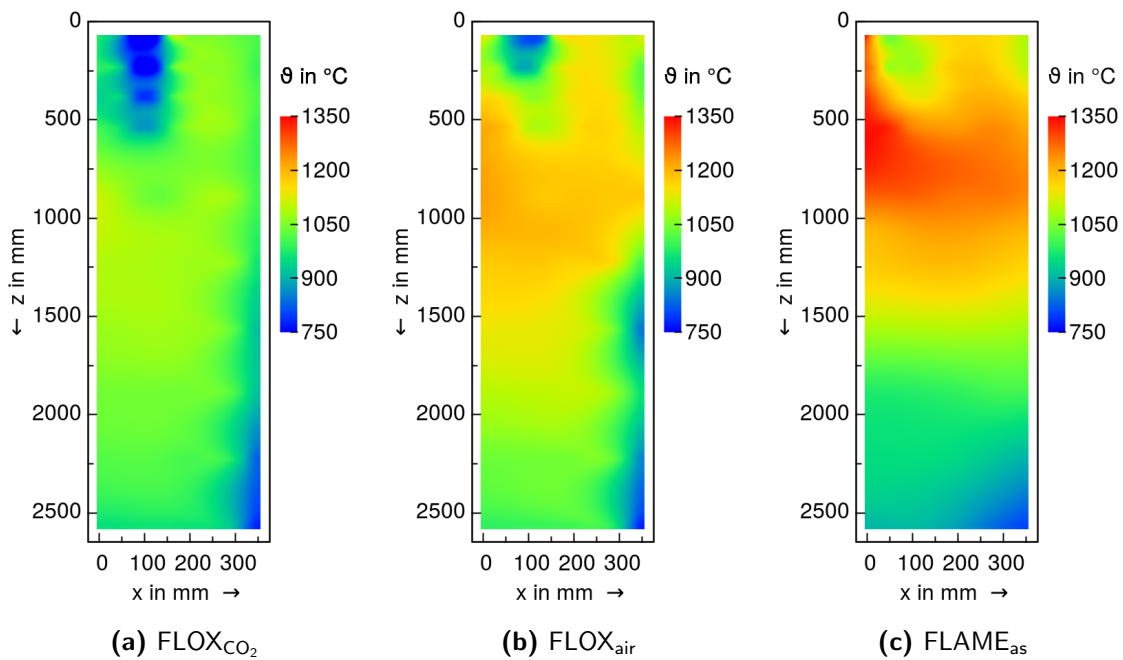


Figure 3.10: Comparison of interpolated temperature fields of flameless and flame-existent conditions

It is remarkable that the dilution of the coal-carrier-gas jet strongly homogenizes the temperature field, compare Figures 3.10a and 3.10b. On the other hand it is observed that the delayed combustion of coal is not very well compensated by mixing with hot flue gases; thus, the temperature remains significantly lower on the furnace axis in FLOX_{CO₂}.

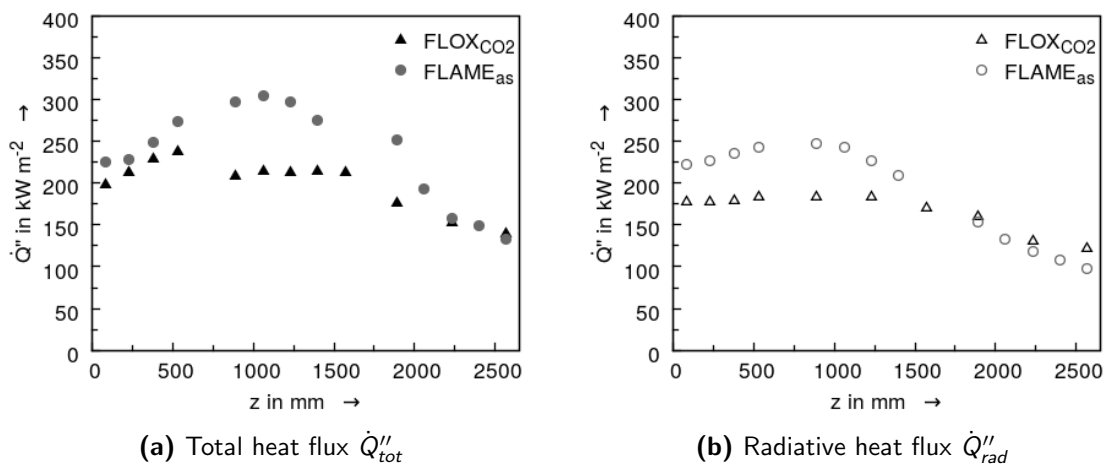


Figure 3.11: Total and radiative heat flux at the walls of FLOX_{CO₂} and FLAME_{as}

In contrast to the temperature measurements, heat flux sampling was only performed for FLOX_{CO₂} and FLAME_{as}, and the results are presented here in Figure 3.11. As for temperature and OH* chemiluminescence, the homogeneity of the quantity in question increases when the

combustion mode is flameless. This was already observed by Orsino et al. [100] and Plessing et al. [108]. It is interesting to note that although the total heat flux of flameless and flame-existent conditions increases in parallel in the beginning, the radiative heat flux does not show such a trend. The total heat flux is quantitatively very similar in the beginning for both conditions, but the radiative heat flux reveals a significant gap. It can be concluded that a strong convective portion, i.e. hot recirculated flue gas, must be present in the upper part of the furnace.

3.6.4 Species evolution and conversion analysis by in-furnace gas concentration measurements

The species evolving from coal pyrolysis and combustion are accessed by suction-probe sampling and measured by FTIR, NDIR, chemiluminescence and paramagnetic analyzers with measurement ranges and uncertainties as given in Table 3.1. The same dense measurement grid as for suction pyrometry and laser Doppler velocimetry is applied in the “all-jets” plane. Each displayed measurement value is an average over a one minute steady-state condition. Fluctuations are respected by the standard deviation calculated alongside with the temporal averaging. Moreover, measurement uncertainties of each measurement device are taken into account. Thus, a total uncertainty for each measurement point is displayed in the following diagrams by error bars. Two characteristic measurement lines are extracted from the data: the centerline at $x = 0$ mm and a near-wall line at $x = 300$ mm, see Figures 3.12 and 3.13, respectively. The centerline exhibits information about coal devolatilization, combustion and mixing of the central coal jet and the side combustion-air jets. The near-wall line gives details on the slim recirculation zone between combustion-air jets and wall as well as on the gas atmosphere in the top part of the furnace which is subsequently mixed in the intruding jets.

The centerline results for O₂ and CO₂ reflect the usage of carrier-gas in the flameless cases and the applied air-staging in the flame case. The latter exhibits an already low O₂ concentration immediately downstream of the burner at $z = 80$ mm which can be related to the low burner air ratio of 0.88 and the fact that strong mixing is induced by the swirled combustion air. For the FLAME_{as} condition, the position of the air-staging probe at $z = 1570$ mm is very well observable when O₂ concentration increases from nearly 0 % to approximately 3.5 % at $z = 1890$ mm which is almost the furnace exit O₂ concentration. The trend of O₂ concentration in the flameless cases is dominated by the choice of the coal-carrier-gas. Whereas it remains close to 0 % in the beginning for FLOX_{CO₂}, it steeply drops from 12 % to nearly 0 % for FLOX_{air}. It can be well identified when the combustion-air jets start mixing in the central coal jet from $z = 1060$ mm and the O₂ concentration starts increasing. Here, it can be seen that the combustion-air jets of FLOX_{CO₂} are stronger than those of FLOX_{air}, as they carry more air and thus more O₂ to the furnace axis. Finally, when the combustion process approaches completion, O₂ concentrations

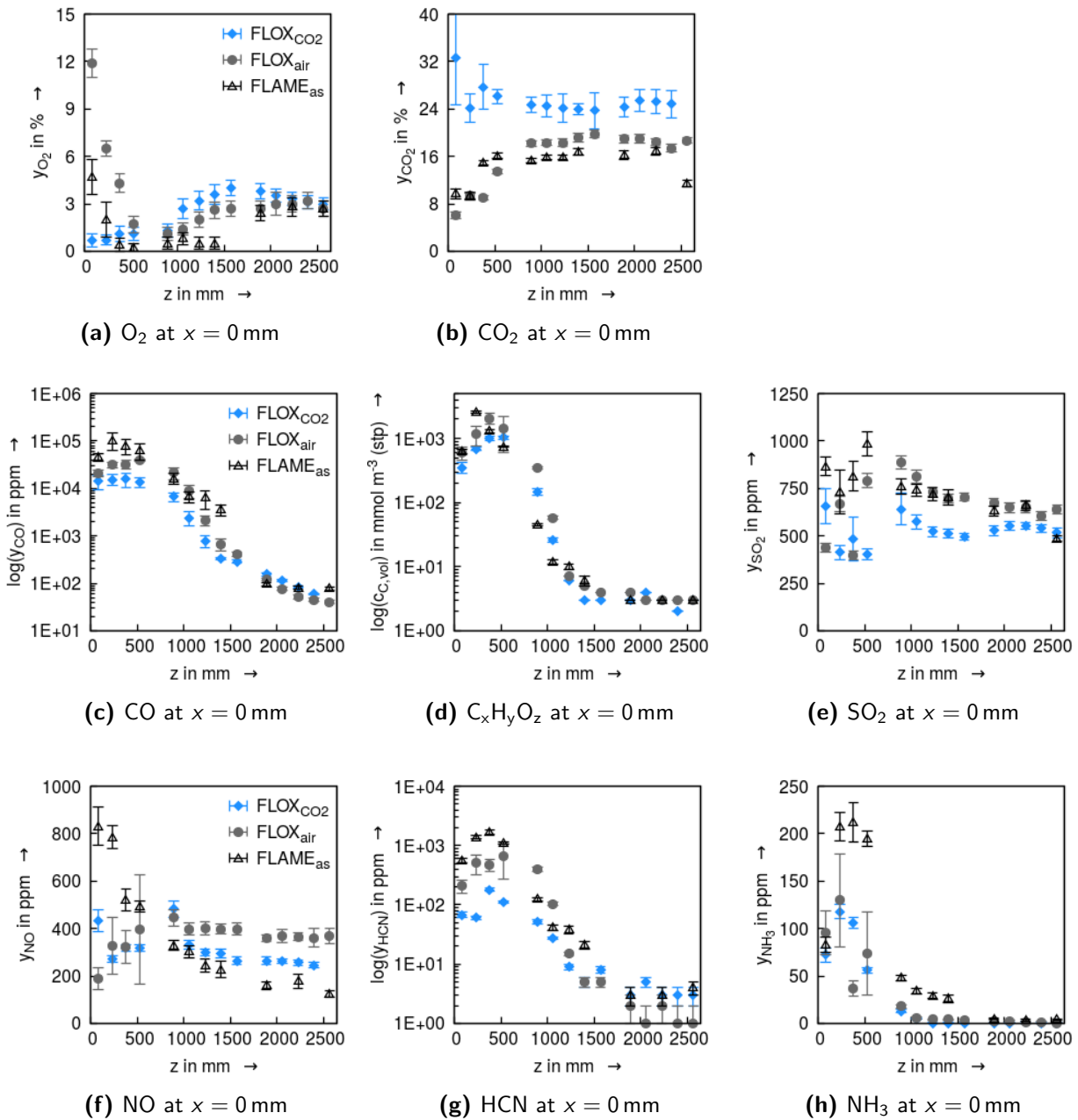


Figure 3.12: Results of in-furnace suction-probe sampling of FLOX_{CO₂}, FLOX_{air} and FLAME_{as} at $x = 0$ mm

on the furnace axis are similar for all three cases as a consequence of similar air ratios. The CO₂ concentration trend of FLOX_{CO₂} is dominated by the coal-carrier-gas jet, resulting in a seven percentage-points higher furnace exit concentration level. The externally diluted cases FLOX_{air} and FLAME_{as} show very similar CO₂ trends.

CO and volatiles trends shown in Figures 3.12c and 3.12d are similar in shape for all three cases. Maxima are achieved for FLAME_{as}, indicating a faster and more intense devolatilization for this case which is related to the higher prevalent temperatures. Volatiles are more quickly

burned and thus the volatiles concentration already achieves a steady-state at approximately $z = 1500$ mm, whereas the CO concentration decreases less rapidly. The latter is due to the char burnout producing CO in parallel. Again, the influence of the sub-stoichiometric atmosphere can be seen for FLAME_{as}: whilst the CO consumption is even slower than in the flameless cases before $z = 1500$ mm, it drops down to comparable values after staging-air is injected.

The SO₂ concentration trends presented in Figure 3.12e picture the combustion process similar to NO, see Figure 3.12f for the flameless cases. FLOX_{air} is characterized by higher concentrations than FLOX_{CO₂} which might be caused by higher temperatures. The SO₂ concentration climbs in both cases from the burner exit until admixture of combustion-air jets becomes dominant on the furnace axis. Downstream, the SO₂ concentrations are decreased by dilution and subsequently stabilize at around 600 ppm. It is interesting to note that the SO₂ trend of FLAME_{as} does not differ from the flameless cases as its NO pendant does. Of course, a higher maximum of the SO₂ concentration is achieved due to higher temperatures in the flame-existent case, but similar concentrations are achieved at the end of the in-furnace measurement zone. Despite this finding, the SO₂ furnace exit concentrations differ by more than 100 ppm from FLAME_{as} to flameless combustion cases. FLAME_{as} exhibits the highest SO₂ concentrations at the furnace exit, i.e. 651 ppm, allowing the conclusion that the SO₂ formation is enhanced in the burnout zone of the conventional flame burner.

Bigger differences can be found in the release, formation and consumption of nitric compounds measured as NO, HCN and NH₃ presented in Figures 3.12f, 3.12g and 3.12h. In FLOX_{air}, the NO concentration starts increasing after the burner until it reaches a high and stable level. In FLOX_{CO₂}, it first drops from $z = 80$ mm to $z = 230$ mm, then it increases as in FLOX_{air} before it falls again to a stable but lower level than that of FLOX_{air}. Stable NO concentration levels are reached for both flameless cases at approximately 1500 mm from the burner exit and are of about 370 ppm (FLOX_{air}) and 260 ppm (FLOX_{CO₂}). The flame-existent case instead reveals a very high initial NO concentration of nearly 840 ppm which is subsequently reduced in the reduction zone until the addition of staging-air. Further downstream, the NO level remains stable, being the lowest of all three cases at about $y_{NO} = 170$ ppm. This contradictory behavior might be caused by the different release rates of NO_x precursors.

The NH₃ concentration is almost doubled in the FLAME_{as} case compared to the flameless cases between axial positions 230 mm and 530 mm. It is converted at nearly zero O₂ conditions in the flame-existent case, whereas especially in FLOX_{air}, the O₂ concentration might be high enough to oxidize NH₃ to NO rather than to reduce NO by means of NH₃. As soon as a sufficient O₂ supply is ensured either by sufficient admixture of combustion-air jets in the flameless cases or by adding staging-air, the NH₃ concentration drops to 0 ppm.

Similarly to NH₃, the NO_x precursor HCN is released at different rates depending on the prevailing temperatures in the devolatilization zone. FLAME_{as} shows one order of magnitude higher HCN concentrations of 1666 ppm than FLOX_{CO₂} with 179 ppm. The HCN release of

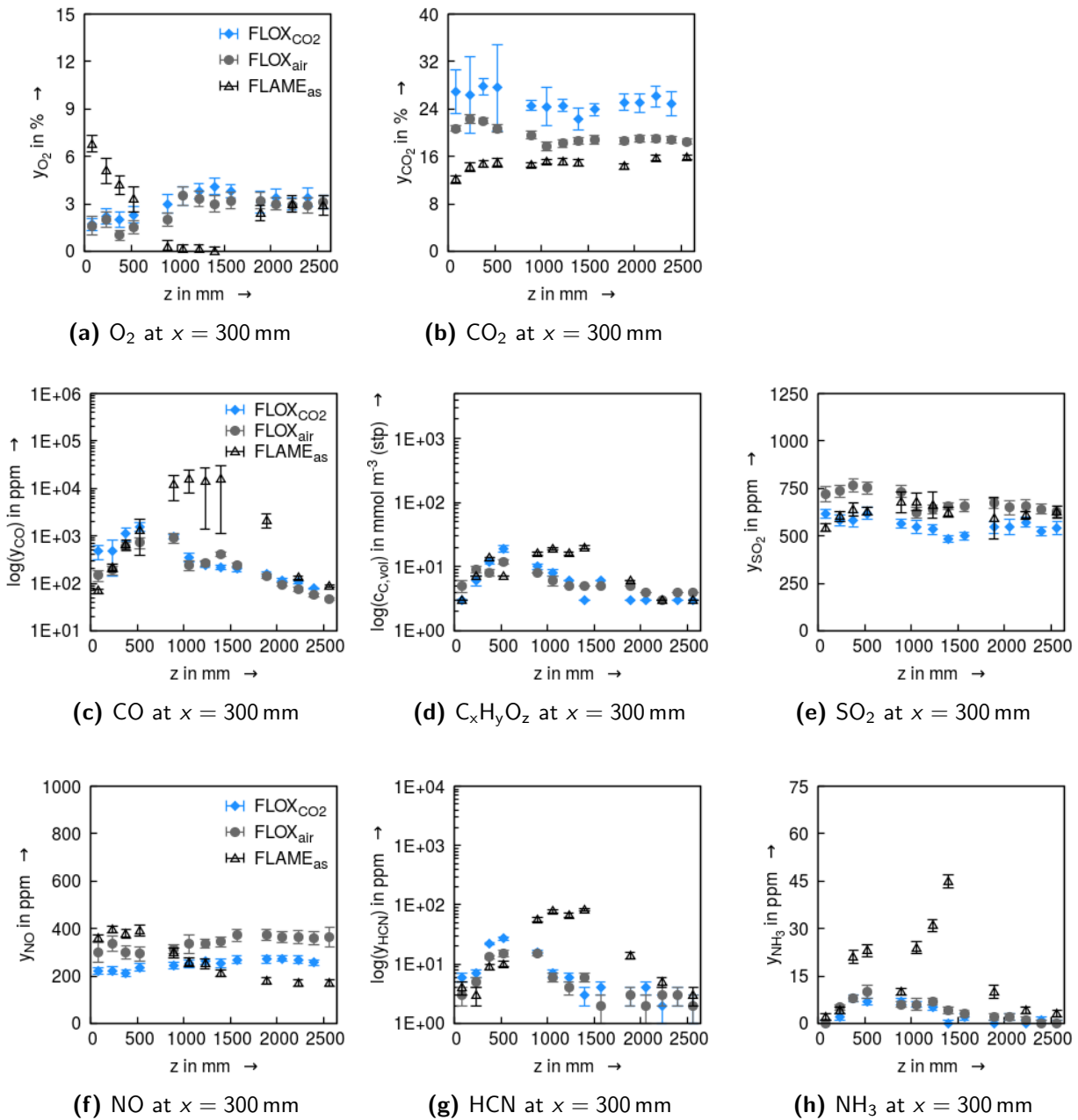


Figure 3.13: Results of in-furnace suction-probe sampling of FLOX_{CO₂}, FLOX_{air} and FLAME_{as} at $x = 300$ mm

the FLOX_{air} case is in between these extrema. HCN consumption is then strongly enhanced by the admixture of O_2 from the combustion-air jets which is most pronounced for FLOX_{air}. After sufficient O_2 is present, HCN also drops to nearly 0 ppm for all three cases.

Along the measurement axis at the radial position $x = 300$ mm from the furnace centerline, the conditions near the wall can be identified. Considering the O_2 concentration displayed on Figure 3.13a, it can be observed for both flameless cases that results are very similar in the near-wall region: a low O_2 concentration in the burner vicinity indicates good recirculation of burned

flue gas, whereas an increase is observed at around $z = 1000$ mm when combustion-air jets expansion reaches the near-wall region and cuts off the recirculation zone further downstream (see Figure 3.6a). It is interesting to note that pollutant concentrations such as SO₂, see Figure 3.13e, and NO, see Figure 3.13f, reveal a stable trend along the measurement axis. This can be related to the strong recirculation of flue gas from areas below $z = 1650$ mm as shown by Figure 3.6a. Moreover, concentrations of highly reactive species such as volatiles, NH₃ and HCN are one or two magnitudes lower than on the furnace axis.

The results of the conventional flame burner are very different. The O₂ concentration reaches its maximum very close to the burner and the furnace top indicating a strong swirl and a fast spreading of the flame towards the furnace walls. Again, O₂ is completely consumed by the occurring reactions and reaches 0% at around $z = 1000$ mm, as was seen before on the furnace axis, cf. Figure 3.12a. Consequently, the concentration of products of incomplete combustion such as CO and volatiles increases until staging-air ensures a sufficient O₂ supply. Similar trends are observed for the NO_x precursors NH₃ and HCN presented in Figures 3.13h and 3.13g. NO concentration instead shows a similar trend as along the furnace axis, however without a maximum in the burner vicinity.

3.6.5 Interim conclusions

The choice of coal-carrier-gas strongly affects the combustion process with the current PT1 burner. NO_x concentrations in FLOX_{air} are increased by more than 50% when compared with FLOX_{CO₂}. It is concluded that this difference may arise from an inhibited fuel-N conversion due to lower O₂ availability in the reaction zone. This has been similarly found by Mei et al. [89]. The deeply air-staged flame case resulted in the lowest NO_x concentrations of all cases. The char burnout is consequently deteriorated, as indicated by the C-in-ash results, measured at 21.1%, 15.4% and 4.0% for FLAME_{as}, FLOX_{CO₂} and FLOX_{air}, respectively. The in-furnace species measurements suggest that NO_x can be effectively mitigated if high portions of nitric compounds are initially released into a reducing atmosphere [106]. The rapid devolatilization of coal particles at strong temperature gradients can generate a high volatile-N share as seen from the flame burner. This is enhanced by high heating rates [13, 132].

The decrease in SO₂ concentrations in flameless conditions is quite significant, but can not be explained thus far. Ristic [115] observed similar SO₂ abatement for experiments in the same facility, but with different coal and burner configurations. It is assumed that the desulfurization product CaSO₄ is preserved in flameless combustion conditions due to mild temperatures below its thermal instability threshold of 1200 °C [24]. Additionally, the high recirculation in flameless combustion allows unreacted particles to continue the flue gas desulfurization as their residence time is increased. Ash analysis from the ESP, bag filter and air preheater exhibits that sulfur content in the ashes increases from FLAME to FLOX_{CO₂} conditions. FLAME and FLOX_{air} are

found to have similar sulfur content in the fly ash which is in contradiction with the differing SO₂ concentrations. Under FLOX_{CO₂} conditions, however, an increase of sulfur content by 23 % in the fly ash is identified.

3.7 Influence of CCG nozzle positioning - PT2 tests

The experience gained in PT1 testing led to the design of the PT2 burner as described in Section 3.1. The PT2 burner features four nozzles on the same pitch-circle diameter: two combustion-air nozzles and two coal-carrier-gas annuli, see Figure 3.2b. Through this layout, the coal emerges directly in the recirculated flue gases. The results of the PT2 burner testing are discussed in the following and cross-compared to those of the PT1 prototype burner presented in Section 3.6.4.

3.7.1 Flue gas analysis and combustion efficiency

Table 3.9 gives an overview on concentration and emission numbers at the furnace exit obtained for FLOX_{CO₂} and FLOX_{air} with the PT2 prototype burner. It additionally includes the results of the PT1 prototype burner testing (cf. also Table 3.7) for ease of comparison.

Table 3.9: Results of continuous flue gas measurements at the furnace exit for flameless conditions with PT2 prototype burner (PT1 results reproduced for ease of comparison)

Dry basis	PT2			PT1	
	FLOX _{CO₂}	FLOX _{air}	FLOX _{air,rot}	FLOX _{CO₂}	FLOX _{air}
y _{O₂} in %	2.2	2.1	3.04	2.8	2.9
y _{CO₂} in %	25.3	17.2	16.5	22.3	17.6
y _{CO} in ppm	74	71	26	181	48
y _{NO_x} in ppm	255	270	396	231	359
y _{SO₂} in ppm	464	561	491	501	545
c _{CO} in mg m ⁻³ (STP) ‡	74	70	27	188	50
c _{NO_x} in mg m ⁻³ (STP) ‡ †	418	438	679	391	611
c _{SO₂} in mg m ⁻³ (STP) ‡	1082	1297	1196	1206	1323

‡ @ 6 % O₂; † NO_x as NO₂

FLOX_{CO₂} and FLOX_{air} in the PT2 prototype burner tests are operated at similar total air ratios of around $n = 1.13$, resulting in very similar furnace exit O₂ concentrations. CO₂ concentrations obviously differ due to the application of CO₂ coal-carrier-gas in FLOX_{CO₂}. The very similar concentrations of CO and NO_x are most striking. This demonstrates the efficiency

of the new burner design in diluting the incoming coal jet with internally recirculated flue gas. In fact, the use of CO₂ as the coal-carrier-gas can be regarded as dispensable, since the advantages are marginal. Compared to the results obtained with the PT1 burner, CO drastically decreases by 59 % for FLOX_{CO₂} and increases by 47 % for FLOX_{air}. NO_x emissions behave in a contrary manner, with a penalty of 10 % for FLOX_{CO₂} and an advantage of 25 % for FLOX_{air}. SO₂ emissions with the PT2 burner decrease in both cases.

The case FLOX_{air,rot} stands out from the two other cases, as the air ratio $n = 1.17$ is noticeably higher, and thus the furnace exit O₂ concentration and NO_x concentration are. CO concentration consequently is decreased.

Combustion efficiency analysis is carried out with the results in Table 3.10. No samples were taken for the FLOX_{air,rot} case, thus it is not listed in the following table. It can be seen that the numbers are very similar for both flameless cases which was different in the PT1 tests. Considering FLOX_{CO₂}, C-in-ash, for example, is lowered from 15.4 % to 6.15 % with the PT2 burner, corresponding to a relative improvement of about 57 %. In contrast, C-in-ash increases from 4.0 % to 6.75 %, when looking at FLOX_{air} which is an increase of about 69 %, relatively spoken. Similar observations were made above in the comparison of CO flue gas concentrations.

Table 3.10: Carbon in ash, unburned carbon and burnout for flameless conditions with PT2 prototype burner (PT1 results reproduced for ease of comparison)

Dry basis		PT2		PT1	
		FLOX _{CO₂}	FLOX _{air}	FLOX _{CO₂}	FLOX _{air}
C-in-ash	in %	6.15	6.75	15.4	4.00
Unburned carbon	in %	0.50	0.55	2.07	0.46
Burnout	in %	99.4	99.3	97.3	99.4

Since the combustion efficiency is mainly influenced by the oxidant availability and the residence time of coal particles in an oxidant-supplying atmosphere, the results can be put in context the following way: thermal load, air ratios and thus volumetric flow rates are very similar in the presented PT1 and PT2 burner tests. Accordingly, the residence time of coal particles in the furnace can be estimated to be in the same range. Thus, the second influencing factor, oxidant availability, remains as a reason for the differences in combustion efficiency. In the case of FLOX_{air}, the change is self-explanatory. Indeed, air remains as the coal-carrier-gas, but the stability of the impinging jets is lowered by the split and relocation of the coal-carrier-gas nozzle and thus, they are quickly diluted by the recirculated flue gas. However, when mixing occurs with the already diluted combustion-air jets further downstream, oxidant availability seems to be too low for the remaining residence time to complete char burnout. With regard to the PT1 prototype burner, the coal-carrier-gas jet is much closer to the combustion-air jets and mixing

occurs earlier when a higher O₂ partial pressure is present. For the PT2 burner with FLOX_{CO₂}, the coal-carrier-gas jet dilution and mixing with combustion-air jets occur the same way as it does for FLOX_{air}. But, the oxidant availability is better in the PT2 burner than in the PT1 burner and thus, the combustion efficiency improves for FLOX_{CO₂}.

Summing up, the coal-carrier-gas jets and combustion-air jets are comparably diluted for both flameless cases in the PT2 burner tests. The dominating factor for char burnout is the oxidant availability in accordance with the remaining residence time in the burnout zone. The coal-carrier-gas jet is dispersed rapidly enough that the choice of coal-carrier-gas becomes of minor importance.

3.7.2 Temperature field and heat release analysis

The heat release in PT2 testing was evaluated via the total and radiative heat flux profiles along the furnace walls and the in-furnace gas temperature measurements. The OH* chemiluminescence imaging, discussed in Section 3.6.3, was only performed in the PT1 tests. Heat flux profiles are presented in Figure 3.14 for FLOX_{CO₂} and FLOX_{air} obtained with the flameless prototype burner PT2. They are compared with the conventional flame burner profiles presented in Section 3.6.3. The observations made for the heat fluxes can be verified and understood from the interpolated gas temperature plots in Figure 3.15. In these plots, data from in-furnace gas temperature suction-probe measurements are interpolated and refer to the same temperature range between 750 and 1350 °C. The relatively fine structure of combustion-air jets can not be exactly captured by suction pyrometry at each location and therefore, the results are prone to averaging.

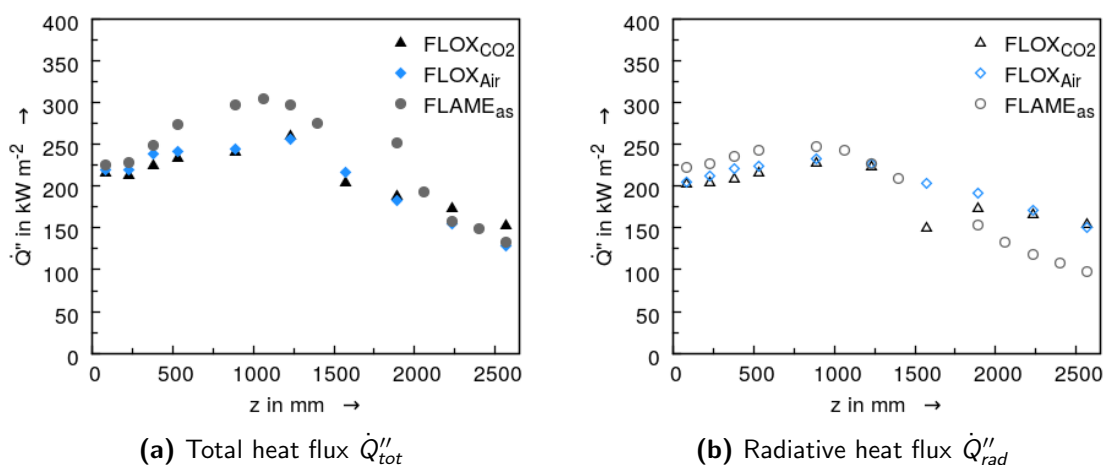


Figure 3.14: Total and radiative heat flux at the wall of FLOX_{CO₂} and FLOX_{air} for the PT2 burner vs. the reference flame burner

Looking at the flameless combustion heat flux profiles, it is observed that the difference

between the two cases is very small for both, total and radiative heat flux. Total heat flux of the PT2 burner does not show a platform between $z = 890$ mm and $z = 1570$ mm, as is seen for the PT1 burner (cf. Figure 3.11). Its radiative fraction exhibits a smoother profile than is seen with the PT1 burner. The latter is closer to the FLAME_{as} condition, especially downstream of $z = 1890$ mm. This can be attributed to the more extended reaction zone with the PT2 burner.

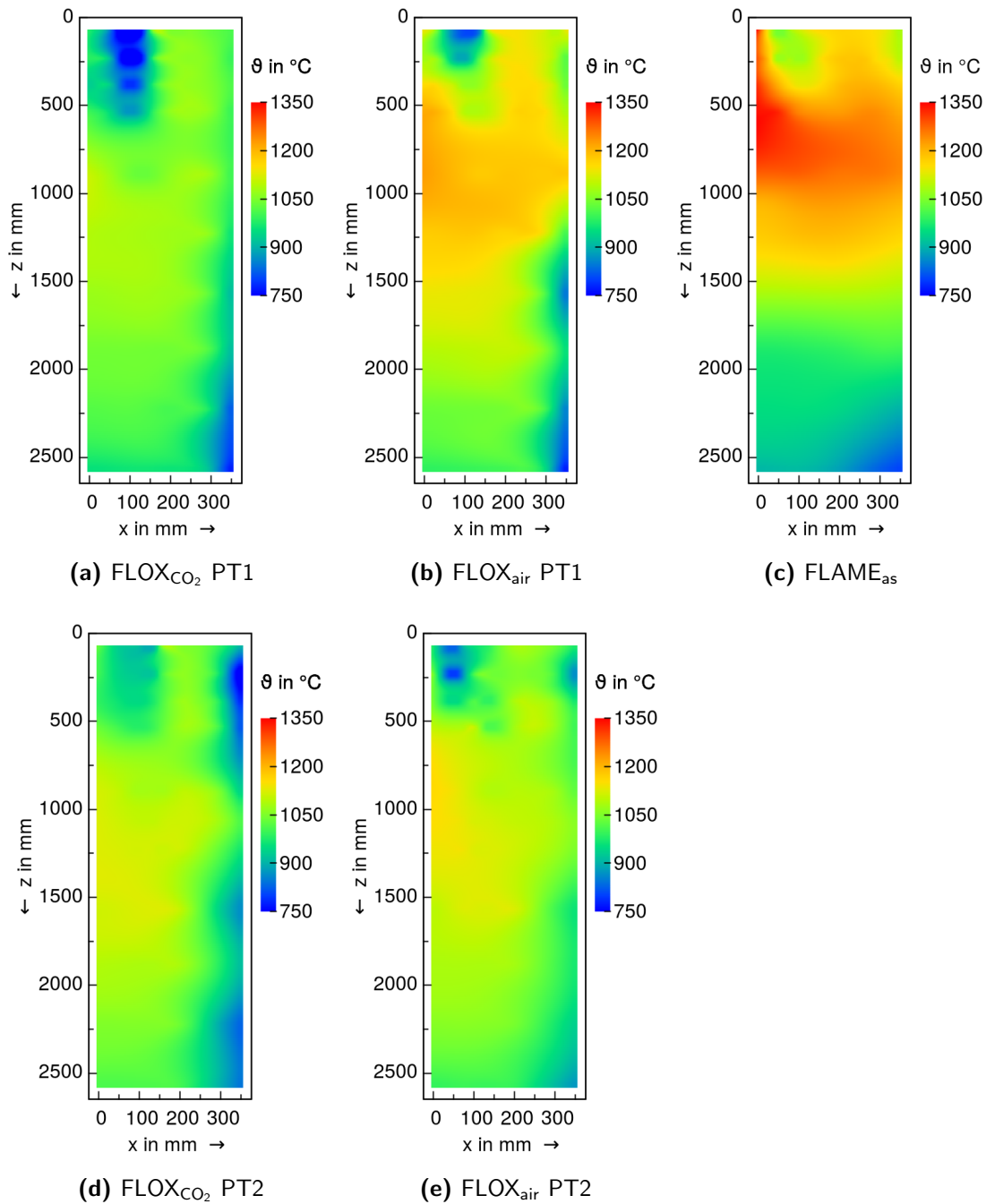


Figure 3.15: Comparison of interpolated temperature fields of flameless PT1 and PT2 conditions and flame-existent condition

From Figure 3.15, the very similar temperature contours of FLOX_{CO₂} and FLOX_{air} with the PT2 burner can be seen. This is reflected by the above described total and radiative heat flux results. Compared to the PT1 burner, temperatures are higher with the PT2 burner for FLOX_{CO₂} and lower for FLOX_{air} which supports the thesis of better homogenization by the PT2 burner. It also becomes clear that the radiative heat flux is initially below the values obtained for the FLAME_{as} condition, and increases downstream of $z = 1890$ mm. The temperature increase in a flame-existent condition is much steeper than in flameless PT2 conditions, but further downstream the gas temperature drops more quickly. In contrast, the temperature level remains higher in flameless conditions and thus, the radiative heat flux is measured at higher levels.

3.7.3 Species evolution and conversion analysis by in-furnace gas concentration measurements

Three characteristic measurement lines are discussed in the following. In addition to the furnace centerline and the near-wall line at $x = 300$ mm, the line of intruding coal-carrier-gas jet at $y = 135$ mm is analyzed in detail. Results of in-furnace gas measurements along the coal jet line are only available for FLOX_{air}. An uncertainty quantification is made as discussed above in Section 3.2.

Figure 3.16 points out the species trends along the near-wall line. Trends of NH₃ and volatiles are not included, as they are without significance. It generally stands out that trends of both flameless conditions are very similar for all species except for CO₂ which is due to the use of the coal-carrier-gas CO₂ instead of air in FLOX_{CO₂}. It is interesting to note that the O₂ concentration begins to develop from $z = 530$ mm in parallel with the NO concentration (cf. Figures 3.16a and 3.16d). They increase for the flameless combustion burner, whereas they drop for the air-staged flame burner. This parallel development can be observed only, if oxygen is present. Otherwise, the NO concentration keeps falling as the O₂ concentration remains at 0% before staging-air injection, as demonstrated in the air-staged flame case. Downstream of staging-air injection at $z = 1890$ mm, NO formation seems to be in equilibrium with NO destruction. This is also valid for the flameless cases. HCN and NH₃ (not shown) trends behave similarly as for the PT1 burner: significant concentrations can only be found in the burner vicinity before combustion-air jets touch the furnace walls. An almost constant SO₂ trend is observed for all cases, with lowest for the FLOX_{CO₂} case.

In Figure 3.17, the results along the furnace axis ($x = 0$ mm) are presented. Additionally, FLOX_{air,rot} results are included which represent measurements undertaken when the burner was rotated clockwise by 90°. The rotation allows for obtaining in-furnace data in the yz -plane, i.e. in the all-jets plane which cuts through the coal-carrier-gas nozzle (cf. Figure 3.2b). It is denoted here that air ratio and overall temperature level differ in the rotated case FLOX_{air,rot}

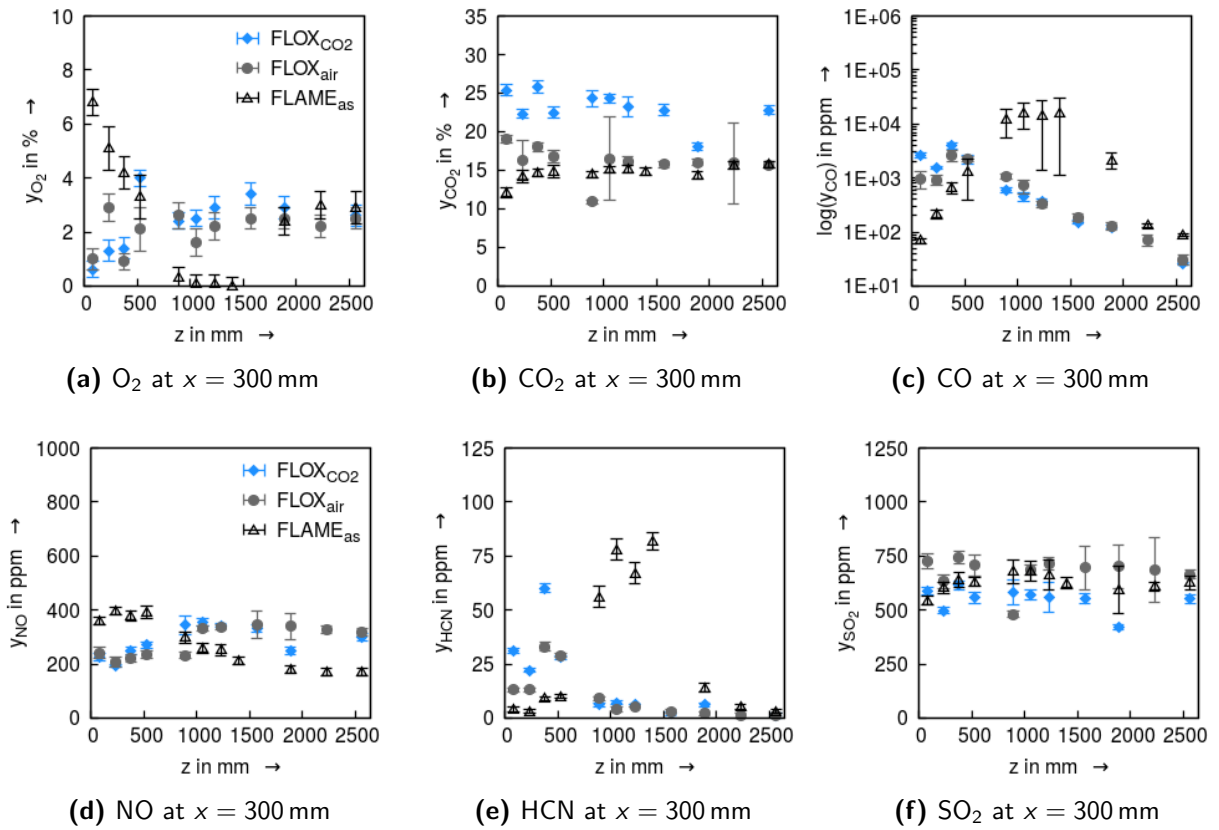


Figure 3.16: Results of in-furnace suction-probe sampling of FLOX_{CO₂} and FLOX_{air} for PT2 burner tests vs. FLAME_{as} at x = 300 mm

from the FLOX_{air} case. The air ratio is 1.17 instead of 1.13, as in FLOX_{air}. Consequently, their results should be judged as two different operating conditions. In-furnace data from FLOX_{air,rot} were only recorded until z = 1230 mm.

Differences are small between FLOX_{CO₂} and FLOX_{air} along the near-wall measurement line. FLOX_{air,rot} instead shows generally higher maxima than the other two flameless cases. This is valid for CO, HCN and volatiles concentrations even though maxima are similarly located. This argues for a higher overall temperature level, forcing a more intense devolatilization. On the contrary, NO concentration can be observed to be higher for all flameless cases than for the air-staged flame burner results at the furthestmost downstream measurement point of FLOX_{air,rot} at z = 1230 mm. Comparing only the three flameless cases, NO concentration is highest for FLOX_{air,rot} which is related to the higher temperature level, since measured O₂ concentrations are equal up to z = 1230 mm. Looking at the furnace exit NO concentrations, 396 ppm compared to 270 ppm are obtained for FLOX_{air,rot} and FLOX_{air}, respectively. It is suspected that the elevated air ratio and thus the lower reducing atmosphere downstream of z = 1230 mm hinders further NO reduction in the FLOX_{air,rot} case.

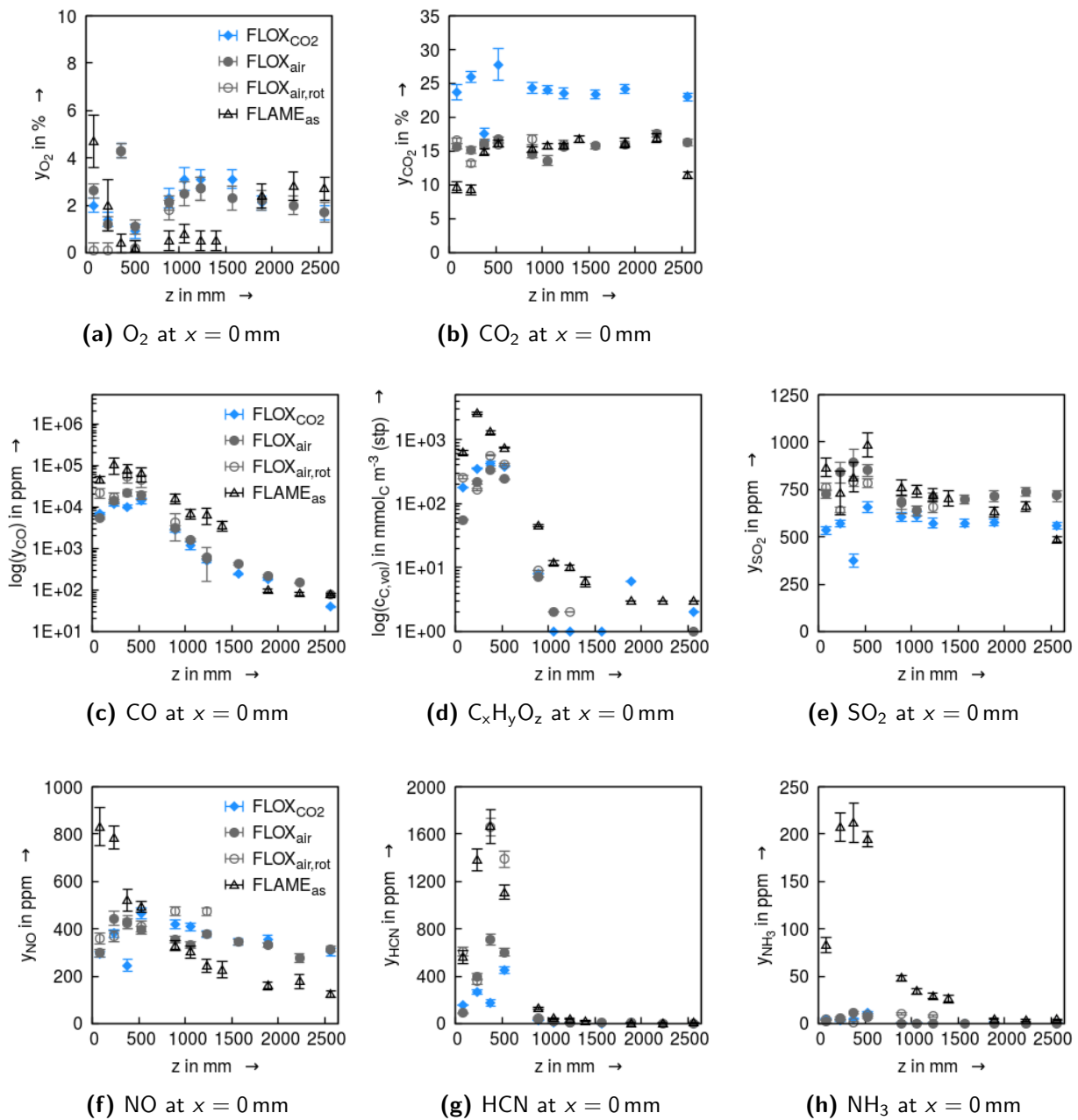


Figure 3.17: Results of in-furnace suction-probe sampling of FLOX_{CO₂}, FLOX_{air} and FLOX_{air,rot} for PT2 burner tests vs. FLAME_{as} at x = 0 mm

Figure 3.18 represents a comparison of in-furnace measurements of PT1 and PT2 burners along the coal-carrier-gas jet axis. For the PT1 burner, this axis equals the furnace center line and in the case of the PT2 burner, it is relocated to $y = 135$ mm, i.e. the coal-carrier-gas nozzle position. O₂ and CO₂ concentration trends are not impacted by the new design. The major differences are identified for CO, volatiles and NO_x precursors. Whilst similar peak CO concentrations are achieved, it falls more quickly downstream of $z = 530$ mm for the PT2 burner. The measured volatiles concentration is strongly reduced in the evolution from PT1

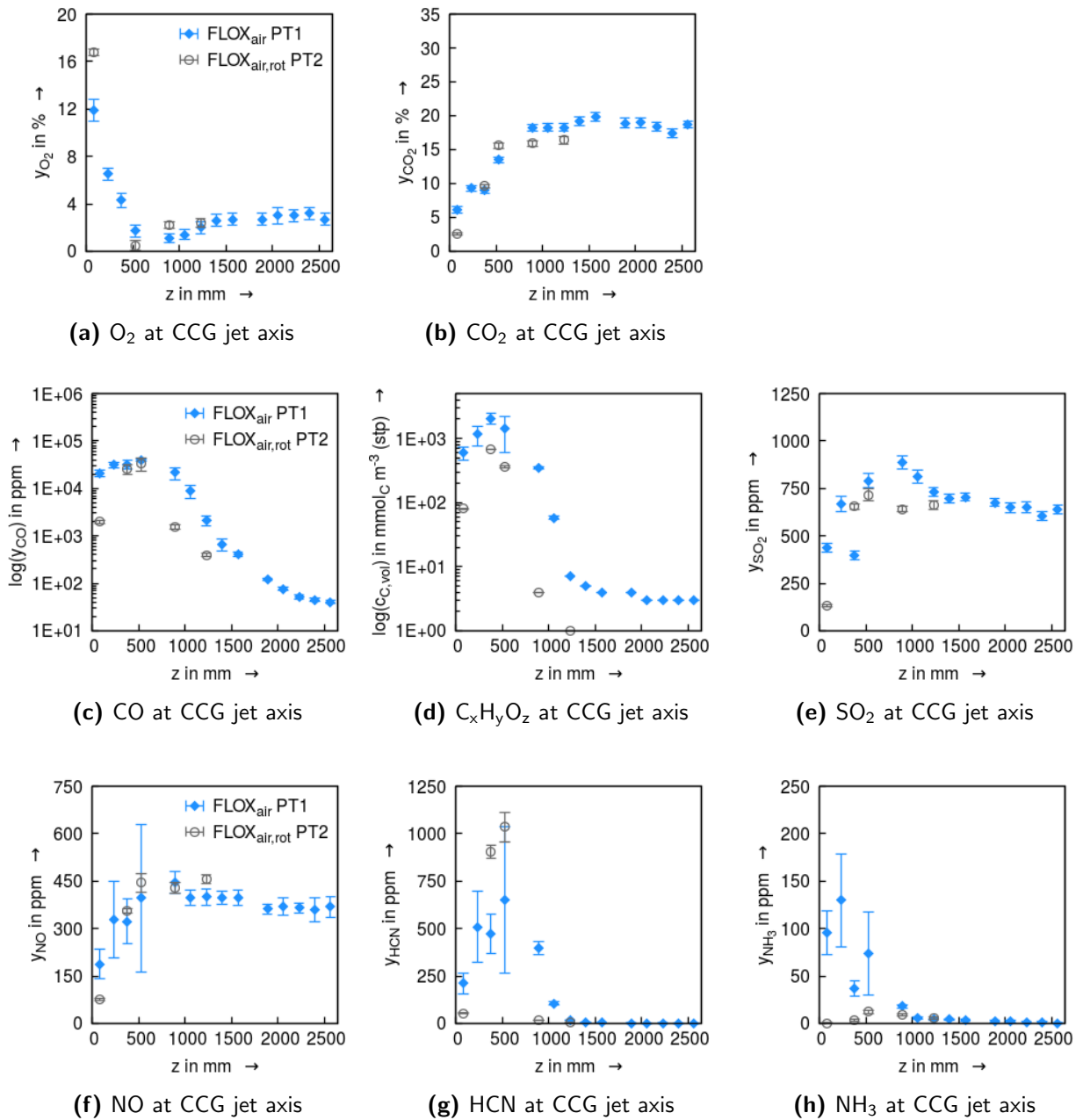


Figure 3.18: Results of in-furnace suction-probe sampling of FLOX_{air} PT1 and FLOX_{air,rot} PT2 along the coal-carrier-gas jet axis at $x = y = 0$ mm and $y = 135$ mm, respectively

to PT2 burner. A contradictory observation is made for HCN and NH_3 , where HCN release is enhanced by the new burner design, whereas NH_3 is close to the detection limit. However, these four trends have a faster decrease and thus a faster consumption of the involved species in common. NO concentrations again reveal similar trends for both burner prototypes, with a tendency to higher levels in FLOX_{air,rot} (PT2).

3.7.4 Interim conclusions

It has been postulated in Section 3.1 that NO should decrease if the release of nitrogenous compounds is enhanced during devolatilization. This seems to be refuted by the findings in Figure 3.18. A higher intermediate NO concentration is obtained despite higher HCN concentrations in the devolatilization zone. Additionally, an increase in the NO concentration is observed at the furnace exit: from 359 ppm with the PT1 prototype burner to 396 ppm with the PT2 prototype burner. On the other hand, it can be stated that the NO concentration at the furnace exit falls to 270 ppm for FLOX_{air} with the PT2 prototype burner. It seems that the finally resulting NO concentration is strongly related to the air ratio n , see Table 3.11.

Table 3.11: Comparison of air ratios and NO concentrations at the furnace exit for FLOX_{air} cases

	FLOX _{air}	FLOX _{air}	FLOX _{air,rot}
Burner prototype	PT2	PT1	PT2
Air ratio n	1.13	1.16	1.17
c_{NO_x} in mg m ⁻³ (STP) ‡	438	611	679

‡ @ 6% O₂; NO_x as NO₂

Nevertheless, the following conclusions can be drawn from both burner prototype testings:

- The PT2 burner design brings advantages known from the use of CO₂ as the coal-carrier-gas to the use of air. Similar results in concentrations and burnout are obtained with both gas types.
- A better mixing of coal particles with recirculated flue gases and thus a faster heating and devolatilization of the coal is achieved. This is indicated by the in-furnace measurements, especially of HCN as a precursor for NO_x: its concentration is found increased by almost 66% in PT2 burner tests. Moreover, similar or even higher CO concentrations are measured along the coal-carrier-gas jet axis with the PT2 burner, arguing again for a better coal conversion.
- The potential of NO_x abatement, however, seems to be limited with both burner prototypes. The achieved minima are 391 and 418 mg m⁻³ (STP) at 6% reference O₂ concentration for the PT1 and the PT2 burner prototype, respectively, if coal-carrier-gas is CO₂. This might be due to a achieved similar recirculation rate K_v , derived with respect to the prior-to-mixing-length L_v . An analysis is made in Section 4.7.2.

It is suggested that O₂ availability should be further decreased in the primary zone which extends towards $z = 1500$ mm in the KSV A furnace. This could either be achieved by a

different burner design, e.g. an asymmetric nozzle arrangement as proposed by Li et al. [82] or by application of air-staging in flameless conditions. Therefore, the mixing of coal particles and oxidizer should be further delayed and enough time for oxidizer jet dilution should be ensured. NO_x reducing reactions can thus properly take place in such fuel-rich conditions. To ensure proper char burnout, a higher overall temperature level can be aimed for. Despite the equal NO_x concentration, the PT2 prototype burner is regarded to be superior to the PT1 prototype burner, due to its more homogeneous gas concentration and temperature profiles.

4 Mathematical Modeling

The mathematical modeling of pulverized flameless combustion is based on the models for conventional flame combustion. Most of the research conducted in this field employs Reynolds or Favre averaging of the governing Navier-Stokes (RANS) equations. Recently works have been published based on a principle known as large-eddy simulations (LES). Those authors claim that LES is superior in flameless combustion modeling, due to the better resolution of turbulence scales, i.e. the fluctuation of the fluid flow can be respected [58, 83]. It is postulated that this higher resolution of the turbulent scales, the so-called eddies, improves the reproduction of the fluid flow. This is especially favorable in combustion regimes such as flameless combustion which depend to a high extent on aerodynamics. A downside is the increased computational effort using LES, and that boundary conditions have to be set that may only be obtained with efforts.

The work at hand is based on the RANS approach, as this work is an outcome of a joint research project involving partners from industry and academia. RANS modeling is currently the most common approach, used in industry and research for its good balance between computational effort and reasonable results. IFK's in-house program code called AIOLOS is employed. One thesis is known dealing with flameless pulverized coal combustion based on this program code [74]. Other researchers have developed and presented model sets for flameless combustion simulation, most of them based on commercial program codes [124, 136].

The mathematical modeling of coal combustion as applied in boilers and industrial furnaces involves many different physical processes and interactions. They can be summarized under three main topics: fluid flow, chemical reactions and heat transfer. According to Schnell [127], these interactions are illustrated in Figure 4.1.

First-order interactions constitute that fluid flow enhances chemical reactions by mixing due to turbulence. On the other hand, the chemical reactions taking place modify the composition of the fluid, and thus can impact the fluid flow. Moreover, chemical reactions either absorb or release energy which needs to be transferred either by radiation, convection or conduction. The energy transferred can cause local temperature changes, and thus changes in density which subsequently affects the fluid flow. Finally, turbulence occurring in the flow field dissipates produced heat.

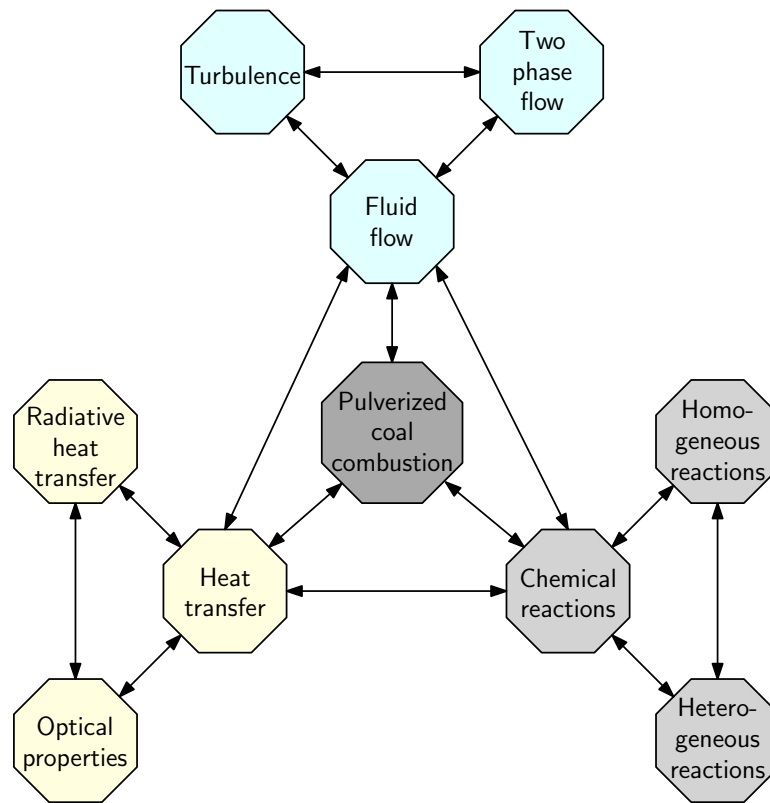


Figure 4.1: Interactions in pulverized coal combustion (adapted from [127])

This leads to the second-order interactions which are restricted to each of the three main physical disciplines. As indicated, fluid flow requires models accounting for turbulence and two-phase flow issues. In the domain of chemical reactions, the homogeneous and heterogeneous reactions taking place need to be modeled. Finally, heat transfer depends on the radiation and optical properties of solid and gaseous components. The governing equations of such a complex problem can only be resolved numerically. The equations and the solution procedure are presented in the following section.

4.1 Basic equations in computational fluid dynamics

The basic set of equations describing a viscous, heat conducting fluid flow are known as Navier-Stokes equations. They describe the conservation of mass, momentum and energy. If reactions of chemical species occur, species conservation has to be ensured by an additional equation, cf. Section 4.1.1. Temporal changes will not be considered in the work at hand; thus the Navier-Stokes equations are time-averaged and mass-averaged, see Section 4.1.3. They can be written in a general form to facilitate their numerical treatment, cf. Section 4.1.4. Multi-phase issues are discussed in Section 4.1.5. Finally, the solution procedure of the discretized equations

is discussed in Section 4.1.6 in conjunction with the convergence criteria applied in the work at hand.

4.1.1 Conservation equations

The Navier-Stokes equations are presented in their most general form and subsequently simplified, in line with the requirements of this work. The equations are written in an index form using $j = 1, 2, 3$ as the primary index and $i = 1, 2, 3$ as the secondary index. Each index represents the three directions in space. The so-called Einstein notation is used for clarity, i.e. that a summation over all defined values of an index is required if the index shows up twice in one term. It is demonstrated for mass conservation equation in the following.

Mass conservation

Mass conservation is expressed by the change of density over time and the change of mass transport over flow. According to the Einstein notation, equation (4.2) is equation (4.1) rewritten in full.

$$\frac{\partial \rho}{\partial t} + \frac{\partial (\rho w_j)}{\partial x_j} = 0 \quad (4.1)$$

$$\frac{\partial \rho}{\partial t} + \frac{\partial (\rho w_1)}{\partial x_1} + \frac{\partial (\rho w_2)}{\partial x_2} + \frac{\partial (\rho w_3)}{\partial x_3} = 0 \quad (4.2)$$

Momentum conservation

Momentum conservation is, on the left-hand-side of equation (4.3), the change of momentum over time and the convective transport of momentum over flow. On the right-hand-side, momentum changes due to external forces induced by pressure p and gravity g_i as well as by viscous stresses τ_{ij} .

$$\frac{\partial (\rho w_j)}{\partial t} + \frac{\partial (\rho w_j w_i)}{\partial x_j} = - \frac{\partial p}{\partial x_i} + \frac{\partial \tau_{ij}}{\partial x_j} + \rho g_i \quad (4.3)$$

For a Newtonian fluid, the induced stresses are linearly related to the velocity derivatives. Thus, the stress tensor τ_{ij} can be expressed by equation (4.4) with the dynamic viscosity of the fluid μ as proportional factor. The Kronecker delta δ_{ij} equals 1 if $i = j$ and otherwise 0.

$$\tau_{ij} = \mu \left(\frac{\partial w_i}{\partial x_j} + \frac{\partial w_j}{\partial x_i} - \frac{2}{3} \frac{\partial u_j}{\partial x_j} \delta_{ij} \right) \quad (4.4)$$

Energy conservation

Energy conservation is described by equation (4.5), again with change over time and convection on the left-hand-side and the diffusive transport and the heat source term S_{heat} on the right-hand-side. Energy is represented by the specific enthalpy h . The diffusive energy transport is characterized by the dimensionless Prandtl number Pr , given in equation (4.6). The heat source term S_{heat} consists of the chemical reaction source term S_{chem} and the radiative source term S_{rad} . If incompressibility of the flow can be assumed, the contribution of energy generated by viscous forces and of pressure-induced volume work can be neglected [105].

$$\frac{\partial(\rho h)}{\partial t} + \frac{\partial(\rho w_j h)}{\partial x_j} = \frac{\partial}{\partial x_j} \left(\frac{\mu}{Pr} \frac{\partial h}{\partial x_j} \right) + S_{heat} \quad (4.5)$$

$$Pr = \frac{\mu c_p}{\lambda} \quad (4.6)$$

Species conservation

Species conservation is similarly expressed as the energy conservation with concentration x_k as the conserved variable and the Schmidt number Sc instead of the Prandtl number Pr describing the diffusive transport. The Schmidt number Sc depends, besides on dynamic viscosity and density, on the binary diffusivity \tilde{D}_k of species k , see equation (4.8). Species source term S_k originates from the reaction mechanism of species formation or consumption.

$$\frac{\partial(\rho x_k)}{\partial t} + \frac{\partial(\rho w_j x_k)}{\partial x_j} = \frac{\partial}{\partial x_j} \left(\frac{\mu}{Sc} \frac{\partial x_k}{\partial x_j} \right) + S_k \quad (4.7)$$

$$Sc = \frac{\mu}{\rho \tilde{D}_k} \quad (4.8)$$

Generally spoken, the sum of all species fractions x_k must equal to 1. Thus, equation (4.7) must be solved $N - 1$ times for N species. The final species is obtained from the mass fraction constraint.

4.1.2 Thermodynamic equations

The above presented equations require a defined relationship of the thermodynamic quantities density ρ , pressure p and temperature T . For the gas mixtures occurring in the work at hand, this relationship is established by means of the ideal gas law, see equation (4.9). Since Mach numbers below 0.3 occur, the difference between prevalent pressure p and reference pressure p_{STP} is negligibly small, thus $p \approx p_{STP}$ is assumed [159]. The molecular weight of the gas mixture is derived via equation (4.10), depending on mass fractions x_k and the molecular weight \tilde{M}_k of each species k .

$$\rho = \frac{p \tilde{M}_{mix}}{\tilde{R} T} \quad (4.9)$$

$$\tilde{M}_{mix} = \left(\sum_{k=1}^n \frac{x_k}{\tilde{M}_{mix}} \right)^{-1} \quad (4.10)$$

Temperature T can be obtained from the calorific equation of state at constant pressure conditions as given in equation (4.11). Therein, $h_{k,STP}$ is the specific enthalpy of species k at a reference temperature T_{STP} , and $c_{p,k}(T)$ is the temperature dependent isobaric individual heat capacity of each species k .

$$h(T) = \sum_{k=1}^n x_k h_k = \sum_{k=1}^n x_k \left(h_{k,STP} + \int_{T_{STP}}^T c_{p,k}(T) dT \right) \quad (4.11)$$

4.1.3 Reynolds and Favre averaging

The presence of turbulence induces strong fluctuations in the flow and reactions. Fluctuations of state variables such as pressure, velocities and temperature do not obey any periodicity or pattern due to the chaotic nature of turbulence. This is exemplified in Figure 4.2 for variable $\phi(x_j, t)$ at any spot in the furnace.

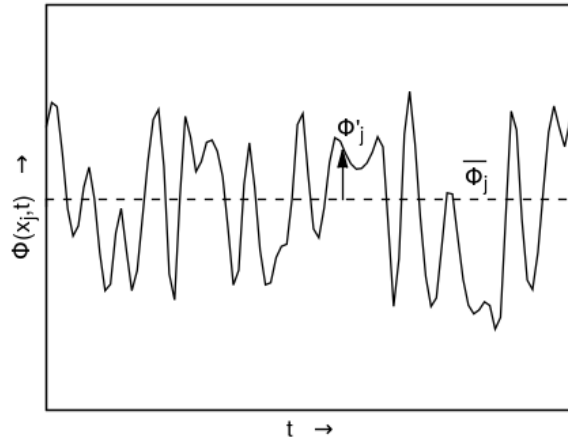


Figure 4.2: Instantaneous variable $\phi(x_j, t)$ over time t in a turbulent flow (adapted from [79])

To resolve the Navier-Stokes equations in full time and space, a large computational effort is required as in direct numerical simulation (DNS). This is currently applied very rarely to coal combustion systems. The turbulent fluctuations, however, are mostly of minor interest in contrast to the main motions of the flow. Thus, Navier-Stokes equations can be time-averaged

which is also known as Reynolds averaging. To account for the instantaneous motions of the flow, a fluctuating part $\phi'(x_j, t)$ is introduced alongside the time-averaged part $\bar{\phi}(x_j)$. This so-called Reynolds decomposition is formally written as shown in equation (4.12) for any instantaneous variable $\phi(x_j, t)$. Temporal averaging is defined by equation (4.13).

$$\phi(x_j, t) = \bar{\phi}(x_j) + \phi'(x_j, t) \quad (4.12)$$

$$\bar{\phi}(x_j) = \frac{1}{\Delta t} \int_0^{\Delta t} \phi(x_j, t) dt \quad (4.13)$$

Applying Reynolds decomposition and time averaging, it is obvious that the temporal average of fluctuations $\bar{\phi}'(x_j, t)$ equals 0. Reynolds averaging is sufficient for incompressible flows such as subsonic flows with Mach numbers below 0.3, leading to the Reynolds-averaged Navier-Stokes equations (RANS equations). In combustion systems, the assumption of incompressibility can not always be maintained due to the strong density gradients caused by heat release and intense reactions. To account for these density fluctuations, density or mass weighting is applied to variables before time averaging, known as Favre averaging. It is described by equation (4.14).

$$\tilde{\phi}(x_j) = \frac{\int_0^{\Delta t} \rho(x_j, t) \phi(x_j, t) dt}{\int_0^{\Delta t} \rho(x_j, t) dt} = \frac{\overline{\rho(x_j, t) \phi(x_j, t)}}{\bar{\rho}(x_j)} \quad (4.14)$$

Formally similar to the Reynolds decomposition, the instantaneous variable $\phi(x_j, t)$ can be decomposed in a Favre-averaged mean part $\tilde{\phi}(x_j)$ and a part $\phi''(x_j, t)$ representing the fluctuations over the Favre-averaged mean.

$$\phi(x_j, t) = \tilde{\phi}(x_j) + \phi''(x_j, t) \quad (4.15)$$

In order to obtain the Favre-averaged Navier-Stokes equations, Favre decomposition is applied to velocities w_j , enthalpy h and thus temperature T , whereas density ρ and pressure p are treated with standard Reynolds decomposition. In contrast to the time-averaged Reynolds fluctuations $\bar{\phi}'$, the time-averaged Favre fluctuations $\bar{\phi}''$ do not equal 0. Instead, it has been shown that $\overline{\rho \phi''}$ equals 0 [158].

Reynolds-averaged mean and Favre-averaged mean are related by applying Reynolds decomposition to ρ and ϕ in equation (4.14). It can be derived from equation (4.16) that Reynolds-averaged and Favre-averaged means become similar, if fluctuations of either density or the state variable are small or of weak correlation.

$$\tilde{\phi}(x_j) = \bar{\phi}(x_j) + \frac{\overline{\rho'(x_j, t) \phi'(x_j, t)}}{\overline{\rho(x_j)}} \quad (4.16)$$

An example of the Favre-averaged momentum equation is shown in equation (4.17).

$$\frac{\partial(\bar{\rho}\tilde{w}_j)}{\partial t} + \frac{\partial(\bar{\rho}\tilde{w}_j\tilde{w}_i)}{\partial x_j} + \frac{\partial(\overline{\rho w_j'' w_i''})}{\partial x_j} = -\frac{\partial\bar{p}}{\partial x_i} + \frac{\partial\bar{\tau}_{ij}}{\partial x_j} + \bar{\rho} g_i \quad (4.17)$$

An additional term $\overline{\rho w_j'' w_i''}$ is introduced without additional equations. These so-called Reynolds stresses are the subject of modeling in Section 4.4.2. For Favre-averaged momentum and energy conservation equations, several assumptions can be made to reduce the unknown terms [77]. Conservation equations for mass (4.1), energy (4.5) and species (4.7) as well as equation of state (4.9) are similarly treated and rewritten as can be found in Leiser [80].

4.1.4 General transport equation

Equations (4.1), (4.3), (4.5) and (4.7) exhibit a certain structural similarity and thus can be rewritten in a general form for the ease of treatment by the same numerical methods. This non-linear partial differential second-order equation accounts for the transient changes $\frac{\partial(\rho\phi)}{\partial t}$, the convective transport $\frac{\partial(\rho w_j \phi)}{\partial x_j}$, diffusion $\frac{\partial}{\partial x_j} \left(\Gamma_\phi \frac{\partial\phi}{\partial x_j} \right)$ with the diffusion coefficient Γ_ϕ and the corresponding sources and sinks S_ϕ . It is given in the standard form and in the Favre- and Reynolds-averaged form in equations (4.18) and (4.19), respectively.

$$\frac{\partial(\rho\phi)}{\partial t} + \frac{\partial(\rho w_j \phi)}{\partial x_j} = \frac{\partial}{\partial x_j} \left(\Gamma_\phi \frac{\partial\phi}{\partial x_j} \right) + S_\phi \quad (4.18)$$

$$\frac{\partial(\bar{\rho}\tilde{\phi})}{\partial t} + \frac{\partial(\bar{\rho}\tilde{w}_j\tilde{\phi})}{\partial x_j} + \frac{\partial(\overline{\rho w_j'' \phi''})}{\partial x_j} = \frac{\partial}{\partial x_j} \left(\Gamma_\phi \frac{\partial\tilde{\phi}}{\partial x_j} \right) + \bar{S}_\phi \quad (4.19)$$

Similarly to the Favre-averaged momentum equation (4.17), the term $\overline{\rho w_j'' \phi''}$ in equation (4.19), known as turbulent scalar fluxes, remains as an artifact of Favre averaging and needs to be derived in the course of turbulence modeling. A detailed derivation and explanation of the equations can be found elsewhere [37, 79, 125]. In the work at hand, steady-state flow phenomena are investigated and the transient term can thus be neglected. Since the equations are used in time-averaged and density-weighted form in the work at hand, time averaging and density weighting will not be further differentiated in the following for the ease of reading.

4.1.5 Turbulent multi-phase modeling

As described above, the continuous space covered by the fluid is represented by control volumina in AIOLOS. There are two possible formulations of the conservation equations depending on whether the coordinate system is fixed or moving with the flow. The latter is called the Lagrangian form and is often used when the motion of particles is of major interest. The fixed formulation is known as Eulerian form and is most common in computational fluid dynamics. It means that each control volume's coordinates rely on a fixed origin and that the control volume is flown through by the fluid. A hybrid method exists called the Euler-Lagrange formulation which is usually applied for dispersed multi-phase, e.g. gas-particle, flows. The continuous phase is then described by the Eulerian formulation and the dispersed phase by the Lagrangian approach. Further descriptions can be found in the literature [10, 12, 79].

The interactions between the phases must be analyzed in order to decide, whether a particle-laden gas flow as in pulverized coal combustion systems requires distinct treatment of each phase or not. The Stokes number St relates the characteristic dynamic time t_{dyn} of the dispersed and thus discontinuous phase to the residence time t_{res} of this phase in the continuous flow field, see equation (4.20). A detailed derivation of the Stokes number St is given elsewhere [79].

$$St = \frac{t_{dyn}}{t_{res}} \quad (4.20)$$

In the case of $St \approx 1$, the discontinuous and continuous phase, i.e. here the particle and gas phase, interact and influence the flow field. If $St \gg 1$, the residence time of the particles in the flow field is low and thus, they are influenced to a negligible extent. If $St \ll 1$, the discontinuous phase does not interact with the continuous phase and is passively following the main flow. The latter case is true for fine particles as are found in pulverized coal combustion.

The discontinuous particle phase must be included in the continuous gas phase to compute a multi-phase flow such as a pulverized coal gas mixture by means of the Eulerian formulation. Therefore, an effective fluid is defined, representing the continuous and discontinuous phases in order to obey the requirements of the homogeneous model. The effective density ρ_{eff} of the fluid is calculated as shown in equation (4.21), where α_G is the gas-phase fraction.

$$\rho_{eff} = \alpha_G \rho_G + (1 - \alpha_G) \rho_P \quad (4.21)$$

4.1.6 Solution procedure and convergence

The equations presented in Section 4.1.1 can be classified as a non-linear, elliptic equation system of second order. This equation system can not be solved by direct computation and thus, it requires an iterative solution algorithm approximating the correct solution. This solution algorithm needs to minimize the error between the computed and the correct solution.

Convergence criteria have to be defined that control the computation progress and initiate the stop as soon as a pre-defined accuracy is achieved.

The numerical solution of the system of coupled non-linear partial differential equations requires their linearization and decoupling. Therefore, methods are applied to transform the continuous differential equations in discontinuous algebraic ones which can be solved at discrete nodes. The used discretization scheme is presented in the following.

Discretization and interpolation schemes

A common method to discretize the space covered by the fluid is the finite volume method which was evaluated amongst others by Schneider [125]. The finite volumes are named cells in the following. The variable ϕ_Y in the cell Y depends on its neighboring cells nb and its own sinks and sources S_{ϕ_Y} . It can be obtained by solving the discretized general transport equation, as shown in equation (4.22).

$$A_Y \phi_Y = \sum_{nb} (A_{nb} \phi_{nb}) + S_{\phi_Y} V \quad \text{with } A_Y = \sum_{nb} A_{nb} \quad (4.22)$$

Often, the source term S_{ϕ_Y} is a function of the variable ϕ_Y and it is desirable to represent this dependence in the discretization equations [104]. Since only linear dependency can be accounted for in equation (4.22), the source term S_{ϕ_Y} is linearized by splitting it into the constant part $S_{\phi_Y}^{\oplus}$ and the coefficient $S_{\phi_Y}^{\ominus}$ of ϕ_Y , see equation (4.23). Applying the linearized source term to equation (4.22), the equation for variable ϕ_Y in cell Y is obtained, as shown in equation (4.24).

$$S_{\phi_Y} = S_{\phi_Y}^{\oplus} + S_{\phi_Y}^{\ominus} \phi_Y \quad (4.23)$$

$$(A_Y - S_{\phi_Y}^{\ominus} V) \phi_Y = \sum_{nb} (A_{nb} \phi_{nb}) + S_{\phi_Y}^{\oplus} V \quad (4.24)$$

For reasons of numerical stability, the coefficient $S_{\phi_Y}^{\ominus}$ shall always be lower or equal to 0, consequently it contains only sinks. The term in parenthesis on the left-hand-side of equation (4.24) remains positive at any condition. As all sinks are included in $S_{\phi_Y}^{\ominus}$, the constant part $S_{\phi_Y}^{\oplus}$ contains the sources of variable ϕ_Y . The process of source term linearization is thoroughly described in Patankar [104].

The finite volumes are arranged as a structured non-staggered grid system in the CFD program code AIOLOS with values of the variable ϕ_Y to be stored in the cell center. The values of ϕ_Y , however, are often required at the cell faces, to allow for the solution of the discretized equations. Different interpolation schemes providing the cell face values based on one or several stored center values were investigated by Schneider [125]. According to Perić [105], the interpolation schemes in fluid flows need to obey three principles: (i) conservativeness, (ii)

boundedness and (iii) transportiveness. Schneider points out that simple first-order interpolation schemes such as the Upwind scheme [104] do not necessarily obey the transportiveness criterion, however they inherit high stability. High stability of the procedure allows for a higher convergence rate. Accuracy can be improved by higher order interpolation schemes such as higher upwind [111] or monotonized linear upwind schemes [99]. The higher accuracy is related to a higher computational effort and thereby a higher CPU time. This was also investigated by Schneider: he found an increased computational effort of 4 % for the Higher Upwind and of 10 % for the Monotonized Linear Upwind schemes when those are applied to one conservation equation. Due to these findings, the Upwind interpolation scheme is chosen in the work at hand, as the conservativeness and boundedness criteria are fulfilled and high numerical stability is expected. Experience with simulations using higher order interpolation schemes showed too little improvement in results compared to the necessary additional effort.

Solution algorithm

The solution algorithm or so-called solver has to find a solution for the equation system given in equation (4.25).

$$\mathbf{A} \phi = \psi \quad (4.25)$$

The matrix \mathbf{A} , also known as the coefficient matrix or system matrix, originates from equation (4.24), including all coefficients A_γ and $S_{\phi_\gamma}^\ominus V$ terms. The solution vector ϕ inherits all variables ϕ_γ of equation (4.24), and the vector ψ consists of the boundary conditions and the non-linear terms of the source term $S_{\phi_\gamma}^\oplus V$.

As the direct solution of this equation system is not possible in most cases, an iterative solution is mandatory. Schneider [125] tested different iterative solvers. According to Schneider, it must be distinguished between the inner and the outer loop of the iteration process. The inner loop is the solution of a conservation equation of a variable ϕ_γ . This solution is computed in each cell based on neighboring cell values known from the previous outer loop. Because the solution in a cell depends on the solution of the neighboring cells, outer loops are required to resolve these interdependencies. In the following, the convergence rate is assessed depending on the inner loops, but of course the overall amount of outer loops determines the computational time. For the present work, two solvers are used.

The red-black successive over-relaxation algorithm is characterized by low computational costs and low storage requirements, however accompanied with a slow convergence rate. It is applied to all equations except the pressure correction equation. The strongly implicit procedure algorithm [139] has higher computational costs and storage requirements, but exhibits a faster convergence rate. Due to its fast convergence rate, the strongly implicit procedure algorithm is applied to the pressure correction equation.

Stability of the solution process can be enhanced by damping the adaption of the solution vector ϕ . The solution vector of the n -th iteration is written as ϕ^n . As the solution vector of the $(n+1)$ -th iteration $\hat{\phi}^{n+1}$ is derived, one can apply only a certain part of the new solution vector and obtain the new solution vector ϕ^{n+1} . This is called relaxation and is displayed in equation (4.26).

$$\phi^{n+1} = \omega \hat{\phi}^{n+1} + (1 - \omega) \phi^n \quad (4.26)$$

It is important to note that the convergence rate depends on the choice of the relaxation factor ω . Low relaxation factors can initially be chosen for stabilizing the convergence process and might be necessary for less stable solvers. The reversed conclusion is that stable solvers can be used with high initial relaxation factors, speeding up the solution of the equation system.

Convergence

As depicted in the previous sections, the convergence rate is influenced by the choice of the discretization scheme, solution procedure and relaxation factors. The rate can be also influenced by the choice of the computational mesh, e.g. based on the cylindrical or Cartesian coordinate system and its resolution. The accuracy of the obtained solution is also controlled by these factors and the computing machine. As the discretization scheme, solution procedure and the computing machine are chosen, the relaxation factors and the computational mesh can be adapted. The latter will be discussed in Section 4.6.

As in any iterative process, a common law for its abortion does not exist, and the abortion criterion is always case-dependent. According to Ferziger and Perić [37], one obtains the approximated solution ϕ^n in the n -th iteration which does not fulfill the original equation and thus results in a residual ϱ^n .

$$\mathbf{A} \phi^n = \psi - \varrho^n \quad (4.27)$$

The aim is to minimize the error between the solution computed in the n -th iteration and the exact solution to an acceptable extent. Which error size is deemed acceptable must be answered by the user. The corresponding error ϵ^n at the current iteration n is defined in equation (4.28):

$$\epsilon^n = \phi - \phi^n \quad (4.28)$$

The residual is obtained by subtraction of equation (4.27) from equation (4.25) and the use of equation (4.28):

$$\mathbf{A} \epsilon^n = \varrho^n \quad (4.29)$$

It can be seen from equations (4.28) and (4.29) that for the calculation of the error or the residual, the exact solution ϕ must be known. This is, however, unknown per definition, so that a computable error indicator is necessary. This is found in the update δ^n between two iterations of the intermediate solution ϕ^n , c.f. equation (4.30). Ferziger and Perić [37] showed that the residual ϱ^n of a linear equation system is linked to the update δ^n .

$$\delta^n = \phi^{n+1} - \phi^n \quad (4.30)$$

As one can conclude from equations (4.28) and (4.29), the error ϵ^n and the residual ϱ^n will become 0 if ideal convergence is achieved. Ideal convergence can be written as shown in equation (4.31).

$$\phi^n = \phi^{n+1} = \phi \quad (4.31)$$

It can be deduced from equation (4.30) that $\delta^n = 0$ is a necessary condition for ideal convergence. However, as the exact solution ϕ of a fluid-dynamic problem usually can only be approximated, δ^n will always remain unequal to 0, and a different metric must be found to determine the simulation accuracy.

Convergence criteria as applied in AIOLOS

In AIOLOS, δ^n is observed for judging the achievement of convergence and accuracy. In order to enable a judgment of the achieved accuracy, the update δ^n is divided by the value ϕ^{n+1} , giving a direct relation between the calculated update and the new value. It is referred to as the relative update δ_{rel}^n . The relative update is calculated as in equation (4.32) for all variables except for the mass defect which is observed from its absolute figure.

$$\delta_{rel}^n = \frac{\delta^n}{\phi^{n+1}} \quad (4.32)$$

In the iterative process, the minimization of δ^n is limited by errors induced by the discretization scheme and the computational mesh resolution as well as the accuracy of the computing machine. The following criteria are defined to determine convergence and accuracy:

- The reduction of the update δ^n or the relative update δ_{rel}^n is in the range of three to four orders of magnitude from the beginning to the abortion of the solution procedure [37].
- The trend of update or relative updates achieves a minimum and stays at this minimum.
- The relative update δ_{rel}^n falls below 0.01 i.e. 1 % of the current value ϕ^{n+1} .

In addition to the updates of the variables, the energy balance and the elemental mass

balances of carbon (C), oxygen (O), hydrogen (H) and ash (A) are checked for being stable and within a threshold of $\pm 2\%$.

By application of these criteria, it must be kept in mind that the update δ^n depends on the relaxation factor ω , see equations (4.26) and (4.30). Therefore, relaxation factors close to 1 shall be aimed for as the iterative process advances. If the recent state is close to the actual solution of the problem, the updates remain stable.

In complex problems such as furnace simulations, the choice of low relaxation factors for the velocity and turbulence variables might be recommended, since the user is usually not able to give an initial guess close to the actual solution. On the other hand, high relaxation factors speed up the convergence remarkably. Thus, a successive increase of the relaxation factors seems to be the best procedure. In this way, one can avoid the simulation getting stuck in a pseudo-solution, i.e. as δ^n achieves an intermediate minimum and the user mistakes it for the absolute minimum.

4.2 Boundary conditions

This section gives information on important boundary conditions not presented in the modeling sections.

Boundary conditions of the variables at walls, inlets, outlets and symmetry boundaries are either of Dirichlet or Neumann i.e. of fixed or gradient type, respectively. Inlet boundary conditions are set as fixed values for all variables except the pressure. Neumann type boundary conditions are applied to all other boundaries, with first-order or second-order gradients. The pressure at the outlet, on the other hand, is linearly extrapolated. For more detailed information, please refer to the literature [37, 125].

Discretization of the particle size distribution

It was stated in Section 4.1.5 that the particle-laden fluid is modeled by a quasi-one-phase Eulerian approach without resolving the particle phase. However, chemical reactions depend on the external surface of the particles and thus on the particle size, as will be pointed out in Section 4.5. The particle size distribution is obtained from mass-based or volume-based methods, such as sieving or laser diffraction. It can be approximated by the Rosin-Rammler distribution, also known as the Weibull distribution. This cumulative density function is given in equation (4.33). The shape parameter λ_{RR} can be seen as a measure of the spread of the particle sizes, whereas the scale parameter k_{RR} refers to a mean diameter of the distribution. Their derivation is described in [172] and they are obtained by transposing equation (4.33), leading to equation (4.34).

$$x_{cum} = 1 - \exp\left(-\frac{D}{k_{RR}}\right)^{\lambda_{RR}} \quad (4.33)$$

$$\ln(-\ln(1 - x_{cum})) = \lambda_{RR} \ln(D) + \ln\left(\frac{1}{k_{RR}}\right)^{\lambda_{RR}} \quad (4.34)$$

Equation (4.34) can be seen as a line equation, i.e. as a function of the particle diameter $\ln(D)$. The results from particle size characterization can be transferred to a diagram with $\ln(D)$ on the x -axis and $\ln(-\ln(1 - x_{cum}))$ on the y -axis. The shape parameter λ_{RR} can be thus derived from the slope of a line fitted through the results of experimental particle size characterization. The scale parameter k_{RR} instead can be obtained by means of the intersection of the fitted line with the y -axis, i.e. if $\ln(D)$ equals 0.

Mass-based methods, such as sieving, and volume-based methods, as laser diffraction is, can be used to obtain the required particle size distribution. Both methods were used, but the sieving is performed only with coal samples from the PT1 experiments (cf. Section 3.4). The sieving result is given in Table 4.1. It was concluded from the laser diffraction results that particle size distribution for coal samples from both the PT1 and PT2 experiments are very similar (cf. Table 3.4). It is assumed that the mass-based sieving analyses would be very similar, too. The mass-based sieving method is regarded more suitable for AIOLOS, as the program is mass-based, too. The particle size distribution and the Rosin-Rammler parameters derived from sieving analysis are used for all simulations, see Table 4.1.

Table 4.1: Mass based particle size distribution properties of Calentur coal

Particle size distribution		Rosin-Rammler parameters	
D_{10} in μm	44.53	λ_{RR} in —	3.80
D_{50} in μm	73.10	k_{RR} in μm	80.5
D_{90} in μm	100.3		

The conduction of the CFD simulation on the basis of a continuous particle size distribution would result in very high computational costs. The continuous particle size distribution is discretized using an equal spacing of the diameters of the particle size range. Consequently, the mass fraction represented by each discretized mean diameter is calculated using the Rosin-Rammler function and its shape and scale parameters λ_{RR} and k_{RR} , respectively. These parameters are fitted to the continuous particle size distribution, as was described before.

The number of intervals i.e. particle size classes, depends on the targeted accuracy. It is noted that a finer discretization increases the computational effort, since more particle size classes have to be computed. Five particle size classes have been found to be a good compromise between accuracy and speed of computation. Finer particle size discretizations were tested, but without a significant impact on the simulation results.

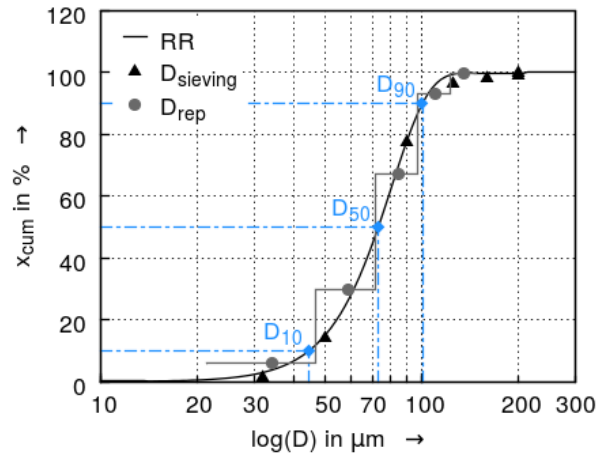


Figure 4.3: Particle size distribution of Calentur coal

The particle size distribution is shown in Figure 4.3: approximation of particle distribution by the Rosin-Rammler function (RR), sieving results ($D_{sieving}$) and the five representative particle diameters D_{rep} as applied in the simulations. The five representative particle size classes are given with their diameter and mass fraction in Table 4.2.

Table 4.2: Representative particle size distribution of Calentur coal used in CFD simulations

D in μm	x in %
34.00	5.89
59.20	23.82
84.40	38.06
110.0	25.79
135.0	6.98

Furnace wall temperatures

The furnace wall temperature ϑ_W is derived from thermocouples located in the wall close to the surface. This measured data was averaged over the measurement period of each operating point. The furnace wall temperature as applied in AIOLOS is discretized along the axial, i.e. z -direction of the furnace. The given z values in Table 4.3 represent the axial distance of each wall section up to which the corresponding temperature prevails.

The discretized temperatures and wall sections of the FLOX_{CO₂} case are compiled in Table 4.3, as this case is discussed in the following Section 4.7. The furnace wall temperatures of the other cases depicted in Table 3.2 can be found in Appendix C.

Table 4.3: Furnace wall temperatures of the FLOX_{CO₂} case

z in mm	ϑ_W in °C
155	1031
380	1050
710	1064
1060	1074
1400	1064
1730	1024
2060	1013
2400	970
5900	912

Inlet conditions

The turbulence intensity at the inlet must be set as a boundary condition and is calculated as displayed in equation (3.4), Chapter 3. The root-mean-square velocity fluctuations are usually unknown, thus the turbulence intensity can be estimated from the Reynolds number for a fully developed pipe flow, see equation (4.35). Therein, the Reynolds number Re is based on the characteristic length of a pipe, the hydraulic diameter D_{hyd} . D_{hyd} equals the pipe diameter D for a conventional pipe as the combustion-air nozzle or the difference of outer and inner diameter for a coaxial pipe as the coal-carrier-gas annulus.

$$I_{turb} = 0.16 Re^{-\frac{1}{8}} \quad (4.35)$$

With equation (4.35), one obtains turbulence intensities of 5.5 % and 3.8 % at the coal-carrier-gas annulus and the combustion-air nozzle, respectively. This is close to the turbulence intensity of 5 % anticipated before the first experimental campaign.

4.3 Heat transfer

The heat transfer in combustion systems is mainly driven by convection and radiation, whereas heat conduction is of minor importance in the furnace itself. It matters in the heat transmission through the furnace walls however. As the enthalpy transport equation has a convection term already, convective heat transfer is implicitly respected.

The major modeling effort lies in the radiative heat transfer phenomenon. Radiation occurs in all directions of space over the whole spectral range, depending on its properties: it can be scattered at particles, it can be absorbed, transmitted or reflected from the fluid. The transport

of radiation represented by the spectral radiative intensity I_ν along the direction \vec{s} is described by the radiative transfer equation (RTE), given in equation (4.36).

$$\frac{dI_\nu(\vec{s})}{ds} = -\beta_\nu I_\nu(\vec{s}) + \kappa_{abs,\nu} I_{b,\nu} + \frac{\sigma_{scat,\nu}}{4\pi} \int_{4\pi} I_\nu(\vec{s}_{scat,in}) \Phi_\nu(\vec{s}_{scat,in} \rightarrow \vec{s}_{scat,out}) d\Omega \quad (4.36)$$

Therein, the spectral extinction coefficient β_ν is the result of summation of the spectral absorption coefficient κ_ν and the spectral scattering coefficient $\sigma_{scat,\nu}$. The spectral blackbody intensity $I_{b,\nu}$ is determined by Planck's spectral distribution of emissive power. $\Phi_\nu(\vec{s}_{scat,in} \rightarrow \vec{s}_{scat,out})$ denotes the scattering phase function from the incoming direction $\vec{s}_{scat,in}$ to the outgoing direction $\vec{s}_{scat,out}$. It is integrated over the solid angle sector $d\Omega$.

According to Leiser [80], the number of radiative transport equations to be resolved can be seen from equation (4.37). It depends on the discretization of the radiative space on the one hand and on the spectral discretization of the wave length range on the other hand. For the spatial discretization, different methods have been developed that can be classified in the three groups zonal, ray tracing and differential methods. A comprehensive review can be found in Ströhle [140].

$$N_{RTE} = N_{\vec{s}} \cdot N_{\Delta\nu} \quad (4.37)$$

In this work, a member of the differential methods group denoted as the discrete ordinates method is employed. The radiative space is discretized by its total solid angle, resulting in a discrete number of directions $N_{\vec{s}}$. The number of directions can be increased to infinity and in that case, the solution of the discrete ordinates method equals the exact solution of the radiative transfer equation. It is limited to 24 in this work, and they are weighted by means of a S_4 quadrature scheme.

In order to restrict N_{RTE} , the spectral discretization $N_{\Delta\nu}$ can be kept low. Scattering, accounted for by scattering coefficient $\sigma_{scat,\nu}$, significantly occurs by particles only, and thus it is neglected for the gas phase. Absorption, accounted for by absorption coefficient $\kappa_{abs,\nu}$, however, is of importance in the gas and particle phase, and is therefore modeled for both phases by separate sub-models.

Gas absorption

The easiest way to achieve $N_{\Delta\nu}$ being low is to assume the gas phase as a gray medium. The spectral dependency is thus neglected. However, the inherited error can become considerably high, if the atmosphere contains significant portions of CO_2 or H_2O . Spectral and global models instead discretize the spectral range, i.e. $N_{\Delta\nu}$ depends on the chosen discretization.

Spectral models incorporate either each spectral line or spectral line bands. The first ap-

proach, known as line-by-line approach, is the computationally most expensive, but most accurate one of the spectral models. It is usually applied for validation of less accurate spectral models. Narrow-band models exhibit a coarser resolution of spectral lines, but they are still too expensive to be used in furnace simulations and serve as a reference, as well. Exponential wide-band models have been used in coal furnace simulations for instance by Ströhle [140] and Erfurth [35]. They assume that absorption and emission concentrates to distinct regions of the spectral range, called bands. It neglects the position of spectral lines within a band and assumes an equal spacing between the spectral lines. Absorptivity and emissivity is highest in the band center and decreases exponentially towards the band limits. Ströhle [140] proposed the use of three gray gases derived from the exponential wide-band model and one clear gas, resulting in $N_{\Delta\nu} = 4$. An exponential wide-band model was tested in the course of the FLOX-COAL-II project. The obtained simulation results, however, can not justify the increased computational effort [55]. Additionally, the computational stability strongly decreased with application of the exponential wide-band model.

Global models do not account for the spectral nature of radiation and provide the optical property for one gray gas. A widely used model in CFD combustion simulations is the weighted sum of gray gases model (WSGGM), developed by Hottel and Sarofim [66]. It obtains the absorption coefficients $\kappa_{abs,G,i}$ for a predefined mixture of i gray gases which can be seen as a pseudo-spectral discretization. It finally derives one absorption coefficient $\kappa_{abs,G}$ by a weighted summation of $\kappa_{abs,G,i}$, that is valid for a narrow range of the supposed gas phase composition. This limited validity is one of the major drawbacks of the WSGGM, and requires careful use.

Particle absorption and scattering

As the fluid in pulverized coal combustion simulations contains particulate matter such as soot, char and ash, their contribution to the radiative heat transfer has to be considered. These solid components of the fluid are assumed as gray, i.e. with no spectral dependency and $N_{\Delta\nu} = 1$. The optical properties of the dispersed particle cloud, the absorption coefficient $\kappa_{abs,P}$ and the scattering coefficient $\sigma_{scat,P}$, are obtained in equations (4.38) and (4.39) by means of the absorption and scattering efficiency factors η_{abs} and η_{scat} , the particle load N_P and the particle diameter D_P [63]. The applied absorption and scattering efficiency factors differ for coal, char and ash and are given in Table 4.4.

$$\kappa_{abs,P} = \frac{\pi}{4} \cdot \eta_{abs} \cdot D_P^2 \cdot N_P \quad (4.38)$$

$$\sigma_{scat,P} = \frac{\pi}{4} \cdot \eta_{scat} \cdot D_P^2 \cdot N_P \quad (4.39)$$

Table 4.4: Absorption and scattering efficiency factors for coal, char and ash

	η_{abs}	η_{scat}
Coal and char	0.85	1.30
Ash	0.85	1.70

The probability of radiation scattering occurring at a particle is given by the scattering phase function $\Phi_\nu(\vec{s}_{scat,in} \rightarrow \vec{s}_{scat,out})$ in equation (4.36) [140]. It can be derived by the Delta-Eddington approximation [70], and thus the effective scattering coefficient is obtained for each direction \vec{s} in the DOM [80, 140].

The absorption coefficient of soot has to be calculated in a different manner, see Leiser [80]. Since the presence of soot is neglected in this work, it is not detailed here.

Combined gas and particle absorption

The total absorption coefficient $\kappa_{abs,tot}$ can now be obtained by the sum of gas and particulate matter absorption coefficients, see equation (4.40).

$$\kappa_{abs,tot} = \kappa_{abs,G} + \kappa_{abs,P} \quad (4.40)$$

The influence of gaseous radiation on the combustion process is of minor importance if particulate matter is present, as results of Gronarz et al. [55] indicate. This was confirmed in this work in simulations comparing the $\kappa_{abs,G}$ obtained from the WSGGM and $\kappa_{abs,G}$ set constant. The total absorption coefficient $\kappa_{abs,tot}$ showed the very similar results regardless of the $\kappa_{abs,G}$ origin. Consequently, temperature remains unaffected [165].

Wall properties

Similar to gas phase and particulate matter, the furnace walls absorb and emit radiation, depending on their optical properties and temperature. The furnace walls are supposed to be a gray body without spectral dependency and they are expected to be diffuse, i.e. they emit or reflect the radiation isotropically [125]. The absorption coefficient $\kappa_{abs,W}$ is set to 0.65.

The convective heat transfer from the fluid to the wall is defined by the convective heat transfer coefficient α_W . It is set to $25 \text{ W (m}^2 \text{ K)}^{-1}$.

4.4 Fluid flow

One challenge in steady-state flow simulations is the modeling of a highly unsteady phenomenon called turbulence. Therefore, models have been developed by various research groups in the

past and are investigated in the course of this work. The computed results of this evaluation are compared against the velocity data obtained from LDV measurements (cf. Chapter 3).

4.4.1 Pressure correction methods

The Mach number of a fluid flow determines if the flow can be treated as incompressible or not. The assumption of incompressible flow facilitates the treatment of the Navier-Stokes equations and the energy conservation. As flameless combustion is characterized by high jet velocities with Mach numbers approaching the incompressibility limit of $Ma \leq 0.3$, Fürst [45] investigated flows with velocities of approximately 100 m s^{-1} prevailing in the furnace, and using the burner setup of this work. He found that Mach numbers up to 0.246 can be expected with the current burner design and thus, incompressibility can be assumed for the flameless combustion investigations.

Incompressible flows do not inherit a direct coupling of the pressure field and the continuity equation, due to the lack of density variation. Thus, it can happen that the pressure field and the velocity field do not satisfy the continuity equation which is however a kinematic constraint on the velocity field [37]. The actual pressure field is, however, not of importance in incompressible flows, since the pressure differences between the discrete nodes drive the flow and thus influence the velocities, as described in the momentum equation. Consequently, it is possible to adapt the pressure field in a way that it satisfies the continuity equation and both, velocity field and pressure field comply with the momentum equation. This is described in so-called pressure correction methods.

A widely used pressure correction method family is based on the semi-implicit method for pressure-linked equations (SIMPLE), proposed by Caretto et al. [16]. The pressure correction method used in this work is called SIMPLE-consistent (SIMPLEC), as proposed by van Doormaal and Raithby [153]. The choice is based on experiences by Schneider [125], who found better convergence rates for this method than for the basic SIMPLE method. To avoid the establishment of a checkerboard pressure distribution which can occur in non-staggered grid arrangements as shown by Patankar [104], Date [31] introduced a smoothing pressure correction approach for the SIMPLE algorithm which was extended to the SIMPLEC algorithm by Anany et al. [6].

The functionality of the pressure correction equations is explained briefly in the following. The momentum equation (4.3) is solved with an estimated value of the pressure p^* , resulting in preliminary velocities w_j^* . When using the velocities w_j^* to solve the continuity equation (4.1), one obtains a mass defect. However, the correct value of pressure p and velocities w_j can be expressed as

$$p = p^* + p^{**} \quad (4.41)$$

$$w_j = w_j^* + w_j^{**} \quad (4.42)$$

where p^{**} and w_j^{**} denote the pressure and velocity corrections, respectively. A momentum equation can be derived for the velocity corrections and thus a coupling between pressure and velocity corrections. By enforcing the continuity equation, the pressure correction p^{**} is derived and thus the correction of the velocities w_j^{**} . For detailed explanations, please refer to [6, 37].

4.4.2 Turbulence modeling

As described in Section 4.1, time-averaged formulation of the conservation equations induces a closure problem for turbulent flows regarding the turbulent scalar fluxes $\overline{\rho w_j'' \phi''}$, of which the Reynolds stresses $\overline{\rho w_j'' w_i''}$ appearing in the momentum equation are individually treated. To overcome the closure problem, so-called turbulence models have been developed at different levels of detail. They include zero, one, two or even more equations, whereas the two-equation group is most widely used in engineering applications. Within this group, the so-called k - ε turbulence models are commonly regarded as a good compromise between accuracy and computational cost. The k - ε turbulence models are based on the assumption made by Boussinesq in the late 19th century that the Reynolds stresses are proportional to the mean velocity gradients, and thus can be treated as additional stresses induced by turbulence. The prevailing viscosity is not defined by fluid properties as the molar viscosity μ is, but depends on the flow. This so-called turbulent or eddy viscosity μ_{turb} is introduced in order to link the turbulent kinetic energy k and its dissipation rate ε , both modeled by individual transport equations. Similar to the shear stress assumption for a Newtonian fluid, the introduction of just one constant value of the turbulent viscosity does not account for anisotropic effects of the flow.

Other models such as the Reynolds stress model (RSM) do not require the calculation of the eddy viscosity, but provide six additional transport equations, each accounting for one Reynolds stress term. RSM is thought to overcome the shortcomings of eddy-viscosity-based models, such as the k - ε model and to be suited to account for the anisotropic nature of turbulent flows. Current RSMs, however, are computationally more costly and less robust than the k - ε models, and thus often remain unconsidered in turbulent flow simulations.

Based on the eddy-viscosity assumption, turbulent scalar fluxes are derived by the gradient-diffusion hypothesis as:

$$\overline{\rho w_j'' \phi''} = \Gamma_{\phi, turb} \frac{\partial \tilde{\phi}}{\partial x_j} \quad (4.43)$$

The turbulent diffusion coefficient $\Gamma_{\phi,turb}$ is defined as:

$$\Gamma_{\phi,turb} = \frac{\mu_{turb}}{\sigma_{\phi,turb}} \quad (4.44)$$

The Reynolds stresses can then be written as in equation (4.45), with the strain rate tensor as given in equation (4.46):

$$\overline{\rho w_j'' w_i''} = -\mu_{turb} \left(2\tilde{S}_{ij} - \frac{2}{3} \frac{\partial \tilde{w}_j}{\partial x_j} \delta_{ij} \right) + \frac{2}{3} \bar{\rho} \tilde{k} \delta_{ij} \quad (4.45)$$

$$\sigma_{ij} = \frac{1}{2} \left(\frac{\partial \tilde{w}_i}{\partial x_j} + \frac{\partial \tilde{w}_j}{\partial x_i} \right) \quad (4.46)$$

The newly introduced last term on the right-hand-side of equation (4.45) contains the turbulent kinetic energy k which is defined in equation (4.47). A detailed derivation can be found in [79].

$$\tilde{k} = \frac{1}{2} \frac{\overline{\rho w_i'' w_i''}}{\bar{\rho}} \quad (4.47)$$

Thus, the eddy viscosity μ_{turb} remains the only unknown that needs to be modeled.

$$\mu_{turb} = C_\mu \bar{\rho} \frac{\tilde{k}^2}{\tilde{\varepsilon}} \quad (4.48)$$

The dissipation rate of turbulent kinetic energy ε can be written as in equation (4.49), assuming that turbulent kinetic energy dissipation only occurs isotropically at the finest scales.

$$\tilde{\varepsilon} = \frac{\mu_{turb}}{\bar{\rho}} \left(\frac{\partial \overline{w_j''}}{\partial x_j} \right)^2 \quad (4.49)$$

By means of the instantaneous and Favre-averaged, i.e. density-weighted, mass and momentum equations, the transport equations of the turbulent kinetic energy k and of the dissipation rate ε can be derived. This is extensively discussed in [158, 171].

For the ease of reading, the Favre-averaged variables will not be further marked by a tilde. The k transport equation given in equation (4.50) persists independently of the chosen k - ε model.

$$\frac{\partial \rho k}{\partial t} + \frac{\partial \rho w_j k}{\partial x_j} = \frac{\partial}{\partial x_j} \left(\Gamma_k \frac{\partial k}{\partial x_j} \right) + G_k + \rho \varepsilon \quad (4.50)$$

Therein, the production term of turbulent kinetic energy G_k is defined as

$$G_k = \mu_{turb} \left[\frac{1}{2} \left(\frac{\partial w_i}{\partial x_j} + \frac{\partial w_j}{\partial x_i} \right)^2 - \frac{2}{3} \left(\frac{\partial w_j}{\partial x_j} \right)^2 \right] \quad (4.51)$$

and the diffusion coefficient Γ_k is given as follows:

$$\Gamma_k = \mu + \frac{\mu_{turb}}{\sigma_k} \quad (4.52)$$

The transport equation of the dissipation rate ε and the coefficients in the presented equations are derived differently for the sub-models of the k - ε turbulence model family. They are discussed in the following.

Standard k - ε model

The standard k - ε model was presented by Launder and Spalding [78] in 1974 and has been applied in many engineering applications, due to its accuracy in many standard problems, its robustness and its efficient cost-benefit ratio. The transport equation of the dissipation rate ε is semi-empirically derived, similarly to the k transport equation. As one can see from equation (4.53), it obeys the form of the general transport equation (4.18) and thus can be solved by the same numerical methods. The turbulent diffusion coefficient of the dissipation rate Γ_ε is given in equation (4.54).

$$\frac{\partial \rho \varepsilon}{\partial t} + \frac{\partial \rho w_j \varepsilon}{\partial x_j} = \frac{\partial}{\partial x_j} \left(\Gamma_\varepsilon \frac{\partial \varepsilon}{\partial x_j} \right) + C_{\varepsilon 1} G_k \frac{\varepsilon}{k} - C_{\varepsilon 2} \rho \frac{\varepsilon^2}{k} \quad (4.53)$$

$$\Gamma_\varepsilon = \mu + \frac{\mu_{turb}}{\sigma_\varepsilon} \quad (4.54)$$

The coefficients in the k and ε transport equations and in the μ_{turb} equation - C_μ , $C_{\varepsilon 1}$, $C_{\varepsilon 2}$, σ_k , σ_ε - have been obtained from benchmark experiments, e.g. pipe flow and flat plate, and are shown in Table 4.5.

Table 4.5: Coefficients of the standard k - ε model

C_μ	$C_{\varepsilon 1}$	$C_{\varepsilon 2}$	σ_k	σ_ε
0.09	1.44	1.92	1.3	1.0

As Launder and Spalding [78] stated, their coefficients were found appropriate to simulations of plane jets and mixing layers. They additionally demonstrated the applicability of the coefficients with predictions of plane jet in a moving stream and a pipe flow. In order to correctly predict axis-symmetric jet behavior, modifications to the coefficients C_μ and $C_{\varepsilon 2}$ were

proposed without claiming the ultimate solution. In the meantime, it was found that the standard k - ε model performs poorly for flows with strong separation or streamline curvature and swirl.

Modified k - ε model

The standard k - ε model suffers from inaccuracy in the prediction of round jets, as already postulated by its developers. The spreading rate of round jets can be overestimated by 40%, as stated by Pope [110]. It was found that a modified coefficient $C_{\varepsilon 1} = 1.6$ leads to better performance of the k - ε model predicting round-jet behavior [96, 110], while other coefficients and the k and ε transport equations are maintained. Coefficients of the modified k - ε model are given in Table 4.6.

Table 4.6: Coefficients of the modified k - ε model

C_μ	$C_{\varepsilon 1}$	$C_{\varepsilon 2}$	σ_k	σ_ε
0.09	1.6	1.92	1.3	1.0

RNG k - ε model

In contrast to the semi-empirically derived equations of the standard k - ε model, equations of the RNG k - ε model were determined by application of the re-normalization group theory to the Navier-Stokes equations [178, 179]. This approach accounts for the turbulent diffusion occurring not only at a single turbulent length scale, but at all scales of the fluid motion. This results in modified coefficients of the ε transport equation. Whereas new values are assigned to most of the coefficients, $C_{\varepsilon 2}$ is now determined by a separate equation:

$$C_{\varepsilon 2} = C_{\varepsilon 2}^* + \frac{C_\mu \eta^3 (1 - \eta \eta_0^{-1})}{1 + \beta \eta^3} \quad (4.55)$$

Equation (4.55) features the expansion parameter $\eta = S k \varepsilon^{-1}$, relating the turbulence properties and the strain rate tensor by the modulus of the strain rate tensor $S = \sqrt{2\sigma_{ij}\sigma_{ij}}$ with σ_{ij} as defined in equation (4.46) [97]. Diffusion coefficients of turbulent kinetic energy and dissipation rate are defined in a different manner than for the standard k - ε model.

$$\Gamma_k = \frac{\mu + \mu_{turb}}{\sigma_k} = \frac{\mu_{eff}}{\sigma_k} \quad (4.56)$$

$$\Gamma_\varepsilon = \frac{\mu + \mu_{turb}}{\sigma_\varepsilon} = \frac{\mu_{eff}}{\sigma_\varepsilon} \quad (4.57)$$

Coefficients of the RNG k - ε model are given in Table 4.7.

Table 4.7: Coefficients of the RNG k - ε model

C_μ	$C_{\varepsilon 1}$	$C_{\varepsilon 2}^*$	σ_k	σ_ε	η_0	β
0.085	1.42	1.68	0.7194	0.7194	4.38	0.012

Realizable k - ε model

The realizable k - ε model as proposed by Shih et al. [129] shares the k equation (4.47) with the standard and the RNG k - ε models. However, the equations of dissipation rate ε and eddy viscosity μ_{turb} are reformulated in order to improve the behavior of the model in terms of realizability concerns. The standard k - ε model does not account for physically realizable limits and thus can become un-realizable at large strain rates, due to negative normal stresses and the violation of the Schwartz' inequality for shear stresses [129]. Realizability constraints are respected by the new equation (4.58), transforming C_μ in a variable, rather than maintaining the constant formulation.

$$C_\mu = \frac{1}{A_0 + A_S U^* \frac{k}{\varepsilon}} \quad (4.58)$$

Therein, the constant A_0 has been determined as 4.0, A_S and U^* are obtained by equations (4.59) and (4.60), respectively, with the strain rate tensor σ_{ij} as defined in equation (4.46).

$$A_S = \sqrt{6} \cos \varphi \quad \text{with} \quad \varphi = \left(\frac{1}{3} \arccos \left(\sqrt{6} \frac{\sigma_{ij} S_{jk} S_{ki}}{(\sqrt{\sigma_{ij} \sigma_{ij}})^3} \right) \right) \quad (4.59)$$

$$U^* = \sqrt{\sigma_{ij} \sigma_{ij} + \Omega_{ij} \Omega_{ij}} \quad \text{with} \quad \Omega_{ij} = \frac{1}{2} \left(\frac{\partial w_j}{\partial x_i} - \frac{\partial w_i}{\partial x_j} \right) \quad (4.60)$$

The derivation of the equation of the dissipation rate ε is based on the mean-square vorticity formulation and leads to the new equation (4.61) with the production term G_k as presented in equation (4.51).

$$\frac{\partial \rho \varepsilon}{\partial t} + \frac{\partial \rho w_j \varepsilon}{\partial x_j} = \frac{\partial}{\partial x_j} \left(\Gamma_\varepsilon \frac{\partial \varepsilon}{\partial x_j} \right) + C_{\varepsilon 1} G_k \frac{\varepsilon}{k} - C_{\varepsilon 2} \rho \frac{\varepsilon^2}{k + \sqrt{\frac{\mu \varepsilon}{\rho}}} \quad (4.61)$$

Diffusion coefficients Γ_k in the k equation (4.47) and Γ_ε in the new ε equation (4.61) are the same as in the standard k - ε model, equations (4.52) and (4.54), respectively. The parameter $C_{\varepsilon 1}$ is given by equation (4.62) and $C_{\varepsilon 2}$ is a constant fixed to 1.9. The parameter η is the same expansion parameter as used in the RNG k - ε model: $\eta = S k \varepsilon^{-1}$ with the strain rate tensor

$S = \sqrt{\sigma_{ij}\sigma_{ij}}$ and σ_{ij} as defined in equation (4.46).

$$C_{\varepsilon 1} = \max\left(0.43; \frac{\eta}{5 + \eta}\right) \quad (4.62)$$

All parameters and constants of the realizable k - ε model are shown in Table 4.8.

Table 4.8: Coefficients of the realizable k - ε model

C_{μ}	$C_{\varepsilon 1}$	$C_{\varepsilon 2}$	σ_k	σ_{ε}	A_0
Eq. 4.58	Eq. 4.62	1.9	1.0	1.2	4.0

Wall treatment in k - ε models

Wilcox [171] shows that turbulent closure models are not capable for predicting the viscous boundary layer at the wall satisfactorily. It is obvious that any viscous flow must obey the no-slip condition at the wall, i.e. $w_x(y_{Wa}) = 0$, for x denoting the velocity direction parallel to the wall and y denoting the normal direction of the wall. It has been found experimentally that a buffer layer exists between the viscous sublayer at the wall where the molecular viscosity μ dominates and the turbulent core region where the turbulent viscosity μ_{turb} prevails. Different asymptotic methods also known as wall functions have been developed in the past to approximate this buffer layer. In the implementation of the k - ε model in AIOLOS, the wall function modifies the turbulent energy production term G_k and the dissipation rate ε depending on the characteristic distance from the wall y_+ . Detailed explanations can be found in the works of Müller [97] and Anany [5].

Discussion of applicability

The variants of the k - ε turbulence closure model presented above exhibit specific advantages and disadvantages regarding their applicability. In the course of flameless combustion research, all of the models presented have been applied and different conclusions have been drawn by the respective authors.

Despite its robustness and good ratio of computation time to accuracy, the standard k - ε model does not seem to be well suited for the simulation of flameless combustion flows, due to its weakness in predicting the spreading rate of round jets and flows with strong streamline curvatures or recirculation. However, the standard k - ε model has been used, especially in the early days of flameless combustion research by some authors [74, 123, 124, 173].

It has been acknowledged that the standard k - ε model lacks the ability of properly predicting the round jet spreading rate [110], and suggestions were made to overcome this deficiency. It

has been reported by various authors that the modified $k-\varepsilon$ model with the altered $C_{\varepsilon 2}$ constant gives better agreement of simulation and experimental data of flameless combustion systems [4, 26, 47, 58]. Some may criticize that modification of one constant in order to fit simulation results to experimental data leads from prediction to “postdiction”. However, as parameters of standard $k-\varepsilon$ models have been calibrated for distinct flow types, other flow types might require a different calibration.

It has been experienced that the RNG $k-\varepsilon$ model performs well for flows with high strain rates, swirl and separation or recirculation. Thus, it could be better capable for accounting for the flow characteristics found in a flameless combustion regime. However, it has only been applied by a few researchers [4, 180]. They did not find superior behavior of the RNG $k-\varepsilon$ model compared to the standard $k-\varepsilon$ model. Moreover, Aminian et al. [4] reported the RNG $k-\varepsilon$ model to give the worst agreement with experimental data of laboratory experiments [29] regarding the mixture fraction. Also Mancini et al. [87] showed, for a pilot scale semi-industrial furnace, that the choice of the RNG $k-\varepsilon$ model suffers from insufficient prediction of entrainment into the weak jet.

The final representative of the $k-\varepsilon$ model family, the realizable $k-\varepsilon$ model, offers the same capabilities as the RNG $k-\varepsilon$ model, in addition to resolving the round jet anomaly. Although it harder achieves convergence compared to the standard $k-\varepsilon$ model, it has recently been applied in most of the flameless combustion research that has been conducted [55, 82, 89, 90, 122, 136, 147, 154, 155].

A comprehensive comparison of the described turbulence models, plus a RSM applied to the laboratory scale jet in hot co-flow burner studied by [29] can be found in Aminian et al. [4], leading to similar conclusions as presented above. Despite that the RSM does not suffer from the isotropic eddy-viscosity assumption as the $k-\varepsilon$ models do, it was not found to give superior results. In fact, it showed the worst performance, jointly with the RNG $k-\varepsilon$ model. Few authors also applied highly sophisticated LES [58, 83] or even DNS [94] approaches, giving a promising perspective for future modeling activities.

Simulations in this work have been performed to verify the best applicable turbulence model for the conducted experiments. Results will be presented in Section 4.7.3.

4.5 Chemical reactions

Reactive turbulent flow modeling results in the requirement of accounting for mixing effects and chemical kinetics. Both may limit or promote the reaction process and thus the progress of combustion. The nature of flameless combustion inherits a distributed reaction zone at moderate temperatures and at lower O_2 concentrations than is known from conventional flame-existent conditions. It needs to be taken into account that finite rate chemistry plays a role

and that the assumption “mixed is burnt” can not be valid in a flameless combustion regime. The dimensionless Damköhler number Da is defined as the ratio of the mixing time scale t_{mix} to the time scale of chemical reactions t_{chem} , see equation (4.63).

$$Da = \frac{t_{mix}}{t_{chem}} \quad (4.63)$$

If mixing is very fast and thus, the mixing time scale is significantly smaller than the chemical time scale, i.e. $Da \ll 1$, perfectly stirred conditions prevail [69].

Szegö et al. [145] modeled a furnace as one perfectly stirred reactor. They concluded that the chosen approach is not valid since the Damköhler number Da is not much lower than 1 in flameless combustion regimes. Consequently, mixing phenomena and finite rate chemistry have to be considered. On the other hand, Mancini et al. [87] showed that modeling the fuel jet and the combustion-air jet as a network of perfectly stirred reactors can reveal good agreement with measured concentrations. This approach, however, accounts for regions of different concentrations such as recirculated flue gas as well as fuel and combustion-air jets. Both approaches have in common that they are not suitable for CFD modeling, since reactions on a cell size level must be accounted for.

Different combustion models are known from flame-existent modeling such as probability density function models, flamelet concepts, the eddy break up model, the eddy dissipation model and the eddy dissipation concept (EDC) model. Whereas the probability density function approach was found unsuited [8, 26, 147, 180], some authors reported good agreement with the eddy break up model [86, 176] and eddy dissipation model [124, 136, 147, 180]. In recent publications, it is postulated that the EDC model reproduces best the turbulence-chemistry interaction present in flameless combustion [4, 26, 32, 74]. It is also applied in the simulations conducted in the course of this work and thus illustrated in Section 4.5.1. Thorough descriptions of the probability density function, the flamelet concepts, the eddy break up and the eddy dissipation model can be found in [49, 85, 107, 134].

4.5.1 Turbulence-chemistry interaction by the EDC model

Turbulent reactive flows are characterized by the simultaneous appearance of two phenomena: turbulence (see Section 4.4.2) and reactions (see Section 4.5.3). Both depend on each other since turbulence introduces energy to the smallest scales of a flow where reactions occur and reactions cause heat release affecting the flow field by the change of local density and thus pressure distribution.

The EDC model links the turbulence and reaction phenomena on the basis of the energy cascade assumption. The turbulence phenomenon can be imagined as a superimposition of vortices, so-called eddies, of different size and frequency. These eddies transport the energy

contained in the main flow through the scales to the finest scales where viscous forces dominate. This transportation process is lossy i.e. parts of the kinetic energy dissipate into heat with increasing progress of dissipation along the transfer cascade. Eventually, all kinetic energy dissipates into heat at the smallest scales, where perfect mixing is achieved and chemical reactions are assumed to take place. These smallest scales are declared as fine structures - denoted by an asterisk * - in the EDC model, in contrast to the surrounding fluid - denoted by superscripted SF - which does not participate in any homogeneous reactions. The concept of fine structure and surrounding fluid is illustrated in Figure 4.4.

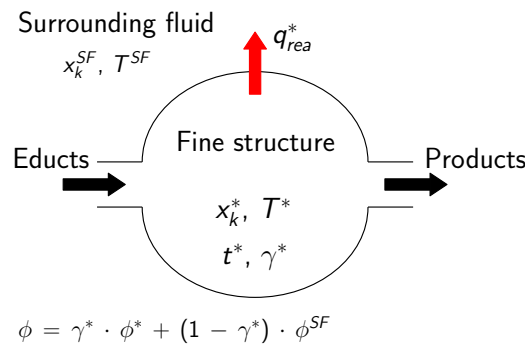


Figure 4.4: Fine structure and surrounding fluid according to the EDC

The turbulent kinetic energy k and its dissipation rate ε represent the two turbulent quantities required by the EDC model and thus they are used to derive the so-called eddy dissipation ratio εk^{-1} . It quantifies the influence of turbulence on the smallest scales and thus on the chemical reactions. The higher this ratio, the larger is the share of fine structures γ^* in the flow. γ^* is defined on a mass basis and is defined by means of the eddy dissipation ratio εk^{-1} , the turbulent kinetic energy k , the kinematic viscosity ν , the EDC exponent $\kappa_{EDC} = 3$ and the model constants $C_{D_1} = 0.134$ and $C_{D_2} = 0.50$, see equation (4.64). The term with C_{D_1} and C_{D_2} summarized as C_λ equals to 2.138.

$$\gamma^* = \left[\left(\frac{3 C_{D_2}}{4 C_{D_1}} \right)^{\frac{1}{4}} \left(\frac{\nu \varepsilon}{k^2} \right)^{\frac{1}{4}} \right]^{\kappa_{EDC}} = \left[C_\lambda \left(\frac{\nu \varepsilon}{k^2} \right)^{\frac{1}{4}} \right]^{\kappa_{EDC}} \quad (4.64)$$

Since all remaining kinetic energy of the smallest eddies dissipates at the fine structure scale, perfect mixing of reactants, i.e. perfectly stirred reactor conditions in the fine structures, can be assumed. This allows for the application of detailed kinetic mechanisms.

As completeness of mixing strongly influences the completion of chemical reactions, the time scale of mass exchange between surrounding fluid and fine structures plays the other important role. The mean time scale t^* is determined by equation (4.65). This term is also often referred to as mean residence time in the fine structure [4, 80, 84], but the time scale [52] term captures the effect of t^* better in the author's opinion. The square root expression of C_{D_2} summarized

as C_t equals 0.4082.

$$t^* = \sqrt{\frac{C_{D_2}}{3}} \sqrt{\frac{\nu}{\varepsilon}} = C_t \sqrt{\frac{\nu}{\varepsilon}} \quad (4.65)$$

Any quantity ϕ representing the mean value can be composed of a mass-weighted fine structure portion ϕ^* and surrounding fluid portion ϕ^{SF} .

$$\phi = \gamma^* \cdot \phi^* + (1 - \gamma^*) \cdot \phi^{SF} \quad (4.66)$$

Besides the exchange of educts and products of chemical reactions, the fine structures release the heat of the chemical reactions q_{rea}^* to the surrounding fluid. Consequently, the fine structure temperature T^* and surrounding fluid temperature T^{SF} can differ.

A detailed explanation of the EDC model can be found in Magel [84] and Leiser [80], jointly with the description of the chemical subsystem and its solution procedure.

Discussion of model constants

As in any model, the constants are derived for distinct conditions and might require adaption if the application range of the model changes. Such an adaption has been made to the EDC exponent κ_{EDC} in equation (4.64) in the course of conventional combustion modeling. Originally, κ_{EDC} was proposed equal to 3 [52]; other researchers found κ_{EDC} equaling 2 matching their simulation results better [5, 80, 97]. From equation (4.64), it can be seen that the choice of $\kappa_{EDC} = 3$ will result in a smaller fine structure share and thus in a lower share of available reactants. This reflects the nature of flameless combustion with distributed reaction zones in a diluted atmosphere, where the density of reaction partners is smaller than in conventional flame conditions.

The modification of the other model constants C_{D_1} and C_{D_2} has been investigated by different researchers with respect to flameless combustion conditions. However, they used the constants' expressions C_λ and C_t and varied them individually without the original dependency of C_{D_1} and C_{D_2} . The increase of C_t leading to an increased fine structure residence time t^* has been studied by Aminian et al. [4] and De et al. [32]. They argue that a larger reaction zone reduces the driving forces balancing the temperature and species gradients between fine structures and the surrounding fluid. Thus, lower mass transport into and from the fine structures results and residence time in the fine structure increases. This would lead to a more complete reaction of the reactants present in the fine structure. In order to account for the reduced fine structure share caused by the lower density of reactants as argued above, the constant C_λ can be modified as well. This has been studied by De et al. [32].

4.5.2 Treatment of chemical reactions

The treatment of chemical reactions has been similarly described by Anany [5] and is briefly reproduced for the ease of understanding of the following sections. Chemical reactions cause consumption or production of a species k . For their description, rate laws are used in the following. Equation (4.67) describes the rate of the molar concentration c of species k by reaction i . It is defined by the reaction rate constant K_i and the molar concentrations c_j of the participating species $j = 1, \dots, J$, including species k . Exponent $n_{i,j}$ determines the reaction order.

$$\left(\frac{dc_k}{dt}\right)_i = K_i \cdot \prod_{j=1}^J c_j^{n_{i,j}} \quad (4.67)$$

Reaction rate constant K_i is obtained by means of the Arrhenius approach in AIOLOS. A general form is given in equation (4.68) with the frequency factor $K_{0,i}$, the activation energy E_i , the absolute temperature T and the general gas constant \tilde{R} . The temperature exponent b_i depends on the reaction i . The quotient of activation energy and general gas constant $E_i \tilde{R}^{-1}$ is often referred to as the activation temperature.

$$K_i = K_{0,i} \cdot T^{b_i} \cdot \exp\left(-\frac{E_i}{\tilde{R} T}\right) \quad (4.68)$$

The relationship between the reactants j of a reaction i is given by means of the stoichiometric coefficients $\nu_{i,j}$, see equation (4.69).

$$\sum_{j=1}^J \nu_{i,j} \tilde{M}_j = 0 \quad (4.69)$$

The stoichiometric coefficient $\nu_{i,j}$ can be used to obtain a reaction rate \dot{R}_i from equation (4.67) valid for any species involved in reaction i . The net production or consumption rate of species k is then determined by summing up all reaction rates with k participating, see equation (4.71).

$$\dot{R}_i = \frac{1}{\nu_{i,k}} \left(\frac{dc_k}{dt}\right)_i \quad (4.70)$$

$$\left(\frac{dc_k}{dt}\right)_{tot} = \sum_{i=1}^I (\nu_{i,k} \cdot \dot{R}_i) \quad (4.71)$$

4.5.3 Coal combustion chemistry

Coal combustion can be classified in pyrolysis, homogeneous gas combustion and heterogeneous char burnout, as illustrated in Figure 4.5. Each of these processes is modeled separately in AIOLOS and is briefly presented here.

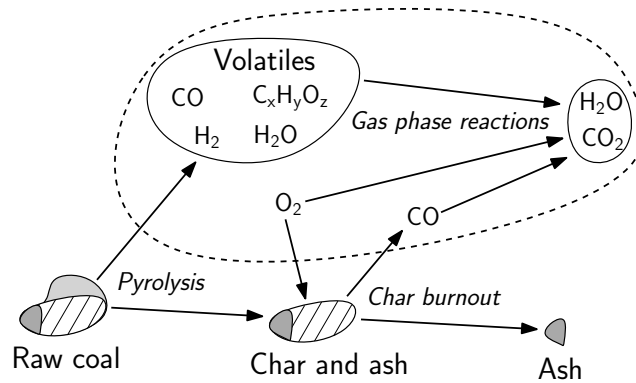
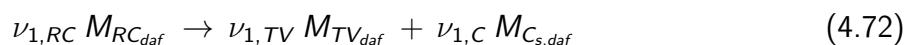


Figure 4.5: Schematic of coal combustion (adapted from [84])

Pyrolysis

Devolatilization of the raw coal is the first step in coal combustion, comprising of heat-up, evaporation of moisture, primary pyrolysis of the coal and secondary pyrolysis of the products, i.e. tar decomposition. Devolatilization can occur in an inert or oxidative atmosphere and influences the further stages of the combustion process by the amount and types of released gases. They depend on the temperature time history of the coal particles and the type and rank of the coal. The fraction of released total gas increases with increasing heating rate and final devolatilization temperatures. The share of light gases grows as coal rank decreases. The residual solid, comprising of char and ash, undergoes heterogeneous reactions in the following, whereas the released volatiles are oxidized by means of homogeneous reactions. For modeling reasons, char is assumed to consist of pure carbon, and ash is treated as inert matter.

The modeling approach of coal devolatilization in AIOLOS is a strong simplification of the real process focusing on the relevant steps for the subsequent combustion process. Drying of the coal is only considered for coals with high moisture content such as lignites or biomass [76]. Otherwise, the moisture of the coal is modeled as water steam. Both moisture and ash are introduced contiguously with the dry and ash free (daf) raw coal. Moisture and ash fraction are known from proximate and ultimate analyses of the coal.



According to Förtsch et al. [42], primary pyrolysis is modeled as a single reaction, splitting the raw coal RC_{daf} into total volatiles (TV_{daf}) and char ($C_{s,daf}$). The resulting total volatile yield comprises of condensable tars ($C_xH_yO_z$) and non-condensable gases such as CO, CO₂, H₂ and H₂O, as well as CH₄ as a light hydrocarbon representative. The share of total volatile yield $\nu_{1,TV}$ and char $\nu_{1,C}$ can be estimated by means of mass balances from the ultimate and proximate coal analyses [42].

On the other hand, the devolatilization process can be modeled separately. Network models assuming the coal as a network of different functional groups bound by links and bridges of varying strength have been developed in the 1980s and are still state-of-art when it comes to coal pyrolysis modeling. The most rewarded representatives of this model group are the chemical percolation devolatilization (CPD) model by Fletcher and co-workers [39, 40, 48, 53] and the functional group - depolymerization, vaporization cross-linking (FG-DVC) model by Solomon and co-workers [133]. In their original forms, both models require detailed knowledge of coal properties which require costly and demanding analysis techniques, for instance ¹³C NMR analysis and thermo-gravimetric FTIR analysis. Correlations have been found, allowing firstly for the derivation of required input parameters on easily accessible data of proximate and ultimate analyses and secondly for the use of coals others than the provided reference coals by interpolation of input parameters from reference coals.

The CPD pyrolysis model is used in the work at hand to obtain yields of tar, volatiles and nitrogen species. The application of such sophisticated devolatilization models allows for detailed estimation of stoichiometric coefficients $\nu_{1,C_xH_yO_z}$ and $\nu_{1,G}$ of primary pyrolysis products tar and non-condensable light gases, respectively. An additional advantage is gained regarding the NO_x formation to be discussed in Section 4.5.4, where detailed knowledge of NO_x precursors' distribution becomes essential. The stoichiometric coefficient of the dry and ash free raw coal $\nu_{1,RC}$ is defined as -1.

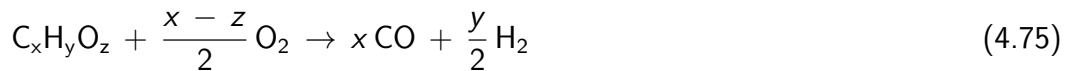
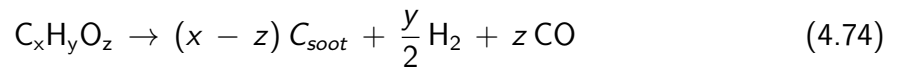
The CPD model applied as the pre-processor is run with three different final pyrolysis temperatures. Primary pyrolysis duration is estimated from experimental data of the KSVa facility and from numerical results. The latter reveal, along the coal-carrier-gas jet, that coal concentration diminishes at $z = 580$ mm which coincides with the methane peak. This also agrees with the experimental methane peak concentration. From experimental LDV results, a total residence time of the coal in the primary pyrolysis zone of 75 ms is estimated. The measured gas temperature equals 1000 °C at $z = 530$ mm, and it equals 1109 °C further downstream at $z = 890$ mm. Numerical results reveal gas temperatures of 955 °C and 1173 °C, respectively. It is assumed that particle and gas temperatures are very similar at this stage of combustion. Due to the different temperatures obtained, three different final pyrolysis temperatures are analyzed in the pre-processing calculations with the CPD pyrolysis model: 1000 °C, 1100 °C and 1200 °C. The results are shown in Table 4.9.

Table 4.9: Char, tar and light-volatile fractions after primary pyrolysis obtained from the CPD model and proximate analysis

Pyrolysis product fractions in % (daf)	$\vartheta_{pyr,max}$			Proximate analysis
	1000 °C	1100 °C	1200 °C	
ζ_{char}^{Pyr}	46.01	42.60	41.12	57.72
ζ_{tar}^{Pyr}	21.98	22.32	23.35	—
ζ_{vol}^{Pyr}	32.01	35.08	35.53	42.28

The differences in char and total volatile (tar and light volatiles) yields between the CPD results and the proximate analysis are related to the very different heating rates of both procedures. Heating rates of approximately 10^5 K s^{-1} as applied in the CPD runs are at least two orders of magnitude larger than those prevalent in the proximate analysis. Moreover, a lower devolatilization peak temperature ($\approx 900 \text{ °C}$) is achieved in the latter. These two boundary conditions are known to favor an elevated char fraction after pyrolysis. In other words, the higher the heating rate and the higher the final temperature, the more volatiles and tar are released. This is affirmed by the CPD results.

During secondary pyrolysis, the previously produced tar is decomposed into light volatiles and soot, or is preferably oxidized if sufficient O_2 is present. Light volatiles formed under fuel-rich tar decomposition conditions are primarily light hydrocarbons i.e. CH_4 at lower temperatures or CO and H_2 at higher temperatures [41]. CO and soot occur in both temperature ranges, cf. reactions (4.73) and (4.74), with increasing soot share at higher temperatures. Oxidative conditions instead favor tar oxidation, resulting in CO and H_2 , as in reaction (4.75). Soot is finally oxidized with O_2 to form CO , as represented by reaction (4.76). The full tar decomposition model as proposed by Förtsch et al. [42] consists of the following reactions:



Whilst soot often occurs in conventional diffusion flames and alters the flame temperature due to enhanced radiative heat transfer, it is expected to play a minor role in flameless combustion conditions. This might be due to the lack of diffusive flame structures and of high temperatures promoting soot formation in conventional flames [17]. Kim [74] investigated several soot formation models and compared the simulation results obtained with and without the

applied soot model to the measurement data obtained from experiments in the IFRF Furnace No. 1 [100]. He states a maximum difference of 100 K between predicted and experimentally obtained temperatures. A closer look to the diagrams provided by Kim can not support his conclusion. Moreover, it is thought that the presented improvements are not worth the additional computational effort. Thus, soot existence is neglected in the work at hand. Accordingly, tar decomposition cuts down on the tar oxidation, see reaction (4.75): its rate is given in equation (4.77) and the kinetic rate parameters by Shaw et al. [128] are shown in Table 4.10.

$$\left(\frac{dc_{C_xH_yO_z}}{dt}\right)_{4.75} = -K_{0,4.75} \cdot \exp\left(-\frac{E_{4.75}}{R T}\right) \cdot c_{C_xH_yO_z} \cdot c_{O_2} \quad (4.77)$$

Heterogeneous char combustion

After devolatilization, the residual solid char is decomposed in heterogeneous reactions to CO and finally to CO₂. Char conversion is complex due to the variety of involved reactions and the physiochemical interactions. It involves several reactions with different agents, such as O₂, CO₂ and H₂O, to mention the most relevant ones. The char conversion with CO₂ is also known as the Boudouard reaction and plays a major role in CO₂-rich atmospheres, as are found in oxy-fuel conditions. Similarly, the char gasification with steam is enhanced in H₂O-rich conditions. Char combustion with O₂, see reaction (4.78), is instead considered the most relevant char conversion reaction in air-fired conditions, and therefore the only one being modeled in AIOLOS for flameless combustion conditions.



The complexity of the char combustion process was broken down by introducing the three-zone concept in the 1950s [170]. It postulates that char combustion is limited either by chemical kinetics, by pore diffusion or by boundary layer diffusion, depending on the temperature. In low temperature conditions or for small particles, char combustion is accordingly limited by chemical kinetics. Pore diffusion becomes restrictive as temperature or particle size increases. This zone is characterized by concentration gradients inside the particle. At high temperatures or for large particles, the boundary layer diffusion determines the reaction rate. Tu et al. [151] suggested a model accounting for the boundary layer diffusion and heterogeneous kinetics limitations called the resistance equation given in (4.79).

$$K_{C_s} = \left(\frac{1}{K_{chem}} + \frac{1}{K_{diff}}\right)^{-1} \quad (4.79)$$

Therein, K_{chem} represents the limitation by chemical kinetics, and is obtained by equation (4.80). It is modeled by first-order kinetics ($n = 1$) with an incorporated Arrhenius equation

with the frequency factor $K_{0, ch}$ and the activation energy E_{chem} , as proposed by Smoot and Pratt [131]. Both frequency factor and activation energy are coal-dependent, and should be chosen for the coal used. The local oxygen partial pressure is p_{O_2} .

$$K_{chem} = K_{0, ch} \cdot \exp\left(-\frac{E_{chem}}{\tilde{R} T}\right) \cdot p_{O_2}^n \quad (4.80)$$

The char conversion is also restricted by boundary layer diffusion which is modeled by K_{diff} . It is calculated according to the expression proposed by Field et al. [38], see equation (4.81). T_{BL} in equations (4.81) and (4.82) is the boundary layer temperature, whereas T_{STP} and p_{STP} in equation (4.82) refer to the standard-temperature-pressure condition and p is the prevalent pressure. The binary diffusivity of O_2 in N_2 at standard-temperature-pressure conditions, $\tilde{D}_{O_2-N_2, STP}$, is $3.49 \cdot 10^{-4} \text{ m}^2\text{s}^{-1}$ in equation (4.82) [5].

$$K_{diff} = \frac{2 M_C \tilde{D}_{O_2-N_2}}{D_j \tilde{R} T_{BL}} \cdot p_{O_2} \quad (4.81)$$

$$\text{with } \tilde{D}_{O_2-N_2} = \tilde{D}_{O_2-N_2, STP} \left(\frac{T_{BL}}{T_{STP}}\right)^{1.75} \frac{p_{STP}}{p} \quad (4.82)$$

The char reaction rate depends on the specific external char particle surface area $a_{ext, j}$ which can be derived by means of the particle diameter D_j and the corresponding density ρ_j , see equation (4.83). As the coal and thus the char particles are distributed over a certain particle size range, c.f. Section 3.4, the char particle size distribution is represented by char particle size classes j . The resulting reaction rate is calculated from the resistance term (equation (4.79)) for each char particle size class j . The chemical kinetics of char conversion by reaction (4.78) are shown in Table 4.10.

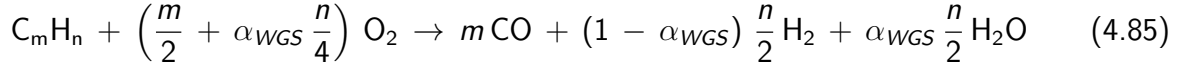
$$a_{ext, j} = \frac{6}{D_j \rho_j} \quad (4.83)$$

$$\left(\frac{dM_{C_j}}{dt}\right)_{4.78} = -K_{C_s} \cdot a_{ext, j} \cdot M_{C_j} \quad (4.84)$$

Homogeneous combustion

Products of primary and secondary pyrolysis as well as of heterogeneous char combustion are further oxidized by homogeneous gas phase reactions. Whereas detailed reactions schemes have been applied by some authors in flameless combustion modeling of gaseous fuels [3, 4, 32, 98], the use of global reaction schemes is state-of-the-art in solid fuel combustion modeling. Homogeneous combustion reactions are represented by a three-step global reaction mechanism, reported by Magel [84].

Light hydrocarbons C_mH_n are oxidized by means of a global reaction, forming intermediates CO and H_2 and H_2O as product of complete oxidation. In contrast to the original kinetic rates derived by Magel, those of Zimont and Trushin [187] are employed as proposed by Förtisch [41].



$$\left(\frac{dc_{C_mH_n}}{dt}\right)_{4.85} = -K_{0,4.85} \cdot \exp\left(-\frac{E_{4.85}}{\tilde{R} T}\right) \cdot c_{C_mH_n} \cdot c_{O_2} \cdot T^{0.5} \quad (4.86)$$

The partial direct conversion of C_mH_n to water vapor is ruled by the α_{WGS} factor. This allows for an implicit consideration of the water-gas-shift reaction as shown in reaction (4.87).



The factor α_{WGS} is calculated assuming a partial equilibrium of H_2 and H_2O , depending on the local stoichiometry: sub-stoichiometric conditions allow for H_2 formation, whereas super-stoichiometric conditions favor the direct conversion to H_2O . The fraction of $[H_2]_{eq}$ and $[H_2O]_{eq}$ is calculated by means of the water-gas-shift equilibrium determined from the local CO and CO_2 concentration and the temperature dependent constant $c_{WGS}(T)$.

$$\alpha_{WGS} = \frac{[H_2]_{eq}}{[H_2O]_{eq} + [H_2]_{eq}} = \left(1 + \frac{[H_2]_{eq}}{[H_2O]_{eq}}\right)^{-1} \quad (4.88)$$

$$\text{with } \frac{[H_2]_{eq}}{[H_2O]_{eq}} = c_{WGS}(T) \frac{[CO]}{[CO_2]} \quad (4.89)$$

The water-gas-shift reaction (c.f. reaction (4.87)) has been investigated in an explicitly implemented form respecting the backward and forward reactions. The observed impact on the simulation results is marginal and thus, the implicit form is chosen.

H_2 from hydrocarbon oxidation in reaction (4.85) and from pyrolysis (c.f. reactions (4.74) and (4.75)) is oxidized to water vapor. The reaction rate of reaction (4.90) is known to be very fast, its kinetic rate parameters are taken from Hautman et al. [60].



$$\left(\frac{dc_{H_2}}{dt}\right)_{4.90} = -K_{0,4.90} \cdot \exp\left(-\frac{E_{4.90}}{\tilde{R} T}\right) \cdot c_{H_2} \cdot c_{O_2}^{0.5} \quad (4.91)$$

Finally, CO is converted by the global reaction displayed in reaction (4.92) to CO₂. This global rate expression represents several elementary reactions [42], including partial equilibrium assumptions between H₂O, O₂, O and OH. Its kinetic rate parameters are taken from Howard et al. [67].



$$\left(\frac{dc_{\text{CO}}}{dt} \right)_{4.92} = -K_{0,4.92} \cdot \exp\left(-\frac{E_{4.92}}{\tilde{R} T}\right) \cdot c_{\text{CO}} \cdot c_{\text{O}_2}^{0.5} \cdot c_{\text{H}_2\text{O}}^{0.5} \quad (4.93)$$

In Table 4.10, the model parameters of the complete coal combustion reaction mechanism are summarized, including the homogeneous, heterogeneous and relevant secondary pyrolysis reactions.

Table 4.10: Coal combustion reactions with kinetic parameters

Reaction	Equations	$K_{0,i}$		$E_i \tilde{R}^{-1}$	Reference
Tar oxidation	4.75, 4.77	$3.80 \cdot 10^7$	$\text{m}^3 (\text{kmol s})^{-1}$	$6.67 \cdot 10^3 \text{ K}$	[128]
Char oxidation	4.78, 4.80	$2.08 \cdot 10^{-3}$	$\text{kg} (\text{m}^2 \text{s Pa})^{-1}$	$9.55 \cdot 10^3 \text{ K}$	[131]
C _m H _n oxidation	4.85, 4.86	$7.28 \cdot 10^9$	$\text{m}^3 (\text{kmol s K}^{0.5})^{-1}$	$2.01 \cdot 10^4 \text{ K}$	[187]
H ₂ oxidation	4.90, 4.91	$1.00 \cdot 10^8$	$\text{m}^{1.5} (\text{kmol}^{0.5} \text{s})^{-1}$	$1.00 \cdot 10^3 \text{ K}$	[60]
CO oxidation	4.92, 4.93	$5.24 \cdot 10^9$	$\text{m}^3 (\text{kmol s})^{-1}$	$1.51 \cdot 10^4 \text{ K}$	[67]

4.5.4 NO_x chemistry

NO_x emitted from combustion processes is usually classified by its source in three groups: prompt NO, thermal NO and fuel NO. Their relevance in combustion processes has been discussed by various researchers and it is summarized in Chapter 1.

It is preferable to introduce an additional chemical subsystem to represent the complex pollutant formation mechanisms. Due to the high amount of additional equations to be solved, pollutant formation in CFD simulations is often considered in a post-processing step, based on a fully converged combustion simulation. This gives the advantage of increased computational speed by only solving one chemical subsystem in the main simulation and in the post-processing simulation, respectively, and of the application of highly detailed pollutant formation mechanisms. The drawback, i.e. the error in mass and energy balances caused by this procedure, is small because of the small share of pollutants compared to the prevalent combustion products H₂O and CO₂ and air component N₂.

Global NO_x model

Various models of NO_x chemistry have been formulated, some at a very high level of detail. Förtsch [41] proposed a global reaction mechanism for the NO_x chemistry in pulverized coal combustion. It has been identified as the most suitable reaction mechanism to reproduce the measured NO_x data. As an alternative approach, the NO_x reaction mechanism proposed by Taniguchi et al. [148] and modified by Gronarz et al. [55] has been implemented in AIOLOS. The results, however, were not as promising as in the FLUENT implementation by Gronarz et al. [55]. A comparison demonstrated that the Taniguchi model shows inferior behavior compared to the Förtsch model [165] in AIOLOS. The main reasons for this obvious difference remain undisclosed but are suspected in the different nature of simulation source codes AIOLOS and FLUENT. Consequently, the applied Förtsch model is briefly described in the following.

The different fuel-N release routes are illustrated in Figure 4.6. The split into the light-gas-N fractions HCN and NH₃, tar-N and char-N strongly depends on the coal and the pyrolysis conditions, as is discussed in the following section. Char-N release is assumed to be 100 % to NO, i.e. $\xi_{NO}^{cbo} = 1$. However, different char-N release routes are possible, i.e. ξ_{NO}^{cbo} , $\xi_{NH_3}^{cbo}$, ξ_{HCN}^{cbo} or $\xi_{N_2}^{cbo}$ can be greater than 0.

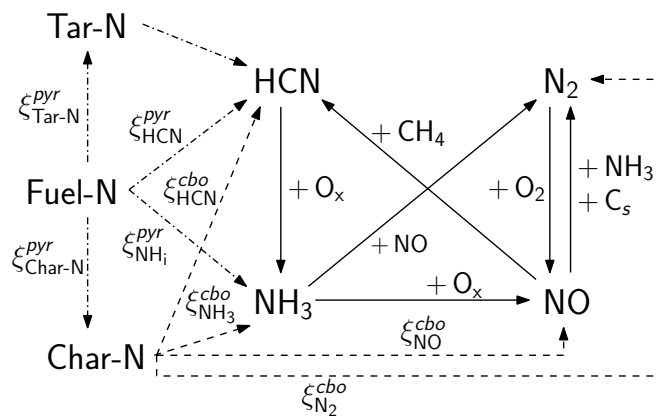


Figure 4.6: Schematic of the NO_x model

In the beginning of char burnout, nitrogen release from char is accelerated in comparison to the mass release at higher temperatures [11, 64]. This is considered by equation (4.94), where the change of nitrogen mass $M_{N,char}$ in the char is related to carbon mass $M_{C,char}$ in the char by means of the total unburned carbon content x_{UC} . The factor β_{UC} is coal-dependent, as the described effect is reinforced with increasing coal rank. β_{UC} is chosen to be 0.4 in the work at hand [41].

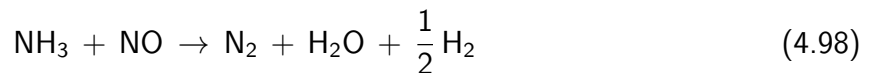
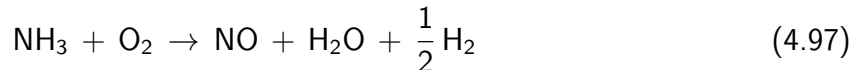
$$\frac{dM_{N,char}}{dM_{C,char}} = \frac{M_{N,char}}{M_{C,char}} (\beta_{UC} \cdot x_{UC} + 1) \quad (4.94)$$

The following reaction sequence includes a CN and NH_i sub-system, represented by HCN and NH₃, respectively. HCN consumption starts with the oxidation by oxygen-containing species. The reaction rate expression was proposed by Mitchell and Tarbell [95].



$$\left(\frac{d\chi_{\text{HCN}}}{dt}\right)_{4.95} = -K_{0,4.95} \cdot \exp\left(-\frac{E_{4.95}}{\widetilde{R} T}\right) \cdot \chi_{\text{HCN}} \cdot \chi_{\text{H}_2\text{O}} \quad (4.96)$$

The NH₃ originating from the pyrolysis nitrogen release (4.108) and from reaction (4.95) further reacts via reactions (4.97) and (4.98) to NO by NH₃ oxidation or to N₂ by NO reduction. The kinetics of these competing reactions are obtained from de Soete [33].



$$\left(\frac{d\chi_{\text{NH}_3}}{dt}\right)_{4.97} = -K_{0,4.97} \cdot \exp\left(-\frac{E_{4.97}}{\widetilde{R} T}\right) \cdot \chi_{\text{NH}_3} \cdot \chi_{\text{O}_2}^{b_{4.97}} \quad (4.99)$$

$$\left(\frac{d\chi_{\text{NH}_3}}{dt}\right)_{4.98} = -K_{0,4.98} \cdot \exp\left(-\frac{E_{4.98}}{\widetilde{R} T}\right) \cdot \chi_{\text{NH}_3} \cdot \chi_{\text{NO}} \quad (4.100)$$

Exponent $b_{4.97}$ in equation (4.99) is calculated via the following expression and is delimited between 0 and 1:

$$b_{4.97} = -1.29666 - 1.31955 \cdot \ln \chi_{\text{O}_2} - 0.44909 \cdot (\ln \chi_{\text{O}_2})^2 - 0.05113 \cdot (\ln \chi_{\text{O}_2})^3 \quad (4.101)$$

NO is additionally reduced by hydrocarbon radicals forming HCN via the reburning mechanism, see reaction (4.102). The relevance of NO reburning has been shown for flameless combustion of gaseous fuels [88, 98]. The reaction rate is taken from Chen et al. [23].



$$\left(\frac{d\chi_{\text{NO}}}{dt}\right)_{4.102} = -K_{0,4.102} \cdot \exp\left(-\frac{E_{4.102}}{\widetilde{R} T}\right) \cdot \chi_{\text{NO}} \cdot \chi_{\text{CH}_i} \quad (4.103)$$

Finally, heterogeneous reduction is included as NO reduction by char, as given in reaction (4.104). Kinetics are obtained from Levy et al. [81]. The external specific char surface area $a_{ext,j}$ of each char particle class j is calculated as shown in equation (4.83).



$$\left(\frac{d\chi_{\text{NO}}}{dt} \right)_{4.104} = -K_{0,4.104} \cdot \exp\left(-\frac{E_{4.104}}{\tilde{R}T}\right) \cdot p_{\text{NO}} \cdot a_{ext,j} \cdot M_{C_j} \quad (4.105)$$

It was pointed out before that thermal NO formation might play a minor, but still a considerable role in a flameless combustion regime. Therefore, it is considered in this NO_x reaction scheme by the Zeldovich mechanism represented by a global reaction (4.106). The kinetic rate is taken from Schnell [126].



$$\left(\frac{d\chi_{\text{NO}}}{dt} \right)_{4.106} = K_{0,4.106} \cdot \exp\left(-\frac{E_{4.106}}{\tilde{R}T}\right) \cdot \chi_{\text{N}_2} \cdot \chi_{\text{O}_2}^{0.5} \quad (4.107)$$

The complete reaction mechanism is summarized in Table 4.11 in conjunction with the kinetic parameters, the frequency factors $K_{0,i}$ and the activation temperatures $E_i \tilde{R}^{-1}$.

Table 4.11: NO_x reaction mechanism including kinetic parameters

Reaction		$K_{0,i}$		$E_i \tilde{R}^{-1}$	Reference
HCN oxidation	4.95, 4.96	$1.94 \cdot 10^5$	s^{-1}	$3.95 \cdot 10^4 \text{ K}$	[95]
NH ₃ oxidation	4.97, 4.99	$2.80 \cdot 10^{10}$	s^{-1}	$3.37 \cdot 10^4 \text{ K}$	[33]
NH ₃ reduction	4.98, 4.100	$3.00 \cdot 10^{12}$	s^{-1}	$3.02 \cdot 10^4 \text{ K}$	[33]
NO reburning	4.102, 4.103	$9.20 \cdot 10^4$	s^{-1}	$9.46 \cdot 10^3 \text{ K}$	[23]
NO reduction (char)	4.104, 4.105	$4.18 \cdot 10^{-4}$	$\text{kmol} (\text{m}^2 \text{ s Pa})^{-1}$	$1.75 \cdot 10^4 \text{ K}$	[81]
NO thermal	4.106, 4.107	$1.80 \cdot 10^{18}$	s^{-1}	$6.81 \cdot 10^4 \text{ K}$	[126]

Derivation of initial nitrogen split from coal nitrogen evolution

Nitrogen release during devolatilization influences the subsequent NO_x formation to a large extent. The split into the light-gas-N fractions HCN and NH₃, tar-N and char-N would be individually investigated for each coal and condition; however, the effort would be too high. For the sub-bituminous coal Calentur used in the work at hand with a nitrogen content of

$\gamma_{N,dry} \approx 1.4\%$ (c.f. Table 3.3), the initial nitrogen split has been determined from a literature survey and proximate analysis on the one hand and the CPD pyrolysis model on the other hand. It is noted that tar and tar-N were not considered in the literature survey. The results of both approaches are compared in the following.

Literature data suggest that char-N and total volatile-N, comprising of tar-N and light-gas-N, represent approximately the same mass percentage as char and volatile matter of the parent coal [106, 132]. Ergo, a char-N fraction of 57.72 % and a total volatile-N fraction of 42.28 % can be roughly guessed on a dry and ash free basis. This is in accordance with maximum 60 % of nitrogen retained in the char, as is determined from proximate analysis, since the prevailing heating rates are very mild compared to an entrained flow reactor. The subsequent split into light-gas-N species HCN and NH_3 is assessed to be 80 % and 20 % of the total volatile-N fraction, respectively.

Application of the CPD devolatilization model allows for a detailed estimation of the initial fuel-N split. The model requires the final pyrolysis temperature, the heating rate and the duration of pyrolysis along with the coal composition data. To quantify the reliability of the results obtained from the CPD model, Alysandratou [2] compared results from the CPD devolatilization model with pyrolysis results from various experimental test rigs available in literature. For details, please refer to Appendix Section C.1.2. Pyrolysis conditions as described above are applied, see Section 4.5.3.

Table 4.12: Relative N-fractions after primary pyrolysis obtained from the CPD model and from literature

Relative N-fractions in %	$\vartheta_{pyr,max}$			Literature
	1000 °C	1100 °C	1200 °C	
ξ_{char-N}^{PYR}	55.64	49.79	46.00	57.72
ξ_{tar-N}^{PYR}	24.10	24.20	25.18	—
ξ_{HCN}^{PYR}	20.26	26.01	28.82	33.82
$\xi_{NH_3}^{PYR}$	—	—	—	8.46
$\xi_{STV-N=tar-N+HCN+NH_3}^{PYR}$	44.36	50.21	54.00	42.28

The CPD pyrolysis model does not account for NH_3 as a light-gas-N fraction, thus the total volatile-N share is split only into HCN and tar-N. As discussed above, tar-N is mainly released as HCN from bituminous coals and thus this is respected in the applied NO_x model, see Figure 4.6. Its release rate is obtained from tar oxidation, see equation (4.75). Soot can be generated during tar decomposition and then serves as a nitrogen carrier [20]. It usually releases its nitrogenous load as NH_3 . However, soot is neglected in the current flameless combustion model, see Section 4.5.3.

Preliminary simulations of flameless pulverized coal combustion on the basis of the CPD model results, as given in Table 4.12, have shown nearly no NH_3 which is in contrast to the experimental findings. Consequently, the light-gas-N split is recalculated according to the following equations (4.109) and (4.110). Therein, $\xi_{\text{tar-N}}^{\text{pyr}}$ is maintained, the tar-N release route is 100 % HCN and a total volatile-N split $\beta_{\text{NH}_3:\text{HCN}}$ between pyrolysis products NH_3 and HCN is applied. $\beta_{\text{NH}_3:\text{HCN}}$ is initially estimated to be 0.2, following the findings of the literature survey.

$$\xi_{\text{TV-N}}^{\text{pyr}} = \xi_{\text{HCN}}^{\text{pyr}} + \xi_{\text{NH}_3}^{\text{pyr}} + \xi_{\text{tar-N}}^{\text{pyr}} \quad (4.108)$$

$$\xi_{\text{NH}_3}^{\text{pyr}} = \beta_{\text{HCN:NH}_3} \cdot \xi_{\text{TV-N}}^{\text{pyr}} \quad (4.109)$$

$$\xi_{\text{HCN}}^{\text{pyr}} = (1 - \beta_{\text{HCN:NH}_3}) \cdot \xi_{\text{TV-N}}^{\text{pyr}} - \xi_{\text{tar-N}}^{\text{pyr}} \quad (4.110)$$

4.6 Grid evaluation for high velocity problems

The actual flow compartment in a furnace, for instance, needs to be transformed in a geometrical model that represents the relevant characteristics of the original setup. The representation of the real geometry by a computational mesh has to balance the two opposing goals of high accuracy and fast computation. High accuracy is achieved by high spatial resolution of the computational mesh and can be further promoted by the application of highly sophisticated cell types. Fast computation is influenced on the one hand by the coding of the CFD program code and its performance on the deployed hardware; on the other hand by the number of cells to be computed. Thus, an important task is to derive a suitable grid for the given problem that should be as coarse as possible but as fine as required. The obtained simulation results must be independent of the chosen grid.

The simple Cartesian test case

A short study on a very simple Cartesian geometry serves as basis for the assessment of achievable accuracy, grid influences and required grid refinements. The computational mesh is square in cross-section, with an edge length of 0.2 m and a length of 2.5 m. It features two centered inlets, the inner one is of round shape with a radius of 0.012 m supplying coal and coal-carrier-gas which is air in this case. The outer annulus is adjacent to the inner inlet with an outer radius of 0.024 m, supplying the combustion air at inlet velocity w_{CA}^0 . In the “ w_{CA}^+ ” and the “ w_{CA}^{++} ” cases, the outer radius of the annulus is reduced to 0.015 m and 0.014 m, respectively. Details on geometry and chosen sub-models are given in Appendix C. The investigated cases are given in Table 4.13, with the corresponding number of cells, minimum cell size and maximum inlet velocity w_{CA} . The given number of cells represents the spatial resolution, and the minimum cell

size indicates the gradients that can be resolved. The maximum inlet velocity w_{CA} corresponds to Mach numbers known from the FLOX cases.

Table 4.13: Characteristics of a simple Cartesian test case

Case name	Number of cells	Minimum cell size (L, W, H)	Initial inlet velocity w_{CA}	Ma_{CA}
Baseline w_{CA}^0	289000	0.004 m, 0.004 m, 0.010 m	16.4 m s^{-1}	0.02
Coarse w_{CA}^0	80828	0.006 m, 0.006 m, 0.015 m	16.4 m s^{-1}	0.02
Refined w_{CA}^0	644688	0.003 m, 0.003 m, 0.0075 m	16.4 m s^{-1}	0.02
Baseline w_{CA}^+	289000	0.004 m, 0.004 m, 0.010 m	82.2 m s^{-1}	0.16
Refined w_{CA}^+	644688	0.003 m, 0.003 m, 0.0075 m	82.2 m s^{-1}	0.16
Refined w_{CA}^{++}	644688	0.003 m, 0.003 m, 0.0075 m	122.2 m s^{-1}	0.25

The study was conducted using the SIMPLEC pressure correction equation and the RNG $k-\varepsilon$ model. The computed results are discussed using the relative updates during the iterative solution process, as derived in equation (4.32). The relative updates of the mass defect, of the velocities in x - and z -direction and of the CO concentration are taken for comparison, averaged over the last 1000 iterations. The derivation of the updates has been given in equation (4.32). They are depicted in Figure 4.7 for the cases shown in Table 4.13. The relative update of the CO concentration allows for evaluation of the species convergence. Elemental balances of C, H, O and ash are not shown in the following, since all results were found to be in a range of $\pm 0.15\%$. Accuracy in the same order of magnitude was obtained for the energy balance converging to values in the range of $\pm 0.40\%$.

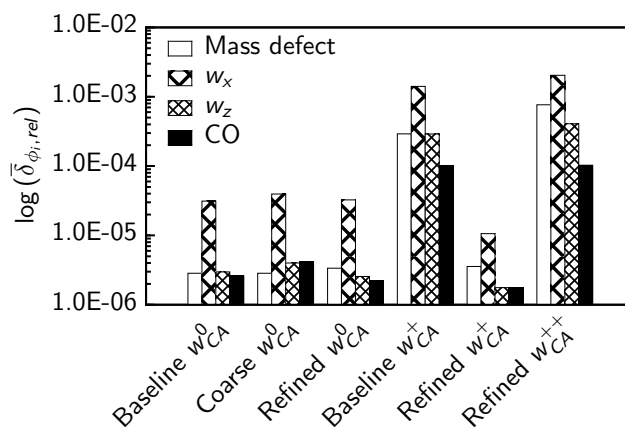


Figure 4.7: Results of grid evaluation

A decreasing and therefore positive trend of all updates δ_{rel} , as derived from equation (4.32), can be seen in Figure 4.7 for increasing spatial resolution and constant inlet velocity w_{CA} . For

the moderate inlet velocity w_{CA}^0 of 16.4 m s^{-1} , the update of the mass defect remains very similar throughout the change in spatial resolution. Updates of velocity components w_x and w_z , and of the CO species show some improvements within the same order of magnitude. It is generally noticed that the relative updates of velocities w_x and w_y are about one order of magnitude bigger than those of the velocity w_z which corresponds to the main flow direction. For the intermediate inlet velocity w_{CA}^+ of 82.2 m s^{-1} , the enhancement by higher spatial grid resolution is eye-catching, since all updates are lowered by about two orders of magnitude. Comparing the baseline mesh and the refined mesh results for the inlet velocities w_{CA}^0 , w_{CA}^+ and w_{CA}^{++} , one can conclude that higher inlet velocities demand a higher spatial resolution in order to obtain updates in the same order of magnitude as in the lower velocity case.

The grid of the KSVA furnace

The simulations in this work are based on the KSVA furnace, see Section 3.1. As an outcome of this study, the mesh of the KSVA furnace is locally refined to achieve a sufficient resolution of key regions of high velocities, intense mixing and reaction zones. The final mesh consists of 646058 cells. Thereof, 50550 cells are of cylindrical type tailored to model round shapes such as the fuel and combustion-air nozzles. The furnace is meshed by Cartesian cell types ensuring faster computation. To ensure a good representation of the furnace roundness, a sufficiently small cell size is chosen.

The positioning and design of the furnace regarding the combustion-air nozzles allows for a reduction of the simulated and calculated geometry to a 180° portion. This reduces the number of cells and thus the computational time. The symmetry boundary conditions are applied at the edges of the cutting plane. This cutting plane is located in the main recirculation zone, i.e. the recirculation plane, as shown in Figure 3.2. Thus, the coal annulus nozzle is cut, but the combustion-air nozzle is modeled completely. Boundary conditions are chosen in a way that mass flow is allowed across the intersection, i.e. the velocity vector is transposed by point symmetry with reference to the furnace axis. In Figure 4.8, the complete mesh is shown on the left-hand-side and a close-up of the burner vicinity is presented on the right-hand-side.

4.7 Simulation results of flameless pulverized coal combustion

This section deals with the representation of simulation results of flameless combustion cases described in Chapter 3. All presented simulations are based on the FLOX_{CO₂} case. Other cases were simulated and reported in the course of the FLOX-COAL-II project [165]. Afterwards, the results of the numerical burner design analysis, of the turbulence model evaluation, of the

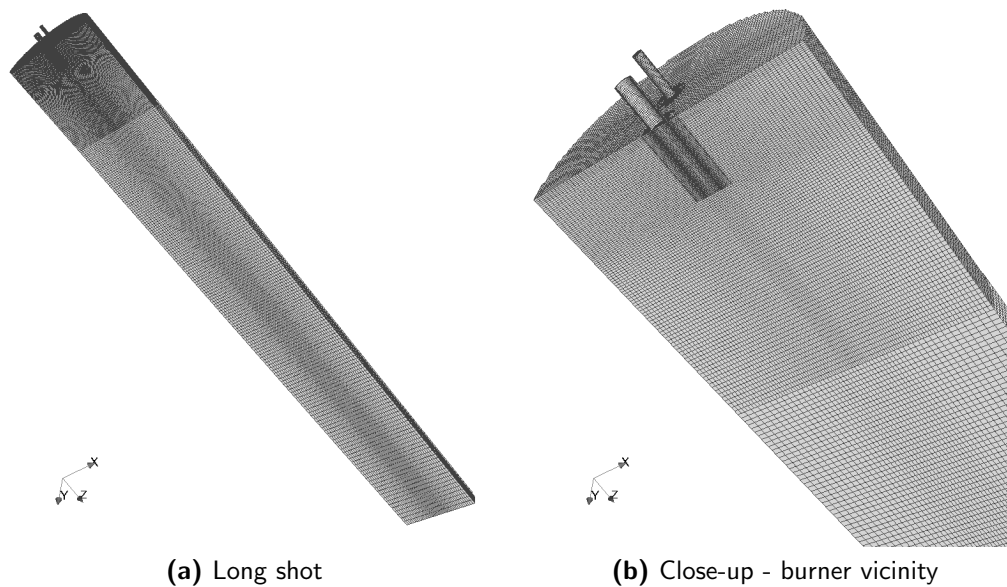


Figure 4.8: Final mesh of the KSVA furnace

turbulence-chemistry interaction model assessment and of the influence of pyrolysis on NO_x formation are presented.

4.7.1 About the comparison of simulation results and experimental data

The measurement techniques applied in the experiments described in Section 3.2 induce some spatial or temporal averaging. Measurement results ideally are given in conjunction with the standard deviation allowing for the estimation of the influence of temporal fluctuations. Results from CFD simulations usually do not reproduce spatial or temporal averaging in a way comparable to the analysis of measurement results. Temporal averaging is implicit to the RANS approach, see Section 4.4.2. The fluctuations are not resolved and thus, standard deviation can not be obtained.

Spatial averaging is present on the basis of the discretized volume as its values are assumed to be constant within its boundaries. This spatial averaging is usually too little to be compared with measurement data from suction probe sampling. Edge lengths of 25 mm and larger are often applied in full boiler simulations, but they decrease below 10 mm in burner testing simulations, requiring a good resolution of the burner and its vicinity. This is also the case for the simulation conducted in the course of this work.

In order to account for the spatial averaging induced by suction probe measurements, simulation results of gas concentrations and gas temperature are treated before comparison. The radius of the sucked gas plume is assumed to be 25 mm in the experiments in accordance

with the appraisal of other researchers [102]. The simulation results are processed by virtually spanning a sphere of radius 25 mm around the actual measurement point and calculating the volume-averaged value of interest ϕ_{vAV} from all finite volumes V_i located within the sphere, see equation (4.111).

$$\phi_{vAV} = \frac{\sum_{i=1}^I (\phi_i \cdot V_i)}{\sum_{i=1}^I V_i} \quad (4.111)$$

This procedure leads to a volume-averaged value of the simulation result which better represents the experimental value. If experimental measurement techniques offer high spatial resolution, as for instance LDV does, the diameter of the averaged volume becomes proportionally smaller. Since information might get lost, the above described volume-averaging is not preferable, if detailed analysis of small-scale gradients are in the focus or if cross-comparison of different simulation programs shall be conducted without comparison with experimental data.

4.7.2 Burner design evaluation

For the following analysis, the numerical domain was assessed either by calculating the average value of the plane (concentrations) or of the jets (temperature). A detailed description of its numerical setup is given in Appendix B.

In the following, the PT2 burner is classified according to the different pitch-circle diameters of the coal-carrier-gas nozzles. The burner PT2 $_{CCG,min}$ is characterized by a diameter of 100 mm, PT2 $_{CCG,med}$ by a diameter of 140 mm and PT2 $_{CCG,max}$ by a diameter of 270 mm. In the latter configuration, the diameter is equal to that of combustion-air nozzle pitching. As illustrated in Figure 4.9a, the coal concentration decreases more rapidly with the new design. This corresponds directly to a faster devolatilization of the coal as the coal splits into volatiles and char in the applied model. A fast devolatilization is preferred because it gives more time for dilution of volatile species with recirculated hot flue gases prior to mixing with the combustion-air. The faster devolatilization is caused by the faster heating of the coal which is observed from the temperature increase in the coal jets, see Figure 4.9c, whilst the overall temperature level remains the same. The heating is emphasized by an improved mixing of hot combustion products with the coal-carrier-gas jets now directly entering the recirculation zone. The positive impact of faster devolatilization on the NO_x concentration y_{NO} is presented in Figure 4.9d. Normalization is made with reference to maximum NO concentration of PT1 burner. When the PT2 burner is applied, it decreases by 20 % compared to that of the PT1 burner.

The devolatilization speed is assessed by the presence of the species coal in the simulation as it undergoes the conversion into the species volatile matter and char. It is observed in Figure 4.9a that the PT2 burner in either configuration ensures a significantly faster decrease in coal concentration in comparison to the PT1 burner. The average coal jet temperature shown in

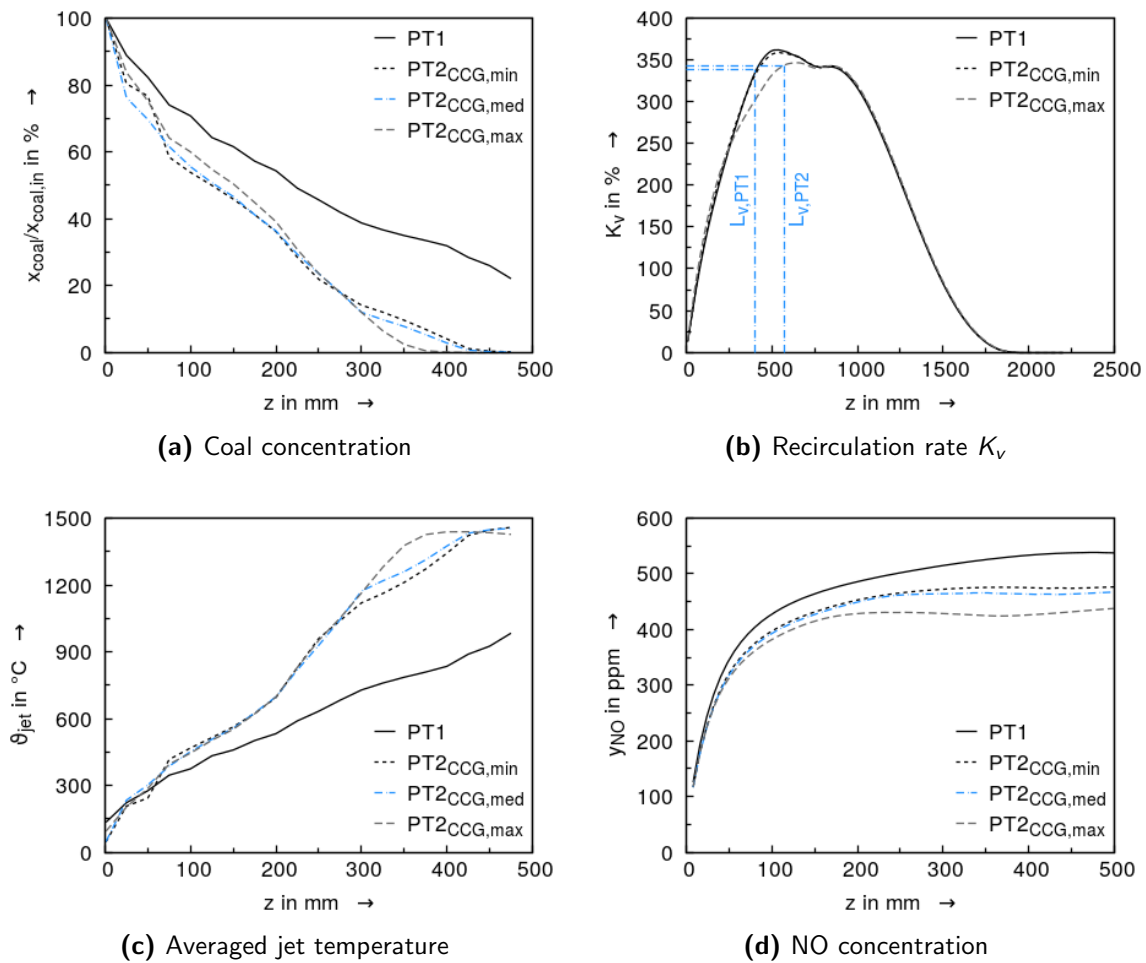


Figure 4.9: Improvements of PT2 burner design on coal devolatilization, recirculation rate, averaged jet temperature and NO concentration

Figure 4.9c is characterized by a fast increase and thus fast devolatilization for the PT2 burner configurations. Similarly to the coal concentration in Figure 4.9a, the configuration with the largest pitch-circle diameter PT2_{CCG,max} achieves the peak temperature first.

Thus, the premises of minimizing the char-N and volatile-N oxidation are respected: Fast devolatilization at higher temperatures shifts the split between volatile-N and char-N in favor of volatile-N. Volatile-N is released in a highly diluted atmosphere ensuring increased reduction to molecular N_2 .

The NO concentration consequently is decreased with the PT2 burner configurations, and the largest reduction is obtained with the PT2_{CCG,max} configuration. The recirculation rate K_V is locally diminished, but mixing with the combustion-air jets is also delayed. The prior-to-mixing length L_V , as is derived from equation (1.12), is increased from PT1 to PT2_{CCG,max}. It can be seen that the PT2 burner prototype achieves the same critical recirculation rate K_V of about 340% as the PT1 burner prototype does, despite a larger prior-to-mixing-length L_V .

This indicates a comparable dilution of the jets at this key stage of flameless combustion.

4.7.3 Turbulence model evaluation

The presented turbulence models of the $k-\varepsilon$ family are compared against the LDV data of FLOX_{CO₂} case obtained with the PT1 prototype burner. For comparison, the radial profiles of the axial velocity w_z are chosen at three downstream positions: $z = 230$ mm, $z = 1060$ mm, $z = 1890$ mm. They illustrate the most significant flow characteristics in the all-jets and recirculation plane, see Figure 4.10. In Figures 4.10a and 4.10b at $z = 230$ mm, the burner vicinity with the dominating combustion-air jets is shown. The main combustion zone with the internal recirculation zone at the walls can be seen in Figures 4.10c and 4.10d at $z = 1060$ mm. Plug flow is approached and combustion-air jet dominance strongly decays in Figures 4.10e and 4.10f at $z = 1890$ mm.

It can be seen that the standard and the modified $k-\varepsilon$ models give the worst agreement with the measured LDV data. While the latter overestimates the axial velocities, the first one predicts velocities that are too low. The RNG and realizable $k-\varepsilon$ models instead better capture the velocities present in the furnace. Despite the previously reported deficiency of the RNG $k-\varepsilon$ model, the best agreement is found in the all-jets and the recirculation plane for all three profile locations. It is noted that all investigated $k-\varepsilon$ models reveal a lack of accuracy in the prediction of the recirculation zone and in the establishment of the plug flow.

The length of the recirculation zone L_{rec} obtained from the simulation results and the measurement data is defined in equation (4.112) and exemplified in Figure 4.11:

$$L_{rec} = L_{reatt} - L_{sep} \quad (4.112)$$

Therein, L_{sep} is the length from the burner exit to the separation point and L_{reatt} is the length from the burner to the reattachment point. Experimental results have been estimated from the LDV measurement data. The position of these lengths is derived from the results closest to the wall at $x = y = 350$ mm.

In Table 4.14, the separation length, the length of the recirculation zone and the reattachment length of the separated flows are given.

In contrast to the velocity profiles presented in Figure 4.10, the standard $k-\varepsilon$ model performs well here and best captures the spatial extension of the recirculation zone in both planes. Whereas the standard $k-\varepsilon$ model is known for over-predicting the spreading rate of turbulent round jets, it gives results closest to the measured values. The other turbulence models known for better prediction of the round-jet spreading rate instead overestimate the reattachment length and the length of the recirculation zone by far. In the recirculation plane, only the RNG $k-\varepsilon$ model is in the same range as the standard $k-\varepsilon$ model. Comparisons of the turbulent kinetic

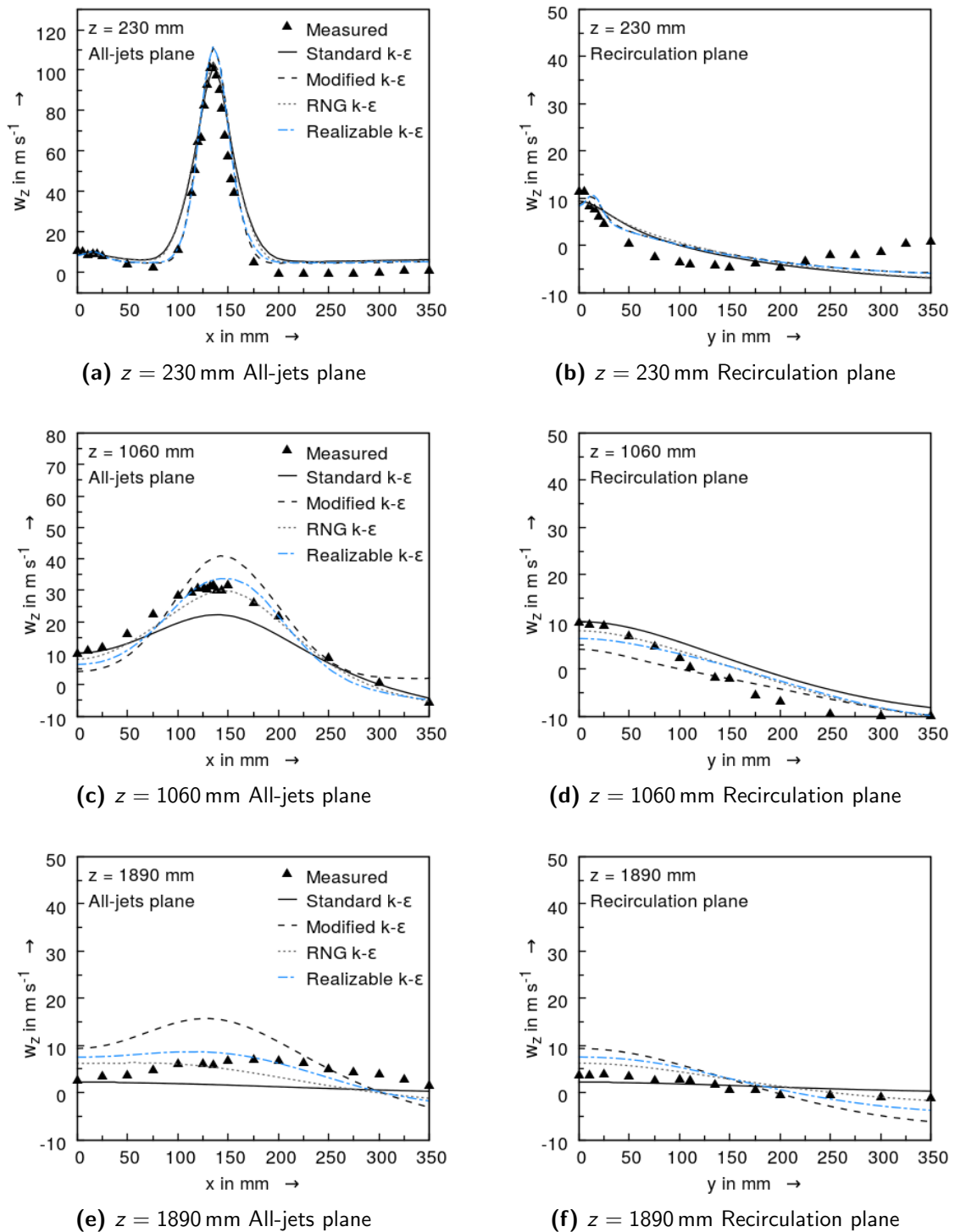


Figure 4.10: Comparison of axial velocity results of simulations with different k - ε models and of experiments

energy k and dissipation rate ε disclose that both are significantly higher for the standard k - ε model. It can be concluded that the energy of the flow is transferred much faster into heat with the standard k - ε model applied and thus, the flow loses its kinetic energy faster. Because

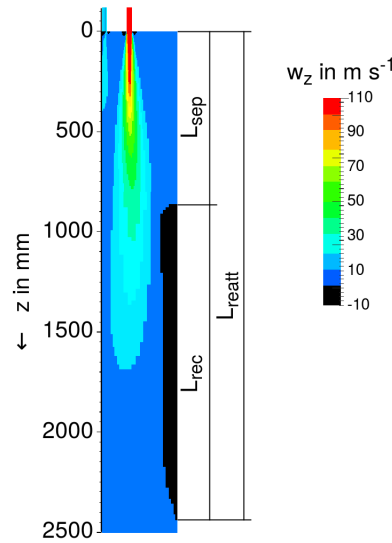


Figure 4.11: Length of recirculation zone, obtained by means of the separation length and the reattachment length, as defined in equation (4.112)

Table 4.14: Separation, recirculation and reattachment length of different $k-\varepsilon$ models in comparison with experimental results

		Standard $k-\varepsilon$ model	Modified $k-\varepsilon$ model	RNG $k-\varepsilon$ model	Realizable $k-\varepsilon$ model	Experiment
All- jets plane	L_{sep} in mm	740	1113	880	890	700
	L_{rec} in mm	995	1487	1410	1470	850
	L_{reatt} in mm	1735	2600	2290	2360	1550
Recircu- lation plane	L_{sep} in mm	0	0	0	0	380
	L_{rec} in mm	1780	2600	2190	2390	1620
	L_{reatt} in mm	1780	2600	2190	2390	2000

of the kinetic energy can be represented by the velocity, this faster decay can be seen from the velocity results in Figure 4.10. Considering the entire furnace diameter, the generation and dissipation of turbulent kinetic energy seems overestimated, as velocity decay is enhanced too much. Similar to Figure 4.10, the worst performance is found for the modified $k-\varepsilon$ model in all categories and thus, it can not be recommended for use here. It is also interesting to state that all turbulence models predict the recirculation zone up to the burner exit level, i.e. the furnace top, whereas the experimental results reveal a downstream flow first.

In consideration of Figure 4.10 and Table 4.14, the RNG $k-\varepsilon$ model is chosen due to its overall superior performance. However, the standard $k-\varepsilon$ model should not be rejected from flameless combustion modeling.

Further improvements in flow field predictions might only be achieved by the application of anisotropic turbulence models such as Reynolds stress models in RANS simulations or by the application of LES. The latter models the Navier-Stokes equations at a more detailed level and causes less loss of information regarding the flow field.

4.7.4 Turbulence-chemistry interaction

Inspired by the investigations of a gaseous flameless combustion system [4, 32], a study has been designed to assess the implications of EDC model constants' variations on the flameless combustion of coal. This study has been conducted by Arastoo [7] in the course of a student research project and the results are discussed in the following.

The study exercises variations of the EDC exponent κ_{EDC} and the constants C_λ and C_t , modifying the fine structure share γ^* (cf. equation (4.64)) and the fine structure time scale for mass exchange t^* (cf. equation (4.65)). Therein, the variations of C_λ and C_t are the same as proposed by Aminian et al. [4] and De et al. [32] in order to allow for a comparison of results. The cases are depicted in Table 4.15.

Table 4.15: Variants of EDC model constants

Case name	κ_{EDC}	C_t	C_λ
Baseline	3	0.4082	2.138
$\kappa_{EDC} = 2$	2	0.4082	2.138
$C_\lambda = 1.0$ [32]	3	0.4082	1.000
$C_t = 3.0$ [4]	3	3.000	2.138

Impacts on temperature and gas concentration profiles are expected from the above variations, since on the one hand, the share of reacting space in the cells i.e. the reactive zone is reduced by increasing κ_{EDC} and reducing C_λ and on the other hand, the mass exchange time scale in the reactive zone is increased by a higher C_t . Thus, gas temperature profiles and gas concentration profiles of CO and O₂ are compared in the following Figure 4.12 against their measured results.

Regarding the temperature trends displayed in Figures 4.12a and 4.12b one can identify the influence of the EDC exponent κ_{EDC} , allowing for too fast reactions in the case of $\kappa_{EDC} = 2$, pointed out by the temperature peak at $x = 70$ mm and $z = 700$ mm. On the contrary, the computed temperature trend matches the measured data quite well in Figure 4.12a for the reduced fine structure share obtained with the choice of $\kappa_{EDC} = 3$. This is verified by the axial temperature trend for z greater than 500 mm. In the burner vicinity, the mixing of hot combustion products and cold feed is not correctly predicted by the turbulence models.

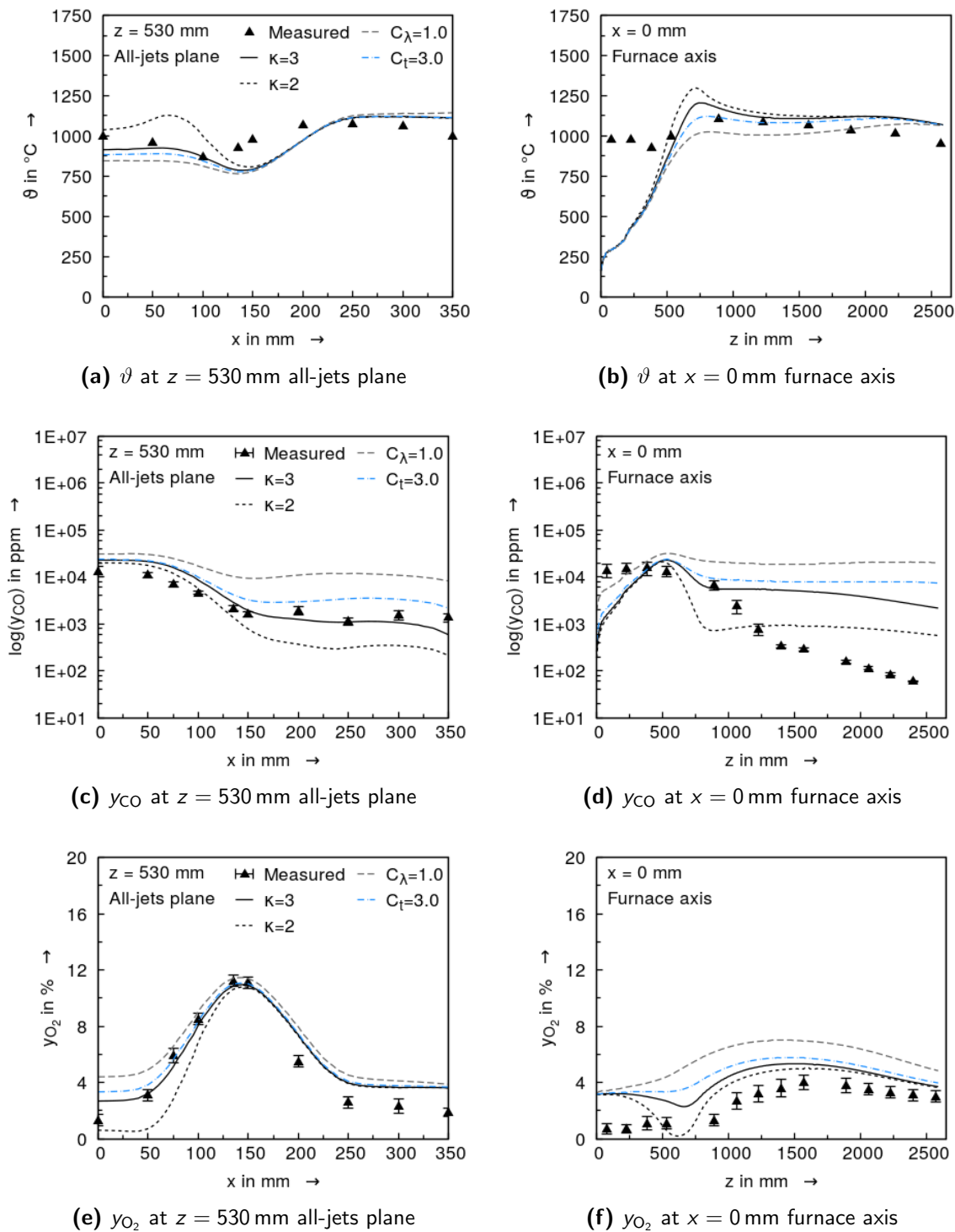


Figure 4.12: Gas temperature, CO and O₂ concentrations for different EDC model constants along radial and axial profiles at $z = 530$ mm and $x = 0$ mm

However, it is assumed that the suction pyrometry induces significant averaging in the burner vicinity and thus the measured temperatures are too high.

CO concentration supports the intensified reaction thesis, when the EDC exponent κ_{EDC} is

reduced from 3 to 2, see Figures 4.12c and 4.12d. They are lower for $\kappa_{EDC} = 2$. However, the computed results correspond better for the choice of $\kappa_{EDC} = 3$. CO concentration fits very well along the presented radial profile. Improvements can be also seen for the CO trend along the furnace axis, but all CO graphs approach a constant value from approximately $z = 900$ mm whereas the measurement data reveal a continuous reduction of CO concentration.

The O_2 concentration trends affirm the conclusions drawn from CO concentration, see Figures 4.12e and 4.12f. Along the furnace axis, the computed O_2 concentration is higher than the measured concentration, especially downstream of $z = 900$ mm, matching the findings of CO concentrations being computed too high.

A decrease of C_λ from 2.138 to 1.000 further reduces the fine structure share γ^* for a constant κ_{EDC} . Consequently, temperature trends are below those of $\kappa_{EDC} = 3$ in regions where reactions take place. Temperature trends coincide elsewhere e.g. in the burner vicinity for z below 500 mm, see Figure 4.12b. Gas concentrations y_{CO} and y_{O_2} show the opposite behavior, i.e. higher concentrations are computed in comparison to the case of $\kappa_{EDC} = 3$, as available reactants are reduced. Compared to the measurement data, the reduction of C_λ worsens the agreement. This is contrary to the findings of De et al. [32], who reported improved computational results with the modified C_λ constant. It is noted that this might depend on the burner and furnace in use which are very different in both cases.

The increase of C_t results in an elevated time scale of mass exchange, t^* , between fine structures and surrounding fluid. As this time scale increases, the mass exchange and thus the available reactants are lowered. The computational results disclose this effect very well. The trend of temperature is equal or lower, and the O_2 and CO concentration are equal or higher, all compared to the baseline case with $C_t = 0.4082$. It can be concluded from the C_t results that the chemical reactions are mixing-limited, i.e. the reaction partners available in the fine structures are fully consumed. In conjunction with the fine structure portion limited by the choice of $\kappa_{EDC} = 3$ instead of 2, the increased time scale of mass exchange and the thereby enhanced mixing limitation seem to impact the reactions during simulation too much in the investigated flameless pulverized coal combustion setup. The observations reported by Aminian et al. [4] disclose decreased temperature and concentration trends which is not consistent with the findings of this work. In the author's opinion, temperature and concentration trends shall develop in opposite directions, when changing the fine structure time scale t^* . But as for De et al. [32], comparability might be restricted due to the differences of setups.

Summing up, the agreement of computational results with experimental data is significantly improved with the choice of κ_{EDC} equal to 3. The adaptation of EDC coefficients C_λ and C_t is not found to reduce the observed deviations. Consequently, the original coefficient setting is recommended.

From the axial simulation results, it can be seen that the first two or three measured results are hardly matched by the simulations. This is partly related to the local disturbance induced by

the probes during in-furnace measurements, whereas computational results are obtained from undisturbed conditions. The agreement between measurement and computational data is likely to be enhanced, if the measurement method preserves the flow field. This can be seen from Figure 4.10 for the applied LDV measurement method. On the other hand, several reasons of inaccuracy can be found on the modeling part of the work which will prohibit a perfect agreement between results from both approaches.

4.7.5 Pyrolysis

The effect of pyrolysis on the combustion process has been highlighted in Section 4.5.3. Therefore, the effects on simulation results are investigated with regards to the trends of gas temperature and gas concentrations. A final pyrolysis temperature of 1000 °C is estimated from the measurement data. The impact of pre-processing with a detailed pyrolysis model (CPD) and the subsequent consideration of tar treated as an intermediate pyrolysis product are analyzed regarding the gas temperature and gas concentrations. In Figure 4.13, measurement and simulation data are displayed along the furnace axis at $x = 0$ mm and the horizontal profile axis at $z = 530$ mm.

It is stated that the presented measurement results of volatiles are only displayed for qualitative comparison in Figure 4.13, since they are an aggregation of several light and heavy volatile species, as specified in Table 3.1.

An evident difference can be seen from temperature trends along the furnace axis which is smoothed with the applied tar model and CPD results. The reason for this can be seen from the CH₄ concentration profiles, exhibiting a reduced CH₄ release due to volatile matter partially evolving as tar. Using the CPD results, the reduced reaction intensity can also be found in the O₂ results (not shown here) where the minimum in the baseline simulation is not present in the simulations including tar. As for CH₄, the CO concentration is slightly lower within the devolatilization zone when the tar model is applied, see Figure 4.13d. However, the influence on the CO concentration is only of marginal extent.

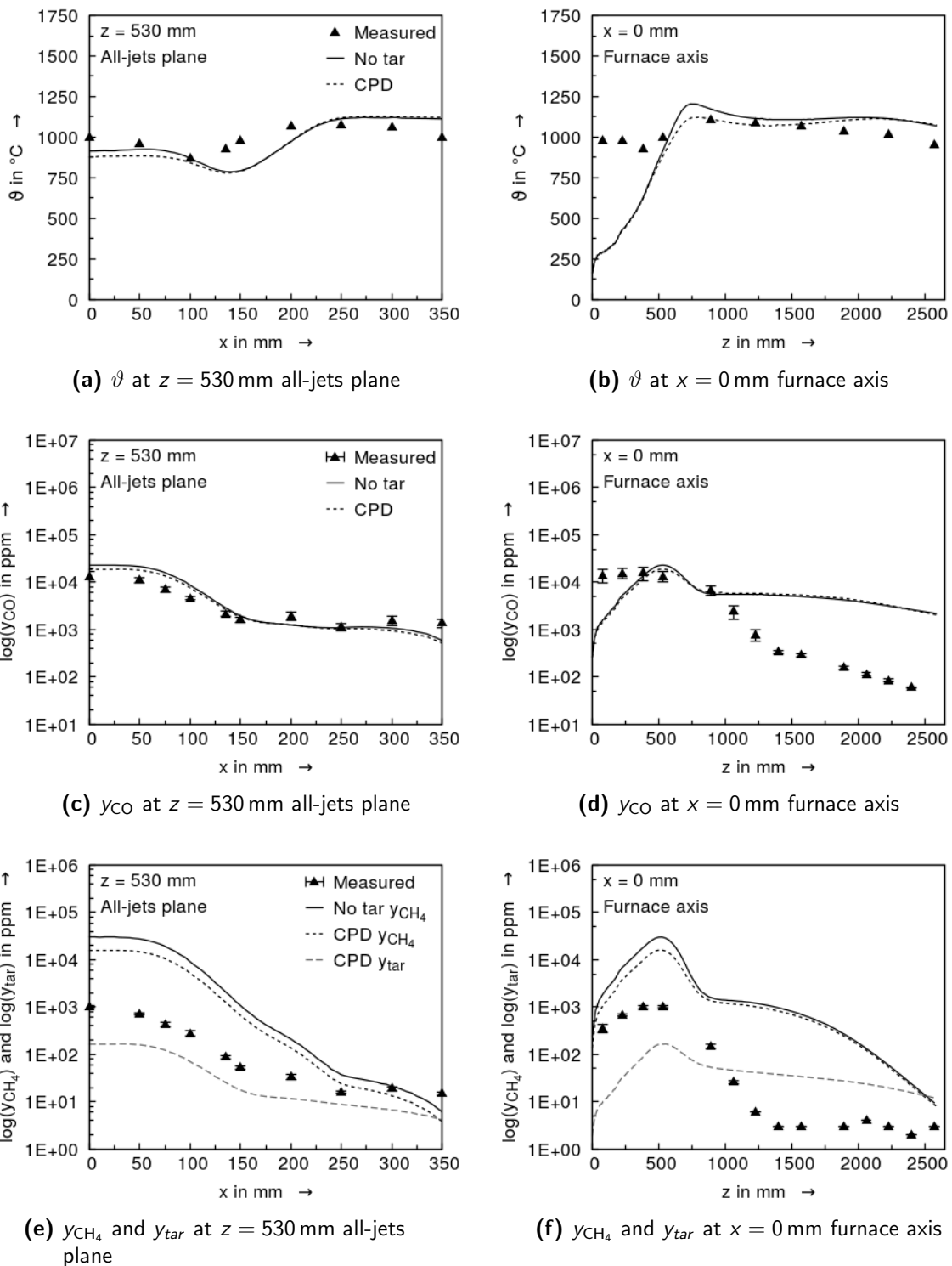


Figure 4.13: Gas temperature, CO and volatiles / tar concentrations for simple pyrolysis model (no tar) and advanced pyrolysis model (CPD 1000 °C) along radial and axial profiles at $z = 530$ mm and $x = 0$ mm

4.7.6 NO_x evolution and conversion

The assessment of NO_x simulations is undertaken with two different foci: First, the influence of the initial nitrogen split and thus the advantages of applying advanced pyrolysis models are discussed. Secondly, the behavior of the NO_x model per se is evaluated.

Starting with the initial nitrogen split evaluation, it is recalled that pyrolysis and NO_x formation are strongly influenced by the amount of nitrogen initially released with volatile matter and tar. It can be controlled by the burner aerodynamics and furnace atmosphere [106]. In contrast, retained char-N will be released mostly as NO and can be only influenced to a small extent: char-N to NO conversion depends on the prevalent O₂ and NO concentrations and on the coal rank [50, 135]. As discussed in Section 4.5.4, the initial fuel-N splitting is not modeled in CFD codes, and has to be obtained either from experiments, literature data or by explicit pyrolysis modeling, e.g. by the CPD model. Pyrolysis experiments were not performed in this work, thus, the influence of initial fuel-N split on the NO_x evolution in the CFD simulation is evaluated based on literature data and the CPD pyrolysis model results.

Results of NO_x post-processing are presented in Figure 4.14 for the PT1 prototype burner in the FLOX_{CO₂} condition. Different initial fuel-N distributions have been taken as a basis of the simulations: literature data and CPD results at three different final pyrolysis temperatures. The CPD results are modified in comparison to Table 4.12 by the total volatile-N split of $\beta_{\text{NH}_3:\text{HCN}} = 0.2$ to account for the NH₃ release during pyrolysis (see Section 4.5.4). The initial fuel-N distributions are compiled in Table 4.16.

Table 4.16: Relative N-fractions after primary pyrolysis obtained from the CPD model and from literature

Relative N-fractions in %	$\vartheta_{\text{pyr,max}}$			Literature
	1000 °C	1100 °C	1200 °C	
$\xi_{\text{char-N}}^{\text{PYR}}$	55.64	49.79	46.00	57.72
$\xi_{\text{tar-N}}^{\text{PYR}}$	24.10	24.20	25.18	—
$\xi_{\text{HCN}}^{\text{PYR}}$	11.39	15.97	18.02	33.82
$\xi_{\text{NH}_3}^{\text{PYR}}$	8.87	10.04	10.8	8.46
$\xi_{\text{TV-N=tar-N+HCN+NH}_3}^{\text{PYR}}$	44.36	50.21	54.00	42.28

It can be seen from Figures 4.14a and 4.14b that the initial HCN release depends on the HCN portion in the light volatiles $\xi_{\text{HCN}}^{\text{PYR}}$ which is the highest for the initial fuel-N distribution compiled from literature data. Secondly, tar-N is released as HCN for the cases with initial fuel-N distribution derived with the CPD model. This results in a slower decay of these simulation results compared to the literature based simulation results. NH₃ peaks in Figures 4.14c and 4.14d increase in accordance with the growing total volatile-N share, see Table 4.16. The

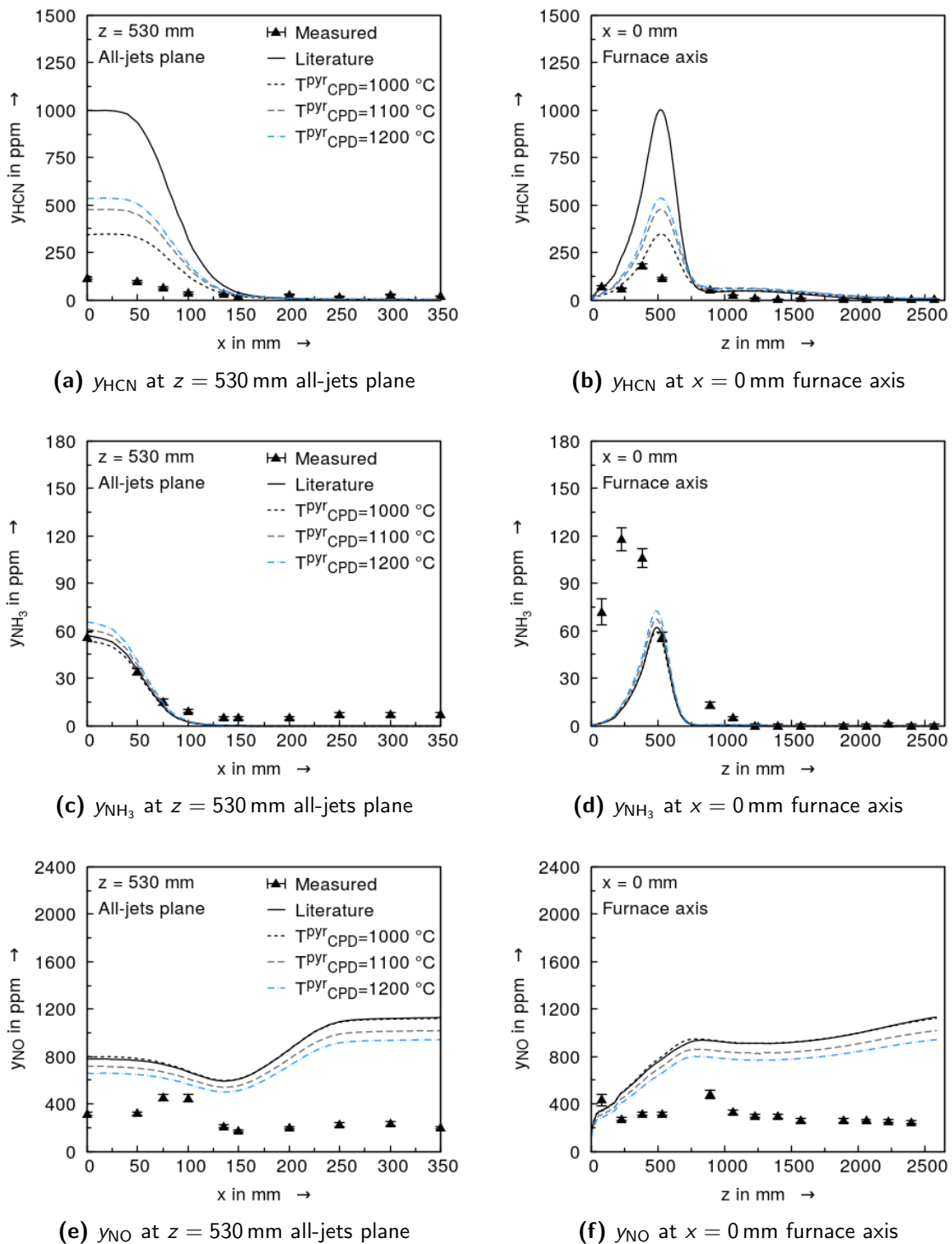


Figure 4.14: Concentrations of nitric species HCN, NH₃ and NO for different initial fuel-N splits in dependence of the final pyrolysis temperature along radial and axial profiles at $z = 530$ mm and $x = 0$ mm

absolute increase of NH₃ concentration with final pyrolysis temperature is weaker compared to that of HCN, due to the applied total volatile-N split $\beta_{NH_3:HCN} = 0.2$, see also Section 4.5.4.

This is in agreement with the knowledge of primary pyrolysis nitrogen evolution [50].

Regarding the NO concentration trend, the positive influence of reduced char-N fraction on the NO abatement is observed. The lowest char-N fraction is obtained for the highest final pyrolysis temperature, see Table 4.16. The more fuel-N is devolatilized in the reducing atmosphere in the burner vicinity, the less conversion into NO takes place in the burner vicinity of $z < 1000$ mm, and the less nitrogenous species are released from the char. Consequently, CPD pyrolysis model results in conjunction with the NO_x model support well the statement of Pershing and Wendt [106] saying that nitrogen devolatilized during pyrolysis can be controlled by burner aerodynamics, and thus can be well reduced, whereas nitrogen retained in the char and released subsequently during the char burnout mainly as NO is difficult to control. This statement made for conventional flame conditions can be transferred to flameless combustion conditions, as the conditions in the char burnout zone are very similar.

In the comparison of computational results of nitrogenous species with the experimental results, the reader can observe strong deviations, see again Figure 4.14. Regarding the computed HCN concentrations, they overshoot the measured concentrations in the pyrolysis zone by far. This is affirmed when the pyrolysis temperature in the CPD model increases. HCN concentration profiles based on the initial fuel-N distribution CPD 1000 °C is in the best agreement with the measured data. In the recirculation zone, i.e. for $x > 150$ mm, and in the char burnout zone, i.e. for $z > 890$ mm, the computed and measured HCN concentrations show the same trends and are in fairly good agreement. The trend of the other considered NO_x precursor NH_3 captures the radial profile at $z = 530$ mm well. The axial profile along the furnace axis, however, shows that NH_3 is too quickly consumed after its release. The trends of NO close to the furnace axis ($x < 150$ mm) in Figure 4.14e follow the measured values, but are partially higher by a factor of two. The concentrations in the recirculation zone are also far too high. They suffer from the continuously growing NO concentrations as the flow moves downstream, see Figure 4.14f. The axial NO concentration trend exhibits the difficulties of the NO_x model to capture the experimental trend and data points. It can be stated that literature data results are closest to those obtained with the CPD model at pyrolysis peak temperature of 1000 °C.

Table 4.17: Final initial N-fractions after primary pyrolysis

Relative N-fractions in %	$\beta_{\text{NH}_3:\text{HCN}}$	
	0.2	0.35
$\xi_{\text{char-N}}^{\text{PYR}}$	55.64	55.64
$\xi_{\text{star-N}}^{\text{PYR}}$	24.10	24.10
$\xi_{\text{HCN}}^{\text{PYR}}$	11.39	4.73
$\xi_{\text{NH}_3}^{\text{PYR}}$	8.87	15.53

Measurements of pyrolysis products conducted by Gövert et al. [165] suggest that the share of NH_3 shall be higher for the Calentur coal than the originally assumed $\beta_{\text{NH}_3:\text{HCN}} = 0.2$.

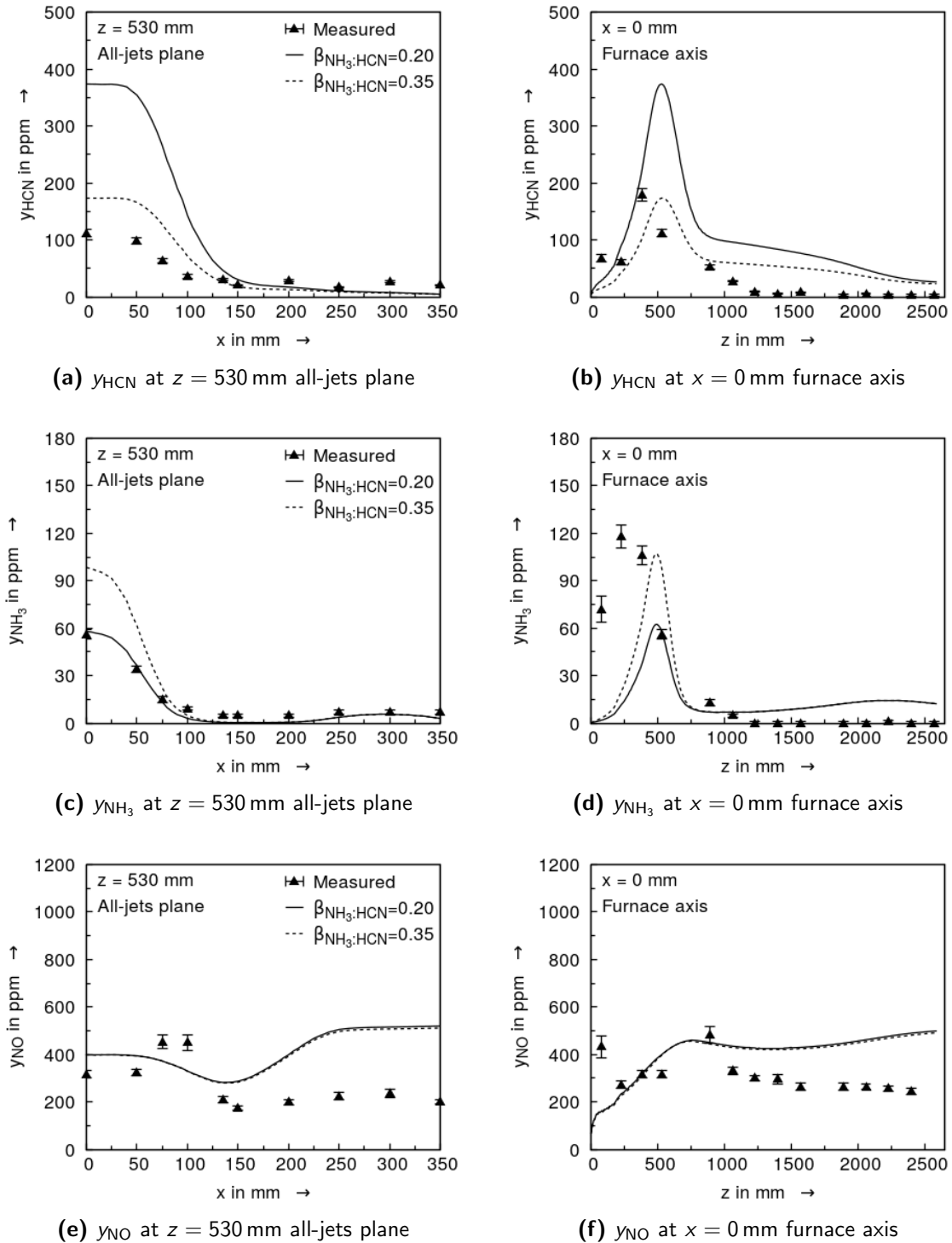


Figure 4.15: Concentrations of nitric species HCN, NH_3 and NO for adapted fuel-N split along radial and axial profiles at $z = 530$ mm and $x = 0$ mm

Consequently, the split of light nitrogenous devolatilization products $\beta_{\text{NH}_3:\text{HCN}}$ is fitted to the experimental results leading to $\beta_{\text{NH}_3:\text{HCN}} = 0.35$. Simulation results with $\beta_{\text{NH}_3:\text{HCN}}$ of 0.35 and 0.2 are shown in Figure 4.15. The initial fuel-N distribution obtained from the CPD predictions is shown in Table 4.17.

It can be seen from Figure 4.15 that the predicted trends of nitrogen precursor HCN are clearly improved with the adapted initial fuel-N split of $\beta_{\text{NH}_3:\text{HCN}} = 0.35$. The HCN concentration is reproduced much more satisfactorily. The predicted trends of NH_3 instead reveal an ambivalent result: the very good match of NH_3 concentration for $\beta_{\text{NH}_3:\text{HCN}} = 0.2$ at $z = 530$ mm is worsened, whereas the trend along the z axis is clearly improved for $\beta_{\text{NH}_3:\text{HCN}} = 0.35$. NO concentration trends are not significantly affected by the modification of total volatile-N split. Despite the ambivalent NH_3 results, the choice of $\beta_{\text{NH}_3:\text{HCN}} = 0.35$ is regarded superior due to the improved match of experimental and numerical HCN concentrations.

As the predicted NO concentration is found to be surprisingly high in the results shown in Figure 4.14, the char-N release path is reassessed. Some researchers using the same or a slightly modified form of this NO_x model assumed char-N to be released as 100 % NH_3 [41, 74, 84]. Others assigned the char-N to HCN [80, 124]. Stadler [136] proposed a different char-N path according to the findings of Park et al. [103]: 67 % N_2 , 28 % NO and 5 % HCN. Those different char-N paths are tested with the current case and results are depicted in Figure 4.16.

It can be seen from Figure 4.16 that a different choice of char-N release path highly influences the NO trend, whereas HCN and NH_3 trends are only marginally altered. This is related to the very high rates of NH_3 reactions (4.97) and (4.98). In the case of the char-N to HCN path, the NO trend moves closer to the measured data, whereas the HCN trend departs from the measurement results. The application of the char-N release paths as used by Stadler [136] does not result in a significant alteration of the NO_x model results. It remains questionable, however, whether a char-N release directly to molecular N_2 can be assumed. The best agreement in HCN, NH_3 and NO concentration profiles is obtained with the char-N to NH_3 path. Since the char-N to NH_3 release path leads to the best agreement of simulation and measurements, it is recommended for this high-volatile bituminous coal in a flameless combustion regime.

The HCN concentration has been found to exceed the measured concentration by far which has already been reported in literature. This might be due to a too low HCN consumption in reaction (4.95), with the reaction rate given in equation (4.96). For the widely applied reaction rate proposed by de Soete [33], Zhang et al. [186] investigated its correction by a factor of 13. The same correction factor is used in the work at hand for the reaction rate originally proposed by Mitchell and Tarbell [95].

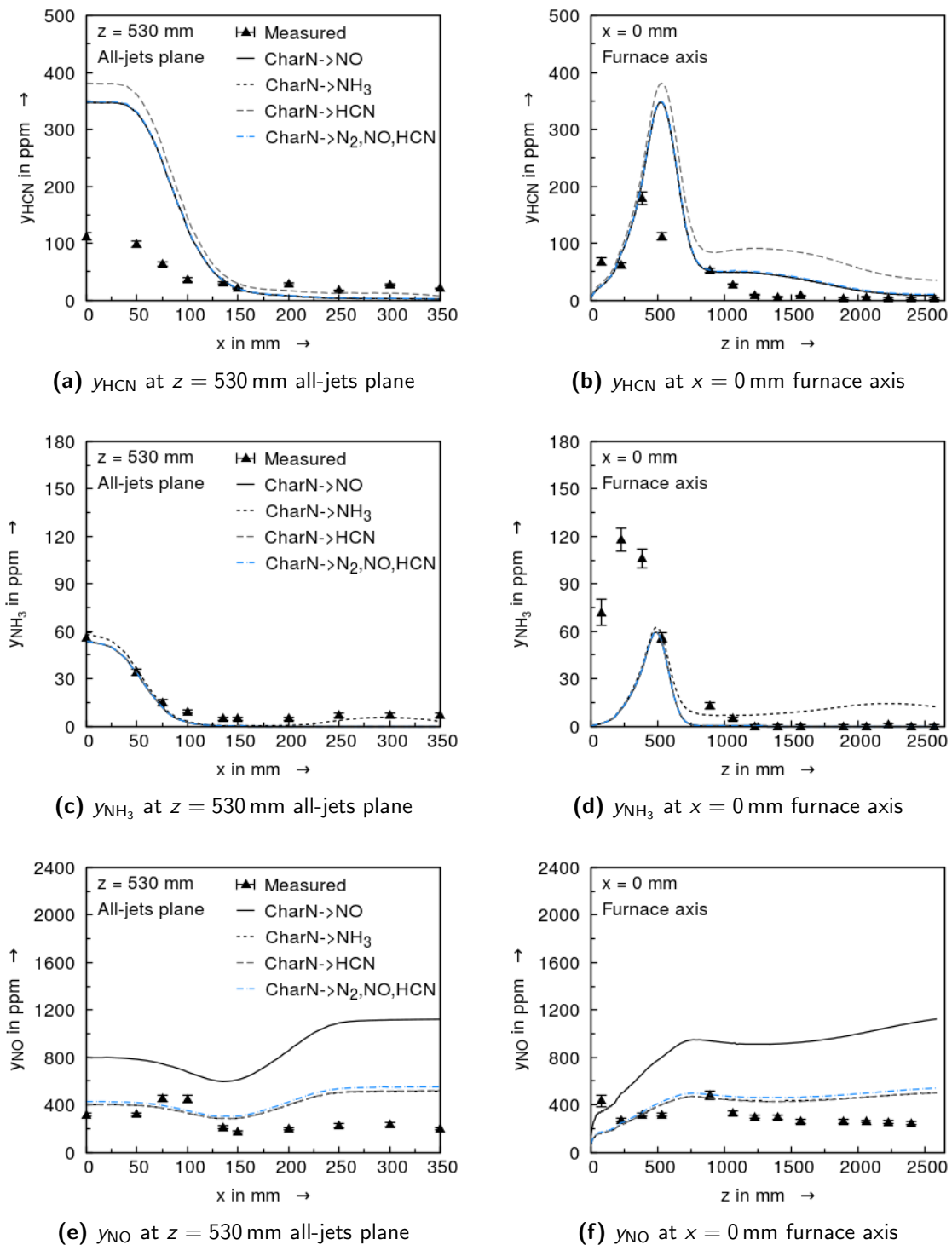


Figure 4.16: Concentrations of nitric species HCN, NH_3 and NO for different char-N release paths along radial and axial profiles at $z = 530$ mm and $x = 0$ mm

The results are displayed in Figure 4.17. A further increase of the HCN oxidation rate is found to be of minor effect. This was also confirmed by other researchers computing the same case with a different CFD code and their own NO_x model [165]. The NH_3 yield remains the

same, despite an increase of HCN conversion to NH_3 by accelerated reaction rate (4.96). This fact is attributed to the fast NH_3 conversion to N_2 and NO , described in equations (4.99) and (4.100). Their kinetics are several orders of magnitude larger than that of the HCN conversion rate. Consequently, the NH_3 trends are not displayed here. The NO yield changes marginally with the altered HCN oxidation rate. This is in contrast to the statement of Zhang et al. [186], claiming increased NO_x concentrations due to the increased HCN oxidation rate.

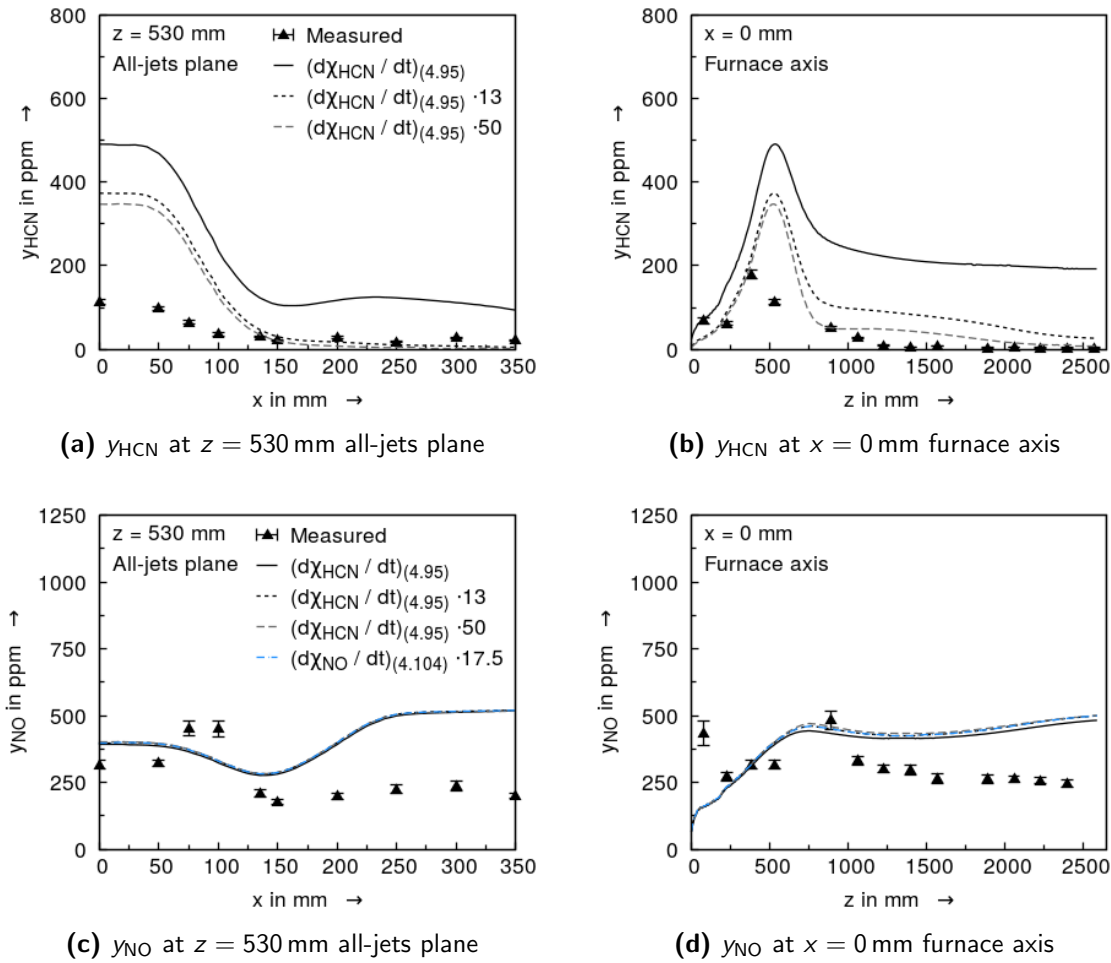


Figure 4.17: Concentrations of HCN and NO for different HCN oxidation rates; additionally concentrations of NO for increased NO reduction rate along radial and axial profiles at $z = 530$ mm and $x = 0$ mm

Zhang et al. [186] additionally propose to modify the NO reduction rate on the char surface by a factor of 17.5, see reaction (4.104) and reaction rate as in equation (4.105). They argue that the char surface depends on its determination method: BET analysis gives smaller char surfaces than the Hg analysis, reported for different coals [27, 143, 185].

The resulting NO concentration profiles are presented in Figures 4.17c and 4.17d for the char-N to NH_3 path, with the HCN oxidation rate altered by a factor of 13 and 50 and with the char surface increased by a factor of 17.5. It can be seen that the reduction of NO on the

char surface is of minor importance, since the increased char surface area a_{ext} does not affect the NO reduction by char significantly.

In conclusion, HCN is over-predicted in the devolatilization zone and its consumption is insufficiently reproduced if the original HCN to NH_3 oxidation rate is employed. Simulation results can be improved by increasing this rate by a factor of 13. The NH_3 and NO yields are insensitive to this alteration, as to the increase of the char surface area meant for enhancing heterogeneous NO reduction. It is pointed out that the investigated NO_x model can only be reasonably applied for the investigated Calentur coal with NH_3 as the char-N release product. Other char-N release paths either worsen the HCN trend or result in NO emissions far from the measurement results. The initial fuel-N split of the investigated coal is recommended to be obtained rather from the CPD pyrolysis model than from literature data of similar coals. Data from pyrolysis experiments of the coal in question is judged to be the most trustworthy but most limited available source. The major drawback of the CPD model is that HCN is the only light gaseous nitrogenous product of the CPD model and thus, factors need to be introduced in order to obtain the desired NH_3 release for the pyrolysis and NO_x mechanisms in the work at hand.

5 Conclusion and Outlook

The main goals of this work were the gathering and analysis of experimental data for the flameless combustion of pulverized coal, the assessment of models used in comprehensive CFD codes with regards to their application to the flameless coal combustion regime, and the attempt to characterize the flameless combustion regime in experiment and simulation by similar methods.

The experiments with two prototype burners for pulverized coal flameless combustion revealed strong differences to a conventional flame burner tested in the same furnace and with the same coal. Typical flameless regime characteristics were found, such as lowered reaction intensities exhibiting only 7% of the conventional flame regime, strong internal recirculation, homogenized concentration fields, homogenized heat flux to the walls and milder temperatures. In contrast to the expectations, NO_x emissions were experienced to be as high as for the tested conventional flame burner but with better coal burnout for the flameless burner. From the conducted measurements, a detailed data set has been extracted for CFD validation activities.

It is noted from the experimental point of view that the application of non-intrusive measurement techniques such as LDV is highly recommendable, since the experimental bias can be strongly reduced or even completely avoided. Intrusive measurement techniques such as suction pyrometry or in-furnace gas concentration measurements induce a disturbance of the flow field and additionally cause a volumetric averaging of the actual value. However, this can be respected in the analysis and more importantly in the comparison of computed and measured results. As simulation accuracy, i.e. its spatial and temporal resolution, increases, this will become of even higher importance.

The testing of two prototype burners designed for flameless pulverized coal combustion disclosed that a high dilution of the coal-carrier-gas jet is necessary for NO abatement. Whilst in the case of the first prototype burner, the dilution is achieved by the use of CO_2 as a carrier gas, it is realized with constructive measures in the case of the second prototype burner. The latter features two coal nozzles placed on top of the recirculation zone induced by the combustion-air jets. As the coal emerges through annulus-shaped nozzles directly into the recirculated hot and low-oxygen flue gas, it gets rapidly heated and devolatilized in an almost inert atmosphere, ensuring enough time before oxidation starts. The oxidation start can be estimated from the prior-to-mixing-length L_v , defining the mixing point of coal and combustion-air jets. The recirculation rate K_v necessary to establish flameless combustion must be achieved before that mixing point, i.e. for $L \leq L_v$, with L denoting the distance to the burner. Thus,

knowing the prior-to-mixing-length L_v from equation (1.12) and the profile of K_v e.g. from a CFD simulation, one can estimate whether flameless combustion is achieved or not.

Whilst the second prototype burner in the favored PT2_{CCG,max} configuration exhibits a larger prior-to-mixing-length L_v than the first prototype burner, both burner prototypes are characterized by a recirculation rate of approximately 340%. After the experimental investigation of the second prototype burner, it was understood that this similarity might be the reason for the similar results of PT1 and PT2 burners. It can be concluded that the observed recirculation rate is too close to the flameless combustion regime limit which is postulated at approximately 300% [176]. Thus, it does not allow for full flameless combustion of pulverized coal, since in both experimental campaigns flame-like structures have been observed.

O₂ availability shall be controlled in the primary burnout zone. Therefore, an asymmetric nozzle arrangement [82] or air-staging are recommended for further investigations. The effectiveness of air-staging can be also concluded from the good performance of the conventional flame burner.

SO_x emissions were found to be reduced by 25% in flameless combustion. It might be due to the milder temperatures present in flameless combustion regime, causing less char and ash particle sintering. That would result in higher surface area available for the SO₂ reduction via CaO and CaCO₃ which are assumed being reactive species present in the ash. However, this hypothesis has not been proven in the work at hand, leaving an open question for future research.

The investigation of the flow field with regards to different turbulence models emphasized the RNG k - ε turbulence model as most suitable for the considered cases. This is somewhat in contrast to the findings by other authors, who are in favor of the realizable k - ε or the standard k - ε model with modified coefficients. Even if generally good agreement is reported for computed and measured velocities, the computational model was not able to reproduce the near-burner aerodynamics satisfactorily. The predicted mixing of hot flue gases and freshly impinging reactants is too weak, resulting in under-prediction of temperatures and over-prediction of local O₂ concentration.

The evaluation of different parameter settings for the turbulence-chemistry interaction model EDC disclosed that the parameter set with the EDC exponent $\kappa_{EDC} = 3$ as originally proposed [52] gives the best agreement of measurement and computed results. Any modification of the model constants influencing the fine structure residence time or mass fraction was not found to be advantageous.

The use of a detailed devolatilization model respecting formation and conversion of tar is highly recommended. It improves the prediction of temperature and O₂ trends, since the presence of tar implies less light volatiles, i.e. methane. Tar release and its onward reactions are much slower than those of methane, thus the reaction intensity in the burner vicinity is decreased when tar is taken into account. The formation of soot has been neglected on the

basis of Kim's [74] results. The CPD pyrolysis model is used in this work to determine the distribution of pyrolysis products, i.e. methane, tar and char.

NO_x modeling has been found to be challenging, due to the low reliability of the input parameters. Coal nitrogen split into light gas-N fractions HCN and NH₃, tar-N and char-N has to be determined prior to the simulation. The CPD pyrolysis model delivers an acceptable coal-N split, depending on the assumed pyrolysis final temperatures and the actual heating rate. Further conversion paths of tar-N and char-N need to be defined on the basis of literature or experience. It has been found that the choice of the char-N release path depends on the chosen NO_x model, and strongly influences the final nitrogenous species concentrations. Furthermore, the HCN oxidation reaction and the heterogeneous NO-char reaction have been modified on the basis of Zhang et al. [186]. Eventually, application of all these findings results in an acceptable agreement of computed and measured nitrogenous species. Trends of nitrogenous species development due to burner modifications can be anticipated with the model at its current state.

Further research is needed in the field of the initial coal-N split. As it has been shown, this split highly influences the NO_x model performance. Therefore, an initial coal-N split model should be capable for determining the split into light gas-N, tar-N and char-N, as the CPD model partially does. Additionally, the prediction of the release paths of char-N would be desirable. The latter has been found to be crucial. Thirdly, efforts should be made to correctly reproduce the near-burner flow field in flameless combustion, as it strongly influences the pyrolysis and prevalent atmosphere and subsequently influences the downstream reactions.

From the modeling part of this work, it is concluded that the grid development must be seen as a key parameter. Not only spatial resolution and thus the reproduction of small scale effects depend on the chosen grid, but also the convergence of the solution. Sufficient grid refinement ensures the application of under-relaxation factors close to 1 which should be striven for. Under-relaxation factors for flow field and chemical subsystem variables are given according to the experiences made and on the basis of literature recommendations.

Finally, it is believed that flameless combustion of pulverized coal can reach similarly good performance as it is known from gaseous fuels. Therefore, the atmosphere during coal devolatilization and primary burnout needs to be controlled. Future application of flameless pulverized coal combustion in oxy-fuel furnaces is thought to be advantageous due to the homogenized temperatures, heat flux and the strong dilution of the oxidant prior to mixing with the coal. The homogenized temperatures and heat flux are anticipated to be of major advantage in oxy-fuel combustion systems, since the temperature depends on the amount of externally recirculated flue gas. The lower the recirculation rate is, the higher is the efficiency of the process [138]. Consequently, achieving higher overall temperatures in conventional and oxy-fuel combustion furnaces by the application of flameless combustion could be one piece of a puzzle in raising the efficiency and the pursued decarbonization of power generation. Direct

O₂ injection at high velocities can be conceived to attain sufficient mixing with recirculated inert flue gases without exposing furnace walls and heat exchangers to very high temperatures, known from state-of-the-art oxy-fuel combustion. First tests have been conducted in the course of the FLOX-COAL-II project [165].

Bibliography

- [1] A. Al-Saffar, E. Bellevrat, P. Benoit, S. Bouckaert, P. Cazzola, H. Daly, O. Durand-Lasserve, M. Gray, S. Holm, P. Janoska, F. Kesicki, C. Pavarini, K. Petrosyan, J. Teter, J. Trüby, D. Wilkinson, and S. Zhang. Energy and Air Pollution: World Energy Outlook Special Report, 2016.
- [2] A. Alysandratou. *Model based prediction of NO_x-precursors evolved from fuel-N during pyrolysis of pulverized coal*. Student Research Project, University of Stuttgart, Stuttgart, 2015.
- [3] J. Aminian, C. Galletti, S. Shahhosseini, and L. Tognotti. Key modeling issues in prediction of minor species in diluted-preheated combustion conditions. *Appl. Therm. Eng.*, 31(16):3287–3300, 2011.
- [4] J. Aminian, C. Galletti, S. Shahhosseini, and L. Tognotti. Numerical Investigation of a MILD Combustion Burner: Analysis of Mixing Field, Chemical Kinetics and Turbulence-Chemistry Interaction. *Flow Turbul. Combust.*, 88(4):597–623, 2012.
- [5] M. N. Anany. *Numerical Modelling of Combustion Processes at Elevated Pressures*. Dissertation, University of Stuttgart. Berichte aus der Energietechnik. Shaker, Aachen, 2010.
- [6] M. N. Anany, U. Schnell, and G. Scheffknecht. Implementation of a smoothing pressure correction approach to the pressure-correction equation in order to maintain the use of SIMPLEC algorithms on non-staggered grids. *Progr. Comp. Fluid Dyn. Int. J.*, 10(1):40, 2010.
- [7] S. A. Arastoo. *Einfluss der Reaktionsmodellierung bei der flammlosen Verbrennung von Kohlenstaub*. Student Research Project, University of Stuttgart, Stuttgart, 2014.
- [8] I. O. Awosope and F. C. Lockwood. Prediction of Combustion and NO_x Emission Characteristics of Flameless Oxidation Combustion. *IFRF Combust. J.*, 2005.
- [9] M. Ayoub, C. Rottier, S. Carpentier, C. Villermaux, A. M. Boukhalfa, and D. Honoré. An experimental study of mild flameless combustion of methane/hydrogen mixtures. *Int. J. Hydrogen Energy*, 37(8):6912–6921, 2012.

- [10] H. D. Baehr and S. Kabelac. *Thermodynamik*. Springer Verlag, Berlin, Heidelberg, 2012.
- [11] L. L. Baxter, R. E. Mitchell, T. H. Fletcher, and R. H. Hurt. Nitrogen Release during Coal Combustion. *Energy Fuels*, 10(1):188–196, 1996.
- [12] R. B. Bird, W. E. Stewart, and E. N. Lightfoot. *Transport phenomena*. Wiley, New York, 2007.
- [13] D. W. Blair, J. O. L. Wendt, and W. Bartok. Evolution of nitrogen and other species during controlled pyrolysis of coal. *Symp. (Int.) Combust.*, 16(1):475–489, 1977.
- [14] F. Breussin, N. Lallemand, and R. Weber. Computing of Oxy-Natural Gas Flames using Both a Global Combustion Scheme and a Chemical Equilibrium Procedure. *Combust. Sci. Technol.*, 160(1):369–397, 2000.
- [15] J. Brix, P. A. Jensen, and A. D. Jensen. Coal devolatilization and char conversion under suspension fired conditions in O₂/N₂ and O₂/CO₂ atmospheres. *Fuel*, 89(11):3373–3380, 2010.
- [16] L. S. Caretto, A. D. Gosman, S. V. Patankar, and D. B. Spalding. Two calculation procedures for steady, three-dimensional flows with recirculation. In *Proc. Third Int. Conf. Numer. Methods Fluid Mech.*, volume 19 of *Lecture Notes in Physics*, pages 60–68. Springer Verlag, Berlin, Heidelberg, 1973.
- [17] A. Cavaliere and M. de Joannon. Mild Combustion. *Prog. Energy Combust. Sci.*, 30(4):329–366, 2004.
- [18] A. Cavigiolo, M. A. Galbiati, A. Effuggi, D. Gelosa, and R. Rota. Mild combustion in a laboratory-scale apparatus. *Combust. Sci. Technol.*, 175(8):1347–1367, 2003.
- [19] J. C. Chen and S. Niksa. Coal devolatilization during rapid transient heating. 1. Primary devolatilization. *Energy Fuels*, 6(3):254–264, 1992.
- [20] J. C. Chen, C. Castagnoli, and S. Niksa. Coal devolatilization during rapid transient heating. 2. Secondary pyrolysis. *Energy Fuels*, 6(3):264–271, 1992.
- [21] S. L. Chen, M. P. Heap, D. W. Pershing, and G. B. Martin. Fate of coal nitrogen during combustion. *Fuel*, 61(12):1218–1224, 1982.
- [22] S. L. Chen, M. P. Heap, D. W. Pershing, and G. B. Martin. Influence of coal composition on the fate of volatile and char nitrogen during combustion. *Symp. (Int.) Combust.*, 19(1):1271–1280, 1982.

- [23] W. Chen, L. D. Smoot, S. C. Hill, and T. H. Fletcher. Global Rate Expression for Nitric Oxide Reburning. Part 2. *Energy Fuels*, 10(5):1046–1052, 1996.
- [24] J. Cheng, J. Zhou, J. Liu, Z. Zhou, Z. Huang, X. Cao, X. Zhao, and K. Cen. Sulfur removal at high temperature during coal combustion in furnaces: A review. *Prog. Energy Combust. Sci.*, 29(5):381–405, 2003.
- [25] G.-M. Choi and M. Katsuki. Advanced low NO_x combustion using highly preheated air. *Energy Conv. Manage.*, 42(5):639–652, 2001.
- [26] F. C. Christo and B. B. Dally. Modeling turbulent reacting jets issuing into a hot and diluted coflow. *Combust. Flame*, 142(1-2):117–129, 2005.
- [27] J.-M. Commandré, B. Stanmore, and S. Salvador. The high temperature reaction of carbon with nitric oxide. *Combust. Flame*, 128(3):211–216, 2002.
- [28] G. Coraggio and M. Laiola. Combustion of NG and pulverized coal in a mixture of oxygen and RFG. *IFRF Doc. F110/y/01*, Livorno, 2009.
- [29] B. B. Dally, A. N. Karpetsis, and R. S. Barlow. Structure of turbulent non-premixed jet flames in a diluted hot coflow. *Proc. Combust. Inst.*, 29(1):1147–1154, 2002.
- [30] B. B. Dally, E. Riesmeier, and N. Peters. Effect of fuel mixture on moderate and intense low oxygen dilution combustion. *Combust. Flame*, 137(4):418–431, 2004.
- [31] A. W. Date. Complete pressure correction algorithm for solution of incompressible Navier-Stokes equations on a non-staggered grid. *Numer. Heat Tr. Part B: Fundamentals*, 29(4):441–458, 1996.
- [32] A. De, E. Oldenhof, P. Sathiah, and D. Roekaerts. Numerical Simulation of Delft-Jet-in-Hot-Coflow (DJHC) Flames Using the Eddy Dissipation Concept Model for Turbulence-Chemistry Interaction. *Flow Turbul. Combust.*, 87(4):537–567, 2011.
- [33] G. G. de Soete. Overall reaction rates of NO and N₂ formation from fuel nitrogen. *Symp. (Int.) Combust.*, 15(1):1093–1102, 1975.
- [34] B. Eck. *Technische Strömungslehre*. Springer Verlag, Berlin, Heidelberg, 1966.
- [35] J. Erfurth. *Radiative heat transfer in coal-fired furnaces and oxycoal retrofit considerations*. Berichte aus der Energietechnik. Shaker, Aachen, 2012.
- [36] C. P. Fenimore. Formation of Nitric Oxide in Premixed Hydrocarbon Flames. *Proc. Combust. Inst.*, 13:373–380, 1970.

- [37] J. H. Ferziger and M. Perić. *Computational Methods for Fluid Dynamics*. Springer Verlag, Berlin, Heidelberg, 2002.
- [38] M. A. Field, D. W. Gill, B. B. Morgan, and P. Hawksley. *Combustion of pulverised coal*. Leatherhead, 1967.
- [39] T. H. Fletcher, A. R. Kerstein, R. J. Pugmire, and D. M. Grant. Chemical percolation model for devolatilization. 2. Temperature and heating rate effects on product yields. *Energy Fuels*, 4(1):54–60, 1990.
- [40] T. H. Fletcher, A. R. Kerstein, R. J. Pugmire, M. S. Solum, and D. M. Grant. Chemical percolation model for devolatilization. 3. Direct use of carbon-13 NMR data to predict effects of coal type. *Energy Fuels*, 6(4):414–431, 1992.
- [41] D. Förtsch. *A kinetic model of pulverised coal combustion for computational fluid dynamics*. Dissertation, University of Stuttgart. Fortschritt-Berichte VDI, Reihe 6: Energietechnik, Nr. 415. VDI Verlag, Düsseldorf, 2003.
- [42] D. Förtsch, F. Kluger, U. Schnell, H. Spliethoff, and K. R. G. Hein. A kinetic model for the prediction of NO emissions from staged combustion of pulverized coal. *Symp. (Int.) Combust.*, 27(2):3037–3044, 1998.
- [43] N. Fricker. How do I measure thermal radiation with an ellipsoidal radiometer?, Combustion file No. 136. *IFRF Online Combustion Handbook C76/y/1/3*.
- [44] N. Fricker. How do I measure total heat transfer with a heat flux meter?, Combustion file No. 138. *IFRF Online Combustion Handbook C76/y/1/6*.
- [45] M. Fürst. *Flow Field Investigations for the CFD-Simulation of Combustion Processes at High Velocities*. Master Thesis, University of Stuttgart, Stuttgart, 2014.
- [46] M. A. Galbiati, A. Cavigiolo, A. Effuggi, D. Gelosa, and R. Rota. MILD Combustion for Fuel-NO_x Reduction. *Combust. Sci. Technol.*, 176(7):1035–1054, 2004.
- [47] C. Galletti, A. Parente, and L. Tognotti. Numerical and experimental investigation of a MILD combustion burner. *Combust. Flame*, 151(4):649–664, 2007.
- [48] D. Genetti, T. H. Fletcher, and R. J. Pugmire. Development and Application of a Correlation of 13 C NMR Chemical Structural Analyses of Coal Based on Elemental Composition and Volatile Matter Content. *Energy Fuels*, 13(1):60–68, 1999.
- [49] P. Gerlinger. *Numerische Verbrennungssimulation: Effiziente numerische Simulation turbulenter Verbrennung*. Springer Verlag, Berlin, Heidelberg, 2005.

- [50] P. Glarborg, A. D. Jensen, and J. E. Johnsson. Fuel nitrogen conversion in solid fuel fired systems. *Prog. Energy Combust. Sci.*, 29(2):89–113, 2003.
- [51] B. Gövert, H. D. Haustein, D. Christ, O. Hatzfeld, and R. Kneer. Reaktionsratenmessung von Steinkohlenkoks in N₂/O₂- und CO₂/O₂-Atmosphäre mittels eines Wirbelschichtreaktors. In *26. Dt. Flammentag: Verbr. Feuer.*, VDI-Berichte 2161. VDI Verlag, Düsseldorf, 2013.
- [52] I. R. Gran and B. F. Magnussen. A Numerical Study of a Bluff-Body Stabilized Diffusion Flame. Part 2. Influence of Combustion Modeling And Finite-Rate Chemistry. *Combust. Sci. Technol.*, 119(1-6):191–217, 1996.
- [53] D. M. Grant, R. J. Pugmire, T. H. Fletcher, and A. R. Kerstein. Chemical model of coal devolatilization using percolation lattice statistics. *Energy Fuels*, 3(2):175–186, 1989.
- [54] S. Grathwohl, O. Lemp, U. Schnell, J. Maier, G. Scheffknecht, F. Kluger, B. Krohmer, P. Mönckert, and G.-N. Stamatelopoulos. Highly Flexible Burner Concept for Oxyfuel Combustion. In *Proc. 1st Oxyfuel Combust. Conf.*, 2009.
- [55] T. Gronarz, M. Habermehl, R. Kneer, M. Weidmann, D. Kurz, and G. Scheffknecht. Numerische Simulation der Stickoxidbildung bei der flammlosen Verbrennung von Kohle. In *26. Dt. Flammentag: Verbr. Feuer.*, VDI-Berichte 2161. VDI Verlag, Düsseldorf, 2013.
- [56] A. K. Gupta. Flame characteristics and challenges with High Temperature Air Combustion. In *Proc. 2000 Int. Joint Power Gen. Conf.*, 2000.
- [57] M. Habermehl. Report on reduced NO_x sub-model, Deliverable 3.2. *Research Fund for Coal and Steel*, 2012.
- [58] M. Hallaji and K. Mazaheri. Comparison of LES and RANS in numerical simulation of turbulent non-premixed flame under MILD combustion condition. In *Proc. Medit. Combust. Symp. 7*, 2011.
- [59] E. Hambly. *The Chemical Structure of Coal Tar and Char During Devolatilization*. Master Thesis, Brigham Young University, Provo, 1998.
- [60] D. J. Hautman, F. L. Dryer, K. P. Schug, and I. Glassmann. A Multiple-step Overall Kinetic Mechanism for the Oxidation of Hydrocarbons. *Combust. Sci. Technol.*, 25: 219–235, 1981.
- [61] P. Heil, D. Christ, D. Toporov, M. Förster, and R. Kneer. Investigations of a Burner for Flameless combustion in CO₂/O₂ Atmosphere. In *Proc. 8th Eur. Conf. Ind. Furnaces Boilers*, 2008.

- [62] M. V. Heitor and A. Moreira. Thermocouples and sample probes for combustion studies. *Prog. Energy Combust. Sci.*, 19(3):259–278, 1993.
- [63] K. H. Hemsath. *Zur Berechnung der Flammenstrahlung: ein Vergleich von gemessener und aus örtlichen Temperaturen und Staubkonzentrationen berechneter Strahlung*. Dissertation, University of Stuttgart, Stuttgart, 1970.
- [64] S. C. Hill and L. Douglas Smoot. Modeling of nitrogen oxides formation and destruction in combustion systems. *Prog. Energy Combust. Sci.*, 26(4-6):417–458, 2000.
- [65] D. Honoré. Advanced measurements in industrial combustion systems. In L. Vervisch, D. Veynante, and J. van Beeck, editors, *Turbulent Combustion*. von Karman Institute for Fluid Dynamics, Sint-Genesius-Rode, 2007.
- [66] H. C. Hottel and A. F. Sarofim. *Radiative transfer*. McGraw-Hill series in mechanical engineering. McGraw-Hill New York, New York, 1967.
- [67] J. B. Howard, G. C. Williams, and D. H. Fine. Kinetics of carbon monoxide oxidation in postflame gases. *Symp. (Int.) Combust.*, 14(1):975–986, 1973.
- [68] T. Ishiguro, S. Tsuge, T. Furuhashi, K. Kitagawa, N. Arai, T. Hasegawa, R. Tanaka, and A. K. Gupta. Homogenization and stabilization during combustion of hydrocarbons with preheated air. *Symp. (Int.) Combust.*, 27(2):3205–3213, 1998.
- [69] F. Joos. *Technische Verbrennung: Verbrennungstechnik, Verbrennungsmodellierung, Emissionen*. Springer Verlag, Berlin, Heidelberg, 2006.
- [70] J. H. Joseph, W. J. Wiscombe, and J. A. Weinman. The Delta-Eddington Approximation for Radiative Flux Transfer. *J. Atmos. Sci.*, 33(12):2452–2459, 1976.
- [71] S. Kambara, T. Takarada, Y. Yamamoto, and K. Kato. Relation between functional forms of coal nitrogen and formation of nitrogen oxide (NO_x) precursors during rapid pyrolysis. *Energy Fuels*, 7(6):1013–1020, 1993.
- [72] M. Katsuki and T. Hasegawa. The science and technology of combustion in highly preheated air. *Symp. (Int.) Combust.*, 27(2):3135–3146, 1998.
- [73] D. Kim, S. Choi, C. R. Shaddix, and M. Geier. Effect of CO₂ gasification reaction on char particle combustion in oxy-fuel conditions. *Fuel*, 120:130–140, 2014.
- [74] J. P. Kim. *Numerical Modeling of MILD Combustion*. Dissertation, University of Stuttgart. Berichte aus der Energietechnik. Shaker, Aachen, 2008.

- [75] S. Kumar, P. J. Paul, and H. S. Mukunda. Studies on a new high-intensity low-emission burner. *Proc. Combust. Inst.*, 29(1):1131–1137, 2002.
- [76] D. Kurz. *Numerische Simulation industrieller Rostfeuerungen nach der Euler-Euler Methode*. Dissertation, University of Stuttgart. Berichte aus der Energietechnik. Shaker, Aachen, 2014.
- [77] J. Larsson. Favre averaged Navier-Stokes equations, 2005. URL http://www.cfd-online.com/Wiki/Favre_averaged_Navier-Stokes_equations. visited: July 26 2107
- [78] B. E. Launder and D. B. Spalding. The numerical computation of turbulent flows. *Comp. Methods Appl. Mech. Eng.*, 3(2):269–289, 1974.
- [79] E. Laurien and H. Oertel jr. *Numerische Strömungsmechanik: Grundgleichungen und Modelle - Lösungsmethoden - Qualität und Genauigkeit*. Springer Fachmedien, Wiesbaden, 2013.
- [80] S. Leiser. *Numerical simulation of oxy-fuel combustion*. Dissertation, University of Stuttgart. Berichte aus der Energietechnik. Shaker, Aachen, 2011.
- [81] J. M. Levy, L. K. Chan, A. F. Sarofim, and J. M. Beér. NO/Char reactions at pulverized coal flame conditions. *Symp. (Int.) Combust.*, 18:111–120, 1980.
- [82] P. Li, F. Wang, Y. Tu, Z. Mei, J. Zhang, Y. Zheng, H. Liu, Z. Liu, J. Mi, and C. Zheng. Moderate or Intense Low-Oxygen Dilution Oxy-combustion Characteristics of Light Oil and Pulverized Coal in a Pilot-Scale Furnace. *Energy Fuels*, 28(2):1524–1535, 2014.
- [83] C. Locci. *Large Eddy Simulations Modelling of Flameless Combustion: Modellierung von flammenloser Verbrennung in Large Eddy Simulationen*. Dissertation, BTU Cottbus-Senftenberg, Cottbus, 2014.
- [84] H.-C. Magel. *Simulation chemischer Reaktionskinetik in turbulenten Flammen mit detaillierten und globalen Mechanismen*. Dissertation, University of Stuttgart. Fortschritt-Berichte VDI, Reihe 6: Energietechnik, Nr. 377. VDI Verlag, Düsseldorf, 1997.
- [85] B. F. Magnussen and B. H. Hjertager. On mathematical modeling of turbulent combustion with special emphasis on soot formation and combustion. *Symp. (Int.) Combust.*, 16:719–729, 1977.
- [86] M. Mancini, R. Weber, and U. Bollettini. Predicting NO_x emissions of a burner operated in flameless oxidation mode. *Proc. Combust. Inst.*, 29(1):1155–1163, 2002.

- [87] M. Mancini, P. Schwöppe, R. Weber, and S. Orsino. On mathematical modelling of flameless combustion. *Combust. Flame*, 150(1-2):54–59, 2007.
- [88] E. Masson, S. Maurel, L. Porcheron, F. Aguilé, P. Meunier, A. Quinqueneau, D. Honoré, and A. M. Boukhalfa. An experimental characterization of flameless combustion at semi-industrial scale. In *14th IFRF Members Conf.*, 2004.
- [89] Z. Mei, P. Li, F. Wang, J. Zhang, and J. Mi. Influences of Reactant Injection Velocities on Moderate or Intense Low-Oxygen Dilution Coal Combustion. *Energy Fuels*, 28(1):369–384, 2014.
- [90] Z. Mei, P. Li, J. Mi, F. Wang, and J. Zhang. Diffusion MILD Combustion of Firing Pulverized-coal at a Pilot Furnace. *Flow Turbul. Combust.*, 95(4):803–829, 2015.
- [91] J. Mi, P. Li, B. B. Dally, and R. A. Craig. Importance of Initial Momentum Rate and Air-Fuel Premixing on Moderate or Intense Low Oxygen Dilution (MILD) Combustion in a Recuperative Furnace. *Energy Fuels*, 23(11):5349–5356, 2009.
- [92] J. Mi, P. Li, and C. Zheng. Impact of injection conditions on flame characteristics from a parallel multi-jet burner. *Energy J.*, 36(11):6583–6595, 2011.
- [93] A. Milani and A. Saponaro. Diluted Combustion Technologies. *IFRF Combust. J.*, 2001.
- [94] Y. Minamoto and N. Swaminathan. Modelling paradigms for MILD combustion. *Int. J. Adv. Eng. Sci. Appl. Math.*, 6(1-2):65–75, 2014.
- [95] J. W. Mitchell and J. M. Tarbell. A Kinetic Model of Nitric Oxide Formation During Pulverized Coal Combustion. *Am. Inst. Chem. Eng. J.*, 28:302–311, 1982.
- [96] A. P. Morse. *Axisymmetric turbulent shear flows with and without swirl*. Dissertation, University of London, London, 1977.
- [97] M. Müller. *Modelling and Simulation of SO_x and NO_x Formation under Oxy-Coal Combustion Conditions*. Dissertation, University of Stuttgart. Berichte aus der Energietechnik. Shaker, Aachen, 2015.
- [98] A. Nicolle and P. Dagaut. Occurrence of NO-reburning in MILD combustion evidenced via chemical kinetic modeling. *Fuel*, 85(17–18):2469–2478, 2006.
- [99] B. Noll. Evaluation of a bounded high-resolution scheme for combustor flow computations. *AIAA J.*, 30(1):64–69, 1992.
- [100] S. Orsino, M. Tamura, P. Stabat, S. Constantini, O. Prado, and R. Weber. Excess Enthalpy Combustion of Coal. *IFRF Doc. F46/y/3*, IJmuiden, 2000.

- [101] H. Oryani, S. Khalilarya, S. Jafarmadar, H. Khatamnezhad, and S. Majidyfar. Numerical Investigation of Influence of Dilution in Air and Fuel Sides on MILD Combustion Burner. *Aust. J. Basic Appl. Sci.*, 5(10):272–279, 2011.
- [102] A. Parente, G. Coraggio, C. Galletti, and L. Tognotti. Verification, validation and uncertainty quantification in industrial combustion modelling: some practical tools. *IFRF Doc. G25/y/01*, Livorno, 2010.
- [103] D.-C. Park, S. J. Day, and P. F. Nelson. Nitrogen release during reaction of coal char with O₂, CO₂, and H₂O. *Proc. Combust. Inst.*, 30(2):2169–2175, 2005.
- [104] S. V. Patankar. *Numerical heat transfer and fluid flow*. Series in computational methods in mechanics and thermal sciences. Hemisphere Pub. Corp. and McGraw-Hill New York, Washington, 1980.
- [105] M. Perić. *A Finite Volume Method for the Prediction of Three-Dimensional Fluid Flow in Complex Ducts*. PhD Thesis, Imperial College of Science and Technology, London, 1985.
- [106] D. W. Pershing and J. O. L. Wendt. Relative Contributions of Volatile Nitrogen and Char Nitrogen to NO_x Emissions from Pulverized Coal Flames. *Ind. Eng. Chem. Proc. Des. Dev.*, 18(1):60–67, 1979.
- [107] N. Peters. Laminar flamelet concepts in turbulent combustion. *Symp. (Int.) Combust.*, 21(1):1231–1250, 1988.
- [108] T. Plessing, N. Peters, and J. G. Wüning. Laseroptical investigation of highly preheated combustion with strong exhaust gas recirculation. *Symp. (Int.) Combust.*, 27(2):3197–3204, 1998.
- [109] J. Pohl and A. F. Sarofim. Devolatilization and oxidation of coal nitrogen. *Proc. Combust. Inst.*, 16:491–501, 1976.
- [110] S. B. Pope. An explanation of the turbulent round-jet/plane-jet anomaly. *AIAA J.*, 16(3):279–281, 1978.
- [111] H. S. Price, R. S. Varga, and J. E. Warren. Application of Oscillation Matrices to Diffusion-Convection Equations. *J. Math. Phys.*, 45(1-4):301–311, 1966.
- [112] A. Ribeirete and M. Costa. Impact of the air staging on the performance of a pulverized coal fired furnace. *Proc. Combust. Inst.*, 32(2):2667–2673, 2009.

- [113] B. Risio. *Effizienz und Verlässlichkeit numerischer Vorhersagen zur rechnergestützten Optimierung von Grosskraftwerksbrennkammern*. Dissertation, University of Stuttgart. Fortschritt-Berichte VDI, Reihe 6: Energietechnik, Nr. 471. VDI Verlag, Düsseldorf, 2001.
- [114] D. Ristic. *Development of a pilot-scale flameless oxidation burner for ultra-low NO_x combustion of pulverised coal*, volume 24188 of *EUR Research Fund for Coal and Steel series*. Publ. Office EU, Luxemburg, 2010.
- [115] D. Ristic. *Feasibility and NO_x reduction potential of flameless oxidation in pulverised coal combustion*. Dissertation, University of Stuttgart. Cuvillier, Stuttgart, 2012.
- [116] D. Ristic, R. Berger, G. Scheffknecht, C. Lacour, D. Honoré, and J. G. Wüning. Experimental study on flameless combustion of pulverised coal under air staging conditions. In *15th IFRF Members Conf.*, 2007.
- [117] D. Ristic, M. Schneider, A. Schuster, G. Scheffknecht, and J. G. Wüning. Investigation of NO_x formation for flameless coal combustion. In *Proc. 7th HiTACG Int. Symp.*, 2008.
- [118] D. Ristic, A. Schuster, and G. Scheffknecht. On the Potential of Flameless Oxidation to Reduce NO_x Emissions from Pulverized Coal Combustion. *IFRF Combust. J.*, 2010.
- [119] D. Ristic, M. Zieba, and G. Scheffknecht. Effect of Near Burner Aerodynamics on NO_x Reduction in Pulverised Coal Flameless Oxidation. In *25. Dt. Flammentag: Verbr. Feuer.*, VDI-Bericht 2056. VDI Verlag, Düsseldorf, Germany, 2011.
- [120] C. Rottier, C. Lacour, G. Godard, B. Taupin, L. Porcheron, R. Hauguel, A. M. Boukhalfa, and D. Honoré. On the effect of air temperature on MILD flameless combustion regime of high temperature furnace. In *4th Eur. Combust. Meeting*, 2009.
- [121] M. Saffari Pour and Y. Weihong. Performance of Pulverized Coal Combustion under High Temperature Air Diluted by Steam. *ISRN Mech. Eng.*, 1(2):1–10, 2014.
- [122] M. Saha, B. B. Dally, P. R. Medwell, and E. M. Cleary. Moderate or Intense Low Oxygen Dilution (MILD) Combustion Characteristics of Pulverized Coal in a Self-Recuperative Furnace. *Energy Fuels*, 28(9):6046–6057, 2014.
- [123] N. Schaffel, M. Mancini, A. Szlek, and R. Weber. Mathematical modeling of MILD combustion of pulverized coal. *Combust. Flame*, 156(9):1771–1784, 2009.
- [124] N. Schaffel-Mancini. *Ecological evaluation of the pulverized coal combustion in HTAC technology*. Dissertation, Silesian University of Technology and Clausthal University of Technology, Clausthal, 2009.

- [125] R. Schneider. *Beitrag zur numerischen Berechnung dreidimensional reagierender Strömungen in industriellen Brennkammern*. Dissertation, University of Stuttgart. Fortschritt-Berichte VDI, Reihe 6: Energietechnik, Nr. 385. VDI Verlag, Düsseldorf, 1998.
- [126] U. Schnell. *Berechnung der Stickoxidemissionen von Kohlenstaubfeuerungen*. Dissertation, University of Stuttgart. Fortschritt-Berichte VDI, Reihe 6: Energietechnik, Nr. 250. VDI Verlag, Düsseldorf, 1991.
- [127] U. Schnell. Numerical modelling of solid fuel combustion processes using advanced CFD-based simulation tools. *Progr. Comp. Fluid Dyn. Int. J.*, 1(4):208, 2001.
- [128] D. W. Shaw, X. Zhu, M. K. Misra, and R. H. Essenhigh. Determination of global kinetics of coal volatiles combustion. *Symp. (Int.) Combust.*, 23(1):1155–1162, 1991.
- [129] T.-H. Shih, W. W. Liou, A. Shabbir, Z. Yang, and J. Zhu. A new k - ε eddy viscosity model for high Reynolds number turbulent flows. *Comp. Fluids*, 24(3):227–238, 1995.
- [130] J. P. Smart and G. S. Riley. Combustion of coal in a flameless oxidation environment under oxyfuel firing conditions: the reality. *J. Energy Inst.*, 85(3):131–134, 2012.
- [131] L. D. Smoot and D. T. Pratt. *Pulverized-Coal Combustion and Gasification: Theory and Applications for Continuous Flow Processes*. Springer US, Boston, 1979.
- [132] P. R. Solomon and M. B. Colket. Evolution of fuel nitrogen in coal devolatilization. *Fuel*, 57(12):749–755, 1978.
- [133] P. R. Solomon, D. G. Hamblen, R. M. Carangelo, M. A. Serio, and G. V. Deshpande. General model of coal devolatilization. *Energy Fuels*, 2(4):405–422, 1988.
- [134] D. B. Spalding. Development of the eddy-break-up model of turbulent combustion. *Symp. (Int.) Combust.*, 16(1):1657–1663, 1977.
- [135] J. P. Spinti and D. W. Pershing. The fate of char-N at pulverized coal conditions. *Combust. Flame*, 135(3):299–313, 2003.
- [136] H. Stadler. *Experimental and numerical investigation of flameless pulverised coal combustion*. Dissertation, RWTH Aachen, Aachen, 2010.
- [137] H. Stadler, D. Ristic, M. Förster, A. Schuster, R. Kneer, and G. Scheffknecht. NO_x-emissions from flameless coal combustion in air, Ar/O₂ and CO₂/O₂. *Proc. Combust. Inst.*, 32(2):3131–3138, 2009.

- [138] R. Stanger, T. Wall, R. Spörl, M. Paneru, S. Grathwohl, M. Weidmann, G. Scheffknecht, D. McDonald, K. Myöhänen, J. Ritvanen, S. Rahiala, T. Hyppänen, J. Mletzko, A. Kather, and S. Santos. Oxyfuel combustion for CO₂ capture in power plants. *Int. J. Greenh. Gas Control*, 40:55–125, 2015.
- [139] H. L. Stone. Iterative Solution of Implicit Approximations of Multidimensional Partial Differential Equations. *SIAM J. Numer. Anal.*, 5(3):530–558, 1968.
- [140] J. Ströhle. *Spectral modelling of radiative heat transfer in industrial furnaces*. Dissertation, University of Stuttgart. Berichte aus der Energietechnik. Shaker, Aachen, 2004.
- [141] S. Su, J. Pohl, D. Holcombe, and J. Hart. Techniques to determine ignition, flame stability and burnout of blended coals in p.f. power station boilers. *Prog. Energy Combust. Sci.*, 27(1):75–98, 2001.
- [142] T. Suda, M. Takafuji, T. Hirata, M. Yoshino, and J. Sato. A study of combustion behavior of pulverized coal in high-temperature air. *Proc. Combust. Inst.*, 29(1):503–509, 2002.
- [143] S. Sun, J. Zhang, X. Hu, S. Wu, J. Yang, Y. Wang, and Y. Qin. Studies of NO—Char Reaction Kinetics Obtained from Drop-Tube Furnace and Thermogravimetric Experiments. *Energy Fuels*, 23(1):74–80, 2009.
- [144] Y. Suzukawa, S. Sugiyama, Y. Hino, M. Ishioka, and I. Mori. Heat transfer improvement and NO_x reduction by highly preheated air combustion. *Energy Conv. Manage.*, 38(10–13):1061–1071, 1997.
- [145] G. Szegö, B. B. Dally, and G. Nathan. Scaling of NO_x emissions from a laboratory-scale mild combustion furnace. *Combust. Flame*, 154(1-2):281–295, 2008.
- [146] G. Szegö, B. B. Dally, and G. Nathan. Operational characteristics of a parallel jet MILD combustion burner system. *Combust. Flame*, 156(2):429–438, 2009.
- [147] D. Tabacco, C. Innarella, and C. Bruno. Theoretical and Numerical Investigation on Flameless Combustion. *Combust. Sci. Technol.*, 174(7):1–35, 2002.
- [148] M. Taniguchi, K. Yamamoto, H. Kobayashi, and K. Kiyama. A reduced NO_x reaction model for pulverized coal combustion under fuel-rich conditions. *Fuel*, 81(3):363–371, 2002.
- [149] W. Tollmien. Berechnung turbulenter Ausbreitungsvorgänge. *J. appl. Math. Mech.*, 6:468, 1926.

- [150] H. Tsuji, A. K. Gupta, T. Hasegawa, M. Katsuki, K. Kishimoto, and M. Morita. *High temperature air combustion: From energy conservation to pollution reduction*. Environmental and energy engineering series. CRC Press, Boca Raton, 2003.
- [151] C. M. Tu, H. Davis, and H. C. Hottel. Combustion Rate of Carbon - Combustion of Spheres in Flowing Gas Streams. *Ind. Eng. Chem.*, 26(7):749–757, 1934.
- [152] United Nations. Paris Agreement, 2015.
- [153] J. P. van Doormaal and G. D. Raithby. Enhancement of the SIMPLE method for predicting incompressible fluid flows. *Numer. Heat Transfer*, 7(2):147–163, 1984.
- [154] M. Vascellari and G. Cau. Influence of turbulence-chemical interaction on CFD pulverized coal MILD combustion modeling. *Fuel*, 101:90–101, 2012.
- [155] M. Vascellari, S. Schulze, P. Nikrityuk, D. Safronov, and C. Hasse. Numerical Simulation of Pulverized Coal MILD Combustion Using a New Heterogeneous Combustion Submodel. *Flow Turbul. Combust.*, 92(1-2):319–345, 2014.
- [156] A. L. Verlaan, S. Orsino, N. Lallemand, and R. Weber. Fluid Flow and Mixing in a Furnace Equipped with the Low-NO_x Regenerative Burner of Nippon Furnace Kogyo, *IFRF Doc. No. F 46/y/1*, IJmuiden, 1998.
- [157] A. L. Verlaan, G. D. Vazquez, M. Kösters, N. Lallemand, S. Orsino, and R. Weber. Excess Enthalpy Combustion of Light and Heavy Fuel Oils. Results of High Temperature Air Combustion Trials, *IFRF Doc. No. F 46/y/2*, IJmuiden, 1999.
- [158] J. B. Vos. *The calculation of turbulent reacting flows with a combustion model based on finite chemical kinetics*. PhD Thesis, TU Delft, Delft, 1987.
- [159] J. Warnatz, R. W. Dibble, and U. Maas. *Combustion: Physical and Chemical Fundamentals, Modeling and Simulation, Experiments, Pollutant Formation*. Springer Verlag, Berlin, Heidelberg, 2006.
- [160] R. Weber, S. Orsino, N. Lallemand, and A. L. Verlaan. Combustion of natural gas with high-temperature air and large quantities of flue gas. *Proc. Combust. Inst.*, 28(1): 1315–1321, 2000.
- [161] R. Weber, J. P. Smart, and W. v. Kamp. On the (MILD) combustion of gaseous, liquid, and solid fuels in high temperature preheated air. *Proc. Combust. Inst.*, 30(2):2623–2629, 2005.

- [162] M. Weidmann, V. Verbaere, G. Boutin, D. Honoré, S. Grathwohl, G. Godard, C. Gobin, H. Dieter, R. Kneer, and G. Scheffknecht. Detailed investigation of flameless oxidation of pulverized coal at pilot-scale (230 kWth). In *6th Int. Conf. on Clean Coal Techn.*. IEA Clean Coal Centre, Thessaloniki, 2013.
- [163] M. Weidmann, S. Grathwohl, H. Dieter, V. Verbaere, G. Boutin, C. Gobin, G. Godard, and D. Honoré. Detaillierte experimentelle Untersuchung der flammlosen Oxidation von Kohlenstaub (230 kWth). In *26. Dt. Flammentag: Verbr. Feuer.*, VDI-Berichte 2161. VDI Verlag, Düsseldorf, 2013.
- [164] M. Weidmann, S. Grathwohl, H. Dieter, G. Boutin, D. Honoré, and G. Scheffknecht. Progress in Flameless Pulverized Coal Burner Design (300 kWth) Based on CFD Simulations and Experimental Investigations. In *39th Int. Techn. Conf. on Clean Coal and Fuel Systems*, Clearwater, Florida, 2014.
- [165] M. Weidmann, B. Gövert, M. Habermehl, O. Hatzfeld, P. Plaza, P. Bocian, E. Cresci, J. G. Wünnig, A. Duncan, H. Grüner, D. Honoré, J. Sawicki, and L. Tlalka. *Development of scale-up methodology and simulation tools for the demonstration of PC-FLOX burner technology in full-scale utility boilers*. EUR Research Fund for Coal and Steel series. Publ. Office EU, Luxemburg, 2015.
- [166] M. Weidmann, V. Verbaere, G. Boutin, D. Honoré, S. Grathwohl, G. Godard, C. Gobin, H. Dieter, R. Kneer, and G. Scheffknecht. Detailed investigation of flameless oxidation of pulverized coal at pilot-scale (230 kWth). *Appl. Therm. Eng.*, 74:96–101, 2015.
- [167] M. Weidmann, D. Honoré, V. Verbaere, G. Boutin, S. Grathwohl, G. Godard, C. Gobin, G. Scheffknecht, and R. Kneer. Experimental characterization of pulverized coal MILD flameless combustion from detailed measurements in a pilot-scale facility. *Combust. Flame*, 168:365–377, 2016.
- [168] F. Weinberg. Heat-Recirculating Burners: Principles and Some Recent Developments. *Combust. Sci. Technol.*, 121(1-6):3–22, 1996.
- [169] J. O. L. Wendt. Fundamental coal combustion mechanisms and pollutant formation in furnaces. *Prog. Energy Combust. Sci.*, 6(2):201–222, 1980.
- [170] E. Wicke. Contributions to the combustion mechanism of carbon. *Symp. (Int.) Combust.*, 5(1):245–252, 1955.
- [171] D. C. Wilcox. *Turbulence modeling for CFD*. DCW Industries, La Cañada, 2010.

- [172] B. A. Wills and T. Napier-Munn. *Wills' mineral processing technology: An introduction to the practical aspects of ore treatment and mineral recovery*. Butterworth-Heinemann, Amsterdam, London, 2006.
- [173] J. A. Wüning. Flammenlose Oxidation von Brennstoff mit hochvorgewärmter Luft. *Chem.-Ing.-Tech.*, 63(12):1243–1245, 1991.
- [174] J. A. Wüning and J. G. Wüning. Flameless oxidation to reduce thermal NO-formation. *Prog. Energy Combust. Sci.*, 23(1):81–94, 1997.
- [175] J. G. Wüning. Derivation of diagramm recirculation ratio over temperature. *Personal communication*, 14.12.2015.
- [176] J. G. Wüning. *Flammlose Oxidation von Brennstoff*. Dissertation, RTWH Aachen, Aachen, 1996.
- [177] J. G. Wüning. Flameless Oxidation. In *6th Int. HiTACG Symp.*, Essen, Germany, 2005.
- [178] V. Yakhot and S. A. Orszag. Renormalization-Group Analysis of Turbulence. *Phys. Rev. Lett.*, 57(14):1722–1724, 1986.
- [179] V. Yakhot, S. A. Orszag, S. Thangam, T. B. Gatski, and C. G. Speziale. Development of turbulence models for shear flows by a double expansion technique. *Phys. Fluids A*, 4(7):1510, 1992.
- [180] W. Yang and W. Blasiak. Numerical study of fuel temperature influence on single gas jet combustion in highly preheated and oxygen deficient air. *Energy J.*, 30(2–4):385–398, 2005.
- [181] W. Yang and W. Blasiak. CFD as applied to high temperature air combustion in industrial furnaces. *IFRF Combust. J.*, 2006.
- [182] J. Yuan and I. Naruse. Effects of Air Dilution on Highly Preheated Air Combustion in a Regenerative Furnace. *Energy Fuels*, 13(1):99–104, 1999.
- [183] Y. B. Zeldovich. The Oxidation of Nitrogen in Combustion and Explosions. *Acta Physiochimica URSS*, 21(4):577–628, 1946.
- [184] H. Zhang, G. Yue, J. Lu, Z. Jia, J. Mao, T. Fujimori, T. Suko, and T. Kiga. Development of high temperature air combustion technology in pulverized fossil fuel fired boilers. *Proc. Combust. Inst.*, 31(2):2779–2785, 2007.
- [185] J. Zhang, S. Sun, X. Hu, R. Sun, and Y. Qin. Modeling NO–Char Reaction at High Temperature. *Energy Fuels*, 23(5):2376–2382, 2009.

-
- [186] J. Zhang, T. Ito, T. Okada, E. Oono, and T. Suda. Improvement of NO_x formation model for pulverized coal combustion by increasing oxidation rate of HCN. *Fuel*, 113: 697–706, 2013.
- [187] V. L. Zimont and Y. M. Trushin. Total combustion kinetics of hydrocarbon fuels. *Combust. Explos. Shock Waves*, 5(4):391–394, 1969.

A An Alternative Approach to Derive the Recirculation Rate K_V

A.1 Definition of prior-to-mixing length L_V

The key parameter K_V needs to be derived at the beginning of the reaction zone to ensure the envisaged dilution, as postulated in Section 4.7.2. Any recirculation mass flow downstream of the start of the reaction zone additionally dilutes the reaction zone, but the dilution at its starting point is mainly responsible for its development, i.e. whether flameless or flame-existent combustion is achieved. This has been shown in Chapter 3.

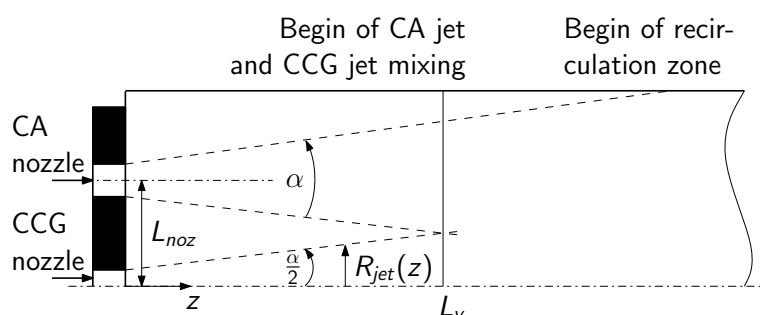


Figure A.1: Concept of prior-to-mixing length L_V

The schematic in Figure A.1 depicts the furnace setup with a flameless burner on the left, equipped with a central coal-carrier-gas (CCG) nozzle and an eccentric combustion-air (CA) nozzle. Accordingly, mixing occurs when the radial jet opening $R_{jet}(z)$ equals half of the distance between the fuel-carrier-gas and combustion-air nozzles, L_{noz} , see equation (A.1). The geometrical length in question is estimated from free jet theory, as is proposed by Wüning [176]. It is called prior-to-mixing length L_V in the following.

$$R_{jet}(L_V) = \frac{1}{2} L_{noz} \quad (\text{A.1})$$

Prior-to-mixing length L_v is then calculated according to equation (A.2).

$$L_v = \frac{R_{jet}(L_v)}{\tan\left(\frac{\alpha}{2}\right)} = \frac{L_{noz}}{2 \tan\left(\frac{\alpha}{2}\right)} \quad (\text{A.2})$$

The turbulent free jet sucks fluid from its surrounding, as it impinges into the furnace. Its spreading angle has been experimentally determined between 20° and 24° [34], and it has been theoretically calculated by Tollmien [149] as 23.8° . As the turbulent free jet spreads, a clear boundary to the surrounding medium is often not distinguishable because of the turbulent entrainment. A smaller spreading angle can be taken for technical applications which accounts for a clear distinction between entrained mass and static fluid. The value of the jet velocity declines from the core to the boundary in the form of a bell-shaped curve over the jet radius. There is a common assumption that the distinguishable boundary of the jet is at that radial position where its velocity is 1 % of its core velocity. This corresponds to a jet opening angle α of 19° Wüning [176] and leads to the final approximation of the prior-to-mixing length L_v , as is shown in equation (A.3).

$$L_v \approx 2.99 L_{noz} \quad (\text{A.3})$$

A.2 Definition of recirculation rate K_v

One disadvantage exists for the characterization by the internal recirculation rate K_v , as is defined in equation (1.10) and reproduced in equation (A.4): it demands the knowledge of the mass flow \dot{M}_{rec} recirculating to the burner. This limits its applicability to computed results or to LDV results from very dense grid measurements.

$$K_v = \frac{\dot{M}_{rec}}{\dot{M}_{CCG} + \dot{M}_{CA} + \dot{M}_f} \quad (\text{A.4})$$

A different approach to determine the recirculation rate K_v was proposed by Cavigiolo et al. [18] and can be used to overcome this issue. They linked the recirculation rate K_v to the O_2 concentration in the reactive jet $x_{O_2,RJ}$ by means of a recycle factor. The recycle factor depends on the furnace and burner geometry, and is found constant for a certain setup [18]. The idea for linking the recirculation rate K_v to the O_2 concentration in the reactive jet $x_{O_2,RJ}$ is used in the following to derive another determination of K_v . The recirculation rate K_v is defined as a mass flow ratio between the recirculation mass flow and the sum of mass flows entering the furnace. Thus, it indicates the dilution of the entering mass flows. The degree of dilution can be expressed by the diminishing O_2 concentration in the reactive jet $x_{O_2,recirc}(z)$. Reduction of O_2 concentration is assumed only to be due to admixture and dilution, before reactions start.

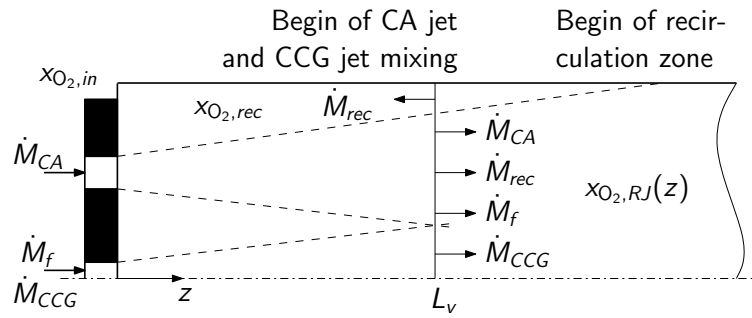


Figure A.2: Concept of reactive jet mixing

The start of reactions is defined by the location where fuel-carrier-gas and combustion-air jets start mixing. The length between burner exit and mixing point is called prior-to-mixing length L_v , as detailed in Section A.1.

The schematic in Figure A.2 shows the relevant mass flows and O_2 concentrations to derive K_v . Therein, a furnace detail is shown with the burner on the left and the entering jets spreading in an 19° angle. The entering mass flows \dot{M}_{CCG} and \dot{M}_{CA} are characterized by the O_2 concentration $x_{O_2,in}$ which is usually that of air. Additional entering fuel mass flow \dot{M}_f commonly does not contain significant O_2 . It is therefore neglected. Where the fuel-carrier-gas and the combustion-air jets start mixing at $z = L_v$, the mass flow in the negative z -direction is taken as the relevant recirculation mass flow \dot{M}_{rec} , caused by the momentum of the impinging fresh reactant jets. The recirculation mass flow can inherit some O_2 , but it is assumed that no reactions take place, and thus, $x_{O_2,recirc}$ is maintained. On the other hand, the fuel carrier-gas mass flow, the combustion-air mass flow and the fuel mass flow jointly with the recirculation mass flow move downstream in the reactive jet with the O_2 concentration $x_{O_2,RJ}(L_v)$. The O_2 concentration in the reactive jet at $z = L_v$ is now derived as follows in equation (A.5).

$$x_{O_2,RJ} = \frac{x_{O_2,in} \cdot (\dot{M}_{CCG} + \dot{M}_{CA}) + x_{O_2,recirc} \cdot \dot{M}_{rec}}{\dot{M}_{CCG} + \dot{M}_f + \dot{M}_{CA} + \dot{M}_{rec}} \quad (A.5)$$

Equation (A.5) is used to determine the recirculation mass flow \dot{M}_{rec} , see equation (A.6).

$$\dot{M}_{rec} = \frac{x_{O_2,in} \cdot (\dot{M}_{CCG} + \dot{M}_{CA}) - x_{O_2,RJ} \cdot (\dot{M}_{CCG} + \dot{M}_f + \dot{M}_{CA})}{x_{O_2,RJ} - x_{O_2,recirc}} \quad (A.6)$$

Taking Wüning's definition of the recirculation rate K_v (equation (1.10) or equation (A.4)), the recirculation mass flow \dot{M}_{rec} can be replaced by the expression derived in equation (A.6).

$$K_v = \left(x_{O_2,in} \cdot \frac{\dot{M}_{CCG} + \dot{M}_{CA}}{\dot{M}_{CCG} + \dot{M}_{CA} + \dot{M}_f} - x_{O_2,RJ} \right) \cdot \frac{1}{x_{O_2,RJ} - x_{O_2,recirc}} \quad (A.7)$$

With the excess O_2 ratio n , as is determined in equation (A.8) and the fuel-specific oxidant demand μ_{oxi} , the recirculation rate K_v can be rewritten (see equation (A.9)). This equation allows for the estimation of K_v without exactly knowing the mass flows, but having knowledge about the fuel and the desired O_2 excess.

$$n = \frac{\dot{M}_{CCG} + \dot{M}_{CA}}{\dot{M}_f \cdot \mu_{oxi}} \quad (A.8)$$

$$K_v = \left(x_{O_2,in} \cdot \frac{n \cdot \mu_{oxi}}{n \cdot \mu_{oxi} + 1} - x_{O_2,RJ} \right) \cdot \frac{1}{x_{O_2,RJ} - x_{O_2,recirc}} \quad (A.9)$$

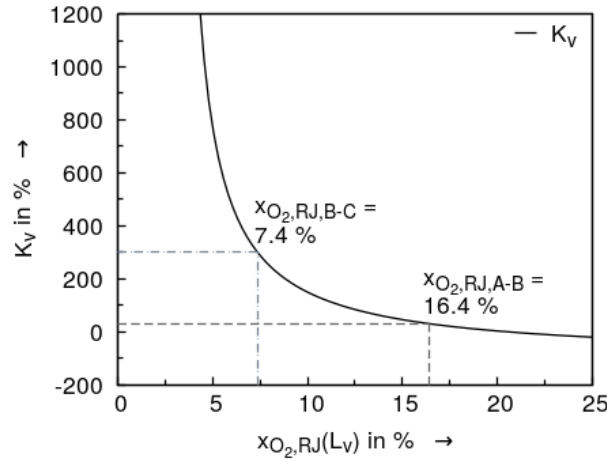


Figure A.3: Recirculation rate K_v over the reactive jet mean O_2 concentration $x_{O_2,RJ}$

In Figure A.3, the recirculation rate K_v is plotted over the O_2 concentration in the reactive jet $x_{O_2,RJ}$, see equation (A.9), for the Calentur coal and air as oxidant. Therefore, an O_2 concentration in the recirculation mass flow of 3.0%, an excess O_2 ratio of 1.15 and a coal-specific air demand of $6.6 \text{ kg}_{air} \text{ kg}_{coal}^{-1}$ are assumed.

Applying the combustion regime limits delineated in Figure 1.1, maximum allowable O_2 concentrations in the reactive jet can be derived for each regime. The maximum allowable O_2 concentration in the reactive jet is calculated to be 7.4%, when the lower limit of the flameless combustion regime (domain C in Figure 1.1) with $K_v = 300\%$ is used in equation (A.9). A higher O_2 concentration would force the combustion in the regime of unstable lifted

flame combustion (domain B in Figure 1.1). Analogously, the minimum O_2 concentration in the reactive jet which is required to maintain a stable flame combustion (domain A in Figure 1.1), can be derived by using the upper regime limit of stable flame combustion in equation (A.9). The O_2 concentration is 16.4 % for $K_v = 30$ %.

It can be derived from Figure A.3 that the mean oxygen concentration in the reactive jet is controlled by the recirculation rate, and that the O_2 concentration $x_{O_2,RJ}$ in the reactive jet determines, whether flameless combustion is achieved or not. From equation (A.5), the main influences on $x_{O_2,RJ}$ are the recirculation mass flow \dot{M}_{rec} , the combustion-air mass flow \dot{M}_{CA} and the mean oxygen concentration of the inflow mass flow rates $x_{O_2,in}$. The latter can only be lowered by external dilution, however which incorporates additional effort and thus penalty. The combustion-air mass flow \dot{M}_{CA} can be varied in a certain range, maintaining the envisaged air ratio n . The recirculation mass rate \dot{M}_{rec} can be adapted by different burner designs, different burner to furnace ratios and other constructive measures. It shall therefore be critically evaluated.

B The Influence of Nozzle Positioning on the Recirculation Rate and the Devolatilization

The positioning of the nozzles is of high importance for achieving flameless combustion conditions. This is firstly due to the definition of the mixing point between combustion-air and coal-carrier-gas jets, i.e. the start of the reaction zone, and secondly, due to the space available for the recirculation mass flow. It is thought that the mixing of both jets is delayed, i.e. prior-to-mixing length L_v increases when the spacing D_{noz} between the combustion-air and coal-carrier-gas nozzles is increased, cf. equation (A.3). Thus, the dilution of both jets is emphasized, as is confirmed by other researchers [82, 130]. Orsino et al. [100] have observed that an increased distance between coal-carrier-gas and combustion-air nozzles supports the development of the reaction zone from lifted flame to flameless combustion. Similar findings are reported by Ristic [115], who conducted experiments at 20 kW_{th} and 300 kW_{th} thermal input, indicating that a higher spacing between combustion-air and coal-carrier-gas nozzles is advantageous. It is expected that arrangements with a lower nozzle number cause a higher recirculation rate K_v , since the space available for recirculating the hot flue gases increases.

Different nozzle position setups are possible: combustion-air nozzles in different numbers and at different positions and distances from the burner central axis; coal-carrier-gas nozzles of different shapes, i.e. hole or annulus, in different numbers and at different positions. The influence of nozzle positioning has been investigated by means of a numerical study conducted with the CFD program code AIOLOS. The burner geometry presented in Section 3.1 is modified to assess different combustion-air pitch-circle diameters D_{CA} and nozzle numbers. The velocity of the jets entering the furnace is held constant.

B.1 Investigated burner geometries

Three different nozzle arrangements of burner prototype PT1 are defined, all of them featuring the central CCG annulus: two combustion-air nozzles on a pitch-circle diameter of $D_{CA,min} = 140$ mm, two combustion-air nozzles on a pitch-circle diameter of $D_{CA} = 270$ mm,

both represented by Figure B.1a; and four combustion-air nozzles on a pitch-circle diameter of $D_{CA,max} = 270$ mm represented by Figure B.1b. $D_{CA} = 270$ mm represents the greatest spacing applicable with respect to constructional restrictions of the test facility. An asymmetrical nozzle arrangement as investigated by Li et al. [82] is not considered in this study.

The investigated geometries of prototype burner PT2 feature the coal-carrier-gas nozzle split in two nozzles, whereas the combustion-air nozzle setup is copied from the PT1 burner with two combustion-air nozzles on a 270 mm pitch-circle. The coal-carrier-gas nozzles are positioned on a same pitch-circle, but rotated by a 90° angle with regard to the combustion-air nozzles, see Figure B.1c. It is aimed to reveal the optimum pitch-circle diameter for the coal-carrier-gas nozzles for the PT2 burner design. Therefore, the combustion-air nozzle position was maintained at $D_{CA} = 270$ mm, and the coal-carrier-gas nozzle pitch-circle diameters of $D_{CCG,min} = 100$ mm, $D_{CCG,med} = 140$ mm and $D_{CCG,max} = 270$ mm were investigated.

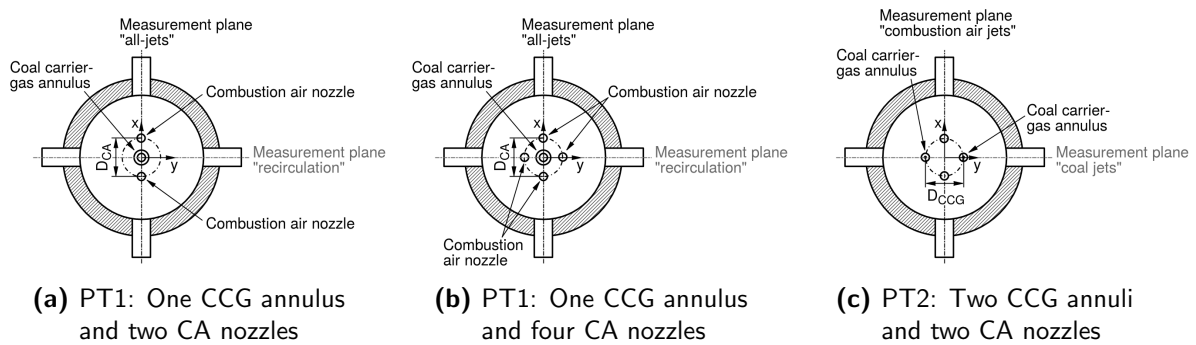


Figure B.1: Investigated coal-carrier-gas and combustion-air nozzle arrangements

B.2 Applied grids and numerical setup

The grids applied in the assessment of the positioning of the coal-carrier-gas and combustion-air nozzles differ from that used in the previously presented computational results. This is mainly due to the chronological order of the work conducted in the course of this thesis. The results have been carefully assessed regarding their independence of the grids in use.

B.2.1 Grid to assess the positioning of the combustion-air nozzles

This numerical study is conducted on a grid based on a cylindrical coordinate system consisting of approximately 235000 cells, representing the furnace dimensions of $L = 2600$ mm and $R = 0.375$ mm. The furnace length L is chosen 200 mm longer than in the assessment of the coal-carrier-gas nozzles positioning in order to capture a potential elongation of the recirculation

zone. Due to the symmetrical nature of both furnace and burner, a 180° section is simulated. The burner is represented by its inlets defined on the furnace front, see Figure B.2a.

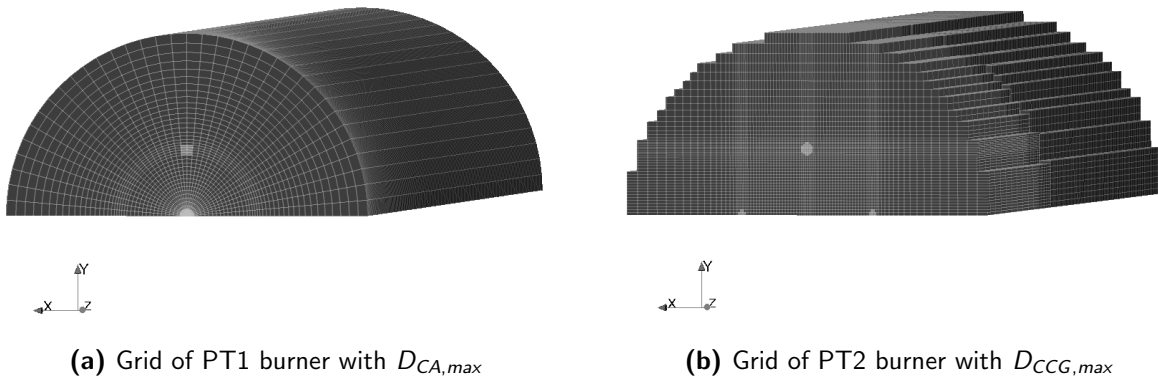


Figure B.2: Numerical domain representation of furnace and burner prototypes

B.2.2 Grid to assess the positioning of the coal-carrier-gas nozzles

Contrary to the study of combustion-air nozzle positioning, the grid used in this study is based on a Cartesian coordinate system with rectangular-shaped cells. The grid used represents the furnace of a length $L = 2400$ mm and the same radius $R = 0.375$ m. Again, a 180° section is modeled due to the symmetrical nature of both furnace and burner.

The grid is further optimized regarding the total number of cells and is modeled by two domains. The number of cells of the top domain changes, because the part downstream and between the coal-carrier-gas nozzles is refined in order to catch the reactions taking place in that zone in the best possible manner. The top domain is modeled by approximately 259000 cells for the smallest pitch-circle diameter $D_{CCG,min} = 100$ mm; approximately 309000 cells are used for the medium diameter $D_{CCG,med} = 140$ mm and approximately 350000 for the largest diameter $D_{CCG,max} = 270$ mm. As the distance between the nozzles increases, the reaction zone between the jets grows and the number of cells goes up. The bottom domain remains unmodified for all three different pitch-circle diameters; it consists of approximately 88000 cells.

Again, the inlets of coal and combustion-air are set on the top of the furnace and are not explicitly modeled. Due to stability reasons, the coal-carrier-gas nozzles are modeled by holes instead of annuli as were used in the experiments. It is assumed that the effect of modifying the diameter between the nozzles can be assessed regardless of the shape of coal-carrier-gas nozzles. The grids for assessing the positioning of the combustion-air nozzles and coal-carrier-gas nozzles are shown in Figure B.2.

B.2.3 Numerical setup

The chosen models are very similar in both studies. They are described in Chapter 4. Different choices are made regarding the pressure correction method which is the SIMPLE method instead of the SIMPLEC method. The turbulence is modeled by the standard $k-\varepsilon$ model which does not perform as well as the RNG $k-\varepsilon$ model recommended in Section 4.7.3. Despite that it might not be the best choice from the recent state of knowledge, its application can be justified as it is used consistently in these studies. The coal combustion is modeled without consideration of tar and soot reactions. The NO_x post-processing uses the NO_x model presented in Section 4.5.4. The initial split of fuel-N is assumed as 50 % volatile-N, i.e. 30 % HCN, 5 % NH_3 and 15 % NO. 50 % of fuel-N is retained in the char and subsequently released as NO. The coal properties are given in Tables 3.3 and 4.2.

The applied relaxation factors differ to those in the main simulations in Chapter 4. They are all set in the range between 0.05 and 0.50, and are compiled in Table B.1.

Table B.1: Applied relaxation factors

Variable ϕ	Assessment of positioning of combustion-air nozzles	Assessment of positioning of coal-carrier-gas nozzles
p	0.30	0.25
w_i	0.20	0.20
k	0.05	0.10
ε	0.05	0.10
h	0.10	0.20
Species	0.30	0.50
Particle classes	0.30	0.30
Radiation source term	0.20	0.20

B.3 Results

The results of assessing the combustion-air nozzle positioning can be summarized as “fewer nozzles and larger spacing lead to a higher internal recirculation rate”. In Figure B.3, the results of the recirculation rate K_v and area-averaged temperature ϑ_{aAv} are depicted. The mixing point of coal-carrier-gas and combustion-air jets is calculated by means of the prior-to-mixing-length L_v as derived in equation (A.3). It is depicted in Figure B.3a by the two blue dotted lines labeled as $L_v(D_{CA,min})$ and $L_v(D_{CA,max})$ for the minimum and maximum combustion-air nozzle position, respectively. From Figure B.3a, it can be seen that the recirculation rate K_v

at the mixing point diminishes when the number of combustion-air nozzles or the combustion-air pitch-circle diameter decrease. Obtained recirculation rates are 260 % and 302 % for four and two combustion-air nozzles at the maximum pitch-circle diameter $D_{CA,max} = 270$ mm, respectively. The recirculation rate decreases significantly to 85 % for the assessed minimum pitch-circle diameter $D_{CA,min} = 140$ mm. The overall recirculation rate maximum of approximately 380 %, obtained for the arrangement of four combustion-air nozzles at the maximum pitch-circle diameter causes the strongest dilution of the reaction zone downstream the mixing point.

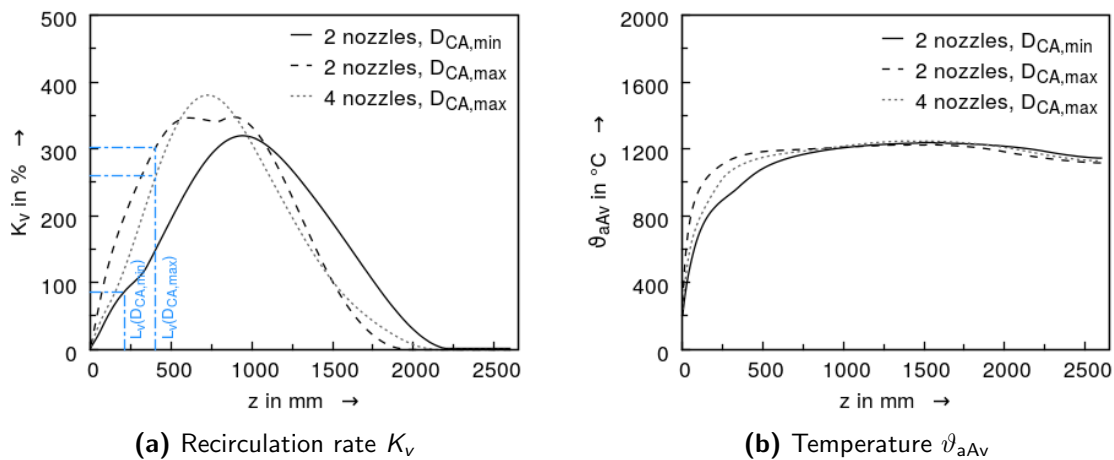


Figure B.3: Effect of combustion-air nozzle position on the recirculation rate K_v and area-averaged temperature ϑ_{aAv} , evaluated with the PT1 burner prototype

The area-averaged temperature results show that a high recirculation rate in the burner vicinity is necessary for a fast heating of the fresh reactants. Peak temperature and the subsequent temperature decrease are similar for all three combustion-air nozzle arrangements, regardless of the recirculation rates achieved in the current setup.

The results of the coal-carrier-gas nozzle positioning study are discussed in Section 4.7.2.

C Modeling Know-How

C.1 Clues and knowledge in numerics

In this section, lessons learned during the work with AIOLOS are explained. It intends to pass the modeling know-how on to other researchers working with AIOLOS.

C.1.1 Relaxation

Relaxation is a very sensitive and case-dependent tool in simulation work. Generally applicable rules are rare, and their application depends on many circumstances, such as boundary conditions, grid refinement, applied models and numeric algorithms. It is obvious that under-relaxation of the iterative process slows down the convergence speed; it is, however, sometimes a necessary measure in order to achieve convergence. The latter applies to most simulations conducted with AIOLOS. The ideal case of all relaxation factors being 1 or close to 1 has been achieved for very simple geometries and moderate flow conditions at fine grids. In AIOLOS, basically all variables calculated by a solver can be subjected to under-relaxation. In the following, the notation as used in the AIOLOS source code is applied. The most important ones are the pressure (*PP*); the velocity components in *x*-, *y*-, *z*-directions (*UU*, *VV*, *WW*); the turbulent kinetic energy (*KK*); the turbulent dissipation rate (*EE*); the enthalpy (*HH*); the species CH₄, H₂, CO₂, O₂, CO, H₂O, tar and soot (*C2*, ..., *C9*); the fuel representatives wet fuel, dry and ash free fuel, dry ash, total char and char particle size classes (*D1*, ..., *D5*); the radiative source term (*SS*). The development of the relative update δ_{rel}^n of the variables which has been introduced in Section 4.1.6, is critical for the assessment of the convergence process. The more the relative update diminishes, the less significant are the changes, i.e. the updates of the variables' values.

The application of relaxation can spoil the derivation of the relative update δ_{rel}^n , as is shown in the following. A variable ϕ is examined. The new value $\hat{\phi}^{n+1}$ based on the *n*-th iteration is derived by resolving equation (4.24). The new update δ^n can now be obtained as given in equation (C.1), already subjected to relaxation by relaxation factor ω_ϕ . The relaxed variable ϕ^{n+1} in the (*n* + 1)-th iteration is calculated as in equation (C.2).

$$\delta^n = \omega_\phi \cdot (\hat{\phi}^{n+1} - \phi^n) \quad (\text{C.1})$$

$$\phi^{n+1} = \phi^n + \delta^n \quad (\text{C.2})$$

A different derivation of the relaxed variable ϕ^{n+1} in the $(n + 1)$ -th iteration is given by equations (C.3) and (C.4). The relaxation factor is applied when ϕ^{n+1} is calculated and thus, the update δ^n remains unrelaxed.

$$\delta^n = \hat{\phi}^{n+1} - \phi^n \quad (\text{C.3})$$

$$\phi^{n+1} = \phi^n + \omega_\phi \cdot \delta^n \quad (\text{C.4})$$

The influence on the relative update δ_{rel}^n becomes obvious by analyzing equation (C.5).

$$\delta_{rel}^n = \frac{\delta^n}{\phi^{n+1}} \quad (\text{C.5})$$

The new variable ϕ^{n+1} is the same, regardless of its derivation from equation (C.2) or (C.4), and thus is the denominator in equation (C.5). It always contains the relaxation factor ω_ϕ which influence becomes small in the course of the iterative progress, because the relaxed update becomes small compared to the variable value ϕ^n .

The numerator is formed by the relaxed or by the unrelaxed update, cf. equation (C.1) or equation (C.3), respectively. The influence of the relaxation factor ω_ϕ is significantly larger in the numerator than in the denominator. Consequently, the relative update δ_{rel}^n can be spoiled if δ^n is calculated by equation (C.1) and the choice of a low relaxation factor ω_ϕ lowers the relative update. This can lead to a wrong assessment of the convergence process: convergence might be assumed due to a low relative update δ_{rel}^n , despite the difference of $\hat{\phi}^{n+1} - \phi^n$ being high and δ^n low only due to a low relaxation factor ω_ϕ .

The Gauss-Seidel and the red-black Gauss Seidel solvers, both available in AIOLOS, allow for relaxation in the solver routine. In the current implementation, the direct in-solver relaxation is only applied when the PISO pressure correction equation is active. The other implemented algorithms, such as the semi-implicit procedure by Stone, the incomplete MLU decomposition and the bi-conjugated gradients do not have the above declared update procedure included.

Most variables in AIOLOS are relaxed in different routines than the solvers. If not specified otherwise below, relaxation takes place in the APMSP routine. The under-relaxation scheme used in this routine was proposed by Patankar [104] and is recommended due to its positive effect on many iterative solution algorithms [37].

The pressure update (PP) can be relaxed in the SIMPLE routine for the SIMPLE, SIMPLEC and ALLSPEED pressure correction methods. The pressure implicit with the splitting of operator (PISO) method instead forces under-relaxation in the solver routine. It is noted that under-relaxation is not recommended in the case of the SIMPLEC pressure correction method, thus ω_{PP} should be 1. The velocity components in x -, y - and z -direction (UU , VV , WW) are under-relaxed in the DVELPCE routine, if the SIMPLEC pressure correction method is active. Otherwise, relaxation is applied in the APMSP routine. The radiative source term (SS) is relaxed in the DOMVREL routine, if the discrete ordinates method is applied for solving the radiative transport equation.

Ferziger and Perić [37] present some recommendations for the choice of the flow-related relaxation factors of the pressure update and the velocity components. In the case of the SIMPLE and ALLSPEED pressure correction methods, the pressure update relaxation factor ω_{PP} is recommended between 0.2 and 0.3, whereas those of the velocity components ω_{UU} , ω_{VV} and ω_{WW} can be 0.8. They obey the relation given as an example in equation (C.6) for the UU velocity component:

$$\omega_{PP} \approx 1.1 - \omega_{UU} \quad (\text{C.6})$$

In the case of the SIMPLEC pressure correction method, ω_{PP} is recommended to be 1, and the velocity relaxation factors shall be chosen to be as high as possible. Experiences in this work show that ω_i greater than 0.8 is sufficient. Relaxation factors of turbulence variables turbulent kinetic energy (KK) and turbulent dissipation rate (EE) can be similarly chosen to those of the velocities. Relaxation factors of other variables presented above, e.g. chemical species, were set to 1 with good experiences. However, their choice is always case-dependent.

Recommended convergence procedure

The following convergence procedure was elaborated in discussions with Habermehl from RWTH Aachen. Generally, under-relaxation of the convergence process is necessary when starting a new simulation. This avoids oscillations or even the abortion of the iteration process. These oscillations can occur when the difference from the initialization to the converged solution is significant and thus the calculated updates are high as well. The relaxation factors can be chosen higher if the initial values of the variables can be guessed close to the final ones, meaning close to the solution. During the convergence process, relaxation factors can be increased, when a local stable minimum of the updates is received. Afterwards, updates can be higher, but shall drop to their previous minimum or even lower. When approaching the converged solution, relaxation factors close to 1 shall be possible. This is a good measure to prove convergence.

Mesh refinement can help to obtain a lower minimum of residuals, see Figure C.5. If and where refinements are required should be derived from the gradients resolved by the recent grid,

see Section C.2. Refinements, however, can also lead to oscillations in the case of turbulence oscillations by formation of a von Karman vortex street which is an unsteady occurrence in a steady-state simulation. Other parameters such as temperatures at a certain position or local energy balance can be additional good measures for the evaluation of the convergence besides the residuals.

C.1.2 A short comparison of the CPD and FG-DVC pyrolysis models

The use of advanced pyrolysis models is promising regarding the increased knowledge about dominant pyrolysis products and the initial nitrogen split. On the downside, some uncertainty in trustworthiness has been experienced during their application in AIOLOS. A brief study and comparison between the CPD and FG-DVC pyrolysis models were conducted by Alysandratou in the course of a student research project. The results are reproduced and commented here in order to give support for answering the question regarding when to choose which pyrolysis model.

In the brief study, the results of simulations conducted with the CPD and FG-DVC models are compared with the results from pyrolysis experiments. Two different experimental setups were found in literature [59], both exhibiting heating rates in the range of 10^4 to 10^5 K s⁻¹: a drop tube reactor and a flat flame burner. The heating rates are comparable to those in the KSVa furnace. Final pyrolysis temperatures are reported as 547 °C, 807 °C and 947 °C for the drop tube experiments and 1377 °C for the flat flame burner experiments. Three experimentally investigated coals, Blue #1, Adaville #1 and Deadman, have been chosen due to their similar composition to the Calentur coal used in this work, see Table C.1.

Table C.1: Ultimate and proximate analysis data of the Blue #1, Adaville #1, Deadman and Calentur coals

		Drop tube	Flat flame burner		For comparison
γ_i, H_o, H_u , dry basis		Blue #1	Adaville #1	Deadman	Calentur
Ultimate analysis					
C	in %	71.7	69.91	66.99	68.81
H	in %	5.30	5.03	4.59	
N	in %	1.26	1.13	1.34	1.34
S	in %	0.63	1.00	0.67	0.96
O (by difference)	in %	17.7	19.38	13.97	13.32
Proximate analysis					
Ash	in %	3.29	3.55	12.44	11.03
Volatiles	in %	46.61	43.98	35.55	37.62

In order to derive the input parameters of the CPD model, the empirical correlation by Genetti et al. [48] has been used. For the FG-DVC model, a program-inherent pre-processor generates the required input data based on the coal composition.

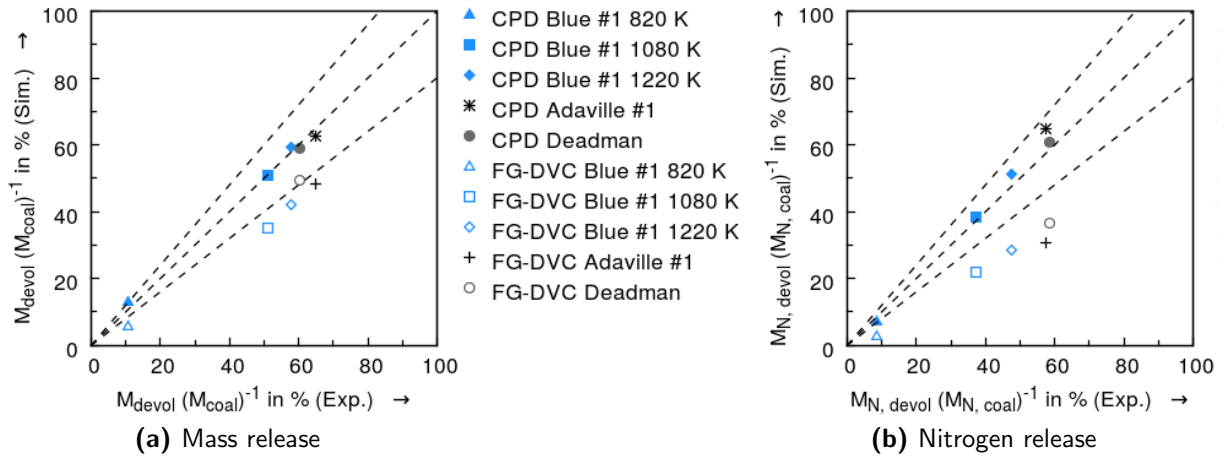


Figure C.1: Cross-comparison of pyrolysis simulations and experiments

In Figure C.1, the mass release and the nitrogen release obtained from simulations with the CPD and the FG-DVC models are compared against the experimental results. Three lines are drawn for assistance in the diagrams: a 0% deviation line, and two 20% deviation lines which limit the acceptable deviation. It is obvious that higher final pyrolysis temperatures lead to higher mass release, cf. the Blue #1 results. It can be seen for the mass release that the simulations conducted with the CPD model (solid symbols) match the experimental results very well. In contrary, the FG-DVC model simulation results (empty symbols) are outside the $\pm 20\%$ range, and thus show significant deviations from the experimental results. Regarding the nitrogen release, this trend is even more pronounced.

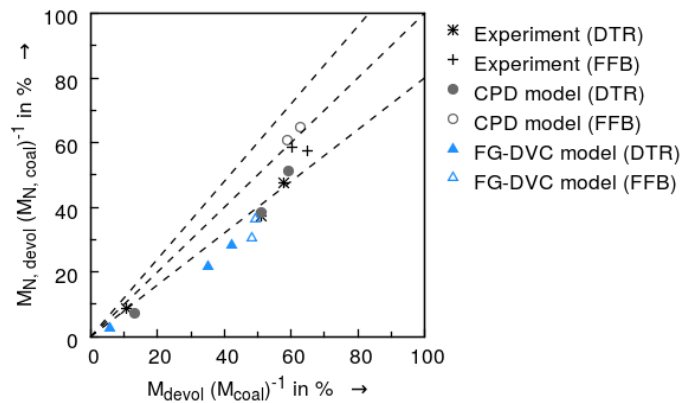


Figure C.2: Cross-comparison of mass and nitrogen release in pyrolysis simulations and in drop tube reactor (DTR) and flat flame burner (FFB) experiments

Hambly [59] reported from his drop tube experiments that the nitrogen release is weaker than the mass release. This is reproduced by both pyrolysis models, as can be seen from Figure C.2. The experimental flat flame burner results also show the same tendency regarding the mass vs. nitrogen release. The CPD model slightly overpredicts the nitrogen release for two cases with high mass and nitrogen release.

It is noteworthy that the two pyrolysis models give different species results of nitrogenous compounds after pyrolysis. The FG-DVC model specifies the char-N, tar-N and light-gas-N portions. The latter is detailed into HCN and NH_3 fractions, as required as input for the AIOLOS NO_x model. The CPD model also returns the char-N and tar-N portions, but HCN is the only respected light-gas-N fraction. This is the reason why the procedure to derive the NH_3 fraction has been developed, as described in Section 4.5.4.

C.2 The simple Cartesian test case

The simple test geometry presented in Section 4.6 is detailed in this section, jointly with further information on the applied models. In addition to the investigation of grid refinement and the impact of increased inlet velocities in Section 4.6, the application of periodic boundary conditions, of the domain decomposition and the variation of relaxation factors are assessed.

C.2.1 Mesh and boundary conditions

The computational mesh is square in cross-section, with an edge length of 0.2 m and a length of 2.5 m. It features two centered inlets; the inner one is of round shape with a radius of 0.012 m supplying coal and coal-carrier-gas air. The outer annulus is adjacent to the inner inlet with an outer radius of 0.024 m, supplying the combustion-air at the inlet velocity w_{CA}^0 . In the w_{CA}^+

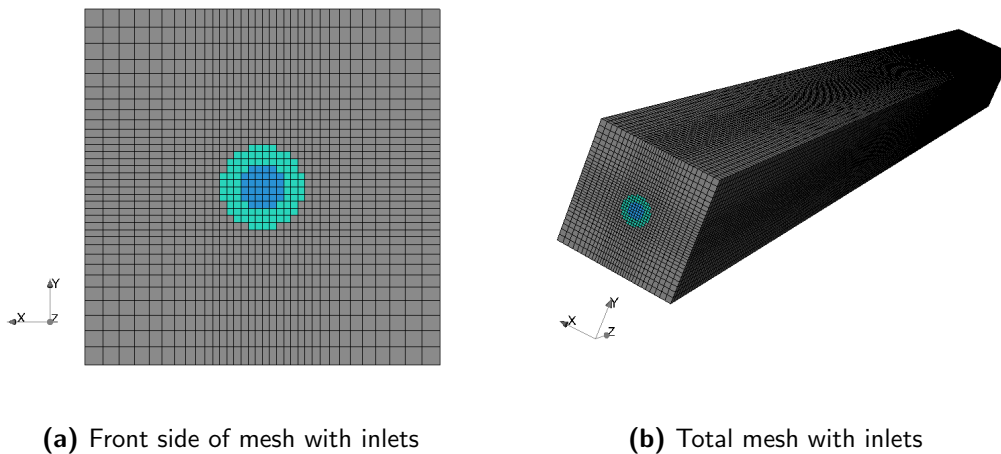


Figure C.3: Mesh of the simple Cartesian test case in the baseline refinement

and the w_{CA}^{++} cases, the outer annulus radius is reduced to 0.015 m and 0.014 m, respectively. The outlet is located on the opposite side of the furnace covering the entire cross-section.

The furnace is discretized by cuboids. In the baseline case, discretization in the x - and y -directions varies from 0.01 m at the outer edges to 0.004 m in the center region. A constant spacing of 0.004 m is used to discretize the inlets area. Discretization in the z -direction is constant with a spacing of 0.01 m. The entire domain is thus modeled by 289000 cells. The discretized geometry with inlets and outlet is shown in Figure C.3.

For the investigation of the influence of spatial resolution, the grid is once coarsened and once refined, resulting in grids of 80828 and 644688 cells, respectively. The evaluation of increased inlet velocities is conducted with inlet velocities of 16.4 m s^{-1} in the w_{CA}^0 case, 82.2 m s^{-1} in the w_{CA}^+ case and 122.2 m s^{-1} in the w_{CA}^{++} case. Both are described in Section 4.6. The cases listed in Table C.2 summarize their characteristics.

Table C.2: Characteristics of the simple Cartesian test case

Case name	Number of cells	Minimum cell size (L, W, H)	Initial inlet velocity w_{CA}	Ma_{CA}
Baseline w_{CA}^0	289000	0.004 m, 0.004 m, 0.010 m	16.4 m s^{-1}	0.02
Coarse w_{CA}^0	80828	0.006 m, 0.006 m, 0.015 m	16.4 m s^{-1}	0.02
Refined w_{CA}^0	644688	0.003 m, 0.003 m, 0.0075 m	16.4 m s^{-1}	0.02
Baseline w_{CA}^+	289000	0.004 m, 0.004 m, 0.010 m	82.2 m s^{-1}	0.16
Refined w_{CA}^+	644688	0.003 m, 0.003 m, 0.0075 m	82.2 m s^{-1}	0.16
Refined w_{CA}^{++}	644688	0.003 m, 0.003 m, 0.0075 m	122.2 m s^{-1}	0.25

Two periodic boundary types are investigated, based on the baseline w_{CA}^0 case: the axis-symmetric and the point-symmetric boundary type. The grid is cut in half alongside its main axis z in the center of the xy -plane, i.e. the entire flow compartment is represented by a 180° section and 144500 cells. The symmetry boundary is applied in the xz -plane, see Figure C.4a. The axis-symmetric boundary type mirrors the velocity in the y -direction on the symmetry plane, not allowing for convective fluxes across the boundary. It is applicable if no significant convective fluxes normal to the periodic boundary plane are expected, for instance in non-swirling flows. The point-symmetric boundary type instead transposes the y -velocities across the symmetry plane, thus allowing for convective fluxes across the boundary. Both boundary types are investigated in the axis-sym- 180° case and point-sym- 180° case. They are represented in Figures C.4b and C.4c, respectively.

Domain decomposition as described by Risio [113] is assessed by dividing the domain into two sub-domains. This procedure is advantageous if a local variation of the discretization is necessary, e.g. in the burner vicinity, or if different cell types are used. Two cases with a two-domain decomposition are investigated, based on the baseline w_{CA}^0 case. In the one case,

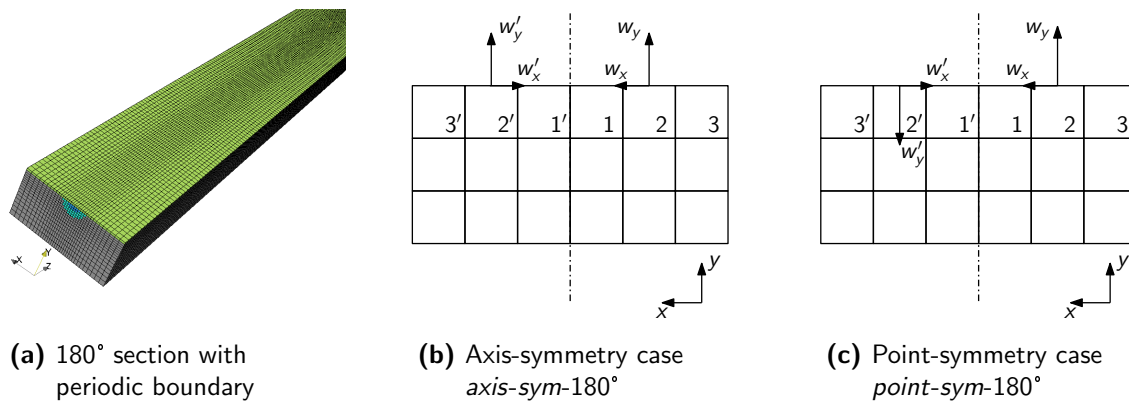


Figure C.4: Periodic boundary conditions in the simple Cartesian test case

no changes are applied to the grid refinement; in the other case, the refinement of the outlet sub-domain is coarsened. The specifications of the investigated cases are given in Table C.3.

Table C.3: Characteristics of the domain decomposition cases

Case name	Number of cells	Minimum cell size (L, W, H)	Initial inlet velocity w_{CA}	Ma_{CA}
Axis-sym-180°	144500	0.003 m, 0.003 m, 0.0075 m	16.4 m s ⁻¹	0.02
Point-sym-180°	144500	0.003 m, 0.003 m, 0.0075 m	16.4 m s ⁻¹	0.02
2-domains	289000	0.004 m, 0.004 m, 0.010 m	16.4 m s ⁻¹	0.02
2-domains coarse	238150	0.004 m, 0.004 m, 0.010 m	16.4 m s ⁻¹	0.02

Lastly, the pressure correction methods SIMPLE and SIMPLEC are investigated in conjunction with the relaxation factors for damping the updating speed of the variables in the iteration process. The choice of the pressure correction method correlates tightly with the choice of the relaxation factors. As pointed out in Section C.1, the relaxation factors of the pressure, i.e. mass defect, update and of the velocity components shall obey equation (C.6) if the SIMPLE algorithm is applied. Besides, the equal choice of the relaxation factors of pressure and velocity components is tested. It is found that the correlation given in equation (C.6) gives the faster convergence rates. The under-relaxation of the pressure, i.e. mass defect, update is not required, if the SIMPLEC pressure correction method is used, see Section C.1. Instead, the velocity updates and thus the turbulence-related updates primarily need to be subjected to under-relaxation. The relaxation factors can be chosen to be as high as possible to ensure stable, but fast convergence. Others, such as species, enthalpy or char particle size distribution, are set to 1.0, i.e. no under-relaxation is applied. The cases with the applied pressure correction methods and the corresponding relaxation factors are given in Table C.4. The simulations are conducted with the mesh and inlet velocities of the baseline w_{CA}^0 case.

Table C.4: Pressure correction methods and correlated relaxation factors applied in the simple Cartesian test case

Case name	Pressure correction method	ω_{PP}	ω_{UU}
Baseline SIMC	SIMPLEC	1.00	0.90
SIMP eq. (C.6)	SIMPLE	0.25	0.85
SIMP max.	SIMPLE	0.85	0.85

Emphasis is placed on the assessment of the fluid dynamic behavior and achievable accuracy of AIOLOS without neglecting the reactive part of the code. Therefore, the updates of the mass defect, of the velocities in all three spatial directions and of the turbulence variables turbulent kinetic energy and dissipation rate are discussed below. Moreover, convergence indicators energy balance and balances of elements C, H, O and ash are presented as well.

The boundary conditions of the simple Cartesian test case simulations are maintained for all cases. The coal-carrier-gas is air at a mass flow rate of 0.0025 kg s^{-1} and an inlet temperature of $200 \text{ }^\circ\text{C}$. A bituminous coal is supplied at a mass flow rate of 0.002 kg s^{-1} ; its composition and particle size distribution are similar to those given in Sections 3.4 and 4.2. The combustion-air mass flow rate is 0.0115 kg s^{-1} at an inlet temperature of $370 \text{ }^\circ\text{C}$. This results in an overall air ratio of 1.19. The wall temperatures are globally set to $800 \text{ }^\circ\text{C}$. The convective heat transfer coefficient to the walls is maintained at $25 \text{ W (m}^2 \text{ K)}^{-1}$; the radiative property of the wall is defined by its emissivity of 0.65.

The physical aspect of radiation is accounted for by the discrete ordinates method as described in Chapter 4. The gas absorption coefficient is chosen to be constant. The turbulence of the flow is modeled by means of the RNG k - ε model. The pressure correction method in use is either the SIMPLE or the SIMPLEC algorithm.

The UPWIND interpolation scheme and the red-black Gauss Seidel solver are applied to all computed variables with exception of the mass defect. It does not require an interpolation scheme from the cell center to the cell faces and thus, the strongly implicit procedure is used. If not stated otherwise, most variables are computed without relaxation, i.e. the relaxation factor is 1. Exceptions are made for the mass defect, the velocity components and the turbulence quantities. If the SIMPLE pressure correction method is applied, a relaxation factor of 0.25 is used for the mass defect and relaxation factors of 0.85 are used for the velocity and turbulence variables w_x , w_y , w_z , k , and ε . In the case of the use of the SIMPLEC pressure correction scheme, relaxation of the mass defect is not required, whereas the relaxation factors of the velocity and turbulence quantities equal 0.9.

The simulations were performed using a parallelized source code version enabling the use of all cores available on a socket. Due to the relatively low number of cells, computation time was deemed acceptable on a local machine featuring a quad-core Intel i5 processor.

C.2.2 Results

The results are presented firstly assessing the grid refinement and the influence of the inlet velocities; secondly evaluating the symmetric boundary conditions; and thirdly assessing the domain decomposition. A summarizing paragraph deals with the relaxation experiences from this brief study. The computed results are discussed using the updates of the mass defect, the velocities in x - and z -, i.e. in the tangential and axial direction, and the CO concentration as given in equation (4.32), averaged over the last 1000 iterations. The relative update of the CO concentration allows for the evaluation of the species convergence. Elemental balances of C, H, O and ash are not shown in the following, since all results were found to be in a range of $\pm 0.15\%$. Accuracy in the same order of magnitude was obtained for the energy balance converging to values in the range of $\pm 0.40\%$. Thus, the simulations are found to obey the two convergence criteria energy and elemental balance defined in Chapter 4, if not stated otherwise.

Influence of the grid refinement and of the initial inlet velocities

The results of the cases in Table C.2 are presented in Figure C.5. Simulations were run up to 15000 iterations, to ensure the achievement of a stable state of convergence.

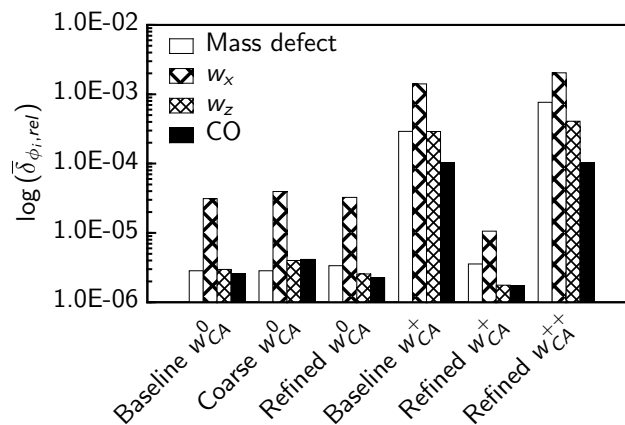


Figure C.5: Evaluation of the grid refinement and of the initial inlet velocities

A decreasing and therefore positive trend of all updates, as derived from equation (4.32), can be seen in Figure C.5 for an increasing spatial resolution and a constant inlet velocity w_{CA} . For the moderate inlet velocity w_{CA}^0 of 16.4 m s^{-1} , the update of the mass defect remains very similar throughout the change in spatial resolution. Updates of velocity components w_z and

w_x and of the CO species show some improvements within the same order of magnitude. It is generally noted that the relative updates of radial and tangential velocities, here represented by w_x , are about one order of magnitude higher than those of the velocity w_z which corresponds to the main flow direction. This was also found when the grid was modified with x as the main flow direction. For the intermediate inlet velocity w_{CA}^+ of 82.2 m s^{-1} , the enhancement by higher spatial grid resolution is eye-catching, since all updates are lowered by about two orders of magnitude. Comparing the baseline mesh and the refined mesh results for the inlet velocities w_{CA}^0 , w_{CA}^+ and w_{CA}^{++} , one can conclude that higher inlet velocities demand a higher spatial resolution, in order to obtain the same reduction of updates as at lower velocities.

Influence of applying symmetry boundary conditions and domain decomposition

Periodic boundaries are investigated by the two cases axis-sym-180° and point-sym-180°. The simulation with axis-symmetry applied to the periodic boundary shows results comparable to the reference case baseline 360°. Elemental and energy balance are inside the limits of $\pm 2\%$. In contrary, the simulation with point-symmetry applied to the periodic boundary violates the energy balance criterion with a computed result of -2.1% . To rank this result, the other simulations achieved energy balance results between 0% and -0.33% . The same trend is seen for the elemental balances of C, H, O and ash: the results of the point-sym-180° case are 1.63% (C), 0.03% (O), 1.64% (H) and 1.68% (ash), compared to -0.03% (C), -0.01% (O), -0.02% (H) and 0.0% (ash) for the reference case.

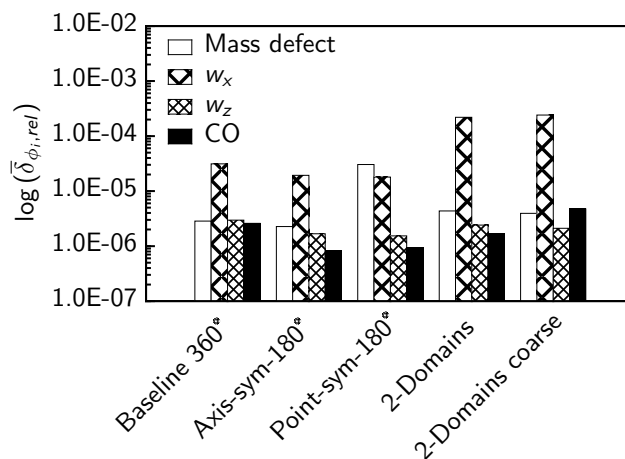


Figure C.6: Results with periodic boundaries

In Figure C.6, the updates of the local mass defect, of the axial and tangential velocities and of the species CO are shown. The achievable accuracy for the mass defect is in the magnitude of $1.00E-06$ for this mesh, achieved by the reference and the axis-sym-180° case. In comparison, the mass defect in the point-sym-180° case is one order of magnitude higher. The CO update is instead slightly lower in both cases with applied periodic boundaries.

When analyzing the effect of domain decomposition on the accuracy, the updates of the mass defect and of the tangential velocity increase. This is attributed to coupling errors occurring, when variable values are transferred from one to the other sub-domain. The gentle increase of the CO update instead can be related to the coarsened grid of the downstream part of the furnace.

Pressure correction methods and relaxation factors

Two pressure correction methods, SIMPLE and its derivative SIMPLEC, were applied in this brief study. In Figure C.7, the updates for both pressure correction methods are shown. One can see that the results are very comparable except for the mass defect update which is one order of magnitude higher in the SIMPLE case. This might be attributed to the fact that the velocity correction is neglected in the SIMPLE algorithm, whereas it is taken into account in the SIMPLEC algorithm (cf. Section 4.4.1). Otherwise, there are no significant differences between both cases.

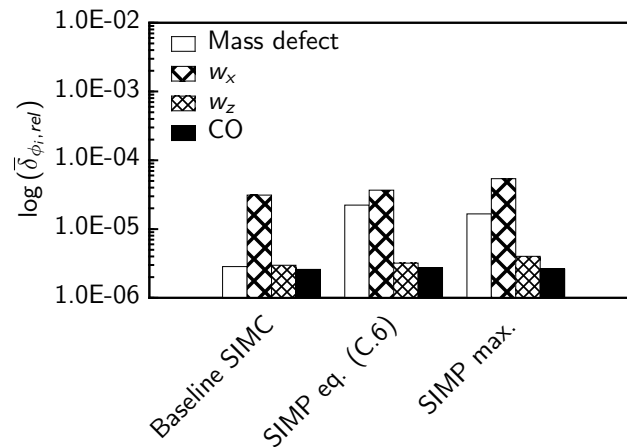


Figure C.7: Updates of mass defect, w_x , w_z and CO for SIMPLE / SIMPLEC pressure correction methods and different relaxation factors

Assessing the influence of the choice of different relaxation factors on the convergence rate of the solution procedure, the iteration count is taken from where a stable horizontal trend of the updates has been identified. For the SIMPLE simulations, the relaxation factors of $\omega_{PP} = 0.25$ and $\omega_{UU} = 0.85$ give the best convergence rates, with stable trends after 2100 iterations. The highest initially applicable relaxation factors are $\omega_{PP} = 0.85$ and $\alpha_{UU} = 0.85$. Stable trends are observed from 2500 onwards. In the SIMPLEC simulations, the relaxation factors of $\omega_{PP} = 1.00$ and $\omega_{UU} = 0.90$ result in the most stable solution procedure, with convergence after 3000 iterations. A higher initial choice of relaxation factor ω_{UU} did not result in a stable convergence process. However, it has been increased up to $\omega_{UU} = 0.99$ after a simulation start with $\omega_{UU} = 0.90$.

Summary of the brief study with the simple Cartesian test case

It has been shown that grid refinement, i.e. higher spatial resolution, can improve the simulation results and the achievable accuracy. It has been also found that a certain accuracy limit exists, set by the computing machine, the program code and other environmental variables. Therefore, a numerical grid can also have too many cells which should be avoided regarding the convergence speed. On the other hand, altering boundary conditions, e.g. higher initial inlet velocities, can enforce the necessity to refine the grid in order to attain the desired accuracy.

Symmetric boundaries can reduce the number of cells and therefore computational time, thus their application is advantageous. If possible, axis-symmetric boundary conditions are applied, due to their better convergence behavior.

Domain decomposition has been found to influence the convergence behavior only mildly. If the grid is locally coarsened, the achievable accuracy can be downgraded.

Regarding the use of the SIMPLE or the SIMPLEC pressure correction method, there are few differences. The SIMPLE algorithm leads to a faster convergence, but the SIMPLEC algorithm ensures a lower mass defect and allows for the application of higher relaxation factors. The relaxation factors shall be chosen to be as high as possible or shall be increased during the convergence process, in order to avoid the stop of the convergence procedure at an illusive state. The initial and final choice of relaxation factors is case-dependent.

C.3 Furnace wall temperatures measured in experiments and simulations

The furnace wall temperature is an important boundary condition in furnace simulations with a strong radiative heat transfer. They are obtained from thermocouples located in the furnace wall, exposed to the same conditions as the furnace wall surface. The measured furnace wall temperatures are given in Table C.5.

Comparison with the gas temperature, measured by suction pyrometry, discloses that gas temperatures at a radial position of $x = 300$ mm are very similar to the measured temperatures at the furnace wall at $x = 375$ mm in the investigated setup. The advantage of using measured gas temperatures as boundary conditions is a higher availability, due to a dense measurement grid. Because of this, gas temperatures at $x = 300$ mm are set as furnace wall boundary conditions in the presented simulations. An exception is made for the FLAME condition, where no gas temperatures were measured and thus the measured wall temperatures are used. They are given in Table C.6. The z -coordinate denotes the further end of a wall section with constant temperature given in the same row. For example, in the FLAME_{as} case, a temperature of 1198 °C is applied to the wall section expanding from $z = 155$ mm to $z = 380$ mm.

Table C.5: Measured furnace wall temperatures of the investigated operating conditions, see Table 3.2

Cases	PT1		PT2		unstaged	air-staged
	FLOX _{CO₂}	FLOX _{air}	FLOX _{CO₂}	FLOX _{air}	FLAME	FLAME _{as}
z in mm	ϑ_W in °C		ϑ_W in °C		ϑ_W in °C	
80	—	—	1021	1033	—	—
230	—	—	1015	1030	—	—
530	1045	1144	—	1030	1215	1104
890	957	946	1101	1115	1215	1208
1230	1077	1156	998	1097	1135	1180
1570	992	815	890	1007	1059	1091
1890	910	1012	996	1014	938	927
2230	910	943	930	951	870	897
2570	906	929	927	936	893	890

Table C.6: Furnace wall temperatures used in simulations

Cases	PT1		PT2		unstaged	air-staged
	FLOX _{CO₂}	FLOX _{air}	FLOX _{CO₂}	FLOX _{air}	FLAME	FLAME _{as}
z in mm	ϑ_W in °C		ϑ_W in °C		ϑ_W in °C	
155	1031	1121	992	1042	—	1143
380	1050	1118	970	1013	—	1198
710	1064	1156	1003	1076	—	1256
1060	1074	1174	1052	1080	—	1212
1400	1064	1136	1030	1080	—	1136
1730	1024	1022	937	1007	—	1004
2060	1013	1058	980	1010	—	—
2400	970	1011	893	972	—	915
5900	912	955	900	912	—	826

C.4 Nitrogen balance in AIOLOS

A nitrogen balance is introduced in AIOLOS, based on the molar amount of all nitrogenous compounds in order to supervise the correct implementation of the NO_x reaction mechanism. This is because the NO_x reaction mechanism is decoupled from the main simulation and is solved in a post-processing step, as explicated in Section 4.5.4. Thereby, an error is induced which is negligible regarding the calculation of concentrations, but relevant for source code development. The nitrogen balance is depicted in Figure C.8.

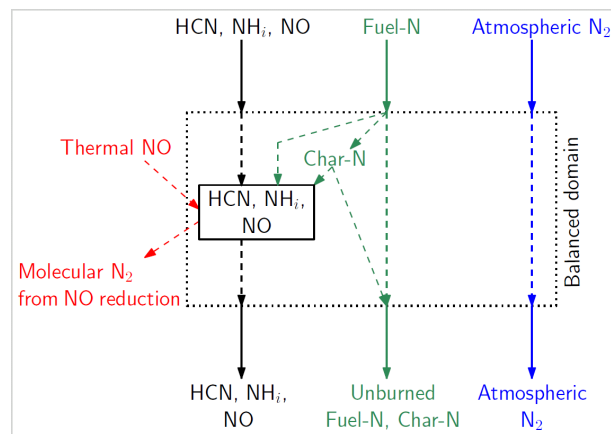


Figure C.8: Nitrogen balance developed for NO_x post-processing

This nitrogen balance accounts for all sinks and sources on a nitrogen molar basis within the domain of interest. The molar amount of atmospheric N_2 originates from the main combustion simulation and is maintained during post-processing. The fuel-N is balanced respecting the different conversion paths, such as char-N and total volatile-N. If residence time is too short to attain complete fuel burnout, some nitrogen might leave the balanced domain as unburned fuel-N. Gaseous nitrogenous compounds such as HCN, NH_3 and NO can enter the balanced domain, but are usually formed within the domain by fuel-N conversion and thermal NO formation. Molecular N_2 from NO reduction leaving the balanced domain is treated as a nitrogen sink. Thermal NO is instead formed from atmospheric N_2 ; its molar amount, however, is retained due to the post-processing approach. Thus, thermal NO must be accounted for as a nitrogen source. By this approach, the observed errors in the nitrogen balance could be reduced to $\pm 2\%$ for a correct implementation.